Delft University of Technology

Bridging cell and tissue mechanics using microfluidics

Boot, R.C.

DOI

Publication date
2024

Document Version
Final published version

Citation (APA)
Boot, R. C. (2024). *Bridging cell and tissue mechanics using microfluidics*. [Dissertation (TU Delft), Delft University of Technology]. https://doi.org/10.4233/uuid:de4118a1-80b5-45fd-90e6-69546ac3b9d0

Important note
To cite this publication, please use the final published version (if applicable).
Please check the document version above.

BRIDGING CELL AND TISSUE MECHANICS USING MICROFLUIDICS

BRIDGING CELL AND TISSUE MECHANICS USING MICROFLUIDICS

Proefschrift

ter verkrijging van de graad van doctor
aan de Technische Universiteit Delft,
op gezag van de Rector Magnificus prof. dr. ir. T.H.J.J. van der Hagen,
voorzitter van het College voor Promoties,
in het openbaar te verdedigen op vrijdag 11 oktober 2024 om 12:30 uur

door

Ruben C. BOOT

Master of Science in Applied Physics,
Technische Universiteit Eindhoven, Nederland,
geboren te Jette, België.

Dit proefschrift is goedgekeurd door de

promotor: dr. P.E. Boukany
copromotor: prof. dr. G.H. Koenderink

Samenstelling promotiecommissie:

Rector Magnificus,	voorzitter
Dr. P.E. Boukany,	Technische Universiteit Delft, promotor
Prof. dr. G.H. Koenderink,	
	Technische Universiteit Delft, copromotor

Onafhankelijke leden:

Prof. dr. V. Garbin	Technische Universiteit Delft
Prof. dr. E.H.J. Danen	
	Universiteit Leiden
Dr. M.E. Aubin-Tam	Technische Universiteit Delft
Dr. K. Guevorkian	Institut Curie, Frankrijk
Dr. D. Vorselen	Wageningen University & Research

An electronic version of this dissertation is available at
http://repository.tudelft.nl/.

For Dolores Cava and Stan Siebelink

Imagine if one day we'd actually do it.

Zaid Rahman

CONTENTS

SUMMARY

The human body is a construction site brimming with internal processes that steer our senses, heal our wounds and make us age. If tissues and organs are scaffolds, then cells are the bricks. Sticking to each other, these minuscule "water balloon-esque" containers filled with proteins are charged with a multitude of tasks. Think about cell division, growth and migration, requiring the cells to change shape when they either generate or are themselves subjected to physical forces. This deformational response, termed cell mechanics, is directly related to the properties of tissues as a whole. Tissue mechanics plays an essential part in initial stages of life as well as in the development of diseases such as cancer. Think about tissues wrapping around each other during embryo growth, or cells leaving a primary tumour to metastasize through the body. Studying tissue mechanics and its dependency on cellular properties therefore forms the key topic in this dissertation.

When letting multiple cells stick to each other in a well, they will aggregate into a spherical ball termed spheroid. Spheroids are a popular model to study the relation between cell and tissue mechanics as they recreate the three-dimensional environment and multicellularity of *in vivo* tissues. Similar to liquid droplets, their surface resists deformation due to a specific tissue surface tension. This tension depends on the strength with which the cells stick to each other, alongside the individual robustness of each cell. Tissue surface tension is directly involved in tissue sorting and fusion, as a tissue with a low surface tension will envelop another tissue with a high surface tension. Spheroid surface tension therefore is an important parameter to measure when experimentally investigating the relation between cell and tissue mechanics. We lay out the available biophysical tools to measure spheroid mechanics through a literature review in **chapter 2**. Additionally, we explain existing theoretical frameworks for spheroid surface tension, and provide implications of cell sorting and tissue mechanics for cell migration and cancer metastasis.

Unfortunately, most existing techniques to measure spheroid mechanics are low in throughput and require tedious handling. For single cell mechanics, many research groups have resorted to the use of microfluidic devices. These chips allow the manipulation of fluids on the microscale by flowing them through micron-sized channels. Cells flowing along with the fluid will squeeze through the narrow channels, allowing rheological measurements of their mechanical properties. Inspired by a previous microfluidic device that aspirated cells in parallel, we have scaled and modified the design to perform spheroid aspiration in parallel. In **chapter 3**, we introduce our microfluidic micropipette aspiration device that allows for high-throughput mechanophenotyping of multicellular spheroids. Here, spheroids are loaded into individual aspiration pockets and deformed in parallel to quantify their mechanics. We show how the device provides accurate spheroid deformation data in comparison to previous studies with a significant increase in throughput (from tens to hundreds of spheroids).

Previously, spheroid surface tension was shown to depend on the pressure with which the spheroid is aspirated, indicating a putative reinforcement of the cells in response to the applied force. Benefiting from the improved throughput of our microfluidic device, we investigated the influence of cell contractility and duration of the applied force on spheroid deformation and its derived surface tension. In **chapter 4**, we demonstrate that larger spheroid deformations result in faster retraction of the cells in the device once the pressure is released, regardless of cellular contractility or applied pressure. Our results therefore indicate deformation-dependent spheroid mechanics and challenge whether spheroid surface tension reinforces.

As abnormal cell mechanics are highly involved in cancer progression, the final part of this dissertation focuses on providing microfluidic tools to unravel the relation between cancer cell deformability and migration. As it turns out, cells have a larger metastatic potential (meaning they are more prone to form secondary tumours) when travelling together as clusters of cells instead of individually migrating. In **chapter 5**, we therefore introduce microfluidic devices to enable the investigation of cluster migration and its advantages over single-cell migration. First, we designed a microfluidic device to study cell deformability with high throughput by flowing cells through parallel blood vessel-sized constrictions. With this device, we demonstrated that differences in cellular stiffness do not directly influence cell strain in the narrow constrictions. Second, we created several microfluidic designs to investigate single cell and cluster cell migration through narrow constrictions in different shapes and sizes. Proof-of-concept experiments demonstrated how live high resolution imaging of cell migration through these constrictions is feasible and opens multiple possibilities to investigate the link between cell deformability and cluster migration.

Finally, we conclude this dissertation in **chapter 6** with a brief outlook on potential future experiments. Most importantly, we believe that a focus on gap junctions, the intercellular connections that allow the exchange of ions and fluids between the cells, could shine further light on spheroid surface tension and its dependency on spheroid size.

Samenvatting

Het menselijk lichaam is een bouwwerf die bruist van de interne processen om onze zintuigen te sturen, onze wonden te helen en ons te laten verouderen. Als weefsels en organen hierbij de steigers zijn, dan zijn cellen de bakstenen. Plakkend aan elkaar worden deze minuscule, "waterballon-achtige", met proteïnen gevulde containers opgezadeld met een veelvoud aan taken. Denk aan celdeling, groei en migratie, waarbij een vereiste is dat de cellen hun vorm aanpassen om fysieke krachten uit te oefenen of zelf te ondergaan. Deze mate van vervorming, genaamd celmechanica, is direct verwant aan de eigenschappen van het weefsel als geheel. Weefselmechanica speelt een essentiële rol in de beginfase van het leven als bij de ontwikkeling van ziektes zoals kanker. Denk hierbij aan weefsels die om elkaar heen kruipen tijdens de groei van een embryo, of cellen die een primaire tumor verlaten om uit te zaaien in het lichaam. De studie van weefselmechanica en de afhankelijkheid van cellulaire eigenschappen vormt daarom het centrale onderwerp in deze thesis.

Als je meerdere cellen in een gefabriceerd kuiltje aan elkaar laat plakken, zullen ze een ronde bal vormen die we een spheroid noemen. Spheroids zijn een populair model om de relatie tussen cel- en weefselmechanica te bestuderen aangezien ze de driedimensionale omgeving en multicellulariteit van *in vivo* weefsels nabootsen. Net als bij vloeistofdruppels weerstaat hun oppervlak vervorming door een specifieke weefseloppervlaktespanning. Deze spanning is afhankelijk van de kracht waarmee de cellen aan elkaar plakken, alsook van de individuele robuustheid van elke cel. Weefseloppervlaktespanning is rechtstreeks betrokken bij het ordenen en mengen van weefsels, waarbij een weefsel met een lage opervlaktespanning zich om een weefsel met hoge oppervlaktespanning heen zal vouwen. Spheroid oppervlaktespanning is zodoende een belangrijke parameter om te meten tijdens de experimentele bestudering van de relatie tussen cel- en weefselmechanica. Aan de hand van een literatuuroverzicht presenteren we in **hoofdstuk 2** de beschikbare technieken om spheroid mechanica te bestuderen. Verder leggen we de bestaande theoretische kaders voor spheroid oppervlaktespanning uit, en bespreken we de implicaties van celordening en weefselmechanica voor celmigratie en kankermetastase.

Jammer genoeg hebben bestaande technieken om spheroid mechanica te bestuderen een lage omzet en een moeizame omgang. Voor het bestuderen van celmechanica zijn meerdere onderzoeksgroepen daarom overgestapt op het gebruik van microfluïdische apparaten. Deze chips maken de manipulatie van vloeistoffen op de microschaal mogelijk door ze door kanaaltjes met een ordegrootte van microns heen te stromen. Cellen die in de vloeistof meestromen zullen zich door de nauwe kanaaltjes heen wringen, wat rheologische metingen van hun mechanica mogelijk maakt. Geïnspireerd door een eerdere microfluïdische chip die cellen parallel naast elkaar kan aspireren, hebben wij het ontwerp opgeschaald en aangepast voor de parallele aspiratie van spheroids. In **hoofdstuk 3** introduceren we onze microfluïdische micropipet aspiratie chip die de

hoge-omzet mechanofenotypering van multicellulaire spheroids mogelijk maakt. Hierbij worden spheroids in individuele aspiratiehokjes geladen en parallel aan elkaar vervormd om hun mechanica te kwantificeren. We tonen aan dat de chip accurate spheroid vervorming data produceert in vergelijking met vorige studies, met een significante toename in omzet (van tientallen tot honderden spheroids).

Eerder is aangetoond dat spheroid oppervlaktespanning afhangt van de druk waarmee de spheroid geaspireerd wordt, wat een mogelijke versteviging van de cellen als reactie op de toegepaste kracht kan betekenen. Dankzij de verbeterde omzet van onze microfluïdische chip hebben we de invloed van celcontractiliteit naast de duur van de toegepaste kracht op spheroid vervorming en de afgeleide oppervlaktespanning onderzocht. In **hoofdstuk 4** tonen we aan dat een grotere vervorming van de spheroid leidt tot een snellere retractie van de cellen in de chip eens de druk wordt verwijderd, onafhankelijk van celcontractiliteit of de grootte van de toegepaste druk. Onze resultaten duiden daarom op een vervorming-afhankelijke spheroid mechanica en dagen uit of spheroid oppervlaktespanning daadwerkelijk verstevigt.

Aangezien abnormale celmechanica een grote rol speelt in de voortzetting van kanker, focust het laatste deel van deze thesis op de creatie van microfluïdische apparaten die de relatie tussen kankercel vervormbaarheid en migratie kunnen onderzoeken. Het is gebleken dat cellen een groter metastatisch potentieel hebben (wat betekent dat ze een grotere kans hebben op het vormen van secundaire tumoren) als ze gezamenlijk als cluster in plaats van individueel reizen. In **hoofdstuk 5** presenteren we daarom microfluïdische chips om de studie van clustermigratie en de voordelen in verhouding tot individuele migratie mogelijk te maken. Eerst hebben we een microfluïdische chip ontwikkeld om cel vervormbaarheid met hoge omzet te bestuderen door de cellen door parallele bloedvat-achtige constricties heen te stromen. Aan de hand van deze chip tonen we aan dat verschillen in de stijfheid van cellen geen directe invloed hebben op celdeformatie in nauwe constricties. Vervolgens hebben we meerdere microfluïdische ontwerpen gemaakt om individuele celmigratie en clustermigratie doorheen constricties met verschillende vormen en groottes te onderzoeken. Proof-of-concept experimenten lieten zien dat live hoge resolutie imaging van celmigratie doorheen deze constricties mogelijk is en meerdere mogelijkheden opent voor de studie van de link tussen cel vervormbaarheid en clustermigratie.

Ten slotte sluiten we deze thesis af in **hoofdstuk 6** met een korte vooruitblik op mogelijke, toekomstige experimenten. Voornamelijk geloven we dat een focus op gap junctions, de intercellulaire verbinding die de uitwisseling van ionen en water tussen cellen mogelijk maakt, meer licht kan laten schijnen op spheroid oppervlaktespanning en diens afhankelijkheid van spheroid-grootte.

1

INTRODUCTION

This was to me among all the marvels that I have discovered in nature the most marvellous among them all.

Antonie van Leeuwenhoek, on seeing "animalcules" in a drop of rainwater.

The cells in our body are frequently subjected to physical forces. They are pushed and pulled upon every time our heart beats, they squeeze through the smallest pores when travelling towards foreign viruses, and they stretch every time we try to touch our toes or lick our elbows. How cells respond to these forces, termed cell mechanics, is essential for growth and health. During early phases of life, cell mechanics is an important determinant of tissue development and shaping [1, 2]. When a tissue gets harmed, cells react to the deformation and start migrating towards the wound in order to heal it [3]. Mechanics are omnipresent, even on the flipside, when mutations make cells lose their original function. Here, cells are provided with a new set of abnormal "skills and tricks" to grow excessively and migrate to distant sites, a process that is known as cancer metastasis [4, 5]. And essential to all these processes is the ability of a cell to respond: to deform and restructure its shape.

Similar to the bones in our body, cells have a so-called cytoskeleton providing them with rigidity and structure [6]. The cytoskeleton consists of three protein polymer networks: actin filaments, microtubules and intermediate filaments (Fig. 1.1A) [7]. Not only do these structures protect the nucleus, located at the core of the cell and keeper of our DNA, but they also provide cells with the ability to migrate and divide (Fig. 1.1B). Alongside the nucleus and the plasma membrane (being the boundary of the cell protecting it from the environment), the cytoskeleton is key in governing cell deformability [8, 9]. In response to a force, cells actively translate mechanical stimuli into a biological response. Cells sense their surroundings via transmembrane proteins, which link the cell's cytoskeleton to the outer environment [10]. For example, the transmembrane protein integrin transmits forces applied in the environment to the inside of the cell and triggers downstream activation of signaling pathways [11, 12]. This process, termed mechan-

1

A
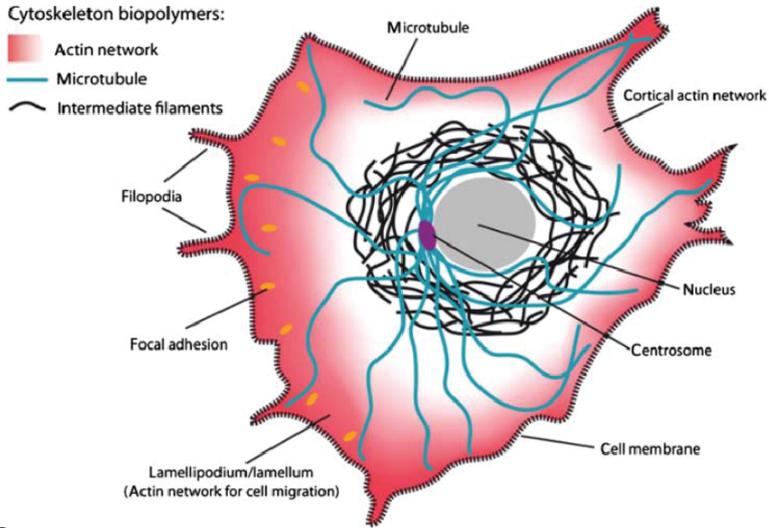
B
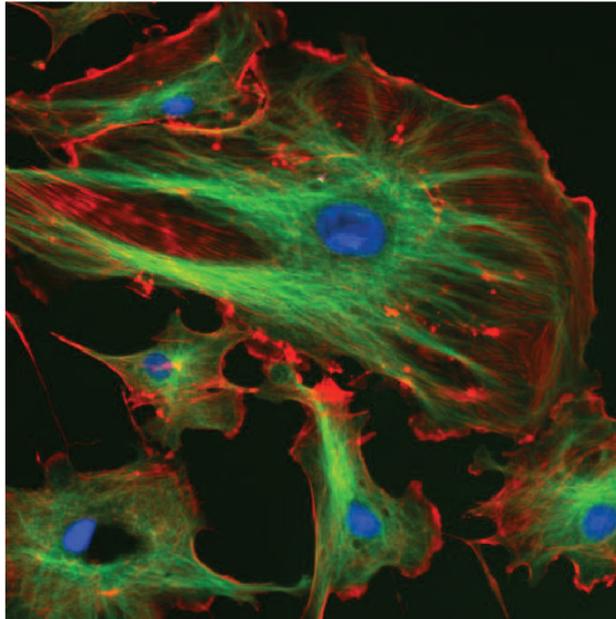
Figure 1.1: A) Schematic of a cell when crawling on a 2D substrate, showing the three cytoskeletal components: the actin network, intermediate filaments and microtubules. When cells migrate, dense and dynamic actin networks form at the leading edge of the cell to pull on the surroundings. Reprinted from [13]. B) Fluorescent image of endothelial cells, demonstrating the nucleus (blue) surrounded by the microtubules (green) and actin filaments (red). Reprinted from Wikimedia Commons.

otransduction, contributes to the sorting and organization of cells into tissues [10, 14, 15].

How tissues deform under physical stress not only follows from the cytoskeletal properties of the constituent cells, but additionally depends on intercellular adhesions (how cells stick to each other) and on the surrounding extracellular matrix (ECM) in which the cells reside [16–18]. Due to this complex interplay, tissue mechanics are not as straightforward as the mechanical properties of normal elastic or viscous (non-living) materials. Elastic materials such as a rubber band increase their stress upon deformation, and regain their original shape once the applied force is removed. Here, elasticity is expressed through the ratio of the applied stress σ (force per area) to the strain ϵ (unitless measure of deformation), giving an elastic modulus $E = \sigma/\epsilon$. Opposite to this, viscous materials like honey keep deforming while a stress is applied and do not return to their original shape after stress removal. Viscous materials are characterized by the viscosity $\eta = \sigma/\dot{\epsilon}$, with $\dot{\epsilon}$ being the strain rate. Both tissues and cells, however, exhibit viscoelastic properties: their deformational behavior to an applied stress is time-dependent, as it transits from an elastic to a viscous behavior with a characteristic time τ [19]. Importantly, the interplay of cells at the tissue-scale regulates future cell fate and tissue maintenance [20, 21]. Understanding how cell and tissue mechanics are intrinsically linked may therefore shed light on important physiological processes such as tissue development and cancer initiation.

1.1. SPHEROID MECHANICS

Multicellular spheroids are a widely used *in vitro* model to investigate the interplay between cellular properties and tissue mechanics. Being spherical balls of cells, they recreate both the multicellularity and three-dimensional (3D) microenvironment of *in vivo* tissues [22, 23]. They are created through the sedimentation and aggregation of dissociated cells in a confined space. Similar to oil drops in water, cells round up into spheroids over time (though more slowly) in order to minimize their surface energy. This behaviour leads to spheroids having a specific surface tension γ, being the amount of force required to stretch their surface per unit length [24]. Spheroid surface tension is governed through an interplay between two cellular properties: (1) The intercellular adhesions, depicting the strength with which cells stick to each other [24], (2) and the cortical (surface) tension of each cell's cortex, being the plasma membrane-associated part of their actin cytoskeletons [25, 26]. When spheroids of different cell types come into contact, differences in their surface tensions will define how the tissues spread [27] and fuse [28, 29], and how the individual cells sort [30] (see Fig. 1.2, upper-left panel). How tissues sort even has implications for cancer cell invasion, as shown in a study where a non-migratory cell type encapsulated an invasive cell type, thereby inhibiting it from migrating out [31]. As physical traits such as compressive stress or tissue stiffness determine whether cancer cells dissociate and move away from a tumour (Fig. 1.2, upper-right panel) [5], investigating the biophysical relation between cell and tissue mechanics through the study of tissue surface tension may therefore provide new insights in cancer cell invasion [32, 33].
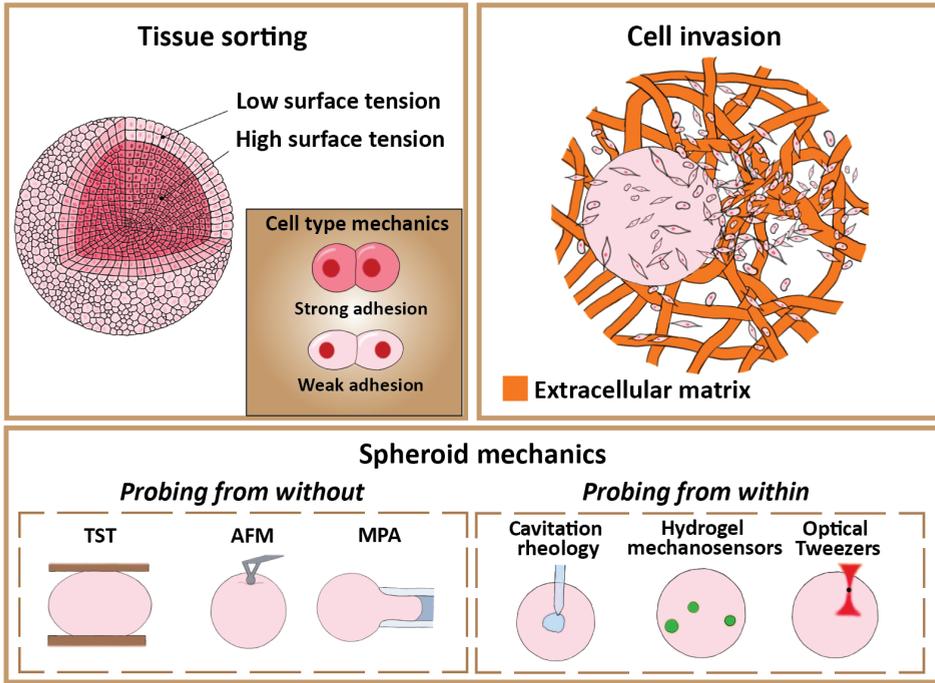
Figure 1.2: Mechanical properties of multicellular spheroids have implications for tissue sorting and cell invasion. Differences in intercellular adhesion govern tissue sorting (top left panel), which has direct implications for cell migration (top right panel). To gain better insights in spheroid mechanics, these multicellular models are studied with a large variety of biophysical tools (bottom panel).

1.1.1. MEASURING TISSUE SURFACE TENSION

Mechanical properties of spheroids, such as elasticity, viscosity and surface tension, can be studied with a large array of experimental techniques (Fig. 1.2, bottom panel) [23, 34, 35]. Especially the tissue surface tension γ can give important insights in the interplay between cell and tissue mechanics [36, 37]. Two conventional techniques to measure γ are tissue surface tensiometry (TST) and micropipette aspiration (MPA). With TST, the spheroid is squeezed between two parallel plates and the surface tension is derived from the resulting change in curvature of the spheroid surface [24]. With MPA, a part of the spheroid is aspirated into a micron-sized pipette under a constant pressure ΔP and the advancing creep length $L(t)$ of the spheroid protrusion is monitored over time (Fig. 1.3a) [38]. In this thesis, we focus on the MPA technique to study our research questions around spheroid mechanics.

When aspirating spheroids with MPA, the cells that squeeze into the micropipette first display a fast elastic deformation δ followed by an apparently linear and slower viscous response with a constant flow rate $\dot{L}_{\infty}$. Here, the elasticity is mainly regulated by the cell-cell adhesion and cellular cytoskeleton, while the viscosity stems from dissipation due to cellular rearrangements [19]. Considering volume conservation of the spheroid
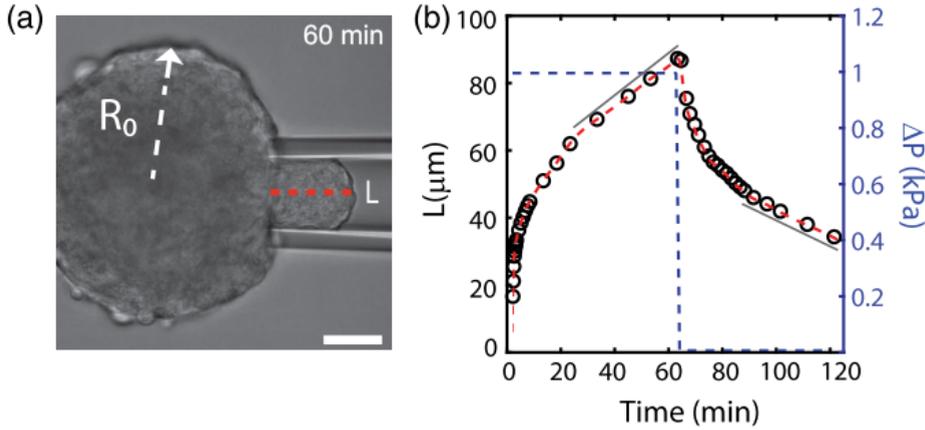
Figure 1.3: (a) Conventional micropipette aspiration, where a spheroid with radius R_0 is aspirated into a pipette with radius R_p at a pressure ΔP. The length of the protrusion of cells $L(t)$ increases over time. Scale 50 μm. (b) The creep length $L(t)$ of an aspiration and retraction experiment on one spheroid plotted versus time. The spheroid is aspirated for one hour at 1 kPa, and then left to retract for another hour. The solid gray lines represent the viscous flow rate $\dot{L}_\infty$. Reprinted with permission from [39], Copyright 2022 by the American Physical Society.

during aspiration, the aspiration force f applied by the pipette is given by

$$f = \pi R_p^2 (\Delta P - \Delta P_c), \tag{1.1}$$

where R_p is the pipette radius, ΔP the applied pressure in the pipette and ΔP_c is the critical pressure required for aspiration of the tissue to occur. Making the analogy with liquid droplets, this critical pressure ΔP_c is related to the surface tension γ through the Young-Laplace law

$$\Delta P_c = 2\gamma \left(\frac{1}{R_p} - \frac{1}{R} \right), \tag{1.2}$$

with R being the spheroid radius [38]. Even though R is not constant throughout the aspiration, it can still be approximated by the initial radius of the aggregate R_0 as $R_p \ll R_0$.

Removing the pressure after spheroid aspiration causes the spheroid protrusion to retract, driven by the surface tension γ (Fig. 1.3b). Importantly, a previous study on the micropipette aspiration of murine sarcoma S180 cell spheroids showed that γ depended on the applied aspiration pressure ΔP. Specifically, spheroid protrusions would retract faster upon pressure release if they had been aspirated at a larger pressure. This finding suggested a putative reinforcement of γ due to an active response of the cells to the mechanical force [38]. However, when subjecting spheroids to a fixed strain with TST by compressing them between plates, no dependency of the measured surface tension on the applied force was observed [30, 40]. This questions whether cells actively reinforce their surface tension with the applied force, or if the current interpretation of viscoelastic spheroid aspiration data is insufficient. A major aim of this dissertation is to provide an answer to this question.
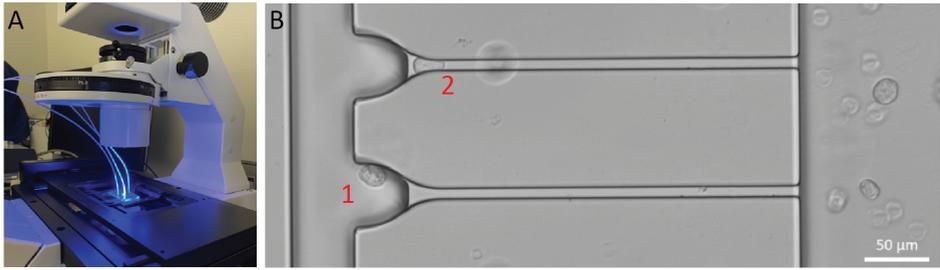
Figure 1.4: (A) Set-up for a microfluidic experiment, with the microfluidic device loaded on the microscope and connected to tubes that flow liquid through the chip. (B) Example of cell deformation in a microfluidic chip. (1) Cells are flown along with media into the device until they arrive at constriction channels. (2) Here, the flow redirects them to squeeze and deform through the microchannels, allowing for strain measurements. Scale 50 μm.

1.1.2. MICROFLUIDICS

Biophysical experiments that measure cell or tissue mechanics are often performed at the microscale, requiring bulky experimental set-ups with a limited possibility for automation and hence a low throughput. There is a clear need to improve this throughput in order to understand differences between cell types or disease conditions [41]. To overcome this challenge, many research groups have resorted to microfluidic devices [42–50].

Microfluidics is the research field of manipulating fluid quantities on the microscale [51]. A typical microfluidic device exists of micron-sized channels on a chip through which fluid can be flown. Microfluidic devices only require low amounts of reagents, can easily be reproduced and enable a high throughput [52]. Depending on the design, different rheological characterization measurements can be performed on the fluids or particles therein (such as cells or spheroids) [53]. When squeezed through narrow channels, cells/spheroids deform under a certain stress (Fig. 1.4). Therefore, microfluidics are highly suitable to measure mechanical properties such as cell strain [44–46, 48], cell elasticity [42, 49, 50] and cell viscosity [50] in a high-throughput manner. However, while many microfluidic devices have been created to study single cell mechanics, a scaled microfluidic device to study spheroid mechanics is still missing. In this dissertation, we introduce our own custom-made device allowing high-throughput measurements on spheroid mechanics to fill this gap.

1.2. CIRCULATING TUMOUR CELL MECHANICS

Metastasis, the process where cancer cells adapt their properties and start migrating through the body, is responsible for ~90% of cancer-associated mortality, making it the core challenge in the treatment of cancer [54, 55]. Deviations from normal cell mechanics strongly affect the progression of this disease. First, tumour cells change their mechanical properties in response to both chemical and mechanical stimuli in order to leave the tumour and migrate into the surrounding stroma (Fig. 1.5A(1)) [56]. As a result of their improved motility, they are subsequently able to reach and enter the bloodstream, in a process known as intravasation (Fig. 1.5A(2)). Here, the metastasizing cells
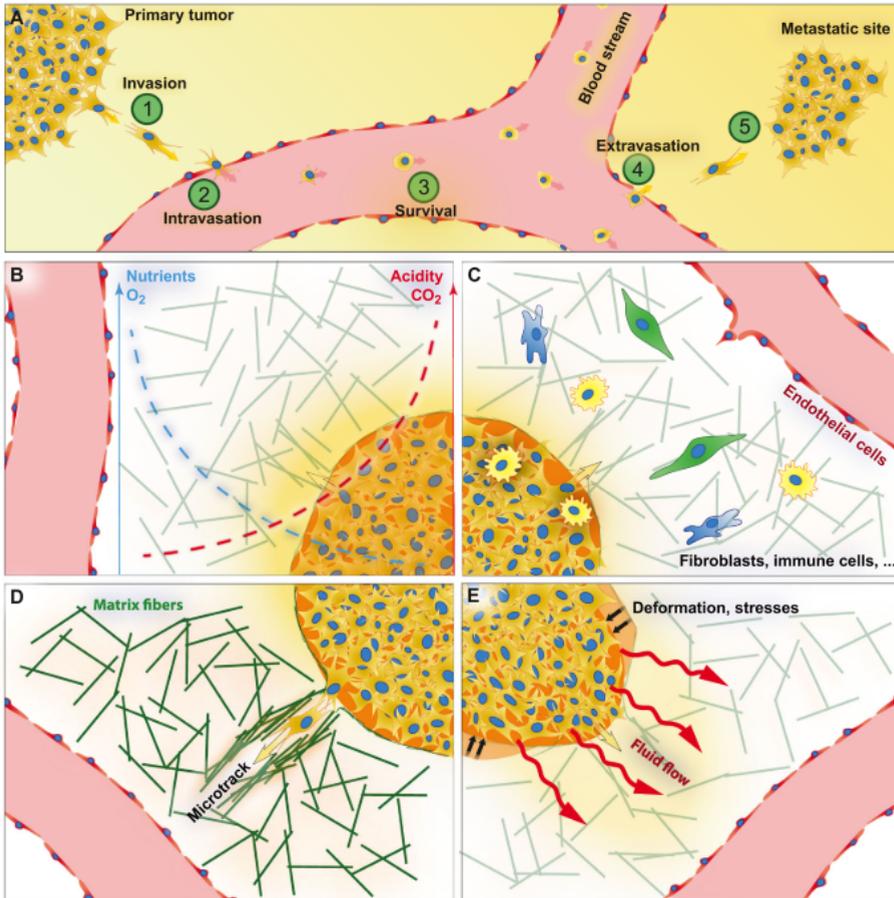
Figure 1.5: (A) The process of metastasis, where cancer cells escape from the primary tumor into the surrounding stroma (1), then cross the vessel wall, enter the circulation and become CTCs (2). The cells that survive in the circulation (3) eventually extravasate by exiting the vessel (4) and seed a secondary tumour at a distant site (5). (B-D) The tumour microenvironment, with (B) biochemical cues (such as lower levels of oxygen and nutrients, and higher levels of acidity and carbon dioxide), (C) cellular cues (from fibroblasts, immune cells and endothelial cells, (D) the extracellular matrix (ECM) with heterogeneous structural properties and (E) mechanical cues, including interstitial fluid pressure and flow, tissue stresses and deformations. Reproduced from [57], licensed under CC BY 3.0.

that have entered the vascular system are rebranded as circulating tumour cells (CTCs) [58]. Of the CTCs that survive in the bloodstream (Fig. 1.5A(3)), some will arrest near the wall of the blood vessel and exit it, in a process known as extravasation (Fig. 1.5A(4)) [59]. Lastly, after further migration through the stroma, some CTCs will eventually halt and form secondary tumours (Fig. 1.5A(5)) [60].

During metastatic migration, cells are constantly influenced by several factors in the tumour microenvironment [57]. These range from biochemical cues such as lower levels of oxygen to mechanical cues like interstitial fluid pressure (Fig. 1.5B-E). As it turns out, individual cell migration is quite inefficient to cope with these signals. Single cancer cells are often killed by the immune system and never even reach the distant tissues [61]. Yet, when CTCs group together and migrate as clusters, their metastatic potential increases significantly for reasons that are not well understood [62–64]. In a recent study, half of all metastatic lesions in orthotopic breast cancer mouse models originated from CTC clusters, even though clusters only constituted ~5% of all CTCs found in the circulation [62]. Individual CTCs are strongly deformed when travelling through narrow blood vessels, often resulting in cell death [65, 66]. However, the CTCs that outlive these compressive forces possibly adapt and improve their survival rate and metastatic potential [67]. Similarly, CTC clusters demonstrate large mechanical deformations when traversing narrow microvessels [68]. Yet, little is known about whether and how physical forces exerted on clusters contribute to a greater metastatic and migrational potential, and what advantages occur when cells migrate collectively [58, 60]. Studying the relation between cell mechanics and migration for single cells versus clusters may therefore provide significant insights into metastasis.

To provide enough statistical significance, large data sets are required when investigating the migrational advantage that cell clusters hold over single cells. We therefore developed custom-made microfluidic devices designed to investigate single cell and cell cluster mechanics in a high-throughput manner. In this dissertation, we first demonstrate a microfluidic device that flows suspended cells through parallel constrictions modeling narrow blood vessels to compare the deformability between cell types. We follow this up with the introduction of microfluidic devices that allow the study of cell migration through various constrictions, in order to couple cell deformability to migration and to identify potential advantages when cells migrate as clusters.

1.3. OUTLINE OF THE THESIS

The aim of this dissertation is to research the interplay between cell and tissue mechanics. More specifically, we investigate how tissue elasticity, viscosity and surface tension arise from single cell properties such as cortical tension and intercellular adhesion. Here, we mainly focus on spheroid models and their surface tension, as this property is directly related to the physiologically relevant process of cell sorting. Two previous publications demonstrating interesting behavior of spheroid surface tension formed the starting point for this dissertation. First, Guevorkian *et al.* demonstrated that the surface tension γ depended on the applied pressure, due to a putative active reinforcement where cells mechanosense the applied pressure [38]. Secondly, Yousafzai *et al.* showed how the surface tension relates to spheroid size, with smaller spheroids having a larger tension [39]. However, both discoveries were made with a low amount of probed spheroids

(~30), with no follow-up studies on possible explanations for these trends. Reproducing these results for varying conditions in a high-throughput manner, and elucidating the cause for a pressure-dependent surface tension therefore formed the cornerstone of this thesis.

First, in **chapter 2**, we provide an overview of the available biophysical tools to probe spheroid mechanics, each with their advantages and shortcomings. Based on literature, we review current studies and theoretical frameworks on how spheroid surface tension is related to single cell mechanics, including cortical tension and intercellular adhesion. We subsequently lay out the implications of cell sorting and differences in tissue mechanics for cell migration and cancer metastasis. Finally, we indicate the research gaps and highlight novel techniques that could help in shedding more light on the biophysical characterization of spheroids.

Then, we focus on overcoming the low throughput of available techniques to study spheroid deformation in **chapter 3**. We introduce a microfluidic micropipette aspiration device that allows for high-throughput mechanophenotyping of multicellular spheroids, by loading spheroids into individual aspiration pockets and deforming them in parallel. We demonstrate how the device produces accurate viscoelastic deformation data when aspirating spheroids of varying cell types at different aspiration pressures.

The high throughput of this microfluidic device allowed us to study spheroid surface tension with an unprecedented amount of spheroid aspiration data. In **chapter 4**, we therefore investigate the influence of cell contractility and time duration of the applied force on spheroid mechanics when deforming viscoelastically. Importantly, we find that larger spheroid deformations lead to faster cellular retraction once the pressure is released, regardless of cellular contractility or applied pressure. Our results therefore indicate a deformation-dependent spheroid viscoelasticity, and challenge whether surface tension truly reinforces.

Moving away from this dissertation's main focus on spheroid mechanics, we then turned our attention to the mechanics of single cells alongside the intermediary size range of cell clusters and its influence on cancer metastasis. In **chapter 5**, we introduce technological developments that will help to unravel differences between single cell and cluster mechanics and to study how these differences influence circulating tumour cluster migration. Firstly, we demonstrate a microfluidic device to study single cell deformability with a large throughput by flowing cells through many blood vessel-sized constrictions in parallel. Using this device, we identified how differences in cellular stiffness through actin depolymerization do not directly influence cell strain when compressed in narrow constrictions. Secondly, we developed a microfluidic device that analyses single cell and cluster migration through narrow constrictions in various shapes and sizes. We demonstrate how live high resolution imaging of cell migration through this physiologically relevant 3D environment will enable the future study of cluster migration and its dependency on cell mechanics.

We conclude this thesis in **chapter 6** with an outlook on potential future experiments to further identify the role of cell mechanics on spheroid viscoelasticity. In our opinion, an intriguing next step to understand spheroid surface tension and its potential spheroid size-dependency would be to investigate the influence of gap junctions on the measured tension. In addition, we provide suggestions on future steps when investigating the link

1

between cell deformability and (cluster) migration. We believe that a focus on intermediate filaments could provide new insights in differences in cell deformability between cell types.

BIBLIOGRAPHY

1. Hahn, C. & Schwartz, M. A. Mechanotransduction in vascular physiology and athero-genesis. *Nature Reviews Molecular Cell Biology* **10,** 53–62. ISSN: 14710072 (2009).

2. Mammoto, T. & Ingber, D. E. Mechanical control of tissue and organ development. *Development* **137,** 1407–1420 (2010).

3. Brugués, A. *et al.* Forces driving epithelial wound healing. *Nat Phys* **10,** 683–690 (2014).

4. Nia, H. T. *et al.* Solid stress and elastic energy as measures of tumour mechanopathol-ogy. *Nat Biomed Eng* **1,** 1–25 (2016).

5. Nia, H. T., Munn, L. L. & Jain, R. K. Physical traits of cancer. *Science* **370,** eaaz0868. ISSN: 10959203 (2020).

6. Fletcher, D. A. & Mullins, R. D. Cell mechanics and the cytoskeleton. *Nature* **463,** 485–492. ISSN: 00280836 (2010).

7. Moujaber, O. & Stochaj, U. The Cytoskeleton as Regulator of Cell Signaling Path-ways. *Trends in Biochemical Sciences* **45,** 96–107. ISSN: 13624326. https://doi.org/10.1016/j.tibs.2019.11.003 (2020).

8. Galie, P. A., Georges, P. C. & Janmey, P. A. How do cells stiffen? *The Biochemical journal* **479,** 1825–1842. ISSN: 14708728 (2022).

9. Friedl, P., Wolf, K. & Lammerding, J. Nuclear mechanics during cell migration. *Current Opinion in Cell Biology* **23,** 55–64. ISSN: 09550674. http://dx.doi.org/10.1016/j.ceb.2010.10.015 (2011).

10. Martino, F., Perestrelo, A. R., Vinarský, V., Pagliari, S. & Forte, G. Cellular mechan-otransduction: From tension to function. *Frontiers in Physiology* **9,** 1–21. ISSN: 1664042X (2018).

11. Hynes, R. O. Integrins: Bidirectional, Allosteric Signaling Machines. *Cell* **10,** 673–687 (2002).

12. Collins, C., Denisin, A. K., Pruitt, B. L. & Nelson, W. J. Changes in E-cadherin rigid-ity sensing regulate cell adhesion. *Proceedings of the National Academy of Sciences of the United States of America* **114,** E5835–E5844. ISSN: 10916490 (2017).

13. Huber, F. *et al.* Emergent complexity of the cytoskeleton: From single filaments to tissue. *Advances in Physics* **62,** 1–112. ISSN: 00018732 (2013).

14. Wozniak, M. A. & Chen, C. S. Mechanotransduction in development: a growing role for contractility. *Nat Rev Mol Cell Biol* **10,** 34–43 (2009).

15. Kamm, R. D. & Kaazempur-Mofrad, M. R. On the molecular basis for mechan-otransduction. *Mechanics & chemistry of biosystems : MCB* **1,** 201–209. ISSN: 15462048 (2004).

1

16. Schiele, N. R. *et al.* Actin cytoskeleton contributes to the elastic modulus of embryonic tendon during early development. *Journal of Orthopaedic Research* **33,** 874–881. ISSN: 1554527X (2015).

17. Heisenberg, C. P. & Bellaïche, Y. Forces in tissue morphogenesis and patterning. *Cell* **153,** 948–962. ISSN: 10974172 (2013).

18. Han, Y. L. *et al.* Cell swelling, softening and invasion in a three-dimensional breast cancer model. *Nature Physics* **16,** 101–108. ISSN: 17452481 (2020).

19. Guevorkian, K., Gonzalez-rodriguez, D., Carlier, C., Dufour, S. & Brochard-Wyart, F. Mechanosensitive shivering of model tissues under controlled aspiration. *PNAS* **108,** 13387–13392 (2011).

20. Dias Gomes, M. & Iden, S. Orchestration of tissue-scale mechanics and fate decisions by polarity signalling. *EMBO Journal,* 1–19 (2021).

21. Janmey, P. A. & Weitz, D. A. Dealing with mechanics: Mechanisms of force transduction in cells. *Trends in Biochemical Sciences* **29,** 364–370. ISSN: 09680004 (2004).

22. Gonzalez-Rodriguez, D., Guevorkian, K., Douezan, S. & Brochard-Wyart, F. Soft Matter Models of Developing. *Science* **82,** 910–917 (2012).

23. Boot, R. C., Koenderink, G. H. & Boukany, P. E. Spheroid mechanics and implications for cell invasion. *Advances in Physics: X* **6,** 1978316. https://doi.org/10.1080/23746149.2021.1978316 (2021).

24. Foty, R. A. & Steinberg, M. S. The differential adhesion hypothesis: A direct evaluation. *Developmental Biology* **278,** 255–263. ISSN: 00121606 (2005).

25. Svitkina, T. M. Actin Cell Cortex: Structure and Molecular Organization. *Trends in Cell Biology* **30,** 556–565. ISSN: 18793088. https://doi.org/10.1016/j.tcb.2020.03.005 (2020).

26. Brodland, G. W. The Differential Interfacial Tension Hypothesis (DITH): A comprehensive theory for the self-rearrangement of embryonic cells and tissues. *Journal of Biomechanical Engineering* **124,** 188–197. ISSN: 01480731 (2002).

27. Ryan, P. L., Foty, R. A., Kohn, J. & Steinberg, M. S. Tissue spreading on implantable substrates is a competitive outcome of cell-cell vs. cell-substratum adhesivity. *Proceedings of the National Academy of Sciences of the United States of America* **98,** 4323–4327. ISSN: 00278424 (2001).

28. Kosheleva, N. V. *et al.* Cell spheroid fusion: beyond liquid drops model. *Scientific Reports* **10,** 1–15. ISSN: 20452322. https://doi.org/10.1038/s41598-020-69540-8 (2020).

29. Grosser, S. *et al.* Cell and Nucleus Shape as an Indicator of Tissue Fluidity in Carcinoma. *Physical Review X* **11,** 011033. https://journals.aps.org/prx/abstract/10.1103/PhysRevX.11.011033 (2021).

30. Schötz, E. M. *et al.* Quantitative differences in tissue surface tension influence zebrafish germ layer positioning. *HFSP Journal* **2,** 42–56. ISSN: 19552068 (2008).

31. Huang, Y. L., Shiau, C., Wu, C., Segall, J. E. & Wu, M. The Architecture of Co-Culture Spheroids Regulates Tumor Invasion within a 3D Extracellular Matrix. *Biophysical Reviews and Letters* **15,** 131–141. ISSN: 1793-0480 (2020).

32. Sauer, F. *et al.* Whole tissue and single cell mechanics are correlated in human brain tumors. *Soft Matter* **17,** 10744–10752. ISSN: 17446848 (2021).

33. Nguyen, L. T., Jacob, M. A. C., Parajón, E. & Robinson, D. N. Cancer as a biophysical disease: Targeting the mechanical-adaptability program. *Biophysical Journal,* 1–13. ISSN: 15420086 (2022).

34. Paluch, E. & Heisenberg, C.-p. Biology and Physics of Cell Shape Changes in Development Review. *Current Biology* **19,** R790–R799. ISSN: 0960-9822. http://dx.doi.org/10.1016/j.cub.2009.07.029 (2009).

35. Narasimhan, B. N. *et al.* Mechanical Characterization for Cellular Mechanobiology: Current Trends and Future Prospects. *Frontiers in Bioengineering and Biotechnology* **8,** 1–9. ISSN: 22964185 (2020).

36. Manning, M. L., Foty, R. A., Steinberg, M. S. & Schoetz, E. M. Coaction of intercellular adhesion and cortical tension specifies tissue surface tension. *Proceedings of the National Academy of Sciences of the United States of America* **107,** 12517–12522. ISSN: 00278424 (2010).

37. David, R. *et al.* Tissue cohesion and the mechanics of cell rearrangement. *Development* **141,** 3672–3682 (2014).

38. Guevorkian, K., Colbert, M.-J., Durth, M., Dufour, S. & Brochard-Wyart, F. Aspiration of Biological Viscoelastic Drops. *Physical Review Letters* **104,** 1–4 (2010).

39. Yousafzai, M. S. *et al.* Active Regulation of Pressure and Volume Defines an Energetic Constraint on the Size of Cell Aggregates. *Physical Review Letters* **128,** 48103. ISSN: 0031-9007. https://doi.org/10.1103/PhysRevLett.128.048103 (2022).

40. Foty, R. A., Pfleger, C. M., Forgacs, G. & Steinberg, M. S. Surface tensions of embryonic tissues predict their mutual envelopment behavior. *Development* **122,** 1611–1620. ISSN: 09501991 (1996).

41. Efremov, Y. M. *et al.* Mechanical properties of cell sheets and spheroids: the link between single cells and complex tissues. *Biophysical Reviews* **13,** 541–561. ISSN: 18672469 (2021).

42. Lee, L. M. & Liu, A. P. A microfluidic pipette array for mechanophenotyping of cancer cells and mechanical gating of mechanosensitive channels. *Lab Chip* **15,** 264–273 (2015).

43. Honaker, L. W., Lagerwall, J. P. & Jampani, V. S. Microfluidic Tensiometry Technique for the Characterization of the Interfacial Tension between Immiscible Liquids. *Langmuir* **34,** 2403–2409. ISSN: 15205827 (2018).

44. Hou, H. W. *et al.* Deformability study of breast cancer cells using microfluidics. *Biomedical Microdevices* **11,** 557–564. ISSN: 13872176 (2009).

1

45. Adamo, A. *et al.* Microfluidics-based assessment of cell deformability. *Analytical Chemistry* **84,** 6438–6443. ISSN: 00032700 (2012).

46. Byun, S. *et al.* Characterizing deformability and surface friction of cancer cells. *Proceedings of the National Academy of Sciences of the United States of America* **110,** 7580–7585. ISSN: 00278424 (2013).

47. Mak, M. & Erickson, D. A serial micropipette microfluidic device with applications to cancer cell repeated deformation studies. *Integrative Biology* **5,** 1374–1384 (2013).

48. Mak, M., Reinhart-King, C. A. & Erickson, D. Elucidating mechanical transition effects of invading cancer cells with a subnucleus-scaled microfluidic serial dimensional modulation device. *Lab on a Chip* **13,** 340–348. ISSN: 14730189 (2013).

49. Chen, Z., Yip, T. F., Zhu, Y., Ho, J. W. K. & Chen, H. The method to quantify cell elasticity based on the precise measurement of pressure inducing cell deformation in microfluidic channels. *MethodsX* **8,** 101247. ISSN: 22150161. https://doi.org/10.1016/j.mex.2021.101247 (2021).

50. Davidson, P. M. *et al.* High-throughput microfluidic micropipette aspiration device to probe time-scale dependent nuclear mechanics in intact cells. *Lab on a Chip* **19,** 3652–3663. ISSN: 14730189 (2019).

51. Chen, Z., Kheiri, S., Young, E. W. & Kumacheva, E. Trends in Droplet Microfluidics: From Droplet Generation to Biomedical Applications. *Langmuir.* ISSN: 15205827 (2022).

52. Ortseifen, V., Viefhues, M., Wobbe, L. & Grünberger, A. Microfluidics for Biotechnology: Bridging Gaps to Foster Microfluidic Applications. *Frontiers in Bioengineering and Biotechnology* **8,** 1–12. ISSN: 22964185 (2020).

53. Giudice, F. D. A Review of Microfluidic Devices for Rheological Characterisation. *Micromachines* **13** (2022).

54. Mierke, C. T. The matrix environmental and cell mechanical properties regulate cell migration and contribute to the invasive phenotype of cancer cells. *Reports on Progress in Physics* **82.** ISSN: 00344885 (2019).

55. Canel, M., Serrels, A., Frame, M. C. & Brunton, V. G. E-cadherin-integrin crosstalk in cancer invasion and metastasis. *Journal of Cell Science* **126,** 393–401. ISSN: 00219533 (2013).

56. Vasilaki, D., Bakopoulou, A., Tsouknidas, A., Johnstone, E. & Michalakis, K. Biophysical interactions between components of the tumor microenvironment promote metastasis. *Biophysical Reviews* **13,** 339–357. ISSN: 18672469 (2021).

57. Sleeboom, J. J. F., Amirabadi, H. E., Nair, P., Sahlgren, C. M. & Toonder, J. M. J. D. Metastasis in context : modeling the tumor microenvironment with cancer-on-a-chip approaches. *Disease Models & Mechanisms* **11** (2018).

58. Peralta, M., Osmani, N. & Goetz, J. G. Circulating tumor cells: Towards mechanical phenotyping of metastasis. *iScience* **25,** 103969. ISSN: 25890042 (Mar. 2022).

59. Follain, G. *et al.* Fluids and their mechanics in tumour transit: shaping metastasis. *Nature Reviews Cancer* **20,** 107–124. ISSN: 14741768 (2020).

60. Gensbittel, V. *et al.* Mechanical Adaptability of Tumor Cells in Metastasis. *Developmental Cell.* ISSN: 18781551 (2020).

61. Mehlen, P. & Puisieux, A. Metastasis: A question of life or death. *Nature Reviews Cancer* **6,** 449–458. ISSN: 1474175X (2006).

62. Aceto, N. *et al.* Circulating tumor cell clusters are oligoclonal precursors of breast cancer metastasis. *Cell* **158,** 1110–1122. ISSN: 10974172. http://dx.doi.org/10.1016/j.cell.2014.07.013 (2014).

63. Aceto, N. Bring along your friends: Homotypic and heterotypic circulating tumor cell clustering to accelerate metastasis. *Biomedical Journal* **43,** 18–23. ISSN: 23194170. https://doi.org/10.1016/j.bj.2019.11.002 (2020).

64. Hou, J.-m. *et al.* Clinical Significance and Molecular Characteristics of Circulating Tumor Cells and Circulating Tumor Microemboli in Patients With Small-Cell Lung Cancer. *Journal of Clinical Oncology* **30,** 525–532 (2012).

65. Yamamoto, N. *et al.* Cellular dynamics visualized in live cells in vitro and in vivo by differential dual-color nuclear-cytoplasmic fluorescent-protein expression. *Cancer Research* **64,** 4251–4256. ISSN: 00085472 (2004).

66. Yamauchi, K. *et al.* Real-time in vivo dual-color imaging of intracapillary cancer cell and nucleus deformation and migration. *Cancer Research* **65,** 4246–4252. ISSN: 00085472 (2005).

67. Perea Paizal, J., Au, S. H. & Bakal, C. Squeezing through the microcirculation: survival adaptations of circulating tumour cells to seed metastasis. *British Journal of Cancer* **124,** 58–65. ISSN: 15321827. http://dx.doi.org/10.1038/s41416-020-01176-x (2021).

68. Au, S. H. *et al.* Clusters of circulating tumor cells traverse capillary-sized vessels. *Proceedings of the National Academy of Sciences of the United States of America* **113,** 4947–4952. ISSN: 10916490 (2016).

1

2

SPHEROID MECHANICS AND IMPLICATIONS FOR CELL INVASION

True knowledge is to be aware of one's ignorance.

Rudolf Virchow, in a letter to his father

Spheroids are widely used in vitro 3D multicellular model systems that mimic complex physiological microenvironments of tissues. As different cell types vary in deformability and adhesion, the choice of (heterogeneous) cell composition will define overall spheroid mechanics, including their viscoelasticity and effective surface tension. These mechanical parameters directly influence cell sorting and possibly cell invasion into the extracellular matrix. Spheroid models therefore provide fundamental insights in the relation between cellular mechanics and important physiological processes, such as tissue formation, embryonic tissue remodeling, and cancer metastasis. In this review chapter, we first summarize and compare current biophysical tools that probe mechanics of spheroids either from the outside or from within, then relate spheroid mechanics to cell mechanics and cell-cell adhesion, and subsequently discuss the role of spheroid mechanics alongside surrounding microenvironment parameters in (cancer) cell migration. We conclude by pointing out the research gaps and drawing the attention to novel techniques that could shed more light on the biophysical characterization of spheroids in the framework of tissue remodeling and cancer metastasis.

2.1. INTRODUCTION

The cells in our body routinely encounter a wide range of physical cues both from intra-cellular forces generated by molecular activity and from external mechanical forces [2]. Cells actively transduce these physical cues into biochemical signals that affect cell morphology, motility, arrangement and function in tissues [3–5]. The mechanical response of cells to forces and other physical cues such as confinement are therefore critical in the regulation of many physiological processes, such as cell division, growth and differentiation [3, 6, 7], tissue remodeling [8], wound-healing [9] and morphogenesis [10], and also in pathological processes like cancer cell invasion [11, 12]. These processes rely heavily on the precise self-organization and mechanics of cellular systems in space and time. Furthermore, deviations from normal mechanical characteristics are directly correlated with the onset and progression of diseases such as cancer cell metastasis, inflammation and abnormal wound repair [13].

The mechanical response of multicellular tissues arises from the properties of the individual cells, alongside the interplay between these cells across multiple length scales [14]. While single cell mechanics are determined by the biophysical properties of their cytoskeleton and plasma membrane, the mechanical properties of tissues as a collective whole are determined by the complex linkage between cell adhesion molecules, the cytoskeleton and the extracellular environment [15, 16]. In order to unravel this complexity, we therefore require techniques that allow us to probe tissue mechanics on different length scales, from the nanoscale to the macroscopic tissue scale.

To probe the mechanical properties of tissues and their responses to physical forces, suitable *in vitro* models that replicate both the multicellular nature and three-dimensional (3D) micro-environment found *in vivo* are required [17, 18]. Nowadays, 3D multicellular systems such as spheroids and organoids have become appealing *in vitro* models to mimic complex physiological microenvironments of tissues. While spheroids are 3D spherical aggregates made from immortalized cell lines or primary cells, organoids arise from embryonic stem cells, induced pluripotent stem cells, or adult stem cells [19]. Organoid models represent the personalized *in vivo* environment more accurately than spheroids, but their generation requires a more complicated process, and is more time-consuming than spheroid production. As such, spheroids have become the most widespread 3D systems for basic biophysical characterization and are the focus in this review chapter. Mechanical forces are integral to spheroid development and self-organization by regulating and changing their overall shape, cell packing density and internal cell arrangement. For instance, the interplay between various physical parameters (such as cell-cell adhesion, cortical tension evoked by the cell's actomyosin cortex, and elasticity) strongly regulates cell sorting in embryos as shown in both 3D aggregates [20, 21] and organoids [22–25]. Spheroids therefore allow us to probe a wide range of key biophysical parameters that influence tissue formation, tumour growth and cell invasion under relevant physical forces (such as shear stress) and gradients of biochemical cues (such as transforming growth factors and nutrients).

Often, tissues subjected to a force demonstrate viscoelastic behavior, with an elastic response at short-time scales and a viscous-like response at long-time scales [26]. When a mechanical load is applied, spheroids alter their shape and microstructure and consequently their mechanical response. This time-dependent behavior and responsiveness

is reminiscent of that found in many glassy and colloidal systems in the field of soft condensed matter [27–31]. Thus, tissue biomechanics has become an appealing field for physicists to apply soft matter principles coupled with biophysical tools. These tools allow us to create a unified conceptual framework and unravel how mechanical forces deform cells in order to create functional healthy tissues and organs, heal wounds or induce pathological conditions such as cancer cell invasion [18, 32–36].

While there are excellent reviews on spheroid formation [37], the role of physical principles in tissue formation [17, 38], jamming transitions (in cancer and morphogenesis) [31, 32] and probing of mechanical stress in living systems [39], a concise review on all the experimental tools for quantification of spheroid mechanics and how these tools have started to reveal mechanisms that govern spheroid mechanics and its implications for cell detachment and migration away from the spheroid is still missing. The main aim of this review is to close this gap by discussing the available state-of-the-art tools (Table 2.1), the relation between spheroid mechanics and tissue sorting, and implications for cell invasion. In the first half, the physiological relevance of spheroids as a 3D *in vitro* model is explained, followed by a discussion on available techniques for the biomechanical characterization of spheroids both from without and within. The second half of this review focuses on the self-organization of tissues and spheroids alongside present theoretical models explaining this phenomenon, focusing on the role of cellular adhesion, cortical tension and their coaction. Spheroid self-organization is subsequently linked to cell invasion in *in vitro* cancer metastasis models, and the influence of experimental parameters like interstitial fluid flows and surrounding extracellular matrix (ECM) type and density is discussed. Finally, the review concludes with a perspective on opportunities for future research. As the biophysics and soft matter communities gain insights into the fundamental mechanical properties of spheroids and what distinguishes multicellular tumour spheroids from healthy cellular aggregates, important biophysical pathways and biomarkers for novel cancer therapeutics can be identified. Moreover, a fundamental understanding of the interplay of individual cell mechanics and cell-cell-interactions in overall tissue mechanics is essential when trying to understand tissue formation, or when designing strategies for tissue regeneration.

2.2. MECHANICS OF 3D MULTICELLULAR SPHEROIDS

2.2.1. THE PHYSIOLOGICAL RELEVANCE OF 3D *in vitro* SPHEROIDS

3D cell culture systems influence cell structure and mechanotransduction in a very different manner compared to traditional 2D monolayer culture set-ups [64]. Many cell types grown on 2D planar substrates become flatter, proliferate at an unnaturally rapid pace and lose their differentiated phenotype in comparison to their *in vivo* counterpart [65, 66]. However, cells regain their physiological form and function when reintroduced in a 3D environment. 3D cellular spheroids are an excellent *in vitro* model for tissues due to their physiologically relevant structure giving them several advantages. Firstly, their mechanical properties can be measured over both intracellular and intercellular length scales. Secondly, spheroids can be grown from a single cell line, allowing the reproduction of experiments on identical and reproducible replicates. Thirdly, cell growth and the biochemical environment, which alter mechanical properties of cells and tissues, can be

2

Technique	Analyzed parameter	Description	Source
Probing from without			
Atomic force microscopy (AFM)	Elastic modulus and viscoelasticity	Measuring cantilever deflection when indenting tissue.	[16, 40–44]
Microtweezers	Elastic modulus	Tracking cantilever bending from customized replaceable cantilevers to determine applied force and tissue stiffness.	[45]
Micropipette aspiration (MPA)	Surface tension, elastic modulus and viscosity	Aspirating spheroid into micron-sized pipette and tracking the displacement of the front of the tongue with respect to the pipette tip over time.	[46–48]
Spheroid fusion	Bulk tissue fluidity	Analyzing coalescence of spheroids for a suitable amount of time (days).	[26, 49–52]
Tissue surface tensiometry (TST)	Surface tension and viscosity	Analyzing relaxation force and shape relaxation after squeezing spheroid between parallel plates.	[21, 26, 51, 53–57]
Probing from within			
Cellular scale			
Cavitation rheology	Tissue interfacial tension and elastic modulus	Analyzing pressure-growth relation for a spherical cavity induced in the material with a needle.	[58–60]
Hydrogel mechanosensors	Spatial distribution of mechanical stress in tissue	Defining the strain (change in volume) of incorporated hydrogel probes, allowing highly localized measurements of traction forces or mechanical pressure.	[61, 62]
Subcellular scale			
Optical tweezers	Cytoplasmic stiffness	Measuring force-displacement relationship of unidirectionally dragged particles that are endocytosed by constituent cells.	[63]

Table 2.1: Techniques to analyse spheroid mechanics from without and within.
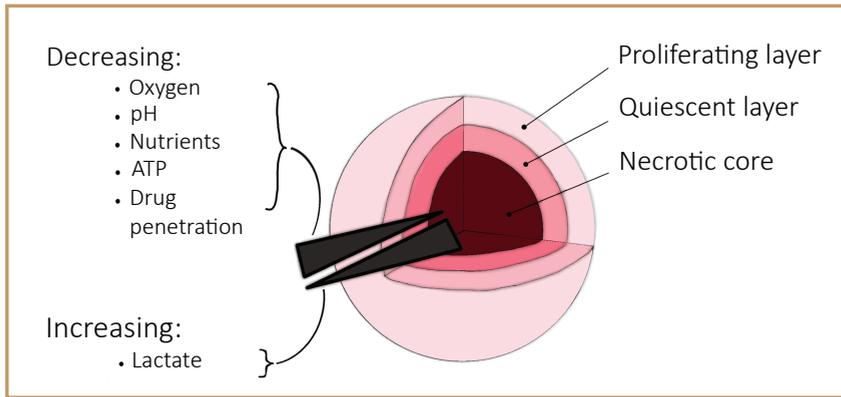
Figure 2.1: Spatial structure of a spheroid. Schematic of a spheroid demonstrating a necrotic core surrounded by quiescent cells and an outer proliferative layer, with a decreasing gradient of among others oxygen and pH towards the core, and an increasing gradient of lactate.

meticulously controlled [67–69]. Due to the 3D nature of spheroids, cells in the core of the spheroid will receive less oxygen and nutrients and experience a lower pH than the outer cells, similar to *in vivo* tumours (Fig. 2.1). When the inner cells are situated beyond the diffusion limit of approximately 200 µm from the edge of the spheroid, cell apoptosis occurs [70, 71]. This results in the formation of a necrotic core surrounded by quiescent cells and an outer proliferating layer [72]. *In vivo*, tissue cells are located no further than 100 to 200 µm from the nearest capillary due to the limited diffusion of oxygen [73]. Cancer cells are capable of signalling for the formation of new blood vessels to overcome this fundamental limitation. This process creates a disorganised vasculature with an ineffective delivery of oxygen and nutrients to the tumour, resulting in similar concentration gradients as for *in vitro* spheroids [72].

Many techniques exist for generating spheroids (Fig. 2.2). These include the hanging drop technique [74], liquid overlay [60, 69], a shaking method that folds cell sheets into spheroids [75], droplet-based microfluidics [76, 77], and many others. Importantly, spheroids can either be grown using a scaffold or by suspending cells in medium surrounded by non-adhesive walls. When using a scaffold, cells anchor to a 3D platform that mimics the extracellular matrix (ECM), which can be either natural (e.g. collagen), semi-synthetic (e.g. chitosan) or fully synthetic (e.g. polycaprolactone) [67]. For non-scaffold suspension-based techniques, cells float towards each other in suspension due to gravity after which they aggregate. Here, ECM is still present inside the spheroid due to proteins excreted by cells during the growth of the aggregate [78]. For a more extensive overview of the available spheroid culturing techniques and methodologies to analyse characteristics like size, growth and protein expression, the reader is referred to other reviews [37, 67, 79].

Importantly, the choice between a scaffold- or non-scaffold-based technique will define the polarity of cells at the tumour spheroid surface [80–82]. Cellular architecture and function are fundamentally dependent on this cell polarity, also termed apical-basal

2
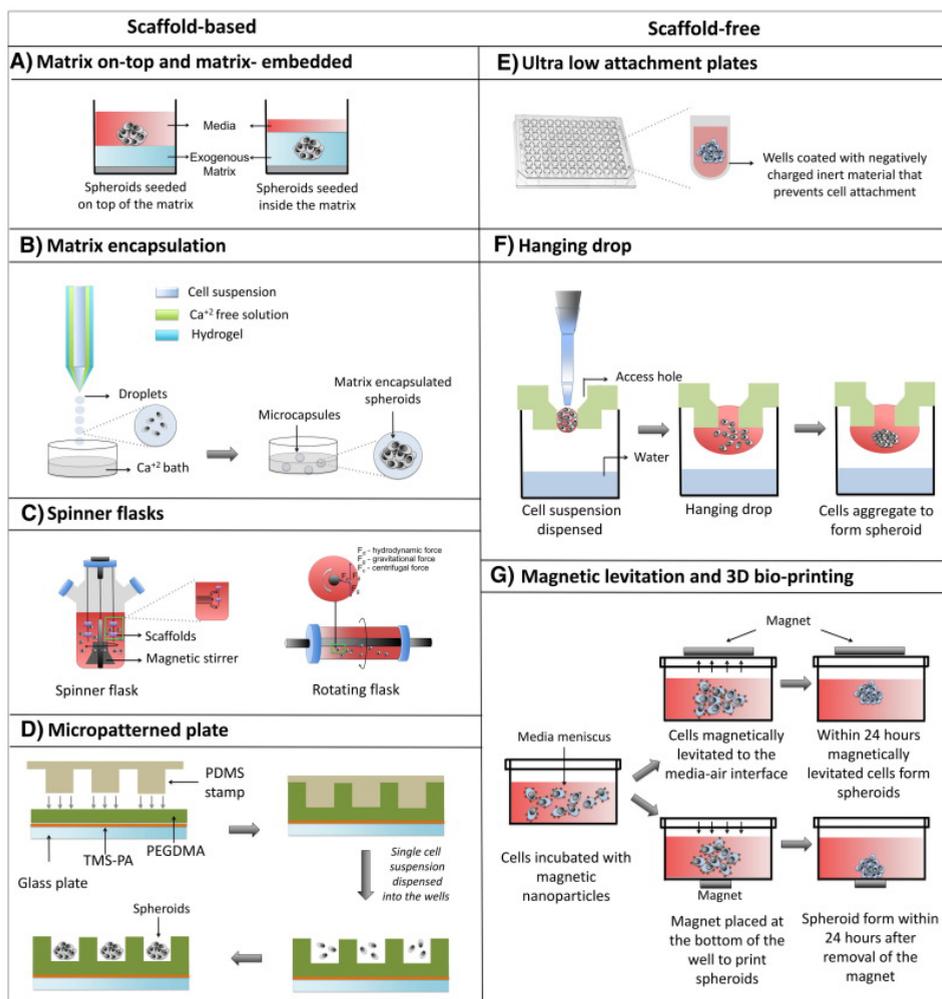
Figure 2.2: Spheroid growing techniques. Sorted into scaffold based (A-D) and scaffold-free techniques (E-G). Reprinted from [37], Copyright 2016, with permission from Elsevier.

properties [83]. Epithelial cells that line the exterior and interior surfaces of our bodies form functionally distinct domains, termed apical and basal, and polarize along an apical-basal axis in order to form selectively permeable barriers (Fig. 2.3(a)) [84]. The apical side of the cell lines the lumen, hollow spaces in some of our major organs, and constitutes an exchange interface with other parts of the body. The basal side faces the basement membrane, the specialized cell surface-associated ECM on which cells live [85]. *In vivo*, the apical-basal polarity can differ between healthy and malignant tissues. For example, the invasive metastatic cancer spheroids found in the peritoneal cavity of

colon cancer patients display a clear apical-out topology that is inverted compared to normal epithelial tissues [86]. *In vitro*, spheroids grown in a type I collagen-scaffold display an apical-in topology while spheroids in suspension have an apical-out architecture on their surface (Fig. 2.3(b)) [80]. As such, the spheroid culturing technique should be carefully selected depending on the relevant *in vivo* tumour model.
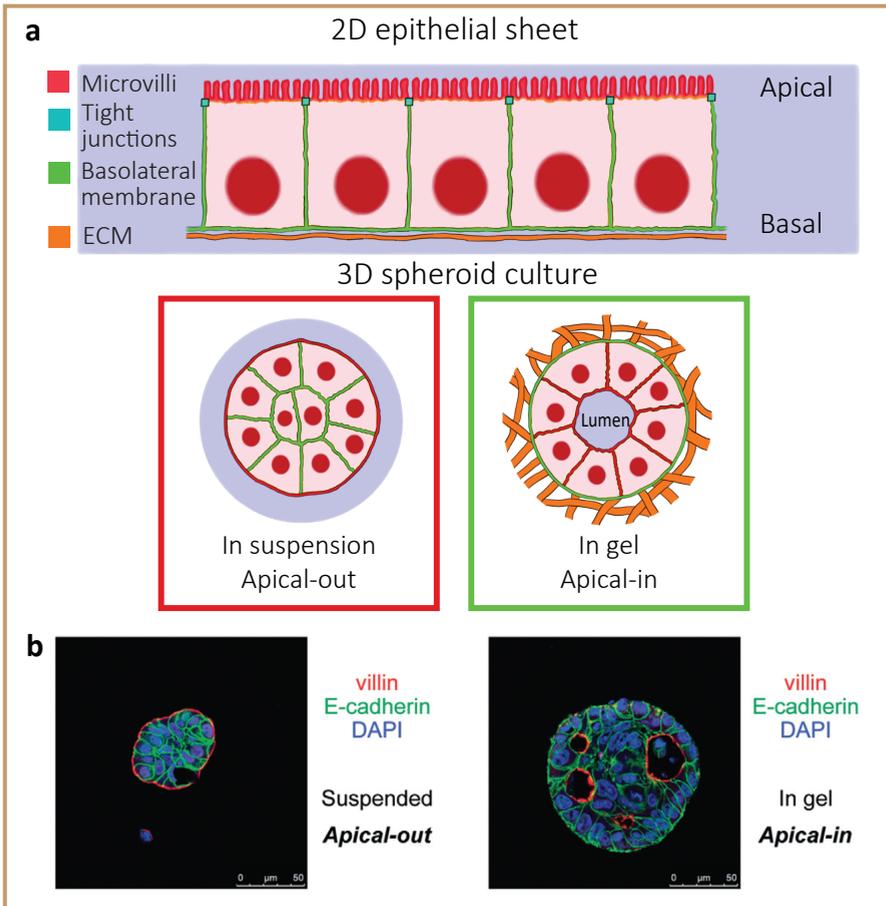
Figure 2.3: Cell polarity in multicellular assemblies. a) Schematic of apical-basal cell polarity in a 2D epithelial sheet where the basal side faces the ECM, and of spheroids, whose polarity depends on culturing technique. b) Immunofluorescence staining of colorectal cancer spheroids both in suspension and embedded in type I collagen cultured for 48 hours, demonstrating apical-out polarity when in suspension or apical-in when in a scaffold. Red: villin; green: E-cadherin; blue: DAPI. (b) is reprinted and adapted from [80], Copyright 2016, with permission from Elsevier.

2.2.2. PROBING SPHEROIDS FROM WITHOUT

SURFACE TENSION AND VISCOSITY

Just like *in vivo* embryonic tissues, heterogeneous spheroids composed of different cell lines are able to display spontaneous tissue segregation [54, 55]. Similar to how one immiscible liquid tends to envelop another due to their difference in surface tensions, one cell line can envelop the other in a binary-mixed spheroid depending on cellular properties [51]. Understanding the physical mechanisms of cell sorting is important both at a fundamental level and at a more practical level in for example the field of 3D tissue bioprinting [52]. In the 1960s, the differential adhesion hypothesis (DAH) was formulated to explain this liquid-like phenomenon, and focused on the concept of tissue surface tension [87–89]. The model states that the rearrangement of cells is guided by the lowering of a cell population's adhesive-free energy as the amount of cell-cell bonding increases. As such, the mutual spreading mechanisms of tissues are specified by their relative surface tensions, which depend on the difference in intercellular adhesion of the different cell types [90, 91]. For a pair of adhesive tissues, the tissue of lower surface tension will envelop the tissue with a higher surface tension [92]. This outcome has proven to be independent of the types of adhesion molecules utilized by the interacting cells [93]. The most widely studied classes of cell-cell adhesion receptors are the cadherins [94]. Spheroids have a surface tension that is a direct and linear function of their cadherin expression level [90]. Thus, a spheroid made out of two cell lines will rearrange in such a way that the cell line with a lower cadherin expression level spreads over the other [93]. Nowadays, there are however more sophisticated models that demonstrate regimes where the DAH breaks down. These will be introduced later on in this chapter.

Perhaps the most straightforward technique to get an indication of relative mechanics between cellular aggregates is **spheroid fusion** [49, 50]. For this technique, two spheroids are brought together and allowed to fuse over time to give an indication of cell motility, also termed bulk tissue fluidity, and surface tension (Fig. 2.4(a)) [26, 51]. Making an analogy between spheroid fusion and the fusion of liquid droplets, the main parameters that define the fusion process are surface tension and viscosity. According to the liquid drop fusion model, higher surface tensions should result in shorter fusion times [95]. However, discrepancies to this model were found when epithelial spheroids with lower apparent surface tension fused faster than mesenchymal spheroids with higher surface tension [50]. This was most likely caused by processes such as extracellular matrix remodeling and dense cell packing in the mesenchymal spheroids. Nevertheless, the technique remains useful as measuring the fusion time gives an indication of how fluid-like or solid-like tissues are. Additionally, the cell and nucleus shapes during fusion give an indication of tissue fluidity and bulk mechanical behavior [49]. In samples from cancer patients, the degree of tissue fluidity is correlated with elongated cell and nucleus shapes, which in turn are linked to a higher motility. Cell and nucleus shape may thus identify metastatic potential during therapeutic treatment.

A widely used method to measure tissue surface tension is **tissue surface tensiometry (TST)**, also known as parallel plate tensiometry [53–56]. Here, a spherical aggregate is placed between two parallel compression plates (Fig. 2.4(b)). Through continuous recording of both the force used to compress the spheroid and its contact angle with the plates, an apparent tissue surface tension is determined using the Laplace equation
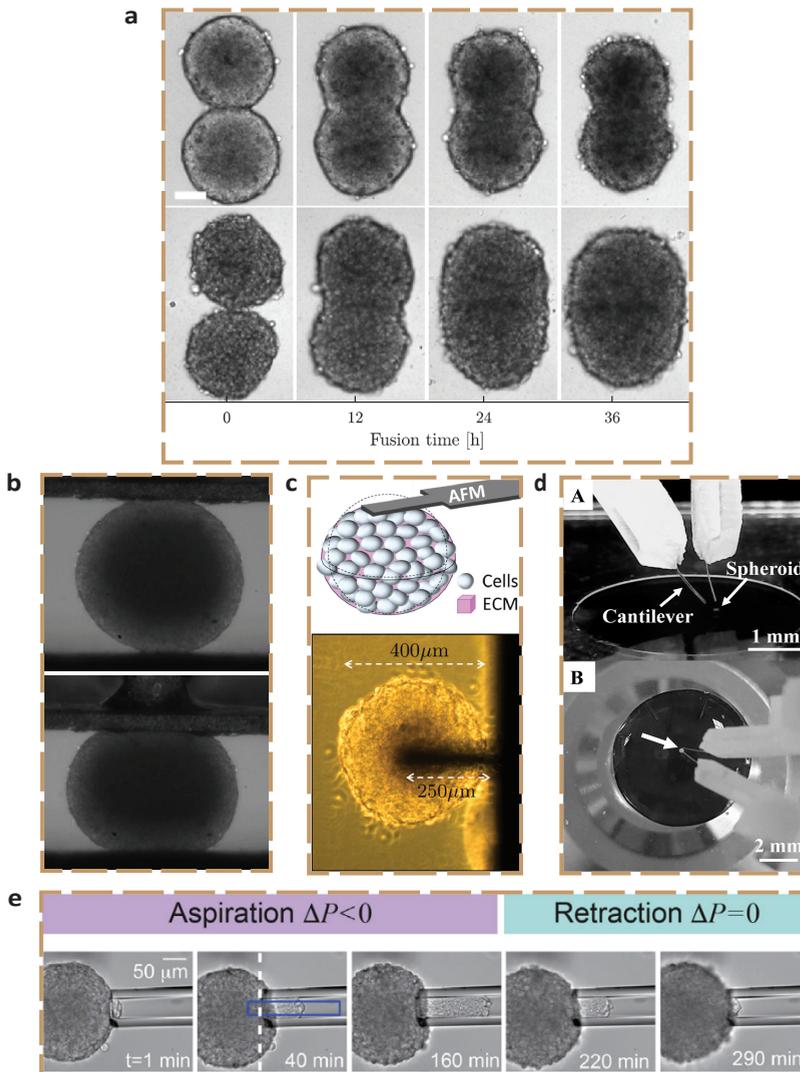
Figure 2.4: Probing spheroids from without. a) **Spheroid fusion** time series demonstrating cell type dependence. Spheroids formed from the non-tumourigenic MCF-10A cell line (top) fuse slower than spheroids made from metastatic MDA-MB-231 cells (bottom). Scale bar: 100 µm. b) **Tissue surface tensiometry** with an uncompressed (top) and compressed (bottom) spheroid in culture medium. c) Schematic and image of a spheroid in contact with a tip-less **AFM** cantilever. d) (A) **Microtweezer** set-up and (B) cantilever tips compressing a spheroid. e) Time series of the **micropipette aspiration** of a spheroid for almost 3 hours, and retraction of the tongue as the aspiration pressure is set back to zero. (a) is reprinted and adapted from [49], licensed under CC BY 4.0; (b) is reprinted and adapted from [57], licensed under CC BY 3.0; (c) is reprinted and adapted from [43], Copyright 2021, with permission from Elsevier; (d) is reprinted and adapted from [45], licensed under CC BY 4.0; (e) is reprinted and adapted from [96], Copyright 2017, with permission from Elsevier.

originally developed for simple liquids [53, 56]. Only when successive compressions at different forces yield a similar surface tension, the spheroid can be considered liquid-like with an actual surface tension. This typically holds as long as spheroids are spherical and cells do not become fixed in position over time, for instance due to possible extracellular matrix build-up [54, 55]. Of course, the assumption that spheroids are similar to liquid droplets is a clear oversimplification. Aggregates of cancer cells for instance often do not round up into spheroids and they often have a rough surface. Nevertheless, measuring the apparent tissue surface tension holds biological relevance when trying to explain observed tissue configurations and cell sorting.

STIFFNESS AND ELASTICITY

It has long been known that cells and tissues can display both solid-like elastic and fluid-like viscous behavior, making them viscoelastic [26]. Techniques that are able to measure this viscoelastic behavior both at a single-cell and tissue-level are of interest for several reasons. Firstly, defining the time-dependent mechanics of cells is necessary not only to see how they deform but also to understand how they transduce external mechanical forces into biochemical-signaling cascades that govern their behavior [97]. Secondly, changes in a cell's deformability defined by cytoskeletal dynamics have long been considered as a biophysical marker with diagnostic and therapeutic potential for malignancy and metastatic ability in cancer cells [98, 99].

A common technique to measure the mechanical properties of single cells and tissues is **atomic force microscopy (AFM)**. The high force sensitivity, spatial resolution and compatibility with living samples make AFM an ideal technique for probing local mechanical properties of tissues, with examples ranging from the rat hippocampus to human breast biopsies [15, 16, 42, 100]. Using a cantilever, the tissue in question is indented at several points in an array in order to map out its stiffness. Knowing the spring constant k of the cantilever, the deflection of the cantilever as a function of indentation depth gives an apparent elastic modulus of the tissue. If the indentations are performed at a single low speed of indentation, solely an apparent pseudo-elastic modulus is determined and the viscoelastic behavior of the tissue is neglected [101]. With a sharp AFM tip, the deformation is highly localized and stress dissipation is determined from viscous drag of the cytoskeletal filaments [102], rather than poroelastic effects [103]. To determine the viscoelastic response of cells or tissues, the AFM can be operated in a dynamic mode using sinusoidal oscillations in force/indentation at a functionally relevant frequency (0.5-4 Hz) [40, 104]. The main advantage of AFM is its nanometer-scale spatial resolution, which allows AFM to evaluate the mechanical heterogeneity between morphologically distinct regions within small biological samples. However, AFM indentations are limited to small depths (<10 μm) making it a surface-based technique [42]. For this reason, it is only suitable to create stiffness profiles of the outer proliferation layer of a spheroid (Fig. 2.4(c)) [43, 44]. The technique is therefore mostly used on single cells and flat tissues and rarely for spheroids.

Microtweezers are a novel technique that is more suitable to measure the stiffness of 3D spheroids [45]. Mimicking a pair of chopsticks, the spheroid is held between two force-sensing microtweezers and is compressed by displacing one of the tweezers with a piezo-bimorph actuator (Fig. 2.4(d)). The Young's modulus of the spheroid is determined by optically tracking the bending of the tweezers upon spheroid compression

with a pattern matching algorithm. The dual cantilevers are easily replaceable and are able to work with forces ranging from less than one hundred nN to one mN. However, the technique requires fabrication of custom-made tweezers as well as careful calibration of their spring constants with a precision mechanical stage. As microtweezers are a novel technique, it has not yet been widely used.

A common technique to measure cell or nucleus mechanics is **micropipette aspiration (MPA)** [105–107]. Here, a step-wise stress is applied to a single cell by aspirating it with a micron-sized glass pipette which has a radius that is approximately 3-4 times smaller than the diameter of the cell [105]. In case of a multicellular tissue, cell aspiration can be performed on different cells on the surface of the tissue to map variations in cell mechanics, as demonstrated recently for mammalian embryos [108]. When increasing the pipette radius, the technique can be used to measure the collective viscoelastic properties and surface tension of spheroids [47, 48]. Here, a constant stress is applied through an underpressure in the pipette after which a tissue tongue flows into the pipette (Fig. 2.4(e)). Assuming that spheroids behave as viscoelastic drops when exposed to a suction force, the response of the spheroid to the aspiration is characterised by tracking the length of the advancing tongue as a function of the applied underpressure. A drawback to this technique is that it is time-consuming to fabricate the micropipettes and align these with the spheroids.

Interestingly, Guevorkian *et al.* [47] showed how the surface tension of aspirated spheroids increased with the applied force. Retraction of the aspirated cell tongue from the pipette was measured at zero pressure, and shown to be dependent on the applied pressure during the aspiration. In other words, spheroids achieved a *reinforced* tissue cohesion after applying a stress, indicating that the cells actively sense and respond to an applied load. Similar cell reinforcements in response to mechanical perturbations have been found in experiments on single culture cells [109, 110]. By contrast, tissue surface tensiometry showed that spheroid surface tensions were independent of the applied force [56]. This discrepancy might be explained by the fact that the aspiration pressure during MPA is only applied to a part of the spheroid, while tissue surface tensiometry exerts a force on the whole spheroid. Future research will have to identify the possible emergence of mechanosensing when applying a local force to a part of the spheroid.

2.2.3. PROBING SPHEROIDS FROM WITHIN

CELLULAR SCALE
Mechanical features of the local microenvironment are well-established to drive cellular processes [3, 4]. Surrounding tissue stiffness affects cell proliferation, migration, differentiation during development [111], tissue homeostasis [112] and disease progression [113, 114]. However, techniques to measure mechanical properties of cells and the extracellular matrix inside tissue are limited. Macroscale tools like TST and MPA are not able to capture local mechanical variations around cells in the interior of a spheroid, as they only measure mechanics of a collective whole from the outside.

An interesting technique to measure the elastic modulus of spheroids from within is **cavitation rheology**, which compares the work of bubble formation to the deformation of the spheroid [58, 60]. A spheroid is transferred into a glass capillary, after which a micron-sized glass needle is inserted into the spheroid using a micro-manipulator

2
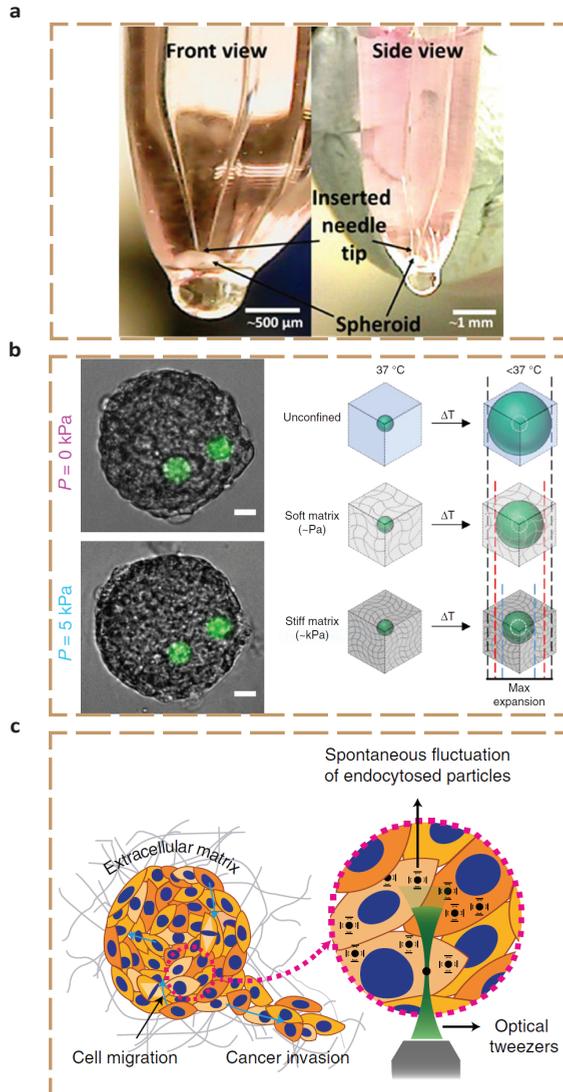
Figure 2.5: Probing spheroids from within. a) **Cavitation rheology**, where a 30 μm needle is inserted into a spheroid to induce a cavity. b) **Hydrogel mechanosensors**, which can either be osmotically compressed (left, scale bar: 20 μm) or are thermoresponsive (right). Their final change in volume is determined by the elasticity of the surrounding tissue. c) Schematic of a spheroid embedded in ECM, where the cytoplasmic mechanics of the periphery cells are determined using **optical tweezers** pulling on endocytosed particles. (a) is reprinted and adapted from [60], licensed under CC BY 4.0; (b) is reprinted and adapted, the left half from [62] and the right half from [61], both licensed under CC BY 4.0; (c) is reprinted and adapted by permission from Springer Nature: Springer *Nature Physics* [63], Copyright 2020.

(Fig. 2.5(a)). By injecting a cavitation medium (air or water), slow pressurization induces an elastic instability in the form of a cavity. The pressure-growth relationship for this induced spherical bubble relates to the elastic modulus of the spheroid [58, 115]. Additionally, comparing the energy associated with bubble formation to the binding energies of the cell surface proteins gives an estimation of the cortical tension of the cells that form the spheroid [60]. During measurements, spheroids are kept in culture medium, which introduces a technical challenge since they can float away from the needle during insertion. Moreover, determined elastic modulus values are only valid in the "thickshell" regime, where the induced cavities are small enough so as to not affect the outer diameter of the spheroid.

Similar to tissues, ECMs exhibit viscoelasticity, mechanical plasticity and nonlinear elasticity, which affect fundamental cellular processes including proliferation, differentiation and migration [116]. When cancerous spheroids are embedded in an ECM scaffold, they remodel the matrix either through contractility or growth, depending on various parameters such as cell type, cellular packing density and ECM stiffness [117–119]. Some cell types form spheroids that, when embedded in collagen gels, induce a contractile pressure at the spheroid-ECM interface, thereby deforming the collagen network inward resulting in tensile forces in the matrix that realign fiber bundles enabling cell invasion [117]. Others form spheroids that grow through cell proliferation, inducing a compressive stress at the spheroid-ECM interface [118, 119]. This stress inhibits cell proliferation but is reversible once the stress is released [120]. In order to measure these highly local tissue mechanics, recent studies have developed the use of **hydrogel mechanosensors** [61, 62]. In contrast to cavitation rheology which actively probes spheroids, these sensors are used for passive probing. Mechanically well-defined elastic polyacrylamide (PAA) microbeads serve as internal cell-like sensors by being incorporated in spheroids grown under mechanical stress (Fig. 2.5(b), left panel) [62]. They are functionalized to promote cellular adhesion, show fluorescence when imaged, and exhibit uniform and well-calibrated elastic properties. The use of PAA gels provides several advantages. Firstly, the elastic modulus can be easily tuned by changing the relative concentration of acrylamide to bisacrylamide [121]. Furthermore, the material is itself inert so cell adhesion only depends on the type of ligand coupled to the bead's surface. The local pressure inside the spheroid is measured by monitoring the strain (change in volume) of the hydrogel beads. The bulk modulus of the beads can be calibrated beforehand by osmotic compression, for instance with high molecular weight dextran that neither penetrates the beads nor the spheroid [43, 122]. At small enough compressions (i.e., small dextran concentrations), the stress/strain relation is linear and the bulk modulus of the beads can be deduced from the slope of the curve. Outside this linear regime, an empirical polynomial Mooney-Rivlin model is used [62]. After determining the bulk modulus of the beads, the pressure profile of the spheroid can be quantified based on before-and-after measurements of the incorporated bead size when osmotically compressing a spheroid. The ideally random distribution of PAA beads across the spheroid enables the determination of the pressure profile along the spheroid radius. Measurements demonstrated that the pressure rises towards the core of the spheroid, explained by the anisotropic arrangement of cells.While these sensors have so far solely been used to identify local pressures in spheroids under isotropic compression, they should also give access to shear stress

measurements once the deformation of the beads under shear is identified. Furthermore, anisotropic stresses have been measured in tissues (though not in spheroids) using oil microdroplets functionalized with ligands for cell surface receptors [123]. Similar to the PAA gels, the deformation from their spherical shape at equilibrium translates to force measurements. However, their lack of compressibility makes them unsuitable to identify the isotropic component of the stress.

Recently, a similar type of mechanosensor has been introduced which is temperature-actuated [61]. Unlike PAA, poly N-isopropylacylamide (PNiPAAM) hydrogels are thermoresponsive gels that remain compact at tissue culture temperatures but swell when cooled by a few degrees (Fig. 2.5(b), right panel). They can be conceptualized as springs that are pre-loaded by thermodynamic expulsion of water before incorporation in the tissue. Decreasing the temperature releases this pre-strain and returns the beads to a new equilibrium volume defined by the rigidity of the surrounding tissue. The change in volume relates to the elasticity of the tissue after creep. These probes could even be injected within *in vivo* mouse tumors where they did not result in signs of additional fibrosis or inflammation over a period of 3 weeks, suggesting their excellent biocompatibility [61]. The PNiPAAM beads are calibrated by encapsulating them in stiffness-tunable polyacrylamide gels with linear elastic properties and measuring their change in radii after releasing the pre-strain.

However, both hydrogel mechanosensors present some limitations. First, the obtained spatial distribution of mechanical stress in tissues lacks a time-dependent component. Secondly, the sensors may be sensitive to local environmental factors such as pH, which can be nonuniform in spheroids [124]. Thirdly, both sensors might affect cell behavior as they are foreign particles and induce a foreign body response [125]. Yet, functionalizing the hydrogel surface with appropriate matrix molecules might provide a way to minimize this. Fourthly, the change in temperature needed for PNiPAAM to obtain the measurement may influence the tissue stiffness, though previous studies have shown that cellular rigidity is not significantly affected between 21 °C and 37 °C [126]. Despite these limitations, the probes provide a unique technique to obtain direct *in situ* mechanical measurements inside spheroids and tissues.

SUBCELLULAR SCALE

Optical tweezers are able to study mechanics within spheroids incorporated in an ECM. While both cavitation rheology and hydrogel mechanosensors probe spheroids at the cellular level, optical tweezers operate at a subcellular level. Optical tweezers have been widely used, in combination with nano- and microfluidics, both in the soft matter field [127] and in biological sciences [128]. The technique uses strongly focused laser light to trap a refractive particle in the focal point [129], providing excellent resolution in positioning (± 1 nm) micron-sized particles and in contactless measuring of forces (± 50 fN) [130]. Recently, optical tweezers have been used to perform active microrheology on migrating cells in the periphery of a spheroid embedded in a collagen matrix (Fig. 2.5(c)) [63]. The mechanical properties of the cytoplasm inside the peripheral cells were measured by embedding small latex particles in the gel that got endocytosed. The force-displacement curve measured upon dragging the particles with the optical tweezer reveals the cytoplasmic stiffness. Importantly, the method is insensitive to the mechanics of the actin cortex that underlies the membrane, which is a principal determinant of cell

surface tension. Additionally, a cell's interior is heterogeneous so care needs to be taken when determining which cellular components regulate the response. Nevertheless, this technique arguably brings us the closest to understanding sub-cellular mechanics inside cell spheroids.

2.3. FROM CELL SORTING TO INVASION

2.3.1. COACTION OF INTERCELLULAR ADHESION AND CORTICAL TENSION

Cell-cell adhesion is mediated by transmembrane proteins called cadherins that interact through extracellular domains [131]. Cadherin bonds are stabilized by the cortical actin network, with the interaction between actin and cadherins being dynamic and mechanoresponsive [132–134]. Cadherins also act as signaling molecules that begin local reorganization of actomyosin when cells come into contact [135]. While the previously discussed DAH has successfully accounted for many observations of tissue sorting, it focuses solely on cell adhesion contributions from cadherins to tissue surface tension, and neglects the role of the cortical actin network [90]. Studies following up on the DAH have however shown that the tissue surface tension actually depends on a balance of adhesion, cortical tension and cortical elasticity [136–138]. These findings helped shape the differential interfacial tension hypothesis (DITH), which relates tissue surface tension to the tension along individual cell-cell interfaces and to the role of actin-myosin activity (Fig. 2.6(a)). The DITH acknowledges that individual cells are not point objects but finite-sized deformable objects that can adapt their geometry. Since the mechanical energy changes with cell shape, the cortical tension evoked by the thin cortical layer of actin beneath the cell membrane has to be involved in the energy balance [139]. To resolve possible discrepancies between the DAH, which states that cell types sort due to cadherin ratios (Fig. 2.6(b)), and the DITH, Manning *et al.* developed a model that explicitly showed how the overall surface tension of a multicellular aggregate is determined by the ratio of adhesion tension to cortical tension, indicating a crossover from adhesion-dominated to cortical tension-dominated behavior [21].

To experimentally demonstrate the coaction of cell adhesion and cortical tension in determining tissue surface tension, Manning *et al.* treated spheroids made of mouse embryonic fibroblasts transfected with P-cadherin with actin-depolymerizing drugs (cytochalasin D and latrunculin A), making the cells not only lose cortical tension but also cell-cell adhesion as the actin anchor of cadherin bonds was weakened [21]. This drug treatment resulted in rounded surface cells and a lower surface tension of the spheroid in contrast to untreated control spheroids that had flat cells at the surface that were stretched across multiple bulk cells in order to maximize cell-cell contact (Fig. 2.6(c)). This finding demonstrated how changes in surface cell shape influence tissue surface tension. When the surface cells are compact, they make fewer adhesive contacts than the bulk cells, and this differential adhesion is the primary contribution to the surface tension just as in liquids. In this scenario, the surface tension varies linearly with the *effective* adhesion as predicted by the DAH. However, the comparison to fluids becomes invalid once surface cells elongate so they can make contacts with multiple bulk cells. In this case, there is no longer an adhesive contribution to the surface tension and the DAH breaks down. The ratio between cortical tension and effective adhesion will determine
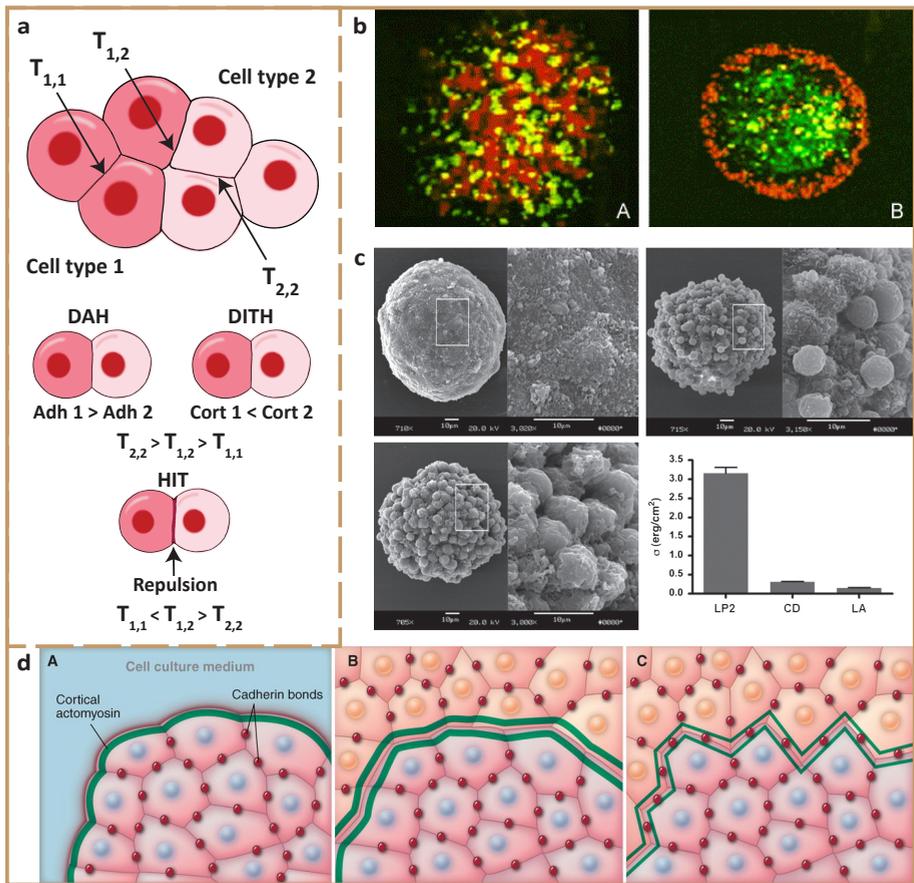
2

Figure 2.6: Cell sorting and tensions. a) Schematic of contact tension in tissues, and the three main models for cell sorting, showing differences in homotypic tensions $T_{1,1}$ and $T_{2,2}$ and heterotypic tension $T_{1,2}$. The DAH is regulated by cell adhesion, while the DITH also involves the role of cytoskeletal components, and the HIT focuses on repulsive mechanisms generated by ephrin-Eph signalling. For the DAH and DITH, heterotypic tensions are intermediate, in contrast to the HIT where they exceed the homotypic tensions. Inspired by [140]. b) Confocal images of a spheroid made from two cell lines transfected to have different N-cadherin ratios. First, (A) the spheroid remains mixed after 4h of incubation (B) but after 24h sorts in accordance with the DAH, with the cell line expressing the lower level of N-cadherin (red) enveloping the cell line expressing higher amounts of N-cadherin (green). c) SEM images of spheroids made from a P-cadherin-transfected L-cell line termed LP2 by the authors; with up-left a control LP2 aggregate, up-right treated with latrunculin A (LA) and down-left treated with cytochalasin D (CD) to depolymerize actin. Down-right shows surface tensions measured for all three types with tissue surface tensiometry. d) Boundary polarization at (A) tissue-culture and (B, C) tissue-tissue interface. Red dots indicate cadherin bonds, green lines indicate higher-than-average actin density where the thickness of the line shows the amount of generated tension. Nuclei are either blue or orange to make a distinction between two cell types. While boundary polarization occurs for tissues in vitro, it (B) may or (C) may not occur at an *in vivo* tissue-tissue interface, possibly explaining differences between *in vivo* and *in vitro* cell sorting. (b) is reprinted from [90], Copyright 2005, with permission from Elsevier; (c) is reprinted from [21], with permission from the authors; (d) is reprinted from [135]. Reprinted with permission from AAAS.

whether surface tension is in a regime where intercellular adhesion is dominant or in one where cortical tension dominates.

While the DAH and DITH are based on the assumption that all cells are roughly identical and can be characterized by properties measured for a single cell, cells at tissue boundaries mechanically differ from those in the interior [141, 142]. Boundary cells actively change their mechanical properties; they mechanically polarize [135]. Using traction force microscopy, cells in pairs and triplets plated on collagen-coated polyacrylamide gels were shown to reorganize their adhesive and cytoskeletal properties. The cells displayed a significantly higher density of actin filaments and a higher tension along the external boundary interfaces compared to the internal interfaces of the pairs and triplets [143]. With increasing 2D cohesive colony size (up to 27 cells) on soft substrates, traction stresses localized at the edge of the colony, demonstrating mechanical polarization at tissue boundaries [141]. Boundary polarization also occurs *in vivo*, for example at compartment boundaries in the *Drosophila* embryo [144, 145]. However, the possible relation between mechanical polarization and tissue sorting remains unclear. Tissue compartmentalization *in vivo* does not always correlate with *in vitro* cell sorting, as has been shown in *Xenopus* embryos [146]. While *in vitro* cell sorting is dominated by short-time scale interactions between the external domains of cadherins, *Xenopus* embryo results suggest that *in vivo* sorting is regulated by long-time scale spatial reorganization of cadherins and cortical tension upon tissue intercalation [146]. The inconsistency between *in vitro* and *in vivo* cell compartmentalization might occur because contact with culture medium for *in vitro* cell aggregates will necessarily mechanically polarize the system (Fig. 2.6(d)). Next to this, cells *in vivo* are in contact with complex extracellular matrix structures, which may influence boundary polarization and thereby cell sorting.

Although differences in cell adhesion and cortical tension suffice to drive cell sorting *in vitro*, recent experiments show that a local discontinuity in contact tension is an additional requirement to build an embryonic boundary and induce tissue separation *in vivo* [140]. In embryonic tissues, membrane-bound proteins such as ephrins and Eph receptors induce local repulsion at heterotypic contacts between different cell types and thereby efficiently sort cell populations and inhibit mixing [147]. This discovery gave birth to the high heterotypic interfacial tension (HIT) model, where ephrin-Eph-mediated repulsion creates a higher tension at the heterotypic boundary between two tissues compared to the tensions at the homotypic contacts inside each separate tissue (Fig. 2.6(a)). This differs from the DAH and DITH, which assume that the homotypic tension is higher in one of the two cell populations and intermediate at the heterotypic boundary [140]. Computer simulations suggest that the most favourable condition for tissue separation is to have low contact tension (the sum of the two cortical tensions at a cell-cell contact) in both tissues that contrasts with the high interfacial tension between the tissues [140]. The strength of cell-cell adhesions within tissues is therefore important for tissue separation as long as it creates the correct difference in tension with the heterotypic interfacial tension. The simulations were confirmed by experiments using *Xenopus* embryonic cell types [140]. Tissue separation still occurred when one of the homotypic tensions was equal to or even higher than the heterotypic tension, as long as this difference was compensated by a large difference between the heterotypic and second homotypic tension. The DAH and DITH assume that tissues are liquid-like and sample

many configurations until they find the minimum free energy states. Kinematic effects such as active cell motility and cell shape fluctuation are assumed to be sufficiently small such that the system dynamics are governed by a free energy [135]. These assumptions have been challenged by experiments in which small changes to single-cell properties caused tissues to transition from a liquid-like to a solid-like state, termed as jamming [148]. The other way around, epithelial cells that are first in a solid-like jammed state can start to exhibit a collective phase that is dynamic, migratory and fluid-like, termed unjammed [149]. Both *in vivo* and *in vitro*, for example for primary human bronchial epithelial cells, cell shapes become more elongated and more variable as the epithelial layer becomes more unjammed [149, 150]. This change in cell shape, parameterized through a shape index, reflects the competition between cell-cell adhesion and cortical tension during the jamming/unjamming transition [148, 150, 151]. Here, rearrangements amongst neighboring cells are seen to be hindered by local energy barriers, defined by a combination of cell-cell adhesion, cortical tension and cellular propulsion. When the propulsive forces are negligible, theory describes how an increase in cell-cell adhesion or decrease in cortical tension can cause energy barriers to decrease or disappear [148, 150, 151]. When this happens, cells unjam. In the process of metastasis, cells usually change their adhesion and cortical tension. In order to migrate, tumour cells lose epithelial characteristics and obtain a more mesenchymal phenotype [152, 153]. This change in characteristics is called the epithelial-mesenchymal transition (EMT). Once tumour cells have metastasized into the secondary organ environment, the reverse process can occur (for example through re-expression of E-cadherin) and the cells undergo a mesenchymal-epithelial transition (MET) [154]. Even though epithelial cells are endowed with plasticity and increased migratory capacity during both EMT and unjamming, the cellular crowded, solid-like epithelial collective can undergo unjamming in the absence of EMT [155]. Changes in EMT marker protein levels like E-cadherin, vimentin and N-cadherin do not correlate with unjamming migratory dynamics [156]. Even more, in forms such as breast cancer, lung cancer and prostate cancer, metastasis is dominated not by dispersion of individual cells but rather by collective migration of clusters, packs or strands [157, 158]. To remain in these clusters, carcinoma cells often stay cohesive and continue to express epithelial markers such as E-cadherin [159, 160]. A recent study with spheroids showed how cell sorting changes depending on the metastatic properties of cancer cells, relating to active cell motility, EMT and jamming [142]. The study analyzed the mechanical properties of three breast cancer cell lines (MCF-10A, MDA-MB-231, MDA-MB-436), selected because they cover a shift in E-, N- and P-cadherin levels characteristic of EMT, mixed the cell lines to form heterogeneous spheroids and looked at the sorting behavior. Surprisingly, the final sorted states of the grown spheroids proved to be incorrectly predicted by the DAH as cell lines with a lower surface tension would not always envelop the ones with a higher surface tension. In contrast to embryonic tissues that do sort in agreement with the DAH [51], cell lines that demonstrate EMT-characteristics apparently do not have to follow these models. Instead of behaving as simple liquids, active cell motility and processes such as cell jamming may play an important part in tissue sorting across the epithelial-mesenchymal transition. Dynamical effects such as directional motility, friction and jamming are therefore of importance when investigating sorting in multicellular tumour spheroids.

Box: Definitions of mechanical parameters characterizing cell spheroids

Cortical tension
The apparent surface tension of a cell, presumed to be dominated by myosin motor-driven contraction of the actin cortex and the interaction of the actin cortex with the membrane. SI unit: N/m.

Stress
Force exerted on a surface area. The direction at which the force is applied to the area determines whether it is a compressive stress (perpendicular to the surface), shear stress (parallel to the surface) or elongational stress (perpendicular to the surface). SI unit: Pa.

Strain
The amount by which a material is deformed. Strain is determined from the change in size of the material before and after a force is applied. Unitless.

Elasticity
The instantaneous response of a material to force by deforming a certain amount that is proportional to the applied stress. An elastic material maintains its deformation while under stress and recovers to its original shape once the stress is removed. A material's 'spring constant' is normally quantified by the elastic modulus, which is the ratio of stress to strain. Depending on how stress and strain directions are specified, three primary moduli are defined: the *Young's modulus* is the ratio of tensile stress to tensile strain, when the object deforms along the same axis of applied forces; the *shear modulus* is the ratio of shear stress to shear strain, when the object shears and deforms at constant volume; the *bulk modulus* is the ratio of volumetric stress to volumetric strain, when the object deforms in all directions when uniformly loaded in all directions. SI unit: Pa.

Viscosity
Response of a material to force by deforming without limit at a rate which is proportional to the stress. A liquid increases its deformation in proportion to the duration of the applied stress, and does not recover its original size/shape once the stress is removed. SI unit: Pa s.

Viscoelasticity
Most soft materials have both elastic and viscous responses, making them viscoelastic. When subjected to a stress, they deform at a rate which is not simply linearly proportional to the stress and partially recover their shape once the stress is removed. Cellular viscoelastic behavior is often phenomenologically described in terms of a network of elastic springs and viscous dashpots connected either in series or in parallel, depending on the model. The creep and stress relaxation of single cells in reality often displays a power law behavior indicating a continuous distribution of timescales [102, 161, 162]. Yet for tissue-level mechanics, the debate on whether power laws describe their viscoelastic response accurately enough is ongoing. As an example, power laws are insufficient to describe the viscoelastic behavior of muscle tissue as it demonstrates a broad distribution of timescales around a characteristic time constant determined by acto-myosin activity [163]. Nevertheless, spring-dashpot models with characteristic timescales remain useful in soft tissue mechanics to extract viscoelastic parameters [47].

Tissue fluidity
Cell motility corresponding to a fluidization of the tissue on the bulk level. When cells readily rearrange and are migratory, the tissue is considered to be fluidlike or unjammed. Here, cells often migrate in multicellular packs and swirls reminiscent of fluid flow. In contrast, when cells are locked in their positions and often have compact shapes, the tissue is called solidlike or jammed [149, 150, 156].

Tissue surface tension
An analogy is made between tissues and liquids, where liquids have a surface tension which equals the free-energy change when the liquid surface is increased by a unit area. Tissues also have an apparent surface tension, which arises from the adhesive interactions between cells and their cortical tensions. SI unit: N/m.

2.3.2. SPHEROID MECHANICS AND CELL MIGRATION

The architecture of heterogeneous spheroids not only defines their surface tension but also critically influences the detachment of cells from the spheroid and cell invasion into the surrounding extracellular matrix. For example, the sorting of heterogeneous spheroids (1:1 ratio metastatic MDA-MB-231 and non-tumorigenic MCF-10A cells) embedded in a collagen matrix modulated the speed, persistence and mean squared displacement of the MDA-MB-231 malignant breast tumour cells (Fig. 2.7(a)) [164]. At approximately 4 days of growth, MCF-10A cells enclosed the MDA-MB-231 cells in the core of the spheroid due to their higher proliferation rate, pointing out how proliferation plays an additional role in cell sorting. The confinement prevented the malignant MDA-MB-231 cells from invading outwards, demonstrating the potential influence of cell sorting on cancer metastasis.

Cells in 3D display multiple modes of migration, among which mesenchymal, amoeboid, lobopodial and collective, depending on the local extracellular microenvironment [167]. They can switch between mesenchymal migration mechanisms depending on lamellipodia, thin membrane protrusions found at the leading edge of migrating cells, and alternative migration mechanisms such as amoeboid migration, characterized by a rounded cell morphology with low adhesive interactions, depending on the degree of confinement they experience [168]. The nucleus serves as an intracellular mechanogauge during these shape deformations [169]. It senses imposed constraints through an increase in nuclear membrane tension, triggering signaling outputs that increase cell migratory capacity through actomyosin contractility, thus linking mechanics to migration [170].

The tumour microenvironment also plays an important role in cell metastasis for spheroid models. [35, 116, 171–173]. For example, interstitial flows can downregulate the cell-cell adhesion molecule E-cadherin on non-tumorigenic cells and promote spheroid invasion [174]. Furthermore, the choice of surrounding ECM type and density in spheroid invasion assays also influences cell mechanics and migration. *In vivo*, interstitial stromal ECM is a heterogeneous fibrillar network of primarily type I collagen [116]. *In vitro*, the incorporation of epithelial cell aggregates in type I collagen induces mesenchymal gene expression and an invasive phenotype. By contrast, epithelial cells incorporated in Matrigel remain non-invasive [166]. In mixtures of collagen and Matrigel, non-tumorigenic MCF-10A breast cancer aggregates become increasingly invasive as the relative collagen content is increased by downregulating their E-cadherin expression while increasing mesenchymal markers like vimentin, fibronectin and Snail (Fig. 2.7(b)). Depending upon cell type and matrix density, cells at the periphery of spheroids embedded in type I collagen switch between distinct modes of invasion in a manner that is reminiscent of a non-equilibrium phase separation [165]. Low collagen densities result in a locally unjammed invasive periphery resembling a fluid-like phase, while high collagen densities ensure non-invasive solid-like behavior (Fig. 2.7(c)). Here, collagen densities define cell volume, shape and motility, making heterogeneities within the spheroid not only regional or subclonal but also mechanical. Within a multicellular tumour spheroid, the core is approximately jammed and solid-like (rounded cell shapes and limited cell motion) while the periphery of the tumour is more fluid-like (elongated cell shapes and larger cell motion) [63, 175]. Han *et al.* used the previously
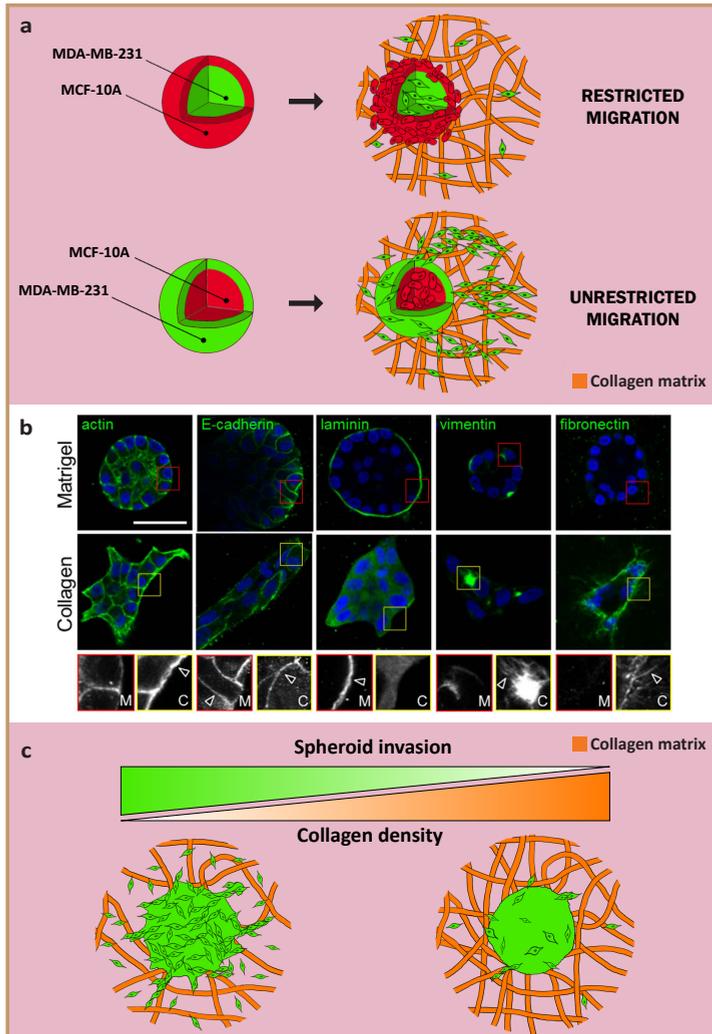
Figure 2.7: Spheroid cell invasion. a) Architecture of heterogeneous spheroids (MDA-MB-231: green and MCF-10A: red) influences cell invasion in collagen matrix. Malignant MDA-MB-231 cells are able to invade collagen when on the outside of the spheroid, but are constricted and (mostly) prevented from migrating when the non-tumorigenic MCF-10A cells enclose the malignant core. Inspired by [164]. b) Spheroid microenvironment is involved in metastatic gene expression. Confocal images of actin, E-cadherin, laminin, vimentin and fibronectin in cell aggregates embedded in gels show an increase in mesenchymal markers and invasion when in collagen compared to Matrigel. Insets and arrows point out changes in Matrigel (red) and collagen (yellow). Scale bar: 50 μm. c) Collagen density influences spheroid invasion and distinct modes of migration. Single-cell migration dominates at low collagen densities (∼ 1 mg/ml), while collective migration orchestrates invasion in higher collagen densities (∼ 4 mg/ml). Inspired by [165]. (b) is reprinted and adapted from [166], licensed under CC BY 4.0.

2

mentioned optical tweezer technique to perform active microrheology on embedded spheroids and demonstrated how the variability in stiffness of different cells within the population increased as the spheroid matured over time. They seeded spheroids in a 3D hydrogel network composed of alginate and Matrigel with a shear modulus of approximately 300 Pa, thus mimicking the mechanical microenvironment of a breast carcinoma *in vivo* [63, 113]. In terms of cell mechanics, cells at the spheroid periphery and invasive branches tended to be softer, larger, longer and more dynamic compared to the cells in the core. Subsequently, they demonstrated how these mechanical changes arise in part from supracellular fluid flow through gap junctions that allow exchange of ions and fluids between cells and amplify cell volume variations in tumours[176]. Blocking these junctions delayed the transition of cells at the periphery into an invasive phenotype. As swelling and softening of peripheral cells are important factors in invasive dynamics, the authors sought to artificially manipulate cell stiffness and volume. Using the chemotherapy medication daunorubicin or overexpression of the actin crosslinking protein α-actinin, the cytoplasmic stiffness of the cells was increased, which diminished invasion of peripheral cells. Invasiveness was quantified as the percentage of spheroids forming invasive branches after 11 days. It will be interesting in the future to explore these effects for different cancer cell types and as a function of ECM composition, in order to better understand the biophysical cues that govern metastasis.

2.4. Conclusion and outlook

Current strategies for the mechanical characterization of 3D multicellular spheroids allow us to understand how mechanical forces regulate tissue formation, cell sorting and cell migration. While several new tools introduced here enable identification of spheroid mechanics both from without and within, a technique that visualizes active mechanosensitive reinforcement of cells and cell-cell contacts is still missing. Furthermore, correlative imaging and multiscale mechanical measurements are needed to deconvolve the contribution of the actomyosin cortex and cell-cell adhesion to overall tissue mechanics. A new noninvasive method to help with this could be CellFIT-3D, a force inference technique that estimates tension maps for 3D cellular systems from image stacks [177]. In addition, artificial intelligence algorithms have been implemented on traction force microscopy to evaluate and predict cellular forces after sufficient training from captured images [178]. This new machine learning-based approach has great potential for being implemented in biophysical tools and invasion assays for more high-throughput and accurate biophysical characterization of spheroids and cell migration. Besides actin and cadherin, the role of other cytoskeletal elements in cell invasion remains largely unexplored. It would be particularly interesting to study the role of intermediate filaments, a family of cytoskeletal filaments that are expressed in a tissue-specific manner. Upon the epithelial-mesenchymal transition, expression of intermediate filaments switches from keratin to vimentin [179]. The mechanical consequences of this switch at the multicellular level are to be identified. Additionally, what physical mechanisms determine whether cells leave individually or as collective strands remains an open question to be further investigated. In summary, identifying the precise relation between spheroid mechanics, cell invasion and involved biological processes will provide new opportunities to understand tissue and cancer biology, and can reveal targets for therapeutic strategies

for cancer treatment.

ACKNOWLEDGEMENTS

2

BIBLIOGRAPHY

1. Boot, R. C., Koenderink, G. H. & Boukany, P. E. Spheroid mechanics and implications for cell invasion. *Advances in Physics: X* **6,** 1978316. https://doi.org/10.1080/23746149.2021.1978316 (2021).

2. Vogel, V. & Sheetz, M. Local force and geometry sensing regulate cell functions. *Nature Reviews Molecular Cell Biology* **7,** 265–275. ISSN: 14710072 (2006).

3. Discher, D. E., Mooney, D. J. & Zandstra, P. W. Growth factors, matrices, and forces combine and control stem cells. *Science* **324,** 1673–1677. ISSN: 00368075 (2009).

4. Van Helvert, S., Storm, C. & Friedl, P. Mechanoreciprocity in cell migration. *Nature Cell Biology* **20,** 8–20. ISSN: 14764679. http://dx.doi.org/10.1038/s41556-017-0012-0 (2018).

5. Bodor, D. L., Pönisch, W., Endres, R. G. & Paluch, E. K. Of Cell Shapes and Motion: The Physical Basis of Animal Cell Migration. *Developmental Cell* **52,** 550–562. ISSN: 18781551 (2020).

6. Wozniak, M. A. & Chen, C. S. Mechanotransduction in development: a growing role for contractility. *Nat Rev Mol Cell Biol* **10,** 34–43 (2009).

7. Tajik, A. *et al.* Transcription upregulation via force-induced direct stretching of chromatin. *Nat Mater* **15,** 1287–1296 (2016).

8. Mammoto, T. & Ingber, D. E. Mechanical control of tissue and organ development. *Development* **137,** 1407–1420 (2010).

9. Brugués, A. *et al.* Forces driving epithelial wound healing. *Nat Phys* **10,** 683–690 (2014).

10. Hahn, C. & Schwartz, M. A. Mechanotransduction in vascular physiology and atherogenesis. *Nature Reviews Molecular Cell Biology* **10,** 53–62. ISSN: 14710072 (2009).

11. Nia, H. T. *et al.* Solid stress and elastic energy as measures of tumour mechanopathology. *Nat Biomed Eng* **1,** 1–25 (2016).

12. Nia, H. T., Munn, L. L. & Jain, R. K. Physical traits of cancer. *Science* **370,** eaaz0868. ISSN: 10959203 (2020).

13. Mierke, C. T. The matrix environmental and cell mechanical properties regulate cell migration and contribute to the invasive phenotype of cancer cells. *Reports on Progress in Physics* **82.** ISSN: 00344885 (2019).

14. Muiznieks, L. D. & Keeley, F. W. Molecular assembly and mechanical properties of the extracellular matrix: A fibrous protein perspective. *Biochimica et Biophysica Acta - Molecular Basis of Disease* **1832,** 866–875. ISSN: 1879260X. http://dx.doi.org/10.1016/j.bbadis.2012.11.022 (2013).

15. Schiele, N. R. *et al.* Actin cytoskeleton contributes to the elastic modulus of embryonic tendon during early development. *Journal of Orthopaedic Research* **33,** 874–881. ISSN: 1554527X (2015).

16. Marturano, J. E., Arena, J. D., Schiller, Z. A., Georgakoudi, I. & Kuo, C. K. Characterization of mechanical and biochemical properties of developing embryonic tendon. *Proceedings of the National Academy of Sciences of the United States of America* **110,** 6370–6375. ISSN: 00278424 (2013).

17. Trepat, X. & Sahai, E. Mesoscale physical principles of collective cell organization. *Nature Physics* **14,** 671–682. ISSN: 17452481. http://dx.doi.org/10.1038/s41567-018-0194-9 (2018).

18. Gonzalez-Rodriguez, D., Guevorkian, K., Douezan, S. & Brochard-Wyart, F. Soft Matter Models of Developing. *Science* **82,** 910–917 (2012).

19. Kim, J., Koo, B. K. & Knoblich, J. A. Human organoids: model systems for human biology and medicine. *Nature Reviews Molecular Cell Biology* **21,** 571–584. ISSN: 14710080. http://dx.doi.org/10.1038/s41580-020-0259-3 (2020).

20. Barone, V. & Heisenberg, C. P. Cell adhesion in embryo morphogenesis. *Current Opinion in Cell Biology* **24,** 148–153. ISSN: 09550674. http://dx.doi.org/10.1016/j.ceb.2011.11.006 (2012).

21. Manning, M. L., Foty, R. A., Steinberg, M. S. & Schoetz, E. M. Coaction of intercellular adhesion and cortical tension specifies tissue surface tension. *Proceedings of the National Academy of Sciences of the United States of America* **107,** 12517–12522. ISSN: 00278424 (2010).

22. Rossi, G., Manfrin, A. & Lutolf, M. P. Progress and potential in organoid research. *Nature Reviews Genetics* **19,** 671–687. ISSN: 14710064. http://dx.doi.org/10.1038/s41576-018-0051-9 (2018).

23. Riccobelli, D. & Bevilacqua, G. Surface tension controls the onset of gyrification in brain organoids. *Journal of the Mechanics and Physics of Solids* **134,** 103745. ISSN: 00225096. https://doi.org/10.1016/j.jmps.2019.103745 (2020).

24. Balbi, V., Destrade, M. & Goriely, A. Mechanics of human brain organoids. *Physical Review E* **101,** 1–8. ISSN: 24700053 (2020).

25. Rozman, J., Krajnc, M. & Ziherl, P. Collective cell mechanics of epithelial shells with organoid-like morphologies. *Nature Communications* **11,** 1–9. ISSN: 20411723 (2020).

26. Jakab, K. *et al.* Relating Cell and Tissue Mechanics : Implications and Applications. *Developmental Dynamics* **237,** 2438–2449 (2008).

27. Sadati, M., Taheri Qazvini, N., Krishnan, R., Park, C. Y. & Fredberg, J. J. Collective migration and cell jamming. *Differentiation* **86,** 121–125. ISSN: 03014681. http://dx.doi.org/10.1016/j.diff.2013.02.005 (2013).

28. Camley, B. A. & Rappel, W.-J. Physical models of collective cell motility: from cell to tissue. *J Phys D Appl Phys* **50,** 113002 (2017).

29. Matoz-Fernandez, D. A., Agoritsas, E., Barrat, J. L., Bertin, E. & Martens, K. Nonlinear Rheology in a Model Biological Tissue. *Physical Review Letters* **118,** 1–5. ISSN: 10797114. arXiv: 1611.05282 (2017).

30. Ranft, J. *et al.* Fluidization of tissues by cell division and apoptosis. *Proceedings of the National Academy of Sciences of the United States of America* **107,** 20863–20868. ISSN: 00278424 (2010).

31. Merkel, M. & Manning, M. L. Using cell deformation and motion to predict forces and collective behavior in morphogenesis. *Seminars in Cell and Developmental Biology* **67,** 161–169. ISSN: 10963634. http://dx.doi.org/10.1016/j.semcdb.2016.07.029 (2017).

32. Oswald, L., Grosser, S., Smith, D. M. & Käs, J. A. Jamming transitions in cancer. *Journal of Physics D: Applied Physics* **50.** ISSN: 13616463 (2017).

33. Mandadapu, K. K., Govindjee, S. & Mofrad, M. R. On the cytoskeleton and soft glassy rheology. *Journal of Biomechanics* **41,** 1467–1478. ISSN: 00219290 (2008).

34. Kollmannsberger, P. & Fabry, B. Linear and nonlinear rheology of living cells. *Annual Review of Materials Research* **41,** 75–97. ISSN: 15317331 (2011).

35. Ilina, O. *et al.* Cell–cell adhesion and 3D matrix confinement determine jamming transitions in breast cancer invasion. *Nature Cell Biology* **22,** 1103–1115. ISSN: 14764679. http://dx.doi.org/10.1038/s41556-020-0552-6 (2020).

36. Angelini, T. E. *et al.* Glass-like dynamics of collective cell migration. *Proceedings of the National Academy of Sciences of the United States of America* **108,** 4714–4719. ISSN: 00278424 (2011).

37. Nath, S. & Devi, G. R. Three-Dimensional Culture Systems in Cancer Research: Focus on Tumor Spheroid Model. *Pharmacology & Therapeutics* **163,** 94–108 (2016).

38. Heisenberg, C. P. & Bellaïche, Y. Forces in tissue morphogenesis and patterning. *Cell* **153,** 948–962. ISSN: 10974172 (2013).

39. Gómez-González, M., Latorre, E., Arroyo, M. & Trepat, X. Measuring mechanical stress in living tissues. *Nature Reviews Physics* **2,** 300–317. ISSN: 2522-5820. https://doi.org/10.1038/s42254-020-0184-6 (2020).

40. Mahaffy, R. E., Park, S., Gerde, E., Käs, J. & Shih, C. K. Quantitative Analysis of the Viscoelastic Properties of Thin Regions of Fibroblasts Using Atomic Force Microscopy. *Biophysical Journal* **86,** 1777–1793. ISSN: 00063495 (2004).

41. Darling, E. M., Zauscher, S. & Guilak, F. Viscoelastic properties of zonal articular chondrocytes measured by atomic force microscopy. *Osteoarthritis and Cartilage* **14,** 571–579. ISSN: 10634584 (2006).

42. Elkin, B. S., Azeloglu, E. U., Costa, K. D. & Morrison, B. Mechanical heterogeneity of the rat hippocampus measured by atomic force microscope indentation. *Journal of Neurotrauma* **24,** 812–822. ISSN: 08977151 (2007).

43. Dolega, M. *et al.* Mechanical behavior of multi-cellular spheroids under osmotic compression. *Journal of the Mechanics and Physics of Solids* **147,** 1–21. ISSN: 00225096. arXiv: 2011.01131 (2021).

44. Vyas, V., Solomon, M., D'Souza, G. G. & Huey, B. D. Nanomechanical Analysis of Extracellular Matrix and Cells in Multicellular Spheroids. *Cellular and Molecular Bioengineering* **12,** 203–214. ISSN: 18655033 (2019).

45. Jaiswal, D. *et al.* Stiffness analysis of 3D spheroids using microtweezers. *PLoS ONE* **12,** 1–21. ISSN: 19326203 (2017).

46. Aoki, T., Ohashi, T., Matsumoto, T. & Sato, M. The Pipette Aspiration Applied to the Local Stiffness Measurement of Soft Tissues. *Annals of Biomedical Engineering* **25,** 581–587 (1997).

47. Guevorkian, K., Colbert, M.-J., Durth, M., Dufour, S. & Brochard-Wyart, F. Aspiration of Biological Viscoelastic Drops. *Physical Review Letters* **104,** 1–4 (2010).

48. Guevorkian, K., Gonzalez-rodriguez, D., Carlier, C., Dufour, S. & Brochard-Wyart, F. Mechanosensitive shivering of model tissues under controlled aspiration. *PNAS* **108,** 13387–13392 (2011).

49. Grosser, S. *et al.* Cell and Nucleus Shape as an Indicator of Tissue Fluidity in Carcinoma. *Physical Review X* **11,** 011033. https://journals.aps.org/prx/abstract/10.1103/PhysRevX.11.011033 (2021).

50. Kosheleva, N. V. *et al.* Cell spheroid fusion: beyond liquid drops model. *Scientific Reports* **10,** 1–15. ISSN: 20452322. https://doi.org/10.1038/s41598-020-69540-8 (2020).

51. Schötz, E. M. *et al.* Quantitative differences in tissue surface tension influence zebrafish germ layer positioning. *HFSP Journal* **2,** 42–56. ISSN: 19552068 (2008).

52. Ayan, B. *et al.* Aspiration-assisted bioprinting for precise positioning of biologics. *Science Advances* **6,** 1–17. ISSN: 23752548 (2020).

53. Mgharbel, A., Delanoë-Ayari, H. & Rieu, J. P. Measuring accurately liquid and tissue surface tension with a compression plate tensiometer. *HFSP Journal* **3,** 213–221. ISSN: 19552068 (2009).

54. Foty, R. A., Pfleger, C. M., Forgacs, G. & Steinberg, M. S. Liquid Properties of Embryonic Tissues: Measurement of Interfacial Tensions. *Physical Review Letters* **72,** 2298–2301 (1994).

55. Foty, R. A., Pfleger, C. M., Forgacs, G. & Steinberg, M. S. Surface tensions of embryonic tissues predict their mutual envelopment behavior. *Development* **122,** 1611–1620. ISSN: 09501991 (1996).

56. Norotte, C., Marga, F., Neagu, A., Kosztin, I. & Forgacs, G. Experimental evaluation of apparent tissue surface tension based on the exact solution of the Laplace equation. *EPL* **81,** 1–6. ISSN: 02955075 (2008).

57. Beatrici, A., Baptista, L. S. & Granjeiro, J. M. Measurement uncertainty evaluation of cellular spheroids surface tension in compressing tests using Young-Laplace equation. *Journal of Physics: Conference Series* **975,** 1–7. ISSN: 17426596 (2018).

58. Zimberlin, J. A., McManus, J. J. & Crosby, A. J. Cavitation rheology of the vitreous: Mechanical properties of biological tissue. *Soft Matter* **6,** 3632–3635. ISSN: 1744683X (2010).

59. Chin, M. S. *et al.* Cavitation rheology as a potential method for in vivo assessment of skin biomechanics. *Plastic and Reconstructive Surgery* **131,** 303e–305e. ISSN: 00321052 (2013).

60. Blumlein, A., Williams, N. & McManus, J. J. The mechanical properties of individual cell spheroids. *Scientific Reports* **7,** 1–10. ISSN: 20452322. http://dx.doi.org/10.1038/s41598-017-07813-5 (2017).

61. Mok, S. *et al.* Mapping cellular-scale internal mechanics in 3D tissues with thermally responsive hydrogel probes. *Nature Communications* **11,** 1–11. ISSN: 20411723. http://dx.doi.org/10.1038/s41467-020-18469-7 (2020).

62. Dolega, M. E. *et al.* Cell-like pressure sensors reveal increase of mechanical stress towards the core of multicellular spheroids under compression. *Nature Communications* **8,** 1–9. ISSN: 20411723 (2017).

63. Han, Y. L. *et al.* Cell swelling, softening and invasion in a three-dimensional breast cancer model. *Nature Physics* **16,** 101–108. ISSN: 17452481 (2020).

64. Baker, B. M. & Chen, C. S. Deconstructing the third dimension-how 3D culture microenvironments alter cellular cues. *Journal of Cell Science* **125,** 3015–3024. ISSN: 00219533 (2012).

65. Duval, K. *et al.* Modeling physiological events in 2D vs. 3D cell culture. *Physiology* **32,** 266–277. ISSN: 15489221 (2017).

66. Jensen, C. & Teng, Y. Is It Time to Start Transitioning From 2D to 3D Cell Culture? *Frontiers in Molecular Biosciences* **7,** 1–15. ISSN: 2296889X (2020).

67. Costa, E. C. *et al.* 3D tumor spheroids: an overview on the tools and techniques used for their analysis. *Biotechnology Advances* **34,** 1427–1441. ISSN: 07349750. http://dx.doi.org/10.1016/j.biotechadv.2016.11.002 (2016).

68. Kelm, J. M., Timmins, N. E., Brown, C. J., Fussenegger, M. & Nielsen, L. K. Method for generation of homogeneous multicellular tumor spheroids applicable to a wide variety of cell types. *Biotechnology and Bioengineering* **83,** 173–180. ISSN: 00063592 (2003).

69. Costa, E. C., Gaspar, V. M., Coutinho, P. & Correia, I. J. Optimization of liquid overlay technique to formulate heterogenic 3D co-cultures models. *Biotechnology and Bioengineering* **111,** 1672–1685. ISSN: 10970290 (2014).

70. Grimes, D. R., Kelly, C., Bloch, K. & Partridge, M. A method for estimating the oxygen consumption rate in multicellular tumour spheroids. *Journal of the Royal Society Interface* **11.** ISSN: 17425662 (2014).

71. Groebe, K. & Mueller-Klieser, W. On the relation between size of necrosis and diameter of tumor spheroids. *International Journal of Radiation Oncology Biology Physics* **34,** 395–401. ISSN: 03603016 (1996).

72. Jamieson, L. E., Harrison, D. J. & Campbell, C. J. Chemical analysis of multicellular tumour spheroids. *Analyst* **140,** 3910–3920. ISSN: 13645528 (2015).

73. Jain, R. K., Au, P., Tam, J., Duda, D. G. & Fukumura, D. Engineering vascularized tissue. *Nature Biotechnology* **23,** 821–823. ISSN: 10870156 (2005).

74. Foty, R. A simple hanging drop cell culture protocol for generation of 3D spheroids. *Journal of Visualized Experiments* **20,** 4–7. ISSN: 1940087X (2011).

75. Shi, W. *et al.* Facile Tumor Spheroids Formation in Large Quantity with Controllable Size and High Uniformity. *Scientific Reports* **8,** 1–9. ISSN: 20452322 (2018).

76. Sabhachandani, P. *et al.* Generation and functional assessment of 3D multicellular spheroids in droplet based microfluidics platform. *Lab on a Chip* **16,** 497–505. ISSN: 14730189 (2016).

77. Lee, S. W. *et al.* In vitro lung cancer multicellular tumor spheroid formation using a microfluidic device. *Biotechnology and Bioengineering* **116,** 3041–3052. ISSN: 10970290 (2019).

78. Yeon, S. E. *et al.* Application of Concave Microwells to Pancreatic Tumor Spheroids Enabling Anticancer Drug Evaluation in a Clinically Relevant Drug Resistance Model. *PLoS ONE* **8,** 1–12. ISSN: 19326203 (2013).

79. Kang, S. M., Kim, D., Lee, J. H., Takayama, S. & Park, J. Y. Engineered Microsystems for Spheroid and Organoid Studies. *Advanced Healthcare Materials* **10,** 1–18. ISSN: 21922659 (2021).

80. Okuyama, H. *et al.* Dynamic change of polarity in primary cultured spheroids of human colorectal adenocarcinoma and its role in metastasis. *American Journal of Pathology* **186,** 899–911. ISSN: 15252191. http://dx.doi.org/10.1016/j.ajpath.2015.12.011 (2016).

81. Weaver, V. M. *et al.* Reversion of the malignant phenotype of human breast cells in three- dimensional culture and in vivo by integrin blocking antibodies. *Journal of Cell Biology* **137,** 231–245. ISSN: 00219525 (1997).

82. Abe-Fukasawa, N., Watanabe, R., Gen, Y., Nishino, T. & Itasaki, N. A liquid culture cancer spheroid model reveals low PI3K/Akt pathway activity and low adhesiveness to the extracellular matrix. *The FEBS Journal,* 1–18 (2021).

83. Dias Gomes, M. & Iden, S. Orchestration of tissue-scale mechanics and fate decisions by polarity signalling. *EMBO Journal,* 1–19 (2021).

84. Riga, A., Castiglioni, V. G. & Boxem, M. New insights into apical-basal polarization in epithelia. *Current Opinion in Cell Biology* **62,** 1–8. ISSN: 18790410. https://doi.org/10.1016/j.ceb.2019.07.017 (2020).

85. Rodriguez-Boulan, E. & Macara, I. G. Organization and execution of the epithelial polarity programme. *Nature Reviews Molecular Cell Biology* **15,** 225–242. ISSN: 14710080 (2014).

86. Zajac, O. *et al.* Tumour spheres with inverted polarity drive the formation of peritoneal metastases in patients with hypermethylated colorectal carcinomas. *Nature Cell Biology* **20,** 296–306. ISSN: 14764679. http://dx.doi.org/10.1038/s41556-017-0027-6 (2018).

87. Steinberg, M. S. On the mechanism of tissue reconstruction by dissociated cells. I. Population kinetics, differential adhesiveness. and the absence of directed migration. *Proceedings of the National Academy of Sciences of the United States of America* **48,** 1577–1582. ISSN: 00278424 (1962).

88. Steinberg, M. S. Mechanism of tissue reconstruction by dissociated cells, II: Time-course of events. *Science* **137,** 762–763. ISSN: 00368075 (1962).

89. Steinberg, M. S. On the Mechanism of Tissue Reconstruction By Dissociated Cells, III. Free Energy Relations and the Reorganization of Fused, Heteronomic Tissue Fragments. *Proceedings of the National Academy of Sciences* **48,** 1769–1776. ISSN: 0027-8424 (1962).

90. Foty, R. A. & Steinberg, M. S. The differential adhesion hypothesis: A direct evaluation. *Developmental Biology* **278,** 255–263. ISSN: 00121606 (2005).

91. Harris, A. K. Is cell sorting caused by differences in the work of intercellular adhesion? A critique of the steinberg hypothesis. *Journal of Theoretical Biology* **61,** 267–285. ISSN: 10958541 (1976).

92. Foty, R. A. & Steinberg, M. S. Cadherin-mediated cell-cell adhesion and tissue segregation in relation to malignancy. *Int. J. Dev. Biol.* **48,** 397–409 (2004).

93. Duguay, D., Foty, R. A. & Steinberg, M. S. Cadherin-mediated cell adhesion and tissue segregation: qualitative and quantitative determinants. *Developmental Biology* **253,** 309–323. ISSN: 00121606 (2003).

94. Kashef, J. & Franz, C. M. Quantitative methods for analyzing cell-cell adhesion in development. *Developmental Biology* **401,** 165–174. ISSN: 1095564X. http://dx.doi.org/10.1016/j.ydbio.2014.11.002 (2015).

95. Dechristé, G., Fehrenbach, J., Griseti, E., Lobjois, V. & Poignard, C. Viscoelastic modeling of the fusion of multicellular tumor spheroids in growth phase. *Journal of Theoretical Biology* **454,** 102–109. ISSN: 10958541 (2018).

96. Guevorkian, K. & Maître, J. L. Micropipette aspiration: A unique tool for exploring cell and tissue mechanics in vivo. *Cell Polarity and Morphogenesis, Methods in Cell Biology* **139,** 187–201. https://doi.org/10.1016/bs.mcb.2016.11.012 (2017).

97. Ingber, D. E. Cellular mechanotransduction: putting all the pieces together again. *The FASEB Journal* **20,** 811–827. ISSN: 0892-6638 (2006).

98. Coughlin, M. F. & Fredberg, J. J. Changes in cytoskeletal dynamics and nonlinear rheology with metastatic ability in cancer cell lines. *Physical Biology* **10.** ISSN: 14783967 (2013).

99. Guck, J. *et al.* Optical deformability as an inherent cell marker for testing malignant transformation and metastatic competence. *Biophysical Journal* **88,** 3689–3698. ISSN: 00063495 (2005).

100. Plodinec, M. *et al.* The nanomechanical signature of breast cancer. *Nature Nanotechnology* **7,** 757–765. ISSN: 17483395 (2012).

101. Fung, Y. C. *Biomechanics: mechanical properties of living tissues* 2nd (Springer-Verlag, New York, 1993).

102. Fabry, B. *et al.* Time scale and other invariants of integrative mechanical behavior in living cells. *Physical Review E - Statistical Physics, Plasmas, Fluids, and Related Interdisciplinary Topics* **68,** 1–18. ISSN: 1063651X (2003).

103. Moeendarbary, E. *et al.* The cytoplasm of living cells behaves as a poroelastic material. *Nature Materials* **12,** 253–261. ISSN: 1476-1122 (2013).

104. Grant, C. A., Twigg, P. C. & Tobin, D. J. Static and dynamic nanomechanical properties of human skin tissue using atomic force microscopy: Effect of scarring in the upper dermis. *Acta Biomaterialia* **8,** 4123–4129. ISSN: 18787568. http://dx.doi.org/10.1016/j.actbio.2012.06.042 (2012).

105. Hochmuth, R. M. Micropipette aspiration of living cells. *Journal of Biomechanics* **33,** 15–22. ISSN: 00219290 (2000).

106. Shojaei-Baghini, E., Zheng, Y. & Sun, Y. Automated micropipette aspiration of single cells. *Annals of Biomedical Engineering* **41,** 1208–1216. ISSN: 00906964 (2013).

107. Schiffhauer, E. S. *et al.* Mechanoaccumulative Elements of the Mammalian Actin Cytoskeleton. *Current Biology* **26,** 1473–1479. file:///C:/Users/Carla%20Carolina/Desktop/Artigos%20para%20acrescentar%20na%20qualifica%7B%5Cc%7Bc%7D%7D%7B%5C~%7Ba%7D%7Do/The%20impact%20of%20birth%20weight%20on%20cardiovascular%20disease%20risk%20in%20the.pdf (2016).

108. Maître, J. L., Niwayama, R., Turlier, H., Nedelec, F. & Hiiragi, T. Pulsatile cell-autonomous contractility drives compaction in the mouse embryo. *Nature Cell Biology* **17,** 849–855. ISSN: 14764679 (2015).

109. Krishnan, R. *et al.* Reinforcement versus fluidization in cytoskeletal mechanoresponsiveness. *PLoS ONE* **4.** ISSN: 19326203 (2009).

110. Wu, Y., Zanotelli, M. R., Zhang, J. & Reinhart-King, C. A. Matrix-driven changes in metabolism support cytoskeletal activity to promote cell migration. *Biophysical Journal* **120,** 1705–1717. ISSN: 15420086. https://doi.org/10.1016/j.bpj.2021.02.044 (2021).

111. Engler, A. J., Sen, S., Sweeney, H. L. & Discher, D. E. Matrix Elasticity Directs Stem Cell Lineage Specification. *Cell* **126,** 677–689. ISSN: 00928674 (2006).

112. Zahn, J. T. *et al.* Age-dependent changes in microscale stiffness and mechanoresponses of cells. *Small* **7,** 1480–1487. ISSN: 16136810 (2011).

113. Acerbi, I. *et al.* Human breast cancer invasion and aggression correlates with ECM stiffening and immune cell infiltration. *Integrative Biology (United Kingdom)* **7,** 1120–1134. ISSN: 17579708 (2015).

114. Najafi, M., Farhood, B. & Mortezaee, K. Extracellular matrix (ECM) stiffness and degradation as cancer drivers. *Journal of Cellular Biochemistry* **120,** 2782–2790. ISSN: 10974644 (2019).

115. Zimberlin, J. A., Sanabria-Delong, N., Tew, G. N. & Crosby, A. J. Cavitation rheology for soft materials. *Soft Matter* **3,** 763–767. ISSN: 1744683X (2007).

116. Chaudhuri, O., Cooper-White, J., Janmey, P. A., Mooney, D. J. & Shenoy, V. B. Effects of extracellular matrix viscoelasticity on cellular behaviour. *Nature* **584,** 535–546. ISSN: 14764687. http://dx.doi.org/10.1038/s41586-020-2612-2 (2020).

117. Mark, C. *et al.* Collective forces of tumor spheroids in three-dimensional biopolymer networks. *eLife* **9,** 1–22. ISSN: 2050084X (2020).

118. Helmlinger, G., Netti, P. A., Lichtenbeld, H. C., Melder, R. J. & Jain, R. K. Solid stress inhibits the growth of multicellular tumor spheroids. *Nature Biotechnology* **15** (1997).

119. Taubenberger, A. V. *et al.* 3D Microenvironment Stiffness Regulates Tumor Spheroid Growth and Mechanics via p21 and ROCK. *Advanced Biosystems* **3,** 1–16. ISSN: 23677478 (2019).

120. Delarue, M. *et al.* Compressive stress inhibits proliferation in tumor spheroids through a volume limitation. *Biophysical Journal* **107,** 1821–1828. ISSN: 15420086 (2014).

121. Tse, J. R. & Engler, A. J. Preparation of hydrogel substrates with tunable mechanical properties. *Current Protocols in Cell Biology* **47,** 10.16.1–10.16.16. ISSN: 19342500 (2010).

122. Dolega, M. E. *et al.* Extra-cellular matrix in multicellular aggregates acts as a pressure sensor controlling cell proliferation and motility. *eLife* **10,** 1–33 (2021).

123. Campàs, O. *et al.* Quantifying cell-generated mechanical forces within living embryonic tissues. *Nature Methods* **11,** 183–189 (2014).

124. Pei, Y. *et al.* The effect of pH on the LCST of poly(N-isopropylacrylamide) and poly(N-isopropylacrylamide-co-acrylic acid). *Journal of Biomaterials Science, Polymer Edition* **15,** 585–594. ISSN: 09205063 (2004).

125. Morais, J. M., Papadimitrakopoulos, F. & Burgess, D. J. Biomaterials/tissue interactions: Possible solutions to overcome foreign body response. *AAPS Journal* **12,** 188–196. ISSN: 15507416 (2010).

126. Sunyer, R., Trepat, X., Fredberg, J. J., Farré, R. & Navajas, D. The temperature dependence of cell mechanics measured by atomic force microscopy. *Physical Biology* **6.** ISSN: 14783975 (2009).

127. Valentine, M. T., Dewalt, L. E. & Ou-Yang, H. D. Forces on a colloidal particle in a polymer solution: A study using optical tweezers. *Journal of Physics Condensed Matter* **8,** 9477–9482. ISSN: 09538984 (1996).

128. Bustamante, C., Bryant, Z. & Smith, S. B. Ten years of tension: single-molecule DNA mechanics. *Nature* **421,** 423–427. ISSN: 00280836 (2003).

129. Ashkin, A. Optical trapping and manipulation of small neutral particles using lasers. *Proceedings of the National Academy of Sciences of the United States of America* **94,** 4853–4860. ISSN: 21622701 (1997).

130. Gutsche, C. *et al.* Micro-rheology on (polymer-grafted) colloids using optical tweezers. *Journal of Physics Condensed Matter* **23.** ISSN: 09538984 (2011).

131. Posy, S., Shapiro, L. & Honig, B. Sequence and structural determinants of strand swapping in cadherin domains: Do all cadherins bind through the same adhesive interface? *J Mol Biol.* **378,** 954–968. ISSN: 15378276. arXiv: NIHMS150003. https://www.ncbi.nlm.nih.gov/pmc/articles/PMC3624763/pdf/nihms412728.pdf (2008).

132. Imamura, Y., Itoh, M., Maeno, Y., Tsukita, S. & Nagafuchi, A. Functional Domains of alpha-Catenin Required for the Strong State of Cadherin-based Cell Adhesion. *Journal of Cell Biology* **144,** 1311–1322 (1999).

133. Chu, Y. S. *et al.* Force measurements in E-cadherin-mediated cell doublets reveal rapid adhesion strengthened by actin cytoskeleton remodeling through Rac and Cdc42. *Journal of Cell Biology* **167,** 1183–1194. ISSN: 00219525 (2004).

134. Yamada, S., Pokutta, S., Drees, F., Weis, W. I. & Nelson, W. J. Deconstructing the Cadherin-Catenin-Actin Complex. *Cell* **123,** 889–901 (2005).

135. Amack, J. D. & Manning, M. L. Knowing the Boundaries : Extending the Differential Adhesion Hypothesis in Embryonic Cell Sorting. *Science* **338,** 212–215 (2012).

136. Lecuit, T. & Lenne, P.-f. Cell surface mechanics and the control of cell shape , tissue patterns and morphogenesis. *Nat Rev Mol Cell Biol* **8,** 633–644 (2007).

137. Krieg, M. *et al.* Tensile forces govern germ-layer organization in zebrafish. *Nature Cell Biology* **10,** 429–436 (2008).

138. Farhadifar, R., Ro, J.-c., Aigouy, B. & Eaton, S. The Influence of Cell Mechanics , Cell-Cell Interactions , and Proliferation on Epithelial Packing. *Current Biology* **17,** 2095–2104 (2007).

139. Brodland, G. W. The Differential Interfacial Tension Hypothesis (DITH): A comprehensive theory for the self-rearrangement of embryonic cells and tissues. *Journal of Biomechanical Engineering* **124,** 188–197. ISSN: 01480731 (2002).

140. Canty, L., Zarour, E., Kashkooli, L., François, P. & Fagotto, F. Sorting at embryonic boundaries requires high heterotypic interfacial tension. *Nature Communications* **8.** ISSN: 20411723. http://dx.doi.org/10.1038/s41467-017-00146-x (2017).

141. Mertz, A. F. *et al.* Scaling of traction forces with the size of cohesive cell colonies. *Physical Review Letters* **108,** 1–5. ISSN: 00319007. arXiv: 1112.5804 (2012).

142. Pawlizak, S. *et al.* Testing the differential adhesion hypothesis across the epithelial-mesenchymal transition. *New Journal of Physics* **17,** 083049. ISSN: 13672630 (2015).

143. Maruthamuthu, V., Sabass, B., Schwarz, U. S. & Gardel, M. L. Cell-ECM traction force modulates endogenous tension at cell-cell contacts. *Proceedings of the National Academy of Sciences of the United States of America* **108,** 4708–4713. ISSN: 00278424 (2011).

144. Monier, B., Pélissier-Monier, A. & Sanson, B. Establishment and maintenance of compartmental boundaries: Role of contractile actomyosin barriers. *Cellular and Molecular Life Sciences* **68,** 1897–1910. ISSN: 1420682X (2011).

145. Laplante, C. & Nilson, L. A. Differential expression of the adhesion molecule Echinoid drives epithelial morphogenesis in Drosophila. *Development* **133,** 3255–3264. ISSN: 09501991 (2006).

146. Ninomiya, H. *et al.* Cadherin-dependent differential cell adhesion in xenopus causes cell sorting in vitro but not in the embryo. *Journal of Cell Science* **125,** 1877–1883. ISSN: 00219533 (2012).

147. Fagotto, F., Winklbauer, R. & Rohani, N. Ephrin-Eph signaling in embryonic tissue separation. *Cell Adhesion and Migration* **8,** 308–326. ISSN: 19336926 (2014).

148. Bi, D., Lopez, J. H., Schwarz, J. M. & Manning, M. L. A density-independent rigidity transition in biological tissues. *Nature Physics* **11,** 1074–1079. ISSN: 17452481. arXiv: 1409.0593 (2015).

149. Atia, L. *et al.* Geometric constraints during epithelial jamming. *Nature Physics* **14,** 613–620. ISSN: 17452481. arXiv: 1705.04660. http://dx.doi.org/10.1038/s41567-018-0089-9 (2018).

150. Park, J. A. *et al.* Unjamming and cell shape in the asthmatic airway epithelium. *Nature Materials* **14,** 1040–1048. ISSN: 14764660 (2015).

151. Bi, D., Yang, X., Marchetti, M. C. & Manning, M. L. Motility-driven glass and jamming transitions in biological tissues. *Physical Review X* **6,** 1–13. ISSN: 21603308. arXiv: 1509.06578 (2016).

152. Hanahan, D. & Weinberg, R. A. Hallmarks of cancer: The next generation. *Cell* **144,** 646–674. ISSN: 00928674. http://dx.doi.org/10.1016/j.cell.2011.02.013 (2011).

153. Thiery, J. P., Acloque, H., Huang, R. Y. & Nieto, M. A. Epithelial-Mesenchymal Transitions in Development and Disease. *Cell* **139,** 871–890. ISSN: 00928674 (2009).

154. Chao, Y. L., Shepard, C. R. & Wells, A. Breast carcinoma cells re-express E-cadherin during mesenchymal to epithelial reverting transition. *Molecular Cancer* **9,** 1–18. ISSN: 14764598 (2010).

155. Mitchel, J. A. *et al.* In primary airway epithelial cells, the unjamming transition is distinct from the epithelial-to-mesenchymal transition. *Nature Communications* **11,** 1–14. ISSN: 20411723. http://dx.doi.org/10.1038/s41467-020-18841-7 (2020).

156. Kim, J. H. *et al.* Unjamming and collective migration in MCF10A breast cancer cell lines. *Biochemical and Biophysical Research Communications* **521,** 706–715. ISSN: 10902104. https://doi.org/10.1016/j.bbrc.2019.10.188 (2020).

157. Friedl, P., Locker, J., Sahai, E. & Segall, J. E. Classifying collective cancer cell invasion. *Nature Cell Biology* **14,** 777–783. ISSN: 14657392 (2012).

158. Christiansen, J. J. & Rajasekaran, A. K. Reassessing epithelial to mesenchymal transition as a prerequisite for carcinoma invasion and metastasis. *Cancer Research* **66,** 8319–8326. ISSN: 00085472 (2006).

159. Padmanaban, V. *et al.* E-cadherin is required for metastasis in multiple models of breast cancer. *Nature* **573,** 439–444. ISSN: 14764687. http://dx.doi.org/10.1038/s41586-019-1526-3 (2019).

160. Fischer, K. R. *et al.* Epithelial-to-mesenchymal transition is not required for lung metastasis but contributes to chemoresistance. *Nature* **527,** 472–476. ISSN: 14764687. http://dx.doi.org/10.1038/nature15748 (2015).

161. Hoffman, B. D., Massiera, G., Van Citters, K. M. & Crocker, J. C. The consensus mechanics of cultured mammalian cells. *Proceedings of the National Academy of Sciences of the United States of America* **103,** 10259–10264. ISSN: 00278424 (2006).

162. Desprat, N., Guiroy, A. & Asnacios, A. Microplates-based rheometer for a single living cell. *Review of Scientific Instruments* **77.** ISSN: 00346748 (2006).

163. Kawai, M. & Brandt, P. W. Sinusoidal analysis: a high resolution method for correlating biochemical reactions with physiological processes in activated skeletal muscles of rabbit, frog and crayfish. *Journal of Muscle Research and Cell Motility* **1,** 279–303. ISSN: 01424319 (1980).

164. Huang, Y. L., Shiau, C., Wu, C., Segall, J. E. & Wu, M. The Architecture of Co-Culture Spheroids Regulates Tumor Invasion within a 3D Extracellular Matrix. *Biophysical Reviews and Letters* **15,** 131–141. ISSN: 1793-0480 (2020).

165. Kang, W. *et al.* Tumor invasion as non-equilibrium phase separation. *bioRxiv,* 1–31 (2020).

166. Carey, S. P., Martin, K. E. & Reinhart-King, C. A. Three-dimensional collagen matrix induces a mechanosensitive invasive epithelial phenotype. *Scientific Reports* **7,** 1–14. ISSN: 20452322 (2017).

167. Yamada, K. M. & Sixt, M. Mechanisms of 3D cell migration. *Nature Reviews Molecular Cell Biology* **20,** 738–752. ISSN: 14710080. http://dx.doi.org/10.1038/s41580-019-0172-9 (2019).

168. Doolin, M. T., Moriarty, R. A. & Stroka, K. M. Mechanosensing of Mechanical Confinement by Mesenchymal-Like Cells. *Frontiers in Physiology* **11,** 1–19. ISSN: 1664042X (2020).

169. Venturini, V. *et al.* The nucleus measures shape changes for cellular proprioception to control dynamic cell behavior. *Science* **370.** ISSN: 10959203 (2020).

170. Lomakin, A. J. *et al.* The nucleus acts as a ruler tailoring cell responses to spatial constraints. *Science* **370.** ISSN: 10959203 (2020).

171. Goncalves, I. G. & Aznar, J. M. G. Extracellular matrix density regulates the formation of tumour spheroids through cell migration. *PLoS Computational Biology* **17,** 1–22. ISSN: 15537358 (2021).

172. Follain, G. *et al.* Fluids and their mechanics in tumour transit: shaping metastasis. *Nature Reviews Cancer* **20,** 107–124. ISSN: 14741768 (2020).

173. Levental, K. R. *et al.* Matrix Crosslinking Forces Tumor Progression by Enhancing Integrin Signaling. *Cell* **139,** 891–906. ISSN: 00928674. http://dx.doi.org/10.1016/j.cell.2009.10.027 (2009).

174. Huang, Y. L. *et al.* Tumor spheroids under perfusion within a 3D microfluidic platform reveal critical roles of cell-cell adhesion in tumor invasion. *Scientific reports* **10,** 9648. ISSN: 20452322 (2020).

175. Valencia, A. M. *et al.* Collective cancer cell invasion induced by coordinated contractile stresses. *Oncotarget* **6,** 43438–43451. ISSN: 19492553 (2015).

176. Mcevoy, E., Han, Y., Guo, M. & Shenoy, V. B. Gap Junctions Amplify Spatial Variations in Cell Volume in Proliferating Solid Tumors. *Nature Communications* **11,** 1–11 (2020).

177. Xu, M., Wu, Y., Shroff, H., Wu, M. & Mani, M. A scheme for 3-dimensional morpho-
     logical reconstruction and force inference in the early C. Elegans embryo. *PLoS
     ONE* **13,** 1–20. ISSN: 19326203 (2018).

178. Li, H. *et al.* Wrinkle force microscopy: a new machine learning based approach
     to predict cell mechanics from images. *arXiv:2102.12069.* arXiv: `arXiv : 2102 .
     12069v1` (2021).

179. Kidd, M. E., Shumaker, D. K. & Ridge, K. M. The role of Vimentin intermediate
     filaments in the progression of lung cancer. *American Journal of Respiratory Cell
     and Molecular Biology* **50,** 1–6. ISSN: 10441549 (2014).

2

<div style="text-align: right; font-size: 2em;">**3**</div>

MECHANOPHENOTYPING OF SPHEROIDS USING A MICROFLUIDIC MICROPIPETTE ASPIRATION CHIP

To understand a phenomenon, scientists must first describe it; to describe it objectively, they must first measure it.

Siddhartha Mukherjee, in *The Emperor of All Maladies*

The mechanical characterization of cell spheroids provides valuable insights in how single-cell mechanics and cell-cell interactions control tissue mechanics and self-organization. However, most measurement techniques are limited to probing one spheroid at a time, require specialized equipment and are difficult to handle. We therefore developed a microfluidic chip that follows the concept of glass capillary micropipette aspiration in order to quantify the viscoelastic behavior of spheroids in an easy-to-handle, more high-throughput manner. Spheroids are loaded in parallel pockets via a gentle flow, after which spheroid tongues are aspirated into adjacent aspiration channels using hydrostatic pressure. After each experiment, the spheroids are easily removed from the chip by reversing the pressure and new spheroids can be injected. The presence of multiple pockets with a uniform aspiration pressure, combined with the ease to conduct successive experiments, allows for a high throughput of tens of spheroids per day. We demonstrate that the chip provides accurate deformation data when working at different aspiration pressures. Lastly, we measure the viscoelastic properties of spheroids made of different cell lines and show how these are consistent with previous studies using established experimental techniques.

3.1. INTRODUCTION

Physical properties like cellular mechanics are of undeniable importance in physiological processes such as morphogenesis [2], tissue remodeling [3], wound-healing [4] and cancer growth [5, 6]. During these events, cells are collectively confined,
squeezed, pushed or pulled upon, affecting their self-organization in time and space. The overall mechanical response to these forces, termed tissue mechanics, will shape the resulting tissue morphology. This response depends on the properties of the single cells alongside the interplay between cells across multiple length scales [7, 8]. While the mechanical deformation of single cells mostly depends on their cytoskeleton, plasma membrane and nuclear stiffness, tissue mechanics are defined through the linkage between cell adhesion molecules, the cytoskeleton and the extracellular environment [9, 10].

Cell spheroids have become a popular *in vitro* model to study tissue mechanics, as they replicate both the multicellular nature and three-dimensional (3D) micro-environment of *in vivo* tissues [11]. These spherical aggregates are made from immortalized cell lines or primary cells that adhere to each other and collectively round up. The resulting spheroid morphology and internal cell arrangement is defined by the interplay between cell-cell adhesion and cortical tension [8, 12, 13]. Probing spheroids with relevant physical forces therefore increases insight in how tissue composition and resulting mechanics relate to tissue sorting, cellular mechanosensing and cell invasion [7, 14, 15].

Spheroid mechanics have been quantified using various techniques, probing either from within or from outside [16]. For example, hydrogel mechanosensors give information on the spatial distribution of mechanical stress within spheroids [17, 18]. Cavitation rheology probes the internal elasticity and tissue interfacial tension by inducing a spherical cavity in the spheroid with a needle [19]. From outside, the elastic modulus has been quantified by squeezing the spheroid between two "chopsticks" termed microtweezers [20]. Atomic force microscopy (AFM) determines the viscoelastic response of a spheroid by indenting the surface with a nano-probe [21, 22], while tissue surface tensiometry (TST) squeezes the spheroid between two plates [8, 12, 23–25] and micropipette aspiration (MPA) aspirates a spheroid tongue in a glass capillary to look at the viscoelastic creep response [14, 26–28]. Additionally, TST and MPA quantify a tissue surface tension, for which the analogy is made between round spheroids and liquid droplets [12, 14, 29]. This surface tension is directly related to tissue sorting, tissue spreading and energetic constraints on the size of spheroids [8, 27, 30].

However, available techniques to quantify spheroid mechanical parameters such as the elastic modulus E, viscosity η and surface tension γ have a limited throughput. First, techniques such as AFM, microtweezers, TST or MPA only probe one spheroid at a time. Second, the handling of nano-cantilevers, small tweezers or glass microcapillaries is a delicate, difficult and time-consuming task. The resulting low throughput is found in the previously mentioned studies probing spheroid mechanics, as these usually report a data set that ranges between a total number of ~5 to 30 probed spheroids. As the technical challenges form a bottleneck on the size of data sets, it is difficult to quantify differences between various spheroid models using present techniques. Given the fact that biological variability tends to be rather large, mechanical phenotyping, for instance to compare different cancer types, or in-depth studies of the role of cytoskeletal compo-

nents or specific (cancer) biomarkers in overall tissue behavior require an assay with higher throughput than what is currently available.

Microfluidic devices are widely used to measure the mechanical properties of single cells at high throughput [31–41]. Here, cell deformability is examined by letting large numbers of cells flow or migrate through narrow channels or micro-pillars. The chip's defined geometries are easily replicated into new chips, making this a highly reproducible set-up. Besides overall cell deformability, these devices are able to quantify more specific mechanical parameters such as both the cell's and nuclear elastic modulus and viscosity. For example, the design of a microfluidic array where single cells land in individual pockets and are aspirated via a pressure gradient enables high-throughput micropipette aspiration [35, 36]. However, applying the same principles to study viscoelastic mechanics of spheroids or tissues, which requires microfluidic chips with larger channel dimensions, has remained unaddressed. While microfluidic devices exist that examine spheroid growth, functionally assess drugs or perform high-throughput compression of *Drosophila* embryos [42–44], a high-throughput microfluidic chip to study spheroid viscoelastic mechanics in parallel and with high reproducibility does not exist to date.

Inspired by the microfluidic micropipette array for single cells [35, 36], we have designed a microfluidic device to perform MPA on multiple spheroids in parallel, thereby drastically increasing the throughput. After each measurement, spheroids can be easily removed from the device by reversing the flow and aspirating them at the inlet, allowing for multiple experiments per chip. As the device is made from a mold, each chip has the exact same dimensions for the micropipette channels, which is much harder to obtain when pulling glass micropipettes for traditional MPA. The aspiration pressure is precise and easily controlled for each measurement by using hydrostatic pressure. With a custom-made Python script for automated image analysis, the creep length of aspirated spheroid tongues can be analyzed to derive the viscoelastic response of the spheroids. Our device can aspirate 8 spheroids in parallel per measurement for multiple runs per day, allowing for much larger data sets while providing the same information as traditional glass micropipette aspiration. Additionally, we show that our microfluidic device is sensitive enough to pick up mechanical differences between different spheroid models, making it a suitable device to mechanically phenotype different cellular systems.

3.2. MATERIALS AND METHODS

3.2.1. CELL CULTURE

Human embryonic kidney 293 (HEK293T) cells were generously provided by the group of Dimphna Meijer (Department of Bionanoscience, Delft University of Technology). They were kept in Dulbecco's Modified Eagle Medium High Glucose (DMEM, Sigma) containing 4.5 g/L glucose, L-glutamine but without sodium pyruvate, and supplemented with 10% Fetal Bovine Serum (FBS, Sigma) and 1% Antibiotic-Antimycotic solution (Gibco).

NIH3T3 embryonic mouse fibroblasts (ATCC CRL-1658) were kept in Dulbecco's Modified Eagle Medium High Glucose (DMEM, Sigma) containing 4.5 g/L glucose, L-glutamine but without sodium pyruvate, and supplemented with 10% Newborn Calf Serum (NCS, Sigma) and 1% Antibiotic-Antimycotic solution (Gibco).

Human mammary MCF10A cells (ATCC CRL-10317) were cultured in DMEM/F12 1:1

medium (Gibco) supplemented with 5% horse serum (Gibco), 0.5 µg/mL hydrocortisone (Sigma), 20 ng/mL human epidermal growth factor (hEGF) (Peprotech), 100 ng/mL cholera toxin (Sigma), 10 µg/mL insulin (Human Recombinant Zinc, Gibco) and 1% Penicillin-Streptomycin 100x solution (VWR Life Science).

All cells were incubated at 37 °C with 5% CO_2 and subcultured at least twice a week.

3.2.2. Spheroid fabrication

Spheroids were generated using a custom-designed microfabricated microwell array platform (which is available at: https://github.com/RubenBoot/ HighThroughput_Spheroid_MPA /blob/main/SpheroidMicrowellArray.dwg), inspired by work from Minglin Ma's lab [45]. Following their protocol, two microwell array platforms were created using standard soft lithography at the Kavli Nanolab Delft to allow for the creation of spheroids with different diameters. Using SU-8 2150 photoresist (Kayaku Advanced Materials) and a µMLA laserwriter (Heidelberg Instruments), the master wafers were designed to have an array of circular microposts. The first wafer had posts with a diameter of 200 µm and height of 220±20 µm, while the second wafer had posts with a diameter of 280 µm and a height of 300±30 µm. The master wafers were coated with trichloro(1H,1H,2H,2H-perfluorooctyl)silane (Sigma-Aldrich) to allow for easy demolding. Microwell arrays were molded from the wafers using polydimethylsiloxane (PDMS) (Sylgard 184, Dow Corning) and curing agent at a mixing ratio of 10:1 (w/w). The arrays were placed in a 12-well cell culture plate (Thermo Fisher Scientific) using rubber glue (Reprorubber), and then sterilized by thoroughly washing with ethanol and leaving under UV light overnight.

Before seeding cells, the arrays were coated with 1% (w/v) Pluronic® F127 (Sigma-Aldrich) solution to prevent cell adhesion to the PDMS. The pluronic solution was removed from the well after 45 minutes of incubating. A cell suspension with a concentration of ±1 x 10^6 cells in matching cell media, obtained through trypsinization, was deposited in the well with the coated array in order to form spheroids. It is important to note that the resulting spheroid dimensions not only depend on the chosen cell concentration but also on the duration of culture, cell adhesion and the cell type-specific proliferation rate. After deposition, cells divide over the microwells and settle at the bottom due to gravity, where they aggregate into spheroids overnight (see Appendix Fig. 3.6). The spheroids were cultured in the wells for either 2 or 3 days before aspiration experiments, changing the media every day. On the day of the experiment, spheroids were gently washed out of the microwells using the same media and brought into suspension.

3.2.3. Design and fabrication of the microfluidic chip

The master wafer was created using standard soft lithography at the Kavli Nanolab Delft. The design is available at https://github.com/RubenBoot/ HighThroughput_Spheroid_MPA. The multi-layer design contains features with different heights, so had to be created in two separate photolithography steps using a µMLA laserwriter (Heidelberg Instruments). The final chip was designed as a combination of two slabs of PDMS, one slab with the aspiration channels 50 µm in height plus the top half of the aspiration pockets ±150 µm in height (see Fig. 3.1A, PDMS slab 1), and the other slab containing the bottom half of the aspiration pockets (PDMS slab 2). The molds
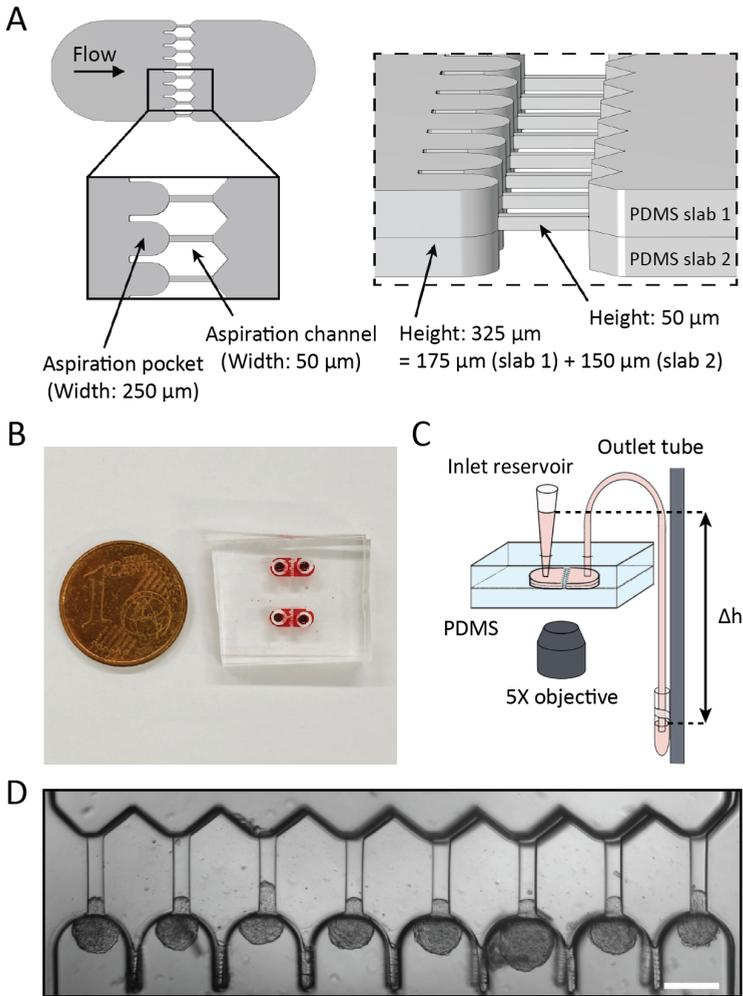
Figure 3.1: Overview of the microfluidic chip. (A) 3D schematic showing (left) the top view of the design and a close-up on the pockets and aspiration channels, and (right) a tilted side view showing the heights of the two separate PDMS slabs and the resulting height when bonded together. (B) Photograph of two actual devices, filled with red dye for visualization and a EU 1 cent coin for scale. (C) Schematic of the experimental set-up. Spheroids enter the PDMS chip at the inlet reservoir, which is a pipette cone, after which they are aspirated with hydrostatic pressure by changing the height Δh of the outlet vial that is mounted to a vertical rod. Note that the drawing is not to scale: in reality, the vertical rod was placed next to the microscope, requiring a 60 cm outlet tube to bridge the distance between the chip and the outlet vial. The experiment was captured with an inverted microscope using a 5x objective. (D) Brightfield top view image of the aspiration pockets loaded with HEK293T cell spheroids aspirated at 700 Pa, scale bar 200 μm.

for both these slabs were fabricated together on one silicon wafer. To obtain this, the first step of the design was created by spinning SU-8 3050 to an average thickness of 50 μm. For this, the SU-8 was first spun at 500 rpm for 10 seconds with an acceleration of 100

rpm/second and then at 3000 rpm for 30 seconds with an acceleration of 300 rpm/second. Then, the SU-8 was soft baked at 95 °C for 15 minutes, after which the laserwriter wrote the first layer. The wafer was post baked at 65 °C for 1 minute, then at 95 °C for 5 minutes and developed in SU-8 developer. The second layer was created with SU-8 2050 and spun to an average thickness of 150 µm. It was first spun at 500 rpm for 10 seconds with an acceleration of 100 rpm/second, after which it was spun at 1200 rpm for 30 seconds at an acceleration of 300 rpm/second. It is important to note that the thickness was not equal over the whole wafer, as the resist covered both the first half of the design (consisting of the micropipette channel and part of the aspiration pocket) and the empty place where the second half of the aspiration pockets will be written. Therefore, one half of the aspiration pockets (see Fig. 3.1A, PDMS slab 2) resulted in a thickness of 150±2 µm, while the other half containing half of the pocket plus the aspiration channel (PDMS slab 1) had a different thickness of 175±25 µm. After spinning, the wafer was soft baked at 65 °C for 5 minutes and then at 95 °C for 30 minutes. The laserwriter wrote the second part of the design, after which the wafer was post baked at 65 °C for 5 minutes, at 95 °C for 12 minutes and then developed. The master wafer was coated with trichloro(1H,1H,2H,2H-perfluorooctyl)silane to allow for easy demolding. PDMS chips were created using Sylgard 184 at a curing agent ratio of 10:1. Individual chips were cut and holes were punched in only one slab of the design for the later introduction of tubing. Both halves of the design were plasma cleaned (Harrick Plasma) for two and a half minutes at 30 W to facilitate bonding, after which one half was slightly wetted with a droplet of distilled water to allow for better alignment. The two halves were put together and aligned using the alignment arrows at the border of the design and an optical microscope (ZEISS Primovert) to check the alignment (see Appendix Fig. 3.7). Finally, the chip was kept in the oven at 65 °C to bond overnight. The bonding overnight usually resulted in a slight misalignment between both halves of the device, potentially due to shrinking of the PDMS [46]. Across the chips used in this study (n = 14), an average misalignment of 16 ± 1 µm (in the range of 10-22 µm) between the side walls of the pockets, and an average misalignment of 12 ± 1 µm (in the range of 5-21 µm) between the front of the pocket and the aspiration channel was measured from brightfield images using ImageJ. We tested by computer simulations that this slight misalignment did not affect our results (see Results and Discussion section). After fabrication, chips could be stored indefinitely and used on the desired day for the experiment.

3.2.4. DATA ACQUISITION

Before each experiment, the chip was filled with 1% Pluronic® F127 (Sigma) solution and left at room temperature to prevent cell adhesion to the PDMS walls. After 45 minutes, the pluronic solution was flushed from the chip using the culture media that matched the cell line used in the experiment. For this, vials with cell-free culture media were connected to the inlet and outlet of the microfluidic chip with PTFE 008T16-030-200 tubing (Diba Industries, inner diameter 0.3 mm, outer diameter 1.6 mm) and a pressure was applied to the media using an MFCS-EZ pressure controller (Fluigent). Once all the pluronic solution, PDMS debris particles and possible air bubbles were flushed out, the tube connected to the inlet was gently unplugged from the chip and a loading reservoir, being a shortened 1 ml pipette tip cut with a scalpel, was plugged into the in-

let. Then, the vial connected to the outlet was disconnected from the pressure controller and mounted to a vertical translation stage (Thorlabs, VAP10) with a ruler on the side such that the pressure in terms of cmH_2O could be read off, to be able to exert a precise hydrostatic aspiration pressure when lowering the stage with the vial compared to the height of the reservoir. Slightly lowering the stage induced a minor flow in the chip towards the aspiration pockets, after which 20 µl of spheroid suspension was pipetted into the reservoir. Spheroids were guided by the flow and entered the aspiration pockets, after which the outlet tube was brought back to the height where no flow is present. For loading, the inlet hole needed to be punched close enough to the aspiration pockets. Otherwise, the volume of space in the loading bay of the chip would be too large and could not induce a high enough flow velocity to sweep the spheroids into the pockets. Spheroids then sedimented to the bottom instead and remained immobile. Once ready to perform the experiment, the vial was manually lowered to the chosen aspiration pressure (in this chapter 500, 700 and 1500 Pa, depending on the studied cell line), thereby inducing spheroid tongue aspiration. The inlet reservoir volume remained constant during the duration of the experiment, confirming that there was no leakage at the corners of the squared aspiration channels and spheroids fully blocked the channels. Whenever a spheroid did not fully block the channel, a clear flow was visible in the aspiration channel and the rare experiments where this occurred were not used for analysis.

Brightfield images of spheroid tongues entering the aspiration channels were captured on an inverted fluorescence microscope (Zeiss Axio-Observer) every 5 seconds for a total of 5 minutes using a 5x/NA 0.16 air objective and ORCA Flash 4.0 V2 (Hamamatsu) digital camera with a resolution of 2048x2048 px^2. We ensured that the full aspiration curve of the tongue was captured by starting the image acquisition before lowering the outlet tube (Movie S1†, to be found online with publication). At the end of the experiment, spheroids were pushed out of the pockets and flown back towards the inlet by raising the outlet vial above the reservoir. There, they were removed from the chip by pipetting them up through the reservoir. This way, new spheroids could be inserted and a new measurement started with the same chip. All experiments were conducted at 37 °C and 5% CO_2 using a stage top incubator (ibidi). Chips were used for 4-5 successive experiments on average, and were always discarded after the final experiment of the day.

3.2.5. COMSOL SIMULATIONS ON PRESSURE DISTRIBUTION IN THE CHIP

The design of the device contains 8 parallel pockets, and thus pressure will redistribute once spheroids start clogging the flow in pockets. To examine the influence of this effect, the pressure distribution was computationally modeled in the 3D design of the device using the finite elements modeling software COMSOL Multiphysics 5.6. Considering the fluid flow to be laminar and following the Navier-Stokes equation [47], the pressure distribution was modeled for two different cases: (1) all pockets are open, or (2) all pockets are clogged, except for one where fluid still flows through the aspiration channel.

The Hagen-Poiseuille equation tells us that the pressure drop over a tubular channel with laminar flow scales with the length of the channel and the inverse of the channel radius to the fourth power [48]. As the design of our device has much larger dimensions than typical microfluidic chips, the cross-sectional area of the tubing connected to the chip now has the same order of magnitude as the cross-sectional area of the de-

3

vice. Therefore, the hydrodynamic resistance across the tubing is considerable and non-negligible as long as a flow is present in the device. It is therefore important to realize that the device is only able to accurately perform spheroid aspiration at a single defined step pressure once *all* pockets are filled with a spheroid, thus blocking the flow.

To examine what pressure spheroids experience in pockets when not all are filled yet, case (1) and (2) were modeled for the design of the device including a 60 cm long rectangular channel with a 300x300 μm cross section that mimics the outlet tube and corresponding pressure drop. The same average length of tubing was used during our experiments. Boundary conditions of 700 Pa at the left edge of the inlet region and 0 Pa at the end of the simulated outlet tube were installed, similar to lowering the outlet tube with 7 cmH$_2$O. These simulations generated the pressure distribution and corresponding fluid flow profile in the device.

3.2.6. High-throughput analysis of spheroid tongue aspiration
The creep length of the spheroid tongues into the aspiration channels over time was extracted from the experimental images using Fiji (https://imagej.net/software/fiji/) and a custom-written Python script (which is available at:
https://github.com/RubenBoot/HighThroughput_Spheroid_MPA /blob/main/
SpheroidAspiration_AnalysisScript.py). First, the brightfield aspiration time-lapse images were rotated to make the aspiration channels vertically oriented (with the tongue creeping upward over time), and then cropped using ZEN software (Zeiss). The cropped region captured the whole aspirated spheroid tongue and aligned the beginning of the channels with the bottom of the cropped images. The cropped time-lapse was saved as a JPEG stack, and converted to binary images using a threshold in Fiji (see bottom two frames in Fig. 3.2A). The threshold value was chosen manually to obtain a clear contrast between the aspirated protrusion edge and the surrounding empty channel. This binary stack was then imported in the Python script. Using the Fiji interface, the x-coordinates of pixels along the horizontal line were manually inserted in the Python script to indicate where the middle of all 8 aspiration channels was located. The script was set up to find the edge of the aspiration protrusion by checking the binary value of every pixel on the vertical line along these coordinates (from top to bottom) and recording the y-coordinate corresponding to the protrusion edge. This analyses was repeated for all images in the stack, returning the set of y-coordinates for all 8 channels and for each time step. Y-coordinates (pixels) were converted into creep lengths (μm) by subtracting the y-coordinate (which is the distance from the top of the image to the protrusion edge) from the total height of the image and multiplying this result with the pixel distance. In some experiments, cells at the protrusion edge of the spheroid tongue were loosely attached and would break off during aspiration, thus altering the protrusion edge structure. Spheroids where this occurred were excluded from analysis, alongside the ones that did not remain round nor retained a constant volume before and during aspiration. All results were collected in a Microsoft Excel file alongside the time step per image.

3.2.7. Statistical analysis
Statistical analysis was performed using Python and Microsoft Excel. Student t-tests were executed using the TTEST function in Excel and p values below 0.05 were consid-
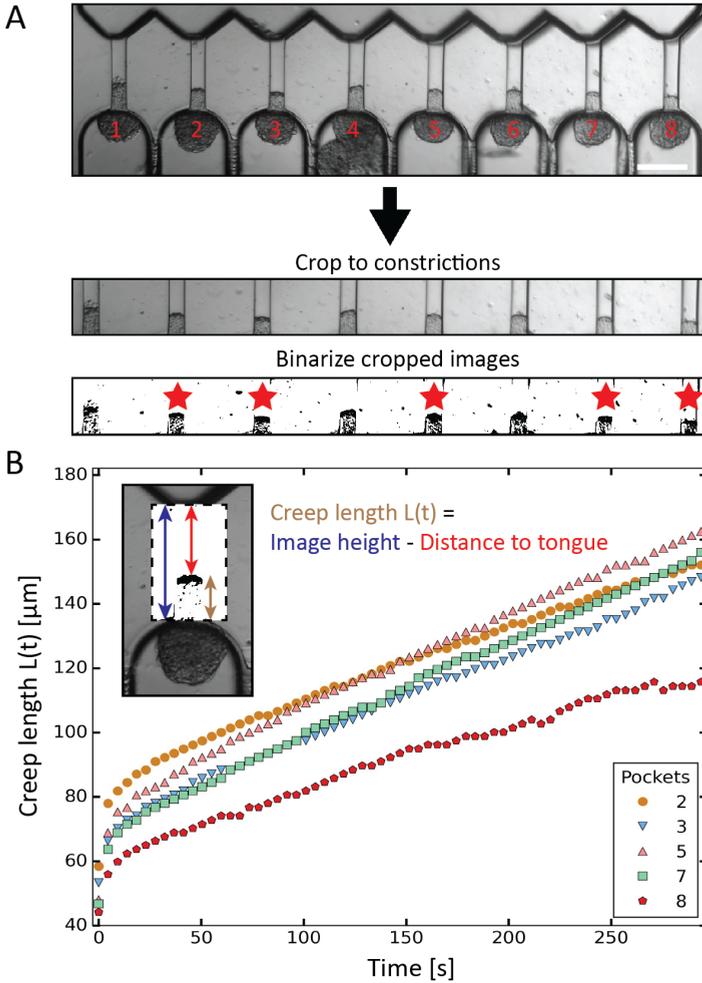
Figure 3.2: Automated data analysis using a custom-written Python script. (A) Preparation workflow before running the script. First, the 8 pocket-time series (scale bar 200 μm) is cropped to the constrictions with spheroid tongues, where the bottom of the cropped images is aligned with the precise start of the aspiration channels. Next, the cropped time series is converted to binary images by setting a threshold using ImageJ. Tongues are analyzed if they have a thresholded edge that does not change structure over time (due to cells breaking off) and belong to spheroids that remain round and retain a constant volume before and during aspiration, here indicated by a red star. (B) Plot of the creep length of the 5 HEK293T cell spheroids (indicated by the red stars in (A), with corresponding pocket numbers) as a function of time, aspirated at 700 Pa. The inset shows how the tongue length is calculated by subtracting the distance from the top of the cropped image to the protrusion edge from the total image height.

ered to be significant. Python was used to do standard error propagation calculations on the fitting parameters to obtain error values. The average human error in reading off the aspiration pressure when manually lowering the outlet vial is defined by the thickness of the lines on the ruler indicating the distances, which is 0.2 cmH_2O (~ 20 Pa), and the

error in dimensions of the aspiration channel is around 5 μm (measured with a Dektak stylus profiler). The error bars in the figures display the standard error of the mean unless indicated otherwise, and are always based on at least two independent experiments with separately prepared chips.

3.3. RESULTS AND DISCUSSION

3.3.1. HIGH-THROUGHPUT DATA EXTRACTION

In order to measure mechanics of cell spheroids in a high-throughput manner, we designed a microfluidic device to parallelize micropipette aspiration. The design consists of 8 parallel aspiration pockets that are 250 μm wide and 325±27 μm tall, in order to be able to contain a single spheroid with a maximum diameter of 250 μm. Each pocket connects to an aspiration channel that is 50 μm wide and 50±2.5 μm tall, chosen to be similar in size to pipette diameters used in previous glass micropipette spheroid aspiration studies (Fig. 3.1A-B) [14, 27]. We decided to implement 8 pockets as it was the maximum number of pockets that fit in the field of view of the 5x microscope objective. To mimic traditional micropipette aspiration as accurately as possible, the multilayer wafer mold was designed to create symmetric aspiration pockets with aspiration channels positioned at the *centerline* of the pockets. This way, spheroids were raised from the device bottom during aspiration (similar to the single cell aspiration device created by Lee *et al.* [36]). Two PDMS halves from the device mold, one side with half the pocket and the other with the other half of the pocket plus the aspiration channel, were aligned under a microscope using alignment arrows incorporated in the design (see Appendix Fig. 3.7) and bonded in the oven overnight.

The chip was flushed with media before starting an experiment. Then, a small volume of spheroid suspension (~ 20 μL) was added to the inlet reservoir. The spheroids were moved into the pockets through the flow induced by lowering a media reservoir connected to the outlet and mounted to a vertical rod, thereby exerting a precise hydrostatic pressure gradient that varied between 500 and 1500 Pa in our experiments, depending on the studied cell type (Fig. 3.1C). Once a spheroid arrived in the pocket, it blocked the flow through the aspiration channel, thus preventing other spheroids from entering the same pocket. Induced pressure gradients, by lowering the outlet media reservoir, were at first kept low enough (below ~200 Pa) to ensure that spheroids did not deform in the aspiration channels yet. Only when all pockets were loaded with spheroids was the outlet reservoir lowered to a level that induced the chosen step pressure for aspiration. Spheroid tongues started creeping in the aspiration channels as they were subjected to the pressure difference between the atmospheric pressure at the inlet reservoir and the hydrostatic pressure exerted by the outlet media tube (Fig. 3.1D). In this way, spheroids experienced the aspiration force in a similar manner as for traditional micropipette aspiration, where spheroids are kept at atmospheric pressure and aspirated by applying an underpressure in a glass capillary.

We developed a custom-made Python script to analyze the spheroid tongue deformations in an efficient and fast manner. Before running the script, brightfield timelapse image series were rotated, cropped and changed into binary images to focus on the creeping protrusions in the channels (Fig. 3.2A). To determine the creep length $L(t)$,

the script derived the distance from the top of the binarized image to the protrusion edge, and subtracted this value from the total image height. The Python script thus extracted the creep lengths for the 8 aspiration channels and each step in time (Fig. 3.2B). We excluded spheroids that were not round before- or did not remain constant in volume during aspiration.

3.3.2. PRESSURE DISTRIBUTION IN THE CHIP

In contrast to microfluidic single cell aspiration chips, where channels have smaller dimensions than the used tubing [35, 36], the required cross-section for channels to flow undeformed spheroids in is as large as the tubing (with a diameter of 300 μm). Therefore, the pressure drop over the tubing is non-negligible in comparison to the pressure drop across the chip. This is a considerable problem, as slight changes in the length of the tubing may cause significant changes in the experienced pressure drop in the microfluidic device. To avoid these pressure drop effects, we designed the device in such a way that the entire flow is stopped once all pockets are filled with spheroids and the pressure gradient is fully defined by the hydrostatic pressure. However, spheroids that are loaded into the device and swept along by the induced flow will reach the aspiration pockets one at a time. Therefore, pressures will redistribute in the device for each spheroid that clogs an aspiration pocket and stops the flow through the adjacent aspiration channel. This might cause a problem, as the spheroids that already arrived in the pockets may experience an aspiration pressure that increases over time when additional pockets fill up with spheroids. Instead, all spheroids should experience a single step pressure to allow correct data analysis. To examine the effect of pressure redistribution, we performed 3D COMSOL simulations for two different cases: (1) all pockets are open, and (2) all pockets are clogged by spheroids except for one. A 60 cm long rectangular channel with a 300x300 μm cross section was incorporated into the 3D design to mimic the outlet tube, as it induces a considerable pressure drop, and a pressure gradient of 700 Pa was simulated across this total geometry. The model showed how the pressure gradient over the aspiration channel increases from ~50 Pa when all pockets are open to ~300 Pa when all but one are clogged (Fig. 3.3A). It is important to note that these values are dependent on the chosen boundary conditions, and in this context simply serve to estimate the extent of this effect. Additionally, we ran an identical simulation as case (2), only now both halves of the design were slightly misaligned by 20 μm in both alignment directions, to test whether the variations between devices had any influence on the pressure drop across the aspiration channels (see Appendix Fig. 3.8). We found that the pressure changed by only a few pascal, demonstrating that the effect of slight misalignment on the aspiration pressure is negligible.

We concluded from these simulations that it is important to ensure that spheroids arrive at the pockets at approximately the same moment in time. Otherwise, spheroids might experience a pressure that starts aspiration when *almost* all pockets are clogged but jumps once the final pocket clogs. In experiments, we discovered that spheroids all start aspirating at the same time as long as we punch the inlet hole close to the pockets and add sufficient spheroids to the inlet reservoir (Fig. 3.3B). To circumvent the effect of pressure redistribution, spheroids were gently flown towards the pockets by inducing a minor pressure gradient (~150 Pa) and were halted before the pockets by bringing the
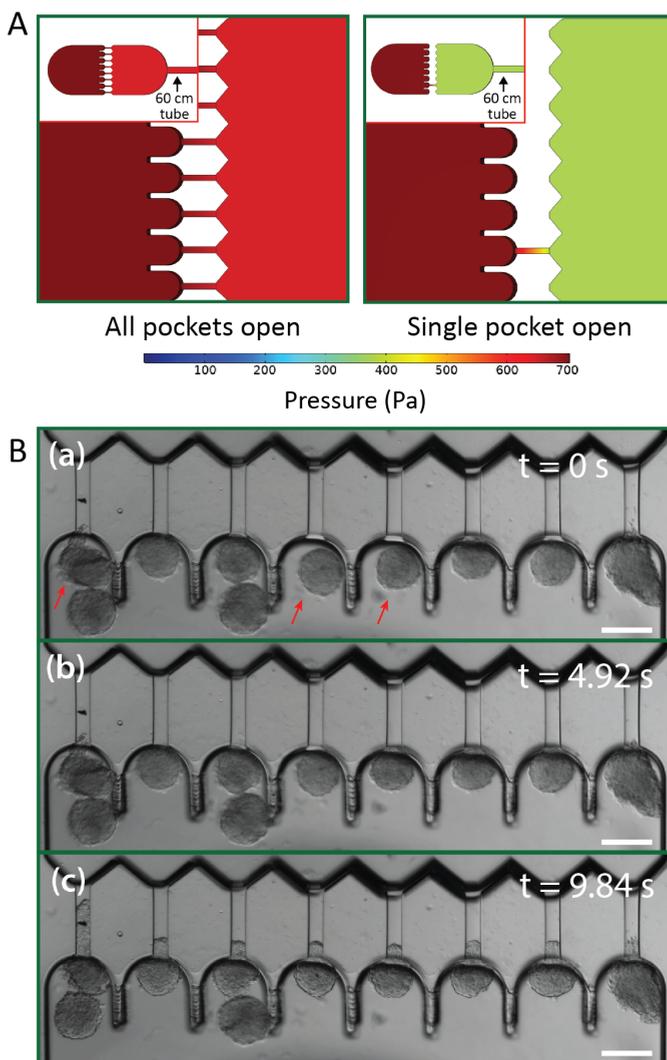
Figure 3.3: Pressure distribution across aspiration pockets. (A) A 3D numerical simulation of the pressure distribution assuming the device is connected to a 60 cm long straight rectangular channel mimicking the outlet tube. A pressure gradient of 700 Pa is simulated for two different configurations: all pockets are open (left), and all pockets but one are clogged by spheroids (right). (B) Brightfield images from an HEK cell spheroid aspiration experiment, demonstrating how simultaneous aspiration starts as soon as all channels are clogged. At first (a), no pressure gradient is present yet and three pockets remain open, indicated by red arrows. Five seconds later (b), a pressure gradient of 500 Pa has been induced and spheroids flow into the pockets but do not clog everything yet. After five more seconds (c), all spheroids have clogged the pockets, thereby blocking further flow and ramping up the pressure to 500 Pa. Spheroids now experience the full induced hydrostatic pressure gradient as evident from the tongues all creeping simultaneously into the aspiration channels. Scale bar 200 μm.

height of the outlet vial back to the starting point with no flow. Then, the final pressure gradient was induced by lowering the outlet vial again, and all spheroids that were floating near the pockets experienced the flow and filled up the remaining unclogged pockets at the same time. This ramped up the pressure, and the spheroids experienced the full pressure gradient, thus starting the measurement at the same time for all pockets.

3.3.3. VALIDATION OF SENSITIVITY AND REPRODUCIBILITY WHEN WORK-ING AT DIFFERENT ASPIRATION PRESSURES

To confirm the sensitivity and reproducibility of our device, we measured the deformability of HEK293T spheroids at two slightly different aspiration pressures of 500 and 700 Pa. The obtained creep data alongside visual confirmation showed that the aspirated spheroids displayed an initial elastic deformation followed by a viscous response (Fig. 3.4A). The tissue relaxation time τ demarcates these two regimes and is given by $\tau = \eta/E$, with η being the viscosity and E the elastic modulus of the spheroid. We fitted this viscoelastic response to different spring-and-dashpot models and compared their coefficient of determination (see Appendix Fig. 3.9). The modified Maxwell model, previously used in studies on spheroid micropipette aspiration [14, 26, 27], proved to fit the data significantly better than other more simple models (see Appendix Table 3.2) and was therefore used to determine the mechanical parameters of our spheroid aspiration measurements. The model consists of four elements (shown in the inset of Fig. 3.4A): a dashpot ξ_t in series with a modified Kelvin-Voigt element, which consists of a spring k_1 in parallel with a dashpot ξ_c and spring k_2 in series. The creep length $L(t)$ in the context of this model is given by:

$$L(t) = \frac{f}{k_1}(1 - \frac{k_2}{k_1 + k_2} e^{\frac{-t}{\tau_c}}) + \frac{f}{\xi_t} t \qquad (3.1)$$

where f is the aspiration force, k_1 is the spring constant for the elasticity of the spheroid, k_2 relates to the initial increase in $L(t)$, ξ_t represents the viscous dissipation of the flowing tongue and τ_c is the rising time of the elastic deformation δ. Here, $\tau_c = \frac{\xi_c(k_1+k_2)}{k_1 k_2}$ with ξ_c being a friction coefficient related to the rising time. Hence, the modified Maxwell model has four fitting parameters: $\delta = f/k_1$, $\dot{L}_\infty = f/\xi_t$ (being the flow velocity at long timescales), $\beta = k_2/(k_1 + k_2)$ and τ_c.

As shown in Fig. 3.4B, the creep length $L(t)$ of the spheroid tongue was smaller for measurements at 500 Pa in comparison to 700 Pa, demonstrating the sensitivity of our device. However, creep length can only be compared for a precise point in time. To quantify differences between the entire measurements, we compared the average elastic deformation δ by fitting Eq. (3.1) to the creep data. The average deformation δ was significantly smaller for measurements performed at 500 Pa ($\delta = 70 \pm 2$ µm) in comparison to 700 Pa ($\delta = 90 \pm 4$ µm), as one would expect when exerting a smaller force (Fig. 3.4C). This demonstrates how the device is sensitive enough to work at small differences in pressure and create reproducible deformations in agreement with theoretical expectations.
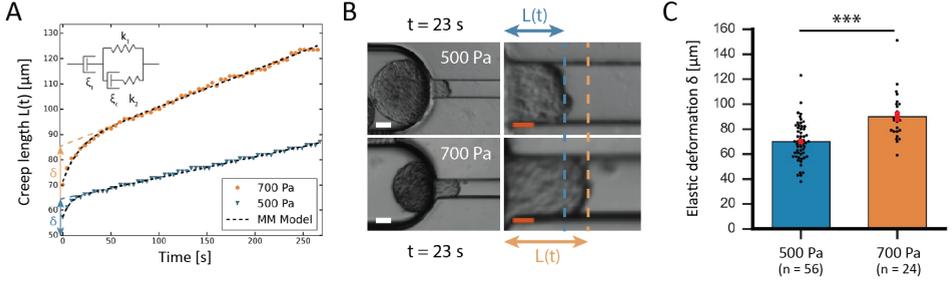
Figure 3.4: Validation of sensitivity of the device to determine spheroid mechanical properties. (A) Comparison plot of the creep length versus time for one HEK cell spheroid aspirated at 700 Pa (orange) and another at 500 Pa (blue). The creep curves are fitted with the modified Maxwell model (black dashed lines), which is explained in the inset. The fast elastic deformation δ equals the intercept of the linear viscous flow with the y-axis, and is shown to be larger when aspirating spheroids at larger pressures. (B) Brightfield images of two separate aspiration experiments for HEK cell spheroids, showing the creep length *L(t)* after 23 s of aspiration at 500 Pa (top) or 700 Pa (bottom), with snapshots focusing on the aspiration pocket (left, scale bar 50 μm) and zoomed in on the aspiration channel (right, scale bar 20 μm). (C) Histograms comparing the average elastic deformation δ for HEK cell spheroids aspirated at different pressures (500 Pa and 700 Pa). ***, p < 0.001 with n = 56 and 24 for 500 Pa and 700 Pa respectively. Error bars are SEM.

3.3.4. MEASUREMENTS ON SPHEROIDS WITH KNOWN MECHANICAL PROPERTIES

To demonstrate the high-throughput mechanical phenotyping capabilities of our device, we measured the mechanical properties of three different cell spheroid models that have been probed in previous studies [49]. In addition to our measurements performed with HEK293T cell spheroids, we studied two stiffer spheroid models made of either NIH3T3 fibroblasts or MCF10A cells. While the HEK293T cell spheroids were probed at 500 and 700 Pa, the two stiffer spheroid models were aspirated at a higher pressure of 1500 Pa as lower pressures would induce a slower deformation and require a longer time scale to analyze the full viscoelastic response (Fig. 3.5A).

In traditional micropipette aspiration, the aspiration force f of the pipette when considering spheroid volume conservation is given by:

$$f = \pi R_p^2 \Delta P, \tag{3.2}$$

where R_p is the radius of the pipette and ΔP the applied underpressure in the pipette [50]. Previous studies on micropipette aspiration of spheroids have pointed out that the actual pressure exerted on the spheroid equals the applied underpressure ΔP minus a critical pressure ΔP_c at which aspiration of the spheroid occurs. When aspirating at a pressure lower than ΔP_c, the spheroid will not deform due to its inherent tissue surface tension γ [14, 27].

To calculate this critical pressure, separate measurements of the retraction of the spheroid tongues are required when the pressure is brought back to zero (see Appendix). In contrast with traditional glass micropipette aspiration, where spheroids remain stuck in the pipette and the tongue slowly retracts, on our device spheroid tongues retracted so fast (displaying a mainly elastic response) that it was impossible to measure a viscoelastic retraction curve when the pressure was brought back to zero (see Movie S2†,

A

@ 1500 Pa, t = 23 s
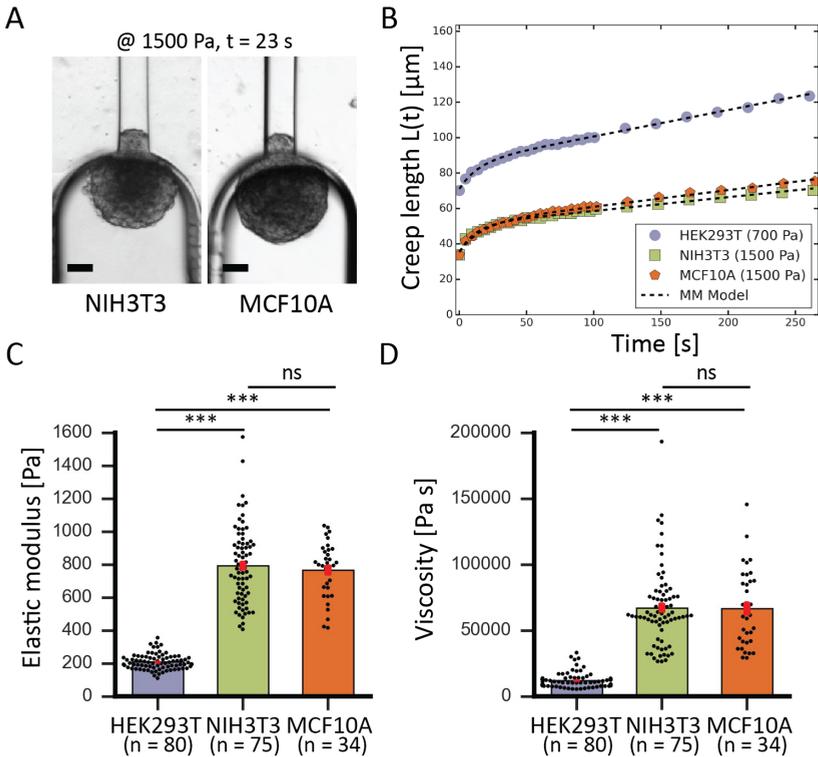
NIH3T3   MCF10A

B

C

D

Figure 3.5: High-throughput comparison of spheroid mechanics for different cell lines. (A) Brightfield snapshots after 23 s of aspiration at 1500 Pa of a NIH3T3 (left) and MCF10A (right) spheroid, scale bars 50 µm. (B) Comparison plot of creep length versus time for a HEK293T spheroid (purple) aspirated at 700 Pa, and a NIH3T3 (green) and MCF10A (orange) spheroid aspirated at 1500 Pa. The creep curves are fitted with the modified Maxwell model (black dashed lines). (C) Average elastic moduli and (D) average viscosity measured for the three different cell lines. ***, $p < 0.001$ and ns is nonsignificant with n = 80, 75 and 34 for HEK293T, NIH3T3 and MCF10A respectively. Error bars are SEM.

to be found online with publication). This effect was consistent for all three cell lines, even when a small aspiration pressure of 100 Pa was kept during retraction to make certain that this fast retraction was not caused by backflow in the chip (see Movie S3†, to be found online with publication). The effect was also not governed by the surface treatment of the aspiration channels, as experiments performed on a chip that was not coated with pluronic F-127 still resulted in an elastic fast retraction that took tens of seconds (see Movie S4†, to be found online with publication). We therefore investigated the effect of accounting for ΔP_c through traditional micropipette measurements on HEK293T spheroids (measuring both aspiration and retraction, see Appendix). We found that ΔP_c ranged between 50 and 150 Pa (when aspirating at 500 Pa), which changes parameter values obtained by fitting aspiration curves by maximally 10-30 % (see Appendix Fig. 3.10 and Table 3.3). Additionally, we saw that the spheroids deformed differently in the glass micropipettes in comparison to our device, displaying a lower elastic deformation

δ and flow velocity $\dot{L}_\infty$. One possible explanation for the discrepancy between our device and traditional MPA is that the chip has square aspiration channels instead of round capillaries, potentially influencing the creep of the tongue due to the different geometry or due to wall friction (PDMS instead of glass). Moreover, the pockets on our chip have rounded walls which the spheroids potentially push back on during relaxation, making them move slightly backwards in the pocket during retraction. We conclude that creep curves obtained with our microfluidic device slightly deviate from glass micropipette aspiration measurements. However, our device has the unique benefit of providing measurements at high throughput, thus allowing systematic comparisons between different cell types. The creep curves obtained with our microfluidic device showed that the two stiffer spheroid models made of NIH3T3 or MCF10A cells had a lower initial elastic deformation δ and slower viscous flow $\dot{L}_\infty$ than the more deformable HEK293T spheroids (Fig. 3.5B). The observed linear viscous response, where creep length does not reach a plateau after the elastic elongation but keeps increasing over time, has also been observed in previous aspiration studies on spheroids that used traditional glass micropipettes [14, 27]. Where in a liquid, viscosity arises from friction between the molecules, for these spheroids the differences in viscous response potentially arise from differences in cell adhesion and cortical strength between the three cell types [12]. All curves were fitted with the modified Maxwell model to extract the relevant mechanical parameters. The first term in Eq. (3.1) characterizes the elastic regime, with $k_1 = \pi R_p E$, while the second term represents the flow at constant velocity $\dot{L}_\infty$ for longer timescales, with $\xi_t = 3\pi^2 \eta R_p$ [14, 51]. As our microfluidic device, unlike traditional glass micropipettes, does not present cylindrical constrictions, a correction for rectangular constrictions needs to be implemented in regards to R_p, as previously done by Davidson *et al* [35, 52]. The effective channel radius R_{eff} is now given by:

$$R_{eff}^4 = \frac{2}{3\pi} \frac{W \times H^3}{(1 + \frac{H}{W})^2 \times f^*},$$ (3.3)

with W and H being the width and height of the rectangular constriction and f^* being a function of the aspect ratio (H/W), given by Son [52]. For W and H values of 50 µm, this results in a corrected channel radius $R_{eff} = 27$ µm.

When fitting obtained creep data with Eq. (3.1), extracting fitting parameters δ and $\dot{L}_\infty$ and plugging in Eq. (3.2), the elastic modulus E is derived as:

$$E = \frac{R_{eff}\Delta P}{\delta},$$ (3.4)

and the viscosity η as:

$$\eta = \frac{1}{3\pi \dot{L}_\infty} R_{eff}\Delta P,$$ (3.5)

where we thus chose not to include ΔP_c as our chip is not able to capture retraction measurements.

The measured average elastic modulus and viscosity of the HEK293T cell spheroids were the same for different applied pressures of 500 and 700 Pa (see Appendix Fig. 3.11).

Cell line	E (Pa)	η (kPa s)	n
HEK293T	210 (±5)	12 (±1)	80
NIH3T3	780 (±30)	67 (±3)	75
MCF10A	770 (±30)	67 (±5)	34

Table 3.1: Spheroid mechanical parameters for different cell lines, derived using the modified Maxwell model and performing a least squares regression of the experimental creep curves

The two data sets were not statistically significant from each other, allowing us to consider them as one population when comparing them with the other two spheroid models. For both NIH3T3 and MCF10A cell spheroids, the average elastic moduli were almost four times as large in comparison to the softer HEK293T cell spheroids, but were not significantly different from each other (Fig. 3.5C). Similarly, both models had a viscosity almost six times larger than for HEK293T spheroids but again were not significantly different from each other (Fig. 3.5D). Additionally, as all spheroids varied in size, we investigated a possible relationship between spheroid size and their mechanical parameters. However, the derived elastic moduli and viscosities proved to be independent of spheroid radius R_0 (in the range of 60-125 µm) for all three spheroid models (see Appendix Fig. 3.12).

The obtained values are consistent with values measured in previous studies (Table 3.1). For HEK293T cell spheroids, we measured an average elastic modulus of ~210 Pa which agrees with parallel-plate compression on HEK293 cell spheroids measuring a range of 200-400 Pa [53]. Our NIH3T3 spheroids had an average modulus of ~780 Pa, which falls within the range of 500-3500 Pa measured with colloidal probe AFM [54]. However, the MCF10A spheroids displayed an average modulus of ~770 Pa which is just below the range of 1250±320 Pa measured by squeezing MCF10A spheroids with microtweezers [20]. This discrepancy could be explained by the fact that this range was determined for only 6 spheroids in the microtweezer study, or potentially squeezing might induce different deformation behavior compared to aspiration. Additionally, the values obtained with our device for HEK293T cell spheroids at 500 Pa differed from the values obtained with traditional glass micropipette aspiration (see Appendix Table 3.3). Aspiration with glass cylinder pipettes (at room temperature) resulted in an elastic modulus E that was approximately two-thirds larger and a viscosity η that was three times as large in comparison to the values measured with our microfluidic device (at 37 °C). Aside from the possible influence of temperature, this distinction is due to differences in dissipation and the rate of rearrangement of cells at the entry of the squared as opposed to cylindrical aspiration channels. Furthermore, we had to omit the critical pressure ΔP_c from our derivations, affecting the absolute values of E and η with an estimated 10-30% based on our traditional MPA measurements on HEK293T cell spheroids. Nevertheless, our results together with previous studies show that relative differences in the mechanical properties of different cell types are much larger than the discrepancies that arise between microfluidic and glass MPA or between different measuring techniques when determining absolute values. Altogether, these results demonstrate that our device is well capable to measure the viscoelastic behavior of multicellular spheroids and determine their mechanical properties in agreement with other experimental techniques.

3

3.4. Conclusion and outlook

We have developed a microfluidic chip that follows the principles of traditional micropipette aspiration to quantify the viscoelastic response of cell spheroids in an efficient manner, making it possible to make statistically meaningful comparisons between different experimental conditions. The chip performs viscoelastic creep measurements as soon as spheroids fill up the 8 parallel aspiration pockets and block further fluid flow. The design of the chip can in principle be adapted to obtain smaller or larger aspiration channels, but this will influence the overall volumetric flow rate through the chip and thus the ease of loading spheroids. Similarly, the number of pockets could be increased, though this would make it more difficult to load them. With the current geometry, our chip is able to obtain reproducible and accurate results and to detect differences upon small changes in pressure. Our results are in agreement with values from previous studies and demonstrate the high-throughput aspect of the chip in context of the much lower output traditional glass micropipette aspiration: the chip is efficient and easy to use in contrast to the cumbersome re-use of glass pipettes, and provides large amounts of data in a smaller amount of time. Therefore, the microfluidic device presented here is a suitable technique to investigate the mechanics of a wide range of tissues, from embryonic to tumor, to provide mechanistic insights in important physiological processes such as tissue remodeling and cancer metastasis.

APPENDIX
3.A. SUPPLEMENTARY INFORMATION

FITTING VISCOELASTIC RESPONSE TO DIFFERENT SPRING-AND-DASHPOT MODELS

We fitted four different spring-and-dashpot models to the viscoelastic response of spheroids aspirated on our microfluidic chip, and compared them by their coefficient of determination (R^2). We tested the Kelvin-Voigt model (K-V, spring and dashpot in parallel), y = A x (1 - exp(B x t)), the Standard Linear Solid model (SLS, a spring followed by a spring and dashpot in parallel), y = A - B x (1 - exp(C x t)), the Standard Linear Liquid model (SLL, a dashpot followed by a spring and dashpot in parallel), y = A x (1 - exp(B x t)) + C x t, and the modified Maxwell model (MM, a dashpot in series with a Kelvin-Voigt element, consisting out of a spring in parallel with a spring and dashpot in series), y = A x (1 - B x exp(C x t)) + D x t. We calculated the coefficient of determination (R^2) value for each model and spheroid type using Python (see Table 3.2).

GLASS CAPILLARY MICROPIPETTE ASPIRATION

HEK293T spheroids were aspirated using pipettes with a diameter of 65±5 μm, fabricated by pulling borosilicate glass pipettes (Harvard Apparatus, 1 mm OD, 0.5 mm ID) with a laser-based puller (Sutter Instruments Co Mode P-2000) and cutting them with a quartz tile. Cell adhesion to the pipette walls was prevented by incubating the pipettes in 2 mg/mL PolyEthyleneGlycol-PolyLysine (PLL(20)-g[3.5]-PEG(2)/PEG(3.4)-Biotin(20%), SuSos AG, Dubendorf, Switzerland) in MRB80 solution (80 mM piperazine-N,N'-bis(2-ethanesulfonic acid) (Pipes), pH 6.8, 4 mM MgCl2, 1 mM EGTA [Sigma]) for 30 minutes. Spheroids were suspended in a CO_2-equilibrated medium and kept in a custom-made sample chamber. The chamber was constructed by adhering two microscope slides to a custom-made aluminum spacer of 3 mm thickness using vacuum grease (Beckman Coulter). The pipette was introduced into the chamber, aligned with a spheroid and an aspiration pressure was attained by vertically displacing a water reservoir connected to the pipette using a vertical translational stage (LTS300, Thorlabs). Spheroids were aspirated using a pressure ΔP = 5 cmH_2O and visualized on an inverted microscope (Nikon Eclipse TI) with a 10x air objective. After aspiration, the pressure gradient was removed and the retraction of the tongue was recorded. The creep advancement of the tongue was recorded with an ORCA Flash 4.0 digital camera using a 1 s interval for a total of 10 minutes, of which 5 minutes corresponded to aspiration and the next 5 minutes to retraction. Data was obtained for two independent experiments, which were performed at room temperature. As the experimental set-up did not include a heating stage to keep the experimental chambers at the physiological temperature of 37 °C, aspiration of spheroids was only performed in the first hour after they came out of the incubator.

The critical pressure ΔP_c to aspirate the spheroids was derived from

$$\Delta P_c = \Delta P \frac{\dot{L^r_\infty}}{\dot{L^a_\infty} + \dot{L^r_\infty}},$$ (3.6)

where $\dot{L^a_\infty}$ and $\dot{L^r_\infty}$ are the aspiration and retraction flow rates respectively [14, 27].
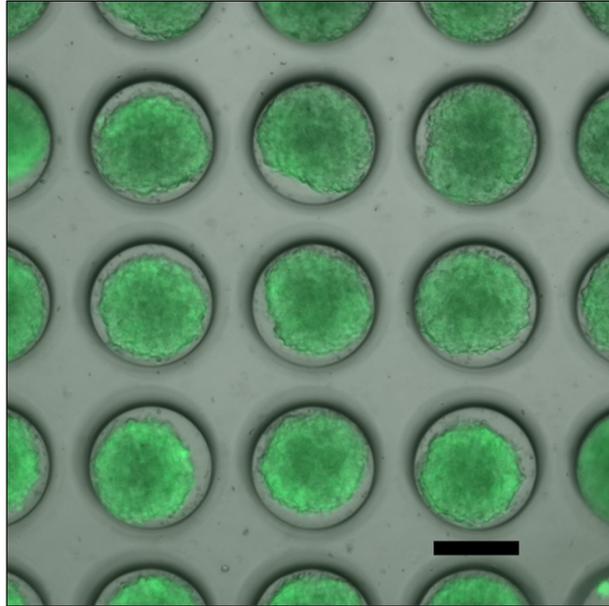
3.B. SUPPLEMENTARY FIGURES

Figure 3.6: Close-up of the microwell array with HEK293T cell spheroids after 3 days of culture. After depositing the cell suspension in the microwell array, cells divide over the wells and aggregate into spheroids to reach a final size that depends on the culturing time, original cell number, and cell type. Here, cells are stained with Calcein AM (AAT Bioquest) for visualization and confirmation of cell viability. The image is an overlay of a brightfield image and a fluorescence image, cropped from an original image taken with an inverted fluorescence microscope (Zeiss Axio-Observer) using a 5x/NA 0.16 air objective. Scale bar 200 μm.
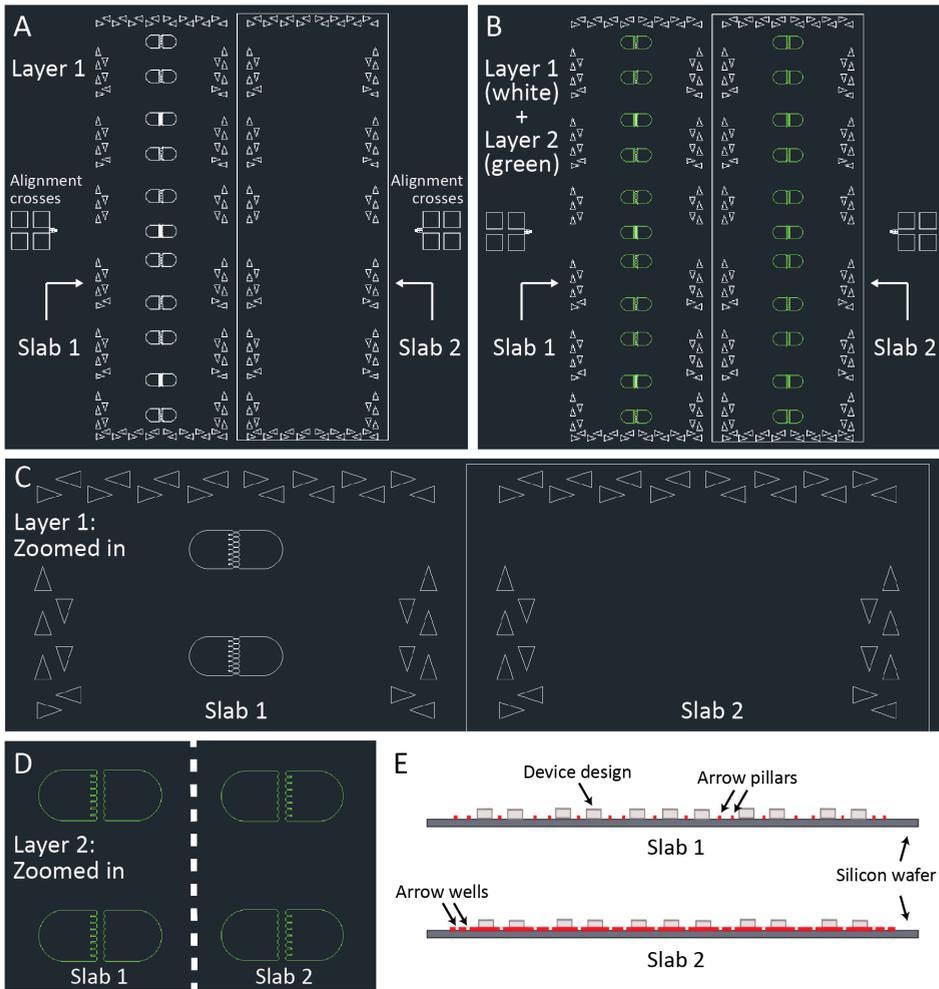
Figure 3.7: Alignment of PDMS slabs using alignment arrows in the design. (A-D) AutoCAD screenshots of the full design that was printed on the silicon wafer using soft lithography. (A) First layer, which was printed to a height of ± 50 μm, with the design enframed with alignment arrows. For slab 1, the alignment arrows are written by the laserwriter (μMLA, Heidelberg Instruments) as pillars, while for slab 2 an entire rectangular surface is written except for empty wells complementary to the arrows of slab 1. Alignment crosses are written to facilitate the alignment of layer 2 with layer 1 in the next step of the writing process. (B) Final developed design, where the second written layer is indicated in green. (C) Zoomed-in section of layer 1, clarifying the placement of alignment arrows. (D) Zoomed-in section of layer 2 (with the middle part cut out) to demonstrate how the right part of the wafer design is mirrored to the left part. This is necessary to create the correct final design, as PDMS slab 2 is turned over when aligning it with PDMS slab 1. (E) Side view of the final developed design on the silicon wafer, which is used for PDMS casting. Slab 1 contains arrow pillars and slab 2 complementary arrow wells (both indicated in red) to facilitate alignment before bonding the two slabs in order to create the final device.
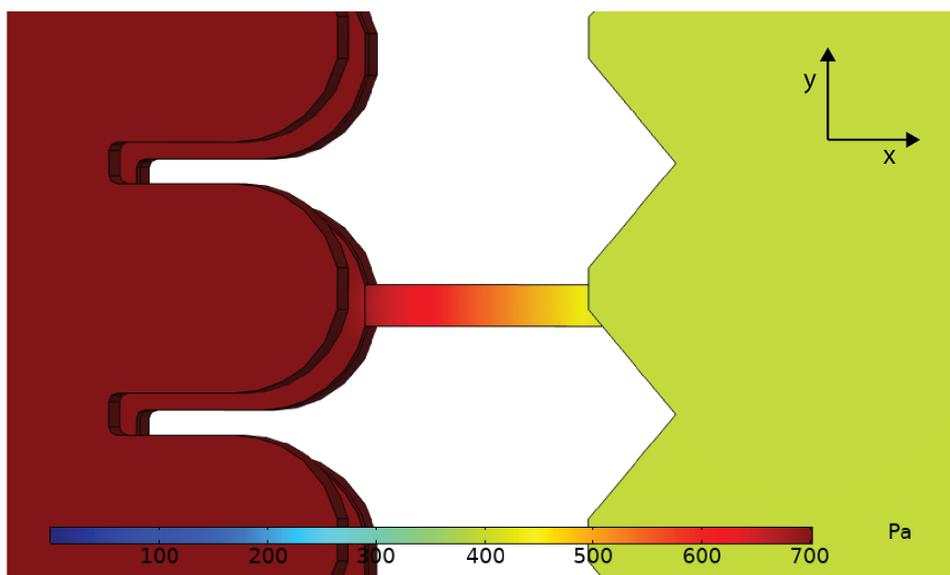
Figure 3.8: Pressure distribution across aspiration channel for a microfluidic device that is misaligned 20 µm along both the x- and y-axis. A 3D numerical COMSOL simulation of the pressure distribution assuming the device is connected to a 60 cm long straight rectangular channel mimicking the outlet tube. A pressure gradient of 700 Pa is simulated for the condition that all pockets but one are clogged by spheroids. The misalignment has negligible effects on the pressure drop across the aspiration channel in comparison to a perfectly aligned chip (Fig. 3.3A).
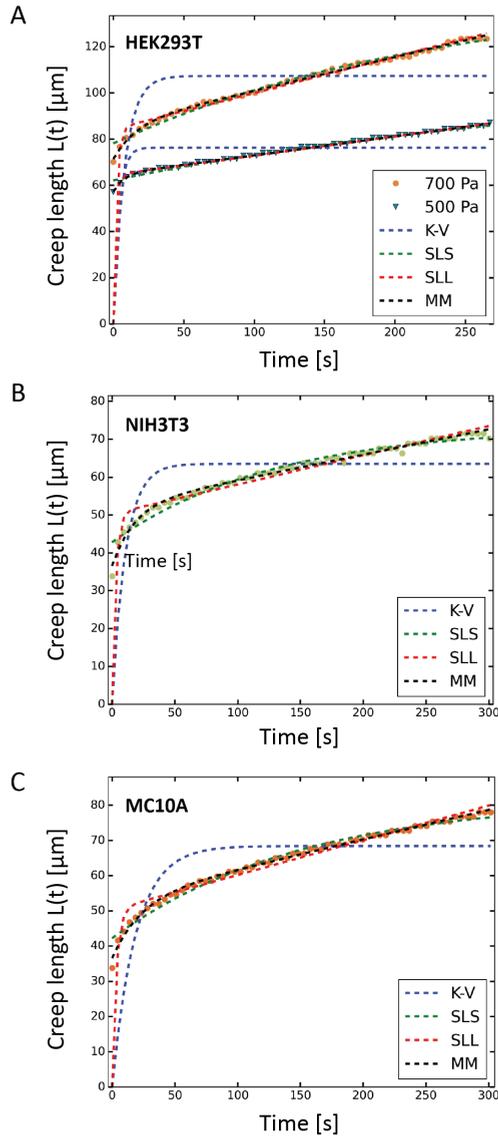
Figure 3.9: Comparison between fits of different spring-and-dashpot models to the viscoelastic creep response of cell spheroids. Measured viscoelastic creep responses over time (solid circles) fitted to four different spring-and-dashpot models (represented by dashed lines), explained in the Supplementary Information, for (A) an HEK293T spheroid aspirated at 500 Pa and one at 700 Pa, (B) an NIH3T3 spheroid aspirated at 1500 Pa, and (C) an MCF10A spheroid aspirated at 1500 Pa. The Kelvin-Voigt (K-V) and Standard Linear Solid (SLS) models do not result in a viscous linear increase with time and are thus not suitable to fit the viscoelastic creep behaviour of spheroids. The Standard Linear Liquid model (SLL) is not able to account for the initial jump in $L(t)$, unlike the modified Maxwell model (MM) due to its additional spring in the Kelvin-Voigt element. Accordingly, the R^2-values are the largest for the MM-model (see Appendix Table 3.2.)
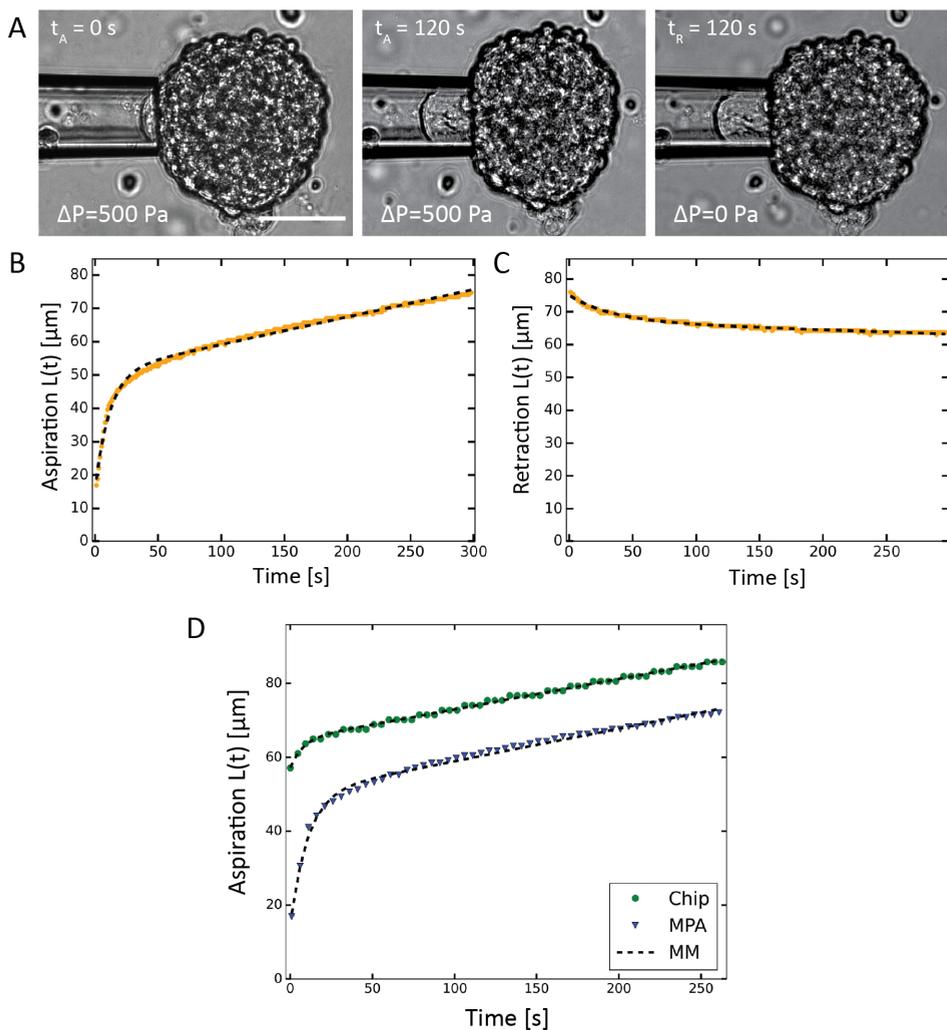
3

Figure 3.10: Glass micropipette aspiration experiment. (A) Brightfield images of the micropipette aspiration of an HEK293T cell spheroid using a glass micropipette with a radius R_p = 32.5 µm. Left and middle panels: images taken during aspiration at a hydrostatic underpressure of ΔP = 500 Pa, at the beginning of the experiment at t_A = 0 s (left) and after t_A = 2 minutes (middle). Right image: After 5 minutes, the pressure gradient is removed and the retraction is measured, here shown after t_R = 2 minutes (right). Scale bar 100 µm. (B) Creep curve (yellow) of the aspiration of the tongue over time, and (C) creep curve (yellow) for the retraction of the tongue, both fitted with the Modified Maxwell model (black dashed lines). (D) Comparison plot of the aspiration creep curves of two HEK293T cell spheroids aspirated at ΔP = 500 Pa, one using our microfluidic device (circles) and one using the traditional glass micropipette (triangles), together with fits to the MM model (dashed lines).
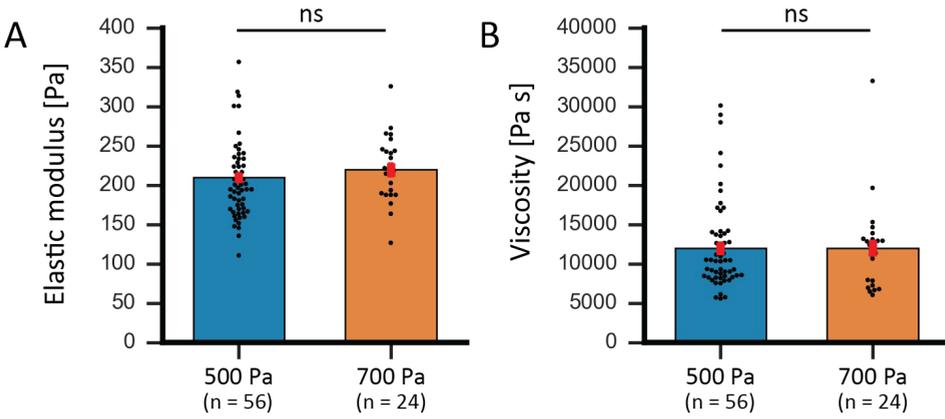
Figure 3.11: Pressure independence of elastic modulus E and viscosity η. (A) Histograms comparing (A) the average elastic modulus E and (B) the average viscosity η for HEK293T cell spheroids aspirated with the microfluidic chip at different pressures (500 Pa and 700 Pa), demonstrating how the two populations are not statistically different from each other when aspirated at different pressures. ns is nonsignificant with n = 56 and 24 for 500 Pa and 700 Pa respectively. Error bars are SEM.
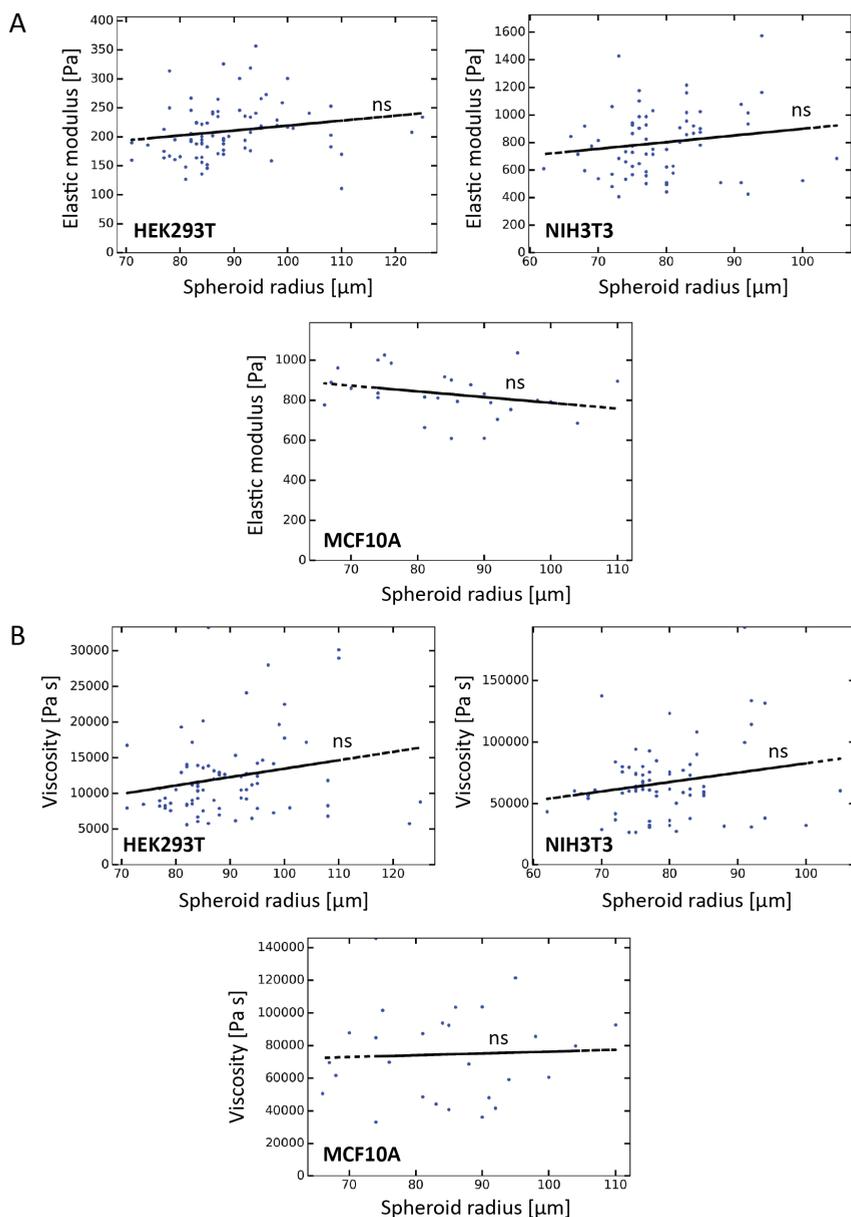
3

3

Figure 3.12: Spheroid size independence of elastic modulus E and viscosity η. Scatter plots of (A) the elastic moduli and (B) viscosities for HEK293T cell spheroids (n = 80, top-left), NIH3T3 cell spheroids (n = 75, top-right) and MCF10A cell spheroids (n = 34, bottom-middle), plotted against the spheroid radius R_0 (measured with ImageJ). All plots are fitted to determine a potential linear relationship (black dashed line), ns is non-significant.

3.C. Supplementary Table

	Coefficient of determination (R^2)			
Model	**HEK293T (500 Pa)**	**HEK293T (700 Pa)**	**NIH3T3 (1500 Pa)**	**MCF10A (1500 Pa)**
Kelvin-Voigt (K-V)	0.18816	0.31271	0.47405	0.58170
Standard Linear Solid (SLS)	0.98363	0.98549	0.96446	0.97898
Standard Linear Liquid (SLL)	0.65010	0.77660	0.84653	0.88069
Modified Maxwell (MM)	0.99640	0.99692	0.98872	0.99505

Table 3.2: Values of the coefficient of determination (R^2) calculated for each model fitted to the viscoelastic creep response of an HEK293T cell spheroid aspirated at 500 Pa and one at 700 Pa, and an NIH3T3 cell spheroid and MCF10A cell spheroid aspirated at 1500 Pa.

Nr.	R_0 (µm)	$E_{\Delta P - \Delta P_c}$ (Pa)	$\eta_{\Delta P - \Delta P_c}$ (kPa s)	$E_{\Delta P}$ (Pa)	$\eta_{\Delta P}$ (kPa s)	ΔP_c (Pa)
1	92	317	30	383	36	86
2	76	237	21	345	31	156
3	99	328	22	419	28	109
4	101	276	18	319	21	68
5	84	281	23	364	30	113
6	87	270	26	374	37	138

Table 3.3: Mechanical characteristics of HEK293T spheroids with different radii R_0 measured by glass micropipette aspiration. The elastic modulus E and viscosity η were derived from creep curves fitted to the Modified Maxwell (MM) model, either using just the applied aspiration pressure ΔP or taking the aspiration pressure corrected for the critical pressure ΔP_c (from Eq. (3.6) in the Appendix, $\Delta P - \Delta P_c$).

3.D. Supplementary Movies

Movie 1: Microfluidic multi-channel aspiration experiment to determine spheroid mechanics. A brightfield video of HEK293T spheroids being aspirated into the aspiration channels under an applied hydrostatic pressure of $\Delta P = 700$ Pa for a total duration of 5 minutes. Scale bar is 200 µm.

Movie 2: NIH3T3 cell spheroids move out of pockets during retraction measurement. A brightfield video of NIH3T3 spheroids being aspirated under a hydrostatic pressure of $\Delta P = 1500$ Pa for the first 10 minutes, after which the pressure gradient is removed and spheroid tongues start retracting. The tongues retract within seconds, making it impossible to record a retraction curve and extract a retraction rate L_∞^r to derive a critical pressure ΔP_c. Scale bar is 200 µm.

Movie 3: MCF10A cell spheroid retraction with remaining small aspiration pressure of 100 Pa. A brightfield video of an MCF10A spheroid being aspirated under a hydrostatic pressure of $\Delta P = 1500$ Pa for the first 10 minutes, after which the pressure gradient

is reduced to a small remaining aspiration pressure of 100 Pa and the spheroid tongue starts retracting. The tongue again retracts rapidly, within seconds, thereby ruling out the probability that this fast retraction is caused by a backflow. Scale bar is 50 μm.

Movie 4: MCF10A cell spheroid retraction in chip without pluronic coating. A bright-field video of an MCF10A spheroid in a chip that was not coated with pluronic F-127 solution, being aspirated under a hydrostatic pressure of $\Delta P = 1500$ Pa for the first 10 minutes after which the pressure gradient is removed and the spheroid tongue starts retracting. The tongue again rapidly retracts, within seconds, thereby demonstrating that this fast retraction is probably not governed by the surface treatment of the aspiration channels. Scale bar is 50 μm.

BIBLIOGRAPHY

1. Boot, R. C. *et al.* High-throughput mechanophenotyping of multicellular spheroids using a microfluidic micropipette aspiration chip. *Lab on a Chip* **23,** 1768–1778. http://arxiv.org/abs/2211.10182 (2023).

2. Hahn, C. & Schwartz, M. A. Mechanotransduction in vascular physiology and atherogenesis. *Nature Reviews Molecular Cell Biology* **10,** 53–62. ISSN: 14710072 (2009).

3. Mammoto, T. & Ingber, D. E. Mechanical control of tissue and organ development. *Development* **137,** 1407–1420 (2010).

4. Brugués, A. *et al.* Forces driving epithelial wound healing. *Nat Phys* **10,** 683–690 (2014).

5. Nia, H. T. *et al.* Solid stress and elastic energy as measures of tumour mechanopathology. *Nat Biomed Eng* **1,** 1–25 (2016).

6. Nia, H. T., Munn, L. L. & Jain, R. K. Physical traits of cancer. *Science* **370,** eaaz0868. ISSN: 10959203 (2020).

7. Jakab, K. *et al.* Relating Cell and Tissue Mechanics : Implications and Applications. *Developmental Dynamics* **237,** 2438–2449 (2008).

8. Foty, R. A., Pfleger, C. M., Forgacs, G. & Steinberg, M. S. Surface tensions of embryonic tissues predict their mutual envelopment behavior. *Development* **122,** 1611–1620. ISSN: 09501991 (1996).

9. Marturano, J. E., Arena, J. D., Schiller, Z. A., Georgakoudi, I. & Kuo, C. K. Characterization of mechanical and biochemical properties of developing embryonic tendon. *Proceedings of the National Academy of Sciences of the United States of America* **110,** 6370–6375. ISSN: 00278424 (2013).

10. Schiele, N. R. *et al.* Actin cytoskeleton contributes to the elastic modulus of embryonic tendon during early development. *Journal of Orthopaedic Research* **33,** 874–881. ISSN: 1554527X (2015).

11. Gonzalez-Rodriguez, D., Guevorkian, K., Douezan, S. & Brochard-Wyart, F. Soft Matter Models of Developing. *Science* **82,** 910–917 (2012).

12. Manning, M. L., Foty, R. A., Steinberg, M. S. & Schoetz, E. M. Coaction of intercellular adhesion and cortical tension specifies tissue surface tension. *Proceedings of the National Academy of Sciences of the United States of America* **107,** 12517–12522. ISSN: 00278424 (2010).

13. Brodland, G. W. The Differential Interfacial Tension Hypothesis (DITH): A comprehensive theory for the self-rearrangement of embryonic cells and tissues. *Journal of Biomechanical Engineering* **124,** 188–197. ISSN: 01480731 (2002).

14. Guevorkian, K., Colbert, M.-J., Durth, M., Dufour, S. & Brochard-Wyart, F. Aspiration of Biological Viscoelastic Drops. *Physical Review Letters* **104,** 1–4 (2010).

15. Han, Y. L. *et al.* Cell swelling, softening and invasion in a three-dimensional breast cancer model. *Nature Physics* **16,** 101–108. ISSN: 17452481 (2020).

16. Boot, R. C., Koenderink, G. H. & Boukany, P. E. Spheroid mechanics and implications for cell invasion. *Advances in Physics: X* **6,** 1978316. https://doi.org/10.1080/23746149.2021.1978316 (2021).

17. Mok, S. *et al.* Mapping cellular-scale internal mechanics in 3D tissues with thermally responsive hydrogel probes. *Nature Communications* **11,** 1–11. ISSN: 20411723. http://dx.doi.org/10.1038/s41467-020-18469-7 (2020).

18. Dolega, M. E. *et al.* Cell-like pressure sensors reveal increase of mechanical stress towards the core of multicellular spheroids under compression. *Nature Communications* **8,** 1–9. ISSN: 20411723 (2017).

19. Blumlein, A., Williams, N. & McManus, J. J. The mechanical properties of individual cell spheroids. *Scientific Reports* **7,** 1–10. ISSN: 20452322. http://dx.doi.org/10.1038/s41598-017-07813-5 (2017).

20. Jaiswal, D. *et al.* Stiffness analysis of 3D spheroids using microtweezers. *PLoS ONE* **12,** 1–21. ISSN: 19326203 (2017).

21. Dolega, M. *et al.* Mechanical behavior of multi-cellular spheroids under osmotic compression. *Journal of the Mechanics and Physics of Solids* **147,** 1–21. ISSN: 00225096. arXiv: 2011.01131 (2021).

22. Vyas, V., Solomon, M., D'Souza, G. G. & Huey, B. D. Nanomechanical Analysis of Extracellular Matrix and Cells in Multicellular Spheroids. *Cellular and Molecular Bioengineering* **12,** 203–214. ISSN: 18655033 (2019).

23. Schötz, E. M. *et al.* Quantitative differences in tissue surface tension influence zebrafish germ layer positioning. *HFSP Journal* **2,** 42–56. ISSN: 19552068 (2008).

24. Norotte, C., Marga, F., Neagu, A., Kosztin, I. & Forgacs, G. Experimental evaluation of apparent tissue surface tension based on the exact solution of the Laplace equation. *EPL* **81,** 1–6. ISSN: 02955075 (2008).

25. Mgharbel, A., Delanoë-Ayari, H. & Rieu, J. P. Measuring accurately liquid and tissue surface tension with a compression plate tensiometer. *HFSP Journal* **3,** 213–221. ISSN: 19552068 (2009).

26. Guevorkian, K., Gonzalez-rodriguez, D., Carlier, C., Dufour, S. & Brochard-Wyart, F. Mechanosensitive shivering of model tissues under controlled aspiration. *PNAS* **108,** 13387–13392 (2011).

27. Yousafzai, M. S. *et al.* Active Regulation of Pressure and Volume Defines an Energetic Constraint on the Size of Cell Aggregates. *Physical Review Letters* **128,** 48103. ISSN: 0031-9007. https://doi.org/10.1103/PhysRevLett.128.048103 (2022).

28. Yadav, V. *et al.* Gradients in solid surface tension drive Marangoni-like motions in cell aggregates. *Physical Review Fluids* **7,** 1–9 (2022).

29. Foty, R. A., Pfleger, C. M., Forgacs, G. & Steinberg, M. S. Liquid Properties of Embryonic Tissues: Measurement of Interfacial Tensions. *Physical Review Letters* **72,** 2298–2301 (1994).

30. Ryan, P. L., Foty, R. A., Kohn, J. & Steinberg, M. S. Tissue spreading on implantable substrates is a competitive outcome of cell-cell vs. cell-substratum adhesivity. *Proceedings of the National Academy of Sciences of the United States of America* **98,** 4323–4327. ISSN: 00278424 (2001).

31. Truongvo, T. N. *et al.* Microfluidic channel for characterizing normal and breast cancer cells. *Journal of Micromechanics and Microengineering* **27,** 1–9. ISSN: 13616439 (2017).

32. Mak, M. & Erickson, D. A serial micropipette microfluidic device with applications to cancer cell repeated deformation studies. *Integrative Biology* **5,** 1374–1384 (2013).

33. Mak, M., Reinhart-King, C. A. & Erickson, D. Elucidating mechanical transition effects of invading cancer cells with a subnucleus-scaled microfluidic serial dimensional modulation device. *Lab on a Chip* **13,** 340–348. ISSN: 14730189 (2013).

34. Hou, H. W. *et al.* Deformability study of breast cancer cells using microfluidics. *Biomedical Microdevices* **11,** 557–564. ISSN: 13872176 (2009).

35. Davidson, P. M. *et al.* High-throughput microfluidic micropipette aspiration device to probe time-scale dependent nuclear mechanics in intact cells. *Lab on a Chip* **19,** 3652–3663. ISSN: 14730189 (2019).

36. Lee, L. M. & Liu, A. P. A microfluidic pipette array for mechanophenotyping of cancer cells and mechanical gating of mechanosensitive channels. *Lab Chip* **15,** 264–273 (2015).

37. Au, S. H. *et al.* Clusters of circulating tumor cells traverse capillary-sized vessels. *Proceedings of the National Academy of Sciences of the United States of America* **113,** 4947–4952. ISSN: 10916490 (2016).

38. Cognart, H. A., Viovy, J. L. & Villard, C. Fluid shear stress coupled with narrow constrictions induce cell type-dependent morphological and molecular changes in SK-BR-3 and MDA-MB-231 cells. *Scientific Reports* **10,** 1–14. ISSN: 20452322. http://dx.doi.org/10.1038/s41598-020-63316-w (2020).

39. Raj, A., Dixit, M., Doble, M. & Sen, A. K. A combined experimental and theoretical approach towards mechanophenotyping of biological cells using a constricted microchannel. *Lab on a Chip* **17,** 3704–3716. ISSN: 14730189 (2017).

40. Adamo, A. *et al.* Microfluidics-based assessment of cell deformability. *Analytical Chemistry* **84,** 6438–6443. ISSN: 00032700 (2012).

41. Chang, Y. N. *et al.* Microfluidic Analysis for Separating and Measuring the Deformability of Cancer Cell Subpopulations. *ACS Omega* **4,** 8318–8323. ISSN: 24701343 (2019).

42. Sabhachandani, P. *et al.* Generation and functional assessment of 3D multicellular spheroids in droplet based microfluidics platform. *Lab on a Chip* **16,** 497–505. ISSN: 14730189 (2016).

43. Ruppen, J. *et al.* A microfluidic platform for chemoresistive testing of multicellular pleural cancer spheroids. *Lab on a Chip* **14,** 1198–1205 (2014).

44. Shorr, A. Z., Sönmez, U. M., Minden, J. S. & Leduc, P. R. High-throughput mechanotransduction in: Drosophila embryos with mesofluidics. *Lab on a Chip* **19,** 1141–1152. ISSN: 14730189 (2019).

45. Song, W. *et al.* Dynamic self-organization of microwell-aggregated cellular mixtures. *Soft Matter* **12,** 5739–5746. ISSN: 17446848 (2016).

46. Lee, S. W. & Lee, S. S. Shrinkage ratio of PDMS and its alignment method for the wafer level process. *Microsystem Technologies* **14,** 205–208. ISSN: 09467076 (2008).

47. Constantin, P. & Foias, C. *Navier-Stokes Equations* (University of Chicago Press, 2020).

48. Liu, R., Jiang, Y., Li, B. & Yu, L. Estimating permeability of porous media based on modified Hagen–Poiseuille flow in tortuous capillaries with variable lengths. *Microfluidics and Nanofluidics* **20,** 1–13. ISSN: 16134990 (2016).

49. Efremov, Y. M. *et al.* Mechanical properties of cell sheets and spheroids: the link between single cells and complex tissues. *Biophysical Reviews* **13,** 541–561. ISSN: 18672469 (2021).

50. Hochmuth, R. M. Micropipette aspiration of living cells. *Journal of Biomechanics* **33,** 15–22. ISSN: 00219290 (2000).

51. Guevorkian, K., Brochard-Wyart, F. & Gonzalez-Rodriguez, D. *Flow dynamics of 3D multicellular systems into capillaries* 193–223. ISBN: 9780128203101. `http://dx.doi.org/10.1016/B978-0-12-820310-1.00008-2` (Academic Press, New York, 2021).

52. Son, Y. Determination of shear viscosity and shear rate from pressure drop and flow rate relationship in a rectangular channel. *Polymer* **48,** 632–637 (2007).

53. Koudan, E. V. *et al.* Multiparametric Analysis of Tissue Spheroids Fabricated from Different Types of Cells. *Biotechnology Journal* **15,** 1–12. ISSN: 18607314 (2020).

54. Jorgenson, A. J. *et al.* TAZ activation drives fibroblast spheroid growth, expression of profibrotic paracrine signals, and context-dependent ECM gene expression. *American Journal of Physiology - Cell Physiology* **312,** C277–C285. ISSN: 15221563 (2017).

4

CELL SPHEROID VISCOELASTICITY IS DEFORMATION-DEPENDENT

If you've made up your mind to test a theory, or you want to explain some idea, you should always decide to publish it whichever way it comes out.

Richard P. Feynman

Tissue surface tension influences cell sorting and tissue fusion. Earlier mechanical studies suggest that multicellular spheroids actively reinforce their surface tension with applied force. Here we study this open question through high-throughput microfluidic micropipette aspiration measurements on cell spheroids to identify the role of force duration and cell contractility. We find that larger spheroid deformations lead to faster cellular retraction once the pressure is released, regardless of the applied force and cellular contractility. These new insights demonstrate that spheroid viscoelasticity is deformation-dependent and challenge whether surface tension truly reinforces.

4.1. INTRODUCTION

The physical response of multicellular tissues to an applied stress is critical in the regulation of various physiological processes, such as embryonic morphogenesis [2, 3], wound healing [4], cell differentiation [5], and cancer metastasis [6, 7]. While the mechanical response of single cells depends on their cytoskeleton, plasma membrane and nuclear stiffness [8, 9], overall tissue mechanics is additionally dependent on intercellular adhesions and the extracellular environment [10–12]. When tissues form and merge, their resulting morphology is defined by this mechanical interplay between cells across multiple length scales, called tissue fluidity [13–15].

To examine the relation between cellular mechanics and tissue fluidity, dissociated cells can be manipulated into a spherical assembly, termed spheroid, by letting them sediment and aggregate in a confined space. Spheroids have become a popular *in vitro* model as they recreate both the multicellularity and three-dimensional (3D) microenvironment of *in vivo* tissues [16, 17]. They round up over time to minimize surface energy, similar to liquid droplets [18]. Previous studies have determined the apparent spheroid surface tension γ, which has been related to tissue spreading [19] and cell sorting [20]. Here, the magnitude of γ and the related cellular arrangement depend on the interplay between the intercellular adhesion and cortical tension of the cells [21–23].

A conventional biophysical tool to measure γ is micropipette aspiration (MPA), where the spheroid is partly aspirated into a micron-sized pipette under a constant stress and the advancing creep length $L(t)$ of the spheroid protrusion is monitored over time [24]. Aspirated spheroids behave like a viscoelastic liquid, first displaying an elastic response followed by an apparently linear viscous response. The constant creep rate $\dot{L}_\infty$ of the linear viscous response during both aspiration and relaxation of the spheroid (once the aspiration pressure is released) is used to calculate the spheroid surface tension γ [24, 25]. Intriguingly, γ was shown to depend on the applied aspiration pressure ΔP, suggesting a reinforcement of γ through an active response of the cells to the mechanical force [24]. However, no dependency of γ on the applied force was observed in parallel-plate uniaxial compression experiments [18, 20]. This raises the question whether cells actively reinforce their surface tension with the applied force or if the current understanding of viscoelastic spheroid aspiration data is insufficient. In this chapter, we address this question by studying how the duration that cells are exposed to different aspiration forces, alongside differences in cell mechanics, affect the tissue surface tension and its possible reinforcement.

4.2. RESULTS AND DISCUSSION

We have developed a microfluidic micropipette aspiration device that allows for a higher throughput than the conventional glass micropipette technique [26]. Where the traditional technique only aspirates one spheroid at a time, our device can aspirate up to eight spheroids simultaneously [Fig. 4.1(a)]. By flowing spheroids into individual parallel aspiration pockets that are aligned with squared constriction channels of 50x50 μm^2 (mimicking micropipettes), parallel creep tests can be applied by lowering a water reservoir attached to the outlet of the device [Materials and methods, and Supplementary Fig. 4.5]. First, a spheroid aspiration measurement is conducted, where the creep length $L(t)$
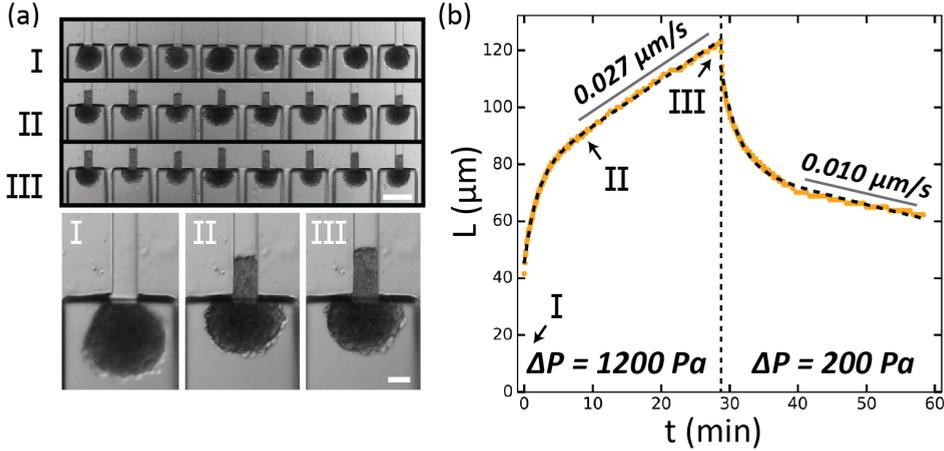
Figure 4.1: Viscoelastic deformation of NIH3T3 spheroids. (a) Brightfield images of 8 NIH3T3 spheroids aspirated at 0 min (I), 10 min (II) and 30 min (III), with an overview of the microfluidic chip (top, scale bar 200 µm), and a single spheroid close-up (bottom, scale bar 50 µm). (b) The creep length $L(t)$, for the spheroid shown in (a, bottom), aspirated at 1200 Pa and left to retract at 200 Pa. The data (orange dots) is fitted with the Modified Maxwell model (black dashed lines), and the derived viscous creep rate values are added to the plot.

increases over time. Next, the pressure is released, thus starting a stress relaxation test, where the protrusion retracts over time.

By fitting the creep data with a modified Maxwell model [[24] and Materials and methods], the fast elastic deformation δ at short times and viscous flow with constant velocity $\dot{L}_\infty$ at long times can be defined for both the aspiration and retraction curves. Assuming volume conservation of the non-aspirated part of the spheroid, the aspiration force for a cylindrical pipette is given by $f = \pi R_p^2 (\Delta P - \Delta P_c)$, with R_p the radius of the pipette and ΔP_c the critical pressure above which aspiration occurs [24]. Assuming that the viscosity η of the spheroid remains unchanged during the aspiration and retraction phase, the critical pressure is deduced from $\Delta P_c = \Delta P \dot{L}_\infty^r / (\dot{L}_\infty^r + \dot{L}_\infty^a)$, where $\dot{L}_\infty^r$ and $\dot{L}_\infty^a$ are the retraction and aspiration flow rates, respectively [for full derivation see Materials and methods]. By applying the Laplace law, the spheroid surface tension is derived from the critical pressure via $\Delta P_c = 2\gamma(\frac{1}{R_p} - \frac{1}{R})$, with R being the spheroid radius, which can be approximated by the initial radius R_0, as $R_p \ll R_0$. Following previous work by Davidson et al. [27, 28], the effective channel radius R_{eff} for our squared 50x50 µm^2 channel is 27 µm [for derivation see Materials and methods].

Homogeneous spheroids of NIH3T3 fibroblast cells and human embryonic kidney (HEK293T) cells were formed using the Sphericalplate 5D (Kugelmeiers) and ranged between 65 and 125 µm in radius through all experiments [Material and methods, and Supplementary Fig. 4.6]. All details on the microfluidic device can be found in our previous study [26] and the Materials and methods. Only spheroids with a constant volume during aspiration were analyzed. During the stress relaxation test, bringing ΔP entirely back to zero often made spheroids move out of the pockets, preventing the monitoring of the protrusion retraction. This was likely due to the presence of a minor backflow in the

microfluidic device, as manually bringing back the outlet reservoir to the exact same starting height proved to be difficult. To circumvent this, all retraction measurements were performed by leaving a minor pressure that still allowed for the protrusion to retract while keeping it in the constriction channel. This led to a small readjustment in the derivation of ΔP_c and γ [Materials and methods].

First, creep aspiration tests were performed on NIH3T3 spheroids for 30 minutes (min), long enough for the protrusions to have entered the linear viscous regime (as the creep rate did not change anymore after 10 min). Next, stress relaxation tests were captured for an identical 30 min [Fig. 4.1(b)]. We found that the derived viscous retraction flow velocity $\dot{L}^r_\infty$ was strongly influenced by the duration of retraction [Supplementary Fig. 4.7]. Even after a 2 hour-long retraction measurement, $\dot{L}^r_\infty$ still decreased over time as the creep curve plateaued [Supplementary Fig. 4.8]. Interestingly, in traditional MPA studies on murine sarcoma (S180) cell spheroids, where no remaining pressure was left during retraction, the flow velocity did appear to be linear over time [24, 25]. We hypothesize that the minor pressure left in our retraction measurements induced the plateau, which would mean that here retraction is not governed by one constant critical pressure ΔP_c. Instead, the spheroid protrusion first retracts with a large ΔP_c upon release of the aspiration pressure, after which the creep curve plateaus due to the remaining pressure counteracting the spheroid now retracting with a smaller ΔP_c. To eliminate active contraction during spheroid retraction, we treated the NIH3T3 spheroids with the myosin II inhibitor Blebbistatin and monitored their retraction at 200 Pa. Now, the spheroids first displayed a minor elastic retraction after which they started aspirating again [Materials and methods, and Supplementary Fig. 4.9]. This demonstrates how for these measurements retraction can not be governed by a constant ΔP_c, as retraction changed into aspiration over time. We therefore hypothesize that spheroid retraction is determined by an interplay between retractile cellular elastic properties and the viscous flow of the spheroid tongue as a cellular collective, each having their own critical pressure governing retraction.

To test whether we observe a reinforcement in γ for increasing ΔP as reported in Ref. [24], measurements with NIH3T3 spheroids were conducted using two slightly differing aspiration pressures (1000 Pa and 1200 Pa) and a large pressure of 2000 Pa, now for only 10 min of aspiration followed by 10 min of retraction at 200 Pa as spheroid volumes were not conserved for aspiration times beyond 10 min. At 1000 and 1200 Pa, we observed pulsed contractions or "shivering" in ca. 50% of the aspiration curves [examples in Supplementary Fig. 4.10], resembling observations reported with glass MPA [29]. This shivering effect did not occur at the large pressure of 2000 Pa, where the protrusion flowed smoothly in the constriction. Despite the shivering, aspiration curves could still be fitted with the modified Maxwell model and retraction curves were comparable for spheroids that did or did not shiver during aspiration [Supplementary Table 4.1]. The small influence of shivering on L^a_∞ did not significantly influence $\dot{L}^r_\infty$ nor γ for different conditions, so we included these data. For the three different aspiration pressures, we indeed observed an apparent force-dependent γ, where the derived surface tension increased for larger ΔP [Fig. 4.2(a)]. Accordingly, the stress relaxation curves demonstrated an increase in retraction flow velocity $\dot{L}^r_\infty$ for larger ΔP [Fig. 4.2(b)], formerly also observed in glass MPA measurements [24]. Previously, this was interpreted as the spheroid
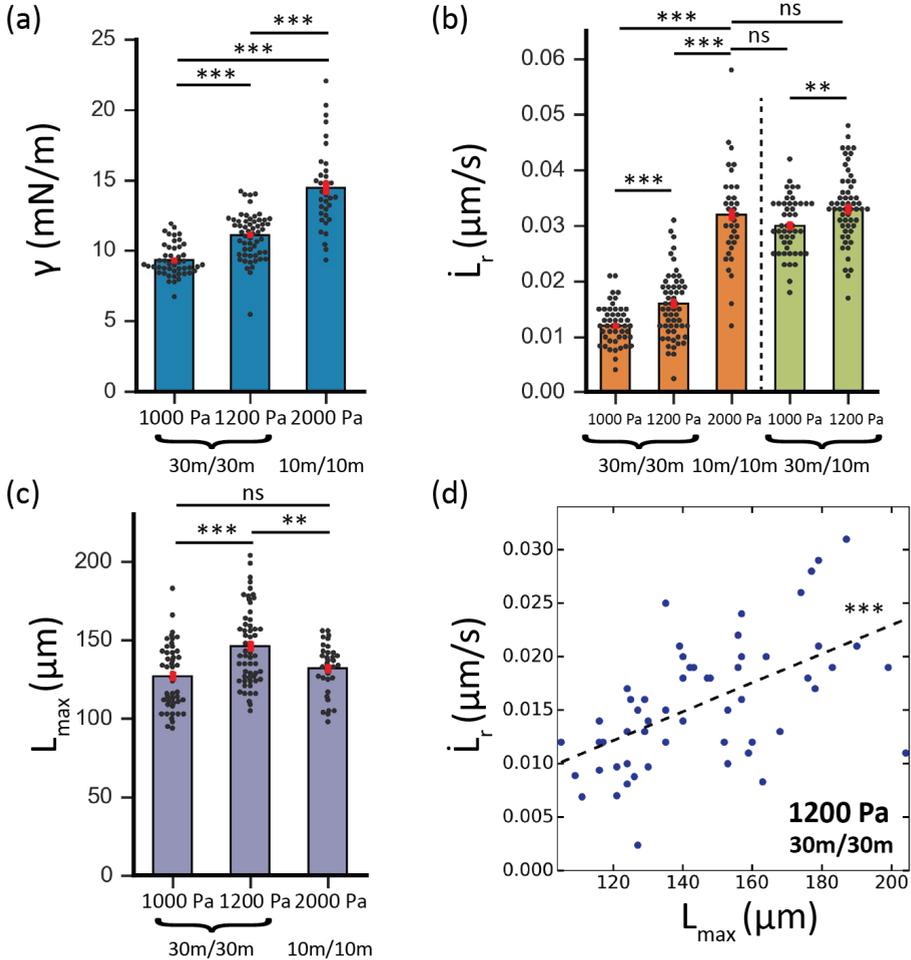
Figure 4.2: Tissue relaxation behavior is deformation-dependent. (a-c) Histograms comparing NIH3T3 spheroids aspirated at 1000 Pa (30 min aspiration, 30 min retraction, n = 48), 1200 Pa (30 min aspiration, 30 min retraction, n = 57), and at 2000 Pa (10 min aspiration, 10 min retraction, n = 35). Retraction was performed at 200 Pa. (a) γ, (b) L_∞^r and (c) L_{max} are compared. For (b), the two green bars on the right of the dotted line depict the derived L_∞^r when only fitting the first 10 min of retraction. (d) L_∞^r plotted versus L_{max} for NIH3T3 spheroids aspirated at 1200 Pa (30 min aspiration, 30 min retraction). **, p < 0.01, ***, p < 0.001 and ns is non-significant. Error bars are SEM.

protrusion actively mechanosensing the magnitude of the aspiration force, causing it to reinforce and retract faster. However, for our measurements $\dot{L}_\infty^r$ depends on the time frame during which the relaxation is investigated. Intriguingly, when fitting only the first 10 min of retraction for the measurement at 1000 Pa, we find that the average $\dot{L}_\infty^r$ at 1000 and 2000 Pa is the same [Fig. 4.2(b), right-side]. While the total deformation length L_{max} of the spheroid protrusion at the end of aspiration is understandably larger when aspirating at larger pressures, we find that the same average length has been reached when aspirating for 30 min at 1000 Pa or 10 min at 2000 Pa, indicating a deformation-dependency for retraction [Fig. 4.2(c)]. Indeed, we find that $\dot{L}_\infty^r$ is linearly dependent on L_{max}, where the further the protrusion has reached after aspiration, the faster it retracts when comparing identical time frames [Fig. 4.2(d), Supplementary Fig. 4.11 (1000 Pa and 2000 Pa)]. In addition, a larger aspiration flow velocity $\dot{L}_\infty^a$ results in a larger L_{max} and thus larger $\dot{L}_\infty^r$ [Supplementary Fig. 4.12]. While these trends were observed at 1000 and 1200 Pa, they were not significant for the measurements at 2000 Pa, likely because of the larger standard deviation in $\dot{L}_\infty^r$ at the shorter timescale, alongside the smaller range in L_{max} and the smaller number of data points. Altogether, these measurements show that $\dot{L}_\infty^r$ and the derived γ do not solely depend on either the applied force or time frame but directly relate to the product of both, being the resulting length of deformation L_{max}.

What cellular properties govern retraction flow velocity and its deformation-dependency is unclear. We therefore sought to investigate the influence of cell contractility on the retraction flow and spheroid viscoelasticity. Alpha-smooth muscle actin (α-SMA), the mesenchymal marker and cytoskeletal protein that is incorporated into stress fibers of fibroblasts, upregulates their contractile activity and ability to remodel tissues [30–32]. We found that increasing the NIH3T3 cell seeding density during fabrication strongly influenced the α-SMA concentration in our spheroids [Fig. 4.3(a-b)]. Western blots analysis showed that doubling the cell seeding density from $1.5x10^6$ (used in Fig. 4.2) to $3x10^6$ cells increased the average protein concentration of α-SMA by a factor of 6 [Supplementary Fig. 4.13]. We hypothesize that cells differentiated at higher density, similar to fibroblasts increasing their α-SMA concentration in response to the cytokine TGF-β1 when seeded at a larger cell density in 2D [33]. Identical to the previous spheroids, we aspirated the $3x10^6$ cell spheroids at 1200 Pa for 30 min and then let them retract at 200 Pa for 30 min. Our results showed that γ did not change, despite the larger concentration of α-SMA [Fig. 4.3(c)]. This was unexpected, as the $3x10^6$ cell spheroids retracted slower [Fig. 4.3(d)]. Additionally, they had a significantly lower aspiration rate $\dot{L}_\infty^a$ and reached less far in the constrictions, demonstrating a smaller deformability [Supplementary Fig. 4.14]. From this, we calculate that the $3x10^6$ cell spheroids have a higher average viscosity of $\eta = 150 \pm 9$ kPa.s in comparison to the $1.5x10^6$ cell spheroids with $\eta = 68 \pm 3$ kPa.s [details in Materials and methods], explaining their different deformability at the same γ. In contrast, previous measurements with parallel-plate tensiometry on spheroids composed of different cell lines showed a linear correlation between bulk viscosity and surface tension [34]. However, our findings on a time-dependent retraction raise the question whether the viscosity and/or ΔP_c remain constant during MPA retraction. If this assumption would prove to be incorrect, disentangling η and γ when interpreting the measured $\dot{L}_\infty^a$ and $\dot{L}_\infty^r$ becomes very difficult, as we are left with two separate responses (aspiration and retraction) each with two unknown variables.
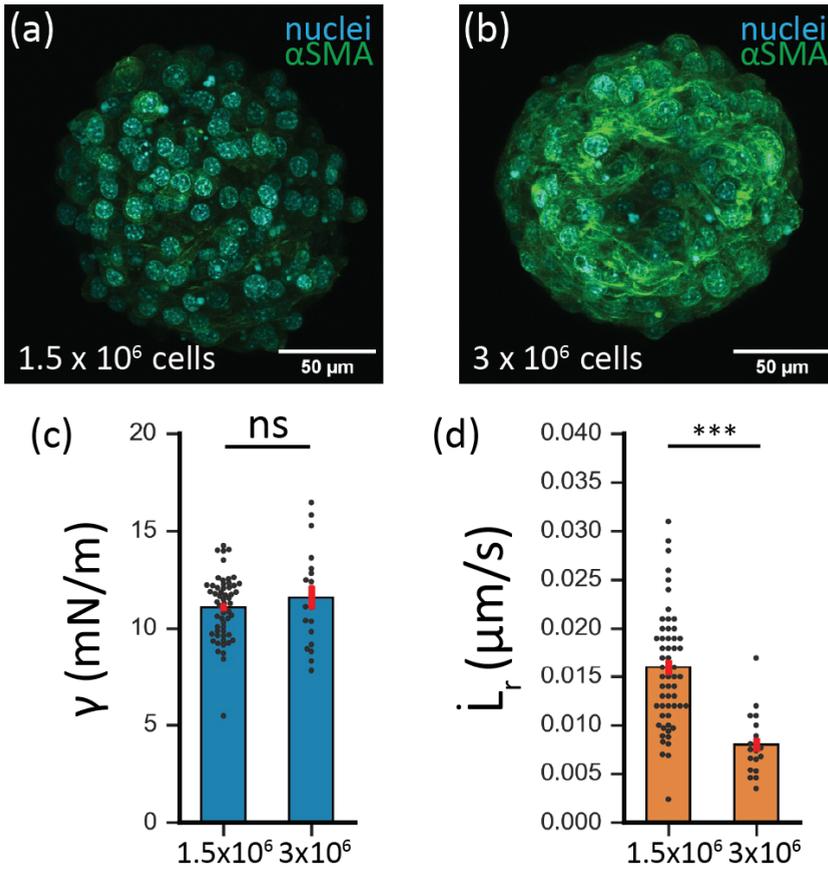
Figure 4.3: A larger concentration of α-SMA does not influence derived tissue surface tension. (a-b) Max intensity confocal fluorescent images of nuclei (cyan) and α-SMA (green) in NIH3T3 spheroids seeded with (a) 1.5×10^6 cells/well and (b) 3×10^6 cells/well. (c-d) Histograms comparing NIH3T3 spheroids aspirated at 1200 Pa at a seeding density of 1.5×10^6 cells (30 min aspiration, 30 min retraction, n = 57) and a seeding density of 3×10^6 cells (30 min aspiration, 30 min retraction, n = 19). Retraction was performed at 200 Pa. (c) γ and (d) $\dot{L}_\infty^r$ are compared. ***, p < 0.001 and ns is nonsignificant. Error bars in histograms are SEM.

To untangle η and ΔP_c, we aspirated spheroids without the influence of ΔP_c, using human embryonic kidney (HEK293T) cell spheroids with a very low surface tension [Fig. 4.4(a)]. In order to keep spheroid volume constant, we aspirated the HEK293T cell spheroids for 5 min at 200 Pa and 500 Pa. We then monitored retraction for 5 min at a remaining minor pressure of 50 Pa. After 200 Pa aspiration, spheroid tongues retracted elastically and then started aspirating again, indicating that their ΔP_c was indeed minimal (below 50 Pa) [Supplementary Fig. 4.15]. Upon 500 Pa aspiration, spheroid tongues deformed further into the constrictions [Fig. 4.4(b)] and now displayed a linear viscous retraction over time, resulting in an average $\gamma = 1.9 \pm 0.1$ mN/m, consistent with a deformation-dependent retraction. Importantly, at these low pressures we find a pressure-dependent viscosity [Fig. 4.4(c)]. This contrasts with our NIH3T3 mea-
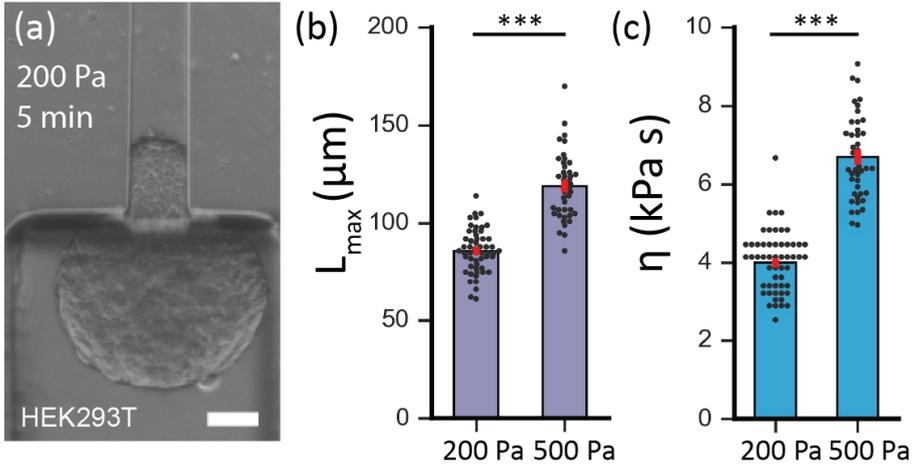
Figure 4.4:   For soft HEK293T cell spheroids, viscosity is pressure-dependent.   (a) Brightfield image of a HEK293T cell spheroid after 5 min of aspiration at 200 Pa. Scale bar 50 μm. (b-c) Histograms comparing HEK293T spheroids aspirated at 200 Pa (5 min aspiration, 5 min retraction, n = 54) and at 500 Pa (5 min aspiration, 5 min retraction, n = 43). Retraction was performed at 50 Pa. (b) L_{max} and (c) η are compared. ***, p < 0.001. Error bars are SEM.

surements, where the viscosity was pressure-independent [Supplementary Fig. 4.16(a)], similar to the previous study by Guevorkian *et al.* with S180 cell spheroids [24]. In our own previous study with a slightly different microfluidic design (aspiration pockets were rounded instead of rectangular) [26], we aspirated HEK293T spheroids at 500 and 700 Pa and also showed their viscosity to be pressure-independent. We believe that the discrepancy with our new data can be explained by the smaller pressure range (factor 1.4, compared to a factor 2.5 in the current work) and the larger standard deviation in $L_\infty^{\dot{a}}$ for our previous microfluidic device. Our new measurements clearly display a significant increase in η when raising the pressure, from $\eta = 4.0 \pm 0.1$ kPa.s at 200 Pa to $\eta = 6.7 \pm 0.2$ kPa.s at 500 Pa [Fig. 4.4(c)]. For 200 Pa, we calculated η by assuming $\Delta P_c = 0$ Pa, thus giving an upper bound for η. For 500 Pa, we calculated η via our derived ΔP_c from $L_\infty^{\dot{a}}$ and $L_\infty^{\dot{r}}$. Interestingly, the proportional change in the initial elastic deformation δ_a during aspiration was larger than the change in $L_\infty^{\dot{a}}$ between the two pressures [Supplementary Fig. 4.17], suggesting that the increase in force differently affects the elastic deformation and the viscous flow of cells. Moreover, we do find a pressure-dependent η for our NIH3T3 spheroid measurements when we reanalyze the data, neglecting the increase in $L_\infty^{\dot{r}}$ and using that ΔP_c is the same at 1000 Pa and 1200 Pa [Supplementary Fig. 4.16(a)]. Similar to the HEK293T measurements, the increase in force induces a larger proportional change in δ_a than for $L_\infty^{\dot{a}}$ [Supplementary Fig. 4.16(b-c)]. This implies that another possible framework exists besides tissue reinforcement, in which not surface tension but spheroid viscosity is pressure-dependent for MPA measurements. In that case, either η or ΔP_c is different between aspiration and retraction, as the flow velocity is deformation-dependent during retraction.

In this study, we have measured a force-dependent spheroid surface tension γ cou-

pled to an increased viscous flow rate $\dot{L}_{\infty}^{r}$ at larger deformations. The reinforcement of γ has previously been explained by an active response of cells to mechanical forces, involving cytoskeletal remodeling potentially due to stress fiber polymerization by myosin II motors, stretch-activated membrane channels or the clustering of cadherins [24, 35–40]. Next to this, spheroid surface tension has also previously been coupled to the size of spheroids [25], where spheroids in the size range of 160-360 µm in diameter displayed a smaller γ as the size increased. Unfortunately, the size range that our microfluidic device can aspirate was too small to reproduce this effect [Supplementary Fig. 4.18]. However, our results have generated new insights in the viscoelastic behavior of spheroids during MPA and the interpretation of γ thanks to the large amount of data we could obtain by high-throughput microfluidic aspiration. We therefore propose a different framework than tissue reinforcement to interpret viscoelastic spheroid MPA data, in which $\dot{L}_{\infty}^{r}$ is governed by the total deformation L_{max}, making η and/or ΔP_c different between aspiration and retraction.

4.3. CONCLUSION

How to distinguish tissue surface tension and viscosity from each other during aspiration measurements, and how to identify whether γ, η or both are pressure-dependent during MPA remains an open question. Previous studies have shown how the liquid-like properties of cellular tissues are determined by tissue flow via cells rearranging and slipping past each other [14, 15, 41–44]. In an experiment with mCherry-transfected NIH3T3 cells and a microfluidic device modified to allow detailed imaging in the constriction channel, we did not observe cells slipping past each other, demonstrating that the viscous flow was unlikely to be governed by cell rearrangements [see Supplementary Movies 1 and 2, and Materials and methods for the device modifications]. We hypothesize that the deformation-dependent viscoelasticity can be explained by the number of individual cells that have been aspirated into the constriction channel. If each cell has its own relaxation rate, then a spheroid protrusion with more cells in series will have a larger $\dot{L}_{\infty}^{r}$, being the sum of all these individual cellular retraction rates. Yet, how the tissues' effective viscosity is precisely governed at the cellular level, and how different cytoskeletal elastic and viscous components work over different timescales to govern ΔP_c remains to be examined. Overall, we show that spheroid viscoelastic behavior is pressure- and deformation-dependent for MPA, challenging the assumption that both η and ΔP_c are identical during aspiration and retraction.

4.4. MATERIALS AND METHODS

4.4.1. CELL CULTURE

NIH3T3 embryonic mouse fibroblasts (ATCC CRL-1658) were kept in Dulbecco's Modified Eagle Medium (DMEM, Gibco) containing 4.5 g L^{-1} glucose, L-glutamine, without sodium pyruvate, and supplemented with 10% Newborn Calf Serum (NCS, Gibco) and 1% antibiotic–antimycotic solution (Sigma-Aldrich). Transfected LifeAct-GFP_NLS mCherry NIH3T3 cells, used for the Supplementary videos, were cultured in Dulbecco's Modified Eagle's Medium (DMEM, Thermo Fisher Scientific), supplemented with 10% Fetal Bovine Serum (FBS, Thermo Fisher Scientific), 1% penicillin/streptomycin (Pen/

Strep, Thermo Fisher Scientific), and 1 µg/ml of Puromycin (Thermo Fisher Scientific).

Human embryonic kidney 293T (HEK293T, ACC 635) cells were kept in DMEM/F12 with GlutaMAX (Gibco), supplemented with 10% Fetal Bovine Serum (FBS, Sigma) and 1% penicillin-streptomycin solution (Gibco).

All cells were incubated at 37 °C with 5% CO_2 in TC T-25 or T-75 flasks (Sarstedt), and subcultured at least twice a week, until a maximum passage number of 30. Cells were periodically checked for mycoplasm.

4.4.2. CELL TRANSFECTION WITH NLS-MCHERRY AND LIFEACT-GFP FOR SUPPLEMENTARY VIDEOS

The pCDNA_Lifeact-GFP_NLS-mCherry was a gift from Olivier Pertz (Addgene plasmid #69058). From this vector, a SmaI-EcoRV fragment containing the NLS-mCHERRY ORF was cloned in the HpaI site of the pLV-CMV-IRES-PURO vector. Next, the EF1a promoter, from pcDEF3, was cloned in the BstZ17I site of pLV-PURO-NLS-mCHERRY. Finally, the NdeI-HincII fragment, containing LifeAct-GFP (from pCDNA_Lifeact-GFP_NLS-mCherry), was cloned in the NdeI-EcoRV sites.

Lentiviruses were produced by co-transfecting cDNA expression plasmids with helper plasmids pCMV-VSVG, pMDLg-RRE (gag/pol), and pRSV-REV into HEK293T cells using polyethyleneimine (PEI). Cell supernatants were harvested 48 hours after transfection and stored at -80 °C. NIH3T3 cells were labelled by infecting for 24 hours with LifeAct-GFP_NLS mCherry expressing lentiviral supernatants diluted 1:1 with cell culture medium and 5 ng/ml of polybrene (Sigma-Aldrich). Forty-eight hours after infection, cells were placed under Puromycin (Thermo Fisher Scientific) selection. Cells were cultured with 1 µg/ml of Puromycin to obtain a stable fluorescent cell line and maintain selection pressure.

4.4.3. SPHEROID PREPARATION

Spheroids were fabricated using the Sphericalplate 5D (Kugelmeiers), a 24-well cell culture plate with 12 functional wells each containing 750 microwells. Depending on the desired NIH3T3 cell spheroid size, cell suspensions with concentrations ranging between 1.5-3 x 10^6 cells, determined with a TC20TM automated cell counter (Bio-Rad), were obtained through trypsinization with 0.25% trypsin-EDTA (Gibco), and subsequently deposited in a functional well to form spheroids. For HEK293T cell spheroids, a total of 0.75 x 10^6 cells was seeded in the well. All cells were deposited in a total final volume of 2 mL of corresponding cell media. After deposition, cells sediment in the microwells due to gravity and aggregate into spheroids. The resulting spheroid dimensions depended on the initial cell concentration, which was observed both by eye and from images taken right before running the MPA experiments. All cell spheroids were cultured in the wells for 2 days before aspiration experiments, and the media was refreshed every day. On the day of the experiment, a spheroid suspension was generated by gently washing the spheroids out of the microwells using the culture media already present in the well, and finally taking out 1 mL of this same media with suspended spheroids.

4.4.4. IMMUNOCYTOCHEMISTRY

Bovine type I collagen 2.4 mg/mL (reported purity ≥ 99.9%, Advanced Biomatrix) was prepared for 3D hydrogels as described in the protocol provided by Advanced Biomatrix. The collagen gel was polymerized in µ-Slide 8 well chambers (ibidi) for 45 minutes at 37 °C. NIH3T3 spheroids were pipetted on top of the collagen gels and incubated for 30 minutes at 37 °C and 5% CO_2 to ensure attachment. Medium was removed from the wells and the spheroids were fixated with 4% formaldehyde (Thermo Fisher Scientific) in phosphate buffered saline (PBS, Sigma-Aldrich) for 10 minutes. After fixation, the spheroids were washed three times with PBS and permeabilized with 0.5% Triton-x 100 (Sigma-Aldrich) in PBS for 3 minutes. Spheroids were blocked overnight in 3% bovine serum albumin (BSA, Sigma Aldrich) in PBS with 0.1% Tween 20 (PBST, Sigma-Aldrich) at 4 °C. The next day, spheroids were incubated overnight with mouse anti-alpha-smooth muscle actin 1:500 (A257, Sigma-Aldrich) in 1.5% BSA/PBST at 4 °C. After incubation, spheroids were washed three times with PBST and incubated with goat anti-mouse 568 (a1105, Thermo Fisher Scientific) 1:1000 and Hoechst 33342 (Thermo Fisher Scientific) 1:1000 in PBST for 4 hours at room temperature. After secondary incubation, spheroids were washed three times with PBST. The spheroids were imaged on a Stellaris 8 confocal microscope (Leica), equipped with a supercontinuum white light laser, 405 nm laser and three hybrid detectors. Imaging was performed with the 405 nm laser, a 568 nm laser line and a 20x/0.75 air objective. For both seeding conditions of 1.5 and 3 million cells, three biological replicates were made that were all used for two technical replicates, resulting in n = 6 for each condition.

4.4.5. WESTERN BLOTTING

Spheroids were transferred to Eppendorf tubes and lysed in cold radioimmunoprecipitation buffer (RIPA, Thermo Fisher Scientific). Lysed samples were agitated at 4 °C for 3 hours, sonicated with a bath sonicator (Branson 2510 Ultrasonic Cleaner, Marshall Scientific) for 30 seconds and stored at -20 °C. Laemmli buffer (Bio-Rad) and 4% beta-mercaptoethanol (Sigma) were added to the lysed samples and heated at 95 °C for 5 minutes. SDS-PAGE was performed with Mini-PROTEAN TGX gels (Bio-Rad) using 120V for 80 minutes. Western Blot was executed with a Trans-Blot Turbo Transfer System (Bio-Rad) and Trans-Blot Turbo Mini 0.2 µm PVDF Transfer Packs (Bio-Rad) and membranes were blocked in 5% Bovine Serum Albumin (BSA, Thermo Fisher Scientific) in PBS overnight. Membranes were stained with primary antibodies: mouse anti-alpha smooth muscle actin (#A257, Sigma-Aldrich) 1:500 and rabbit anti-GAPDH (#CST2118S, Bioke) 1:1000 in 5% BSA overnight on a shaker at 4 °C. Membranes were washed thrice with 0.1% Tween (Sigma-Aldrich) in PSB (PSBT) on a shaker, and incubated for 3 hours with secondary antibodies: rabbit anti-mouse HRP (#ab97051, Abcam) 1:5000 and goat anti-rabbit HRP (#ab6728, Abcam) 1:5000 in PBST. Afterwards, membranes were washed thrice with PBST and imaged with an enhanced luminol-based chemiluminescent substrate kit (Thermo Fisher Scientific) on a gel imager (Bio-Rad). For each seeding condition (1.5 and 3 million cells), two biological replicates were made (n = 2). Signal intensities of α-SMA and GAPDH bands were measured in ImageJ with three regions of interest (ROIs), each subtracted from different background spots in the corresponding lane, resulting in six datapoints for each condition [45]. To compare relative α-SMA protein

levels between cells, α-SMA band intensities were normalized to corresponding GAPDH band intensities.

4.4.6. Blebbistatin treatment

Myosin II inhibitor (-) Blebbistatin (Abcam) was dissolved in dimethyl sulfoxide (DMSO) at a stock concentration of 5 mM. Spheroids were incubated in a dilution concentration of 10 μM for at least 3 hours before experiments.

4.4.7. Fabrication of microfluidic aspiration device

The microfluidic micropipette aspiration chip used in this study is an updated version of the chip introduced in our previous study [26]. In contrast to the previous design with round spheroid aspiration pockets, the pockets in this study were squares to minimize the contact area between the spheroids and the walls of the pockets [Supplementary Fig. 4.5(a)]. The updated design is available at:

https://github.com/RubenBoot/HighThroughput_Spheroid_MPA. The multi-layered design contains features with different heights, which were created in two separate photolithography steps using a μMLA laserwriter (Heidelberg Instruments). The final chip was designed as a combination of two slabs of crosslinked polydimethylsiloxane (PDMS) (Sylgard 184, Dow Corning); one slab containing the aspiration channels of 50 μm in height plus the top half of the aspiration pockets, and the other slab having the bottom half of the aspiration pockets. The first layer was created by spinning SU-8 3050 (Kayaku Advanced Materials) to an average thickness of 50 μm. For this, the SU-8 was first spun at 500 rpm for 10 seconds with an acceleration of 100 rpm per second and then at 3500 rpm for 30 seconds with an acceleration of 300 rpm per second. Subsequently, the SU-8 was soft baked at 95 °C for 15 minutes, after which the laserwriter wrote the first layer. The wafer was post baked at 65 °C for 1 minute, then at 95 °C for 5 minutes and developed in SU-8 developer (Propylene glycol monomethyl ether acetate (PGMEA), Sigma-Aldrich). The second layer was created with SU-8 2050 (Kayaku Advanced Materials), and spun to an average thickness of 170 μm. For this height, the SU-8 was first spun at 500 rpm for 10 seconds with an acceleration of 100 rpm per second. Then, it was spun for 30 seconds with an acceleration of 300 rpm per second at 1100 rpm. The thickness was slightly unequal across the whole wafer, as the resist covered both the first half of the pockets from the first layer as well as the empty spot where the other half of the pockets in the second layer would be written. Therefore, one half of the aspiration pockets including the aspiration channel resulted in a thickness of 176 ± 9 μm while the other half of the pocket had a different thickness of 160 ± 20 μm. After spinning, the wafer was soft baked at 65 °C for 5 minutes and then at 95 °C for 30 minutes. The laserwriter wrote the second part of the design, after which the wafer was post baked at 65 °C for 5 minutes, then at 95 °C for 12 minutes and then developed again.

The master wafer was coated with trichloro(1H,1H,2H,2H-perfluorooctyl)silane to allow for easy demolding, and PDMS chips were created using Sylgard 184 at a curing agent ratio of 10:1. Individual chips were cut and 2 mm holes were punched in only one slab of the design for the introduction of tubing using a revolving punch plier (Knipex). To facilitate bonding, both halves of the design were plasma cleaned (Harrick Plasma) for two and a half minutes at 30 W, after which one half was slightly wetted with a droplet

of distilled water to aid the alignment. The two halves were aligned with the help of the alignment arrows at the border of the design and by using an optical microscope (ZEISS Primovert) to check the alignment. Finally, the chips were kept in the oven at 65 °C to bond overnight. After fabrication, they could be stored indefinitely and used on the desired day for experiments.

Modification of microfluidic chip for Supplementary Movies 1 and 2, available online with arXiv publication

When imaging cells inside the microfluidic device consisting out of two bonded PDMS slabs, we could only get the cells in focus with the 5x/NA 0.16 air objective of our inverted fluorescence microscope using an excitation wavelength of 587 nm and an emission wavelength of 610 nm (Zeiss Axio-Observer). As we needed higher resolution to observe individual cells moving in the constriction channel for Movies 1 and 2, we created a modified chip by bonding only the PDMS slab including the constriction channel directly to a glass coverslip. This modified chip was only 175 μm high, with the constriction channel positioned at the bottom of the device. The experiment in Movies 1 and 2 therefore does not represent exactly the same aspiration and retraction conditions as in the rest of the experiments performed in this study, but it does provide valuable insights into the movement of cells within the constriction during aspiration of spheroids.

4.4.8. MICROFLUIDIC ASPIRATION DATA ACQUISITION

The microfluidic aspiration data was acquired following a similar protocol as in our previous study [26]. To prevent cell adhesion to the PDMS walls, the chip was coated before each experiment with 1% Pluronic® F127 (Sigma) in PBS (Gibco) solution and left at room temperature. After 45 minutes, the Pluronic solution was flushed from the chip using the culture medium that matched the cell line used in the experiment. Vials with cell-free culture media were connected to the inlet and outlet of the microfluidic chip using PTFE 008T16-030-200 tubing (Diba Industries, inner diameter 0.3 mm, outer diameter 1.6 mm) and a pressure was applied to the media with a MFCS-EZ pressure controller (Fluigent). After the Pluronic solution, small PDMS debris and possible air bubbles were flushed out, the tube connected to the inlet was gently unplugged from the chip, and a loading reservoir, being a shortened 1 ml pipette tip cut with a scalpel, was plugged into the inlet. Then, the vial connected to the outlet was disconnected from the pressure controller and mounted to a vertical translation stage (Thorlabs, VAP10) with a ruler on the side where the pressure in terms of cmH_2O could be read off from. The average human error in reading off the pressure was defined by the thickness of the lines on the ruler indicating the distances, which was $0.2\ cmH_2O$ (~ 20 Pa). This allowed us to exert a precise hydrostatic aspiration pressure when lowering the stage with the vial compared to the height of the reservoir [Supplementary Fig. 4.5(b)]. Slightly lowering the stage induced a minor flow in the chip towards the aspiration pockets, after which 20 μL of spheroid suspension was pipetted into the reservoir. Guided by the flow, spheroids entered the aspiration pockets, after which the outlet tube was brought back to the original height to stop the flow again. Once ready to perform the experiment, the vial was manually lowered to the chosen aspiration pressure, thereby inducing spheroid tongue aspiration.

The inlet reservoir volume remained constant during the duration of the experiment, confirming that there was no leakage at the corners of the squared aspiration channels and spheroids fully blocked the channels. A clear flow was visible in the constriction channel whenever a spheroid did not fully block it, and the rare experiments where this occurred were not used for analysis.

Brightfield images of spheroid protrusions entering the constriction channels were captured on an inverted fluorescence microscope (Zeiss Axio-Observer) using a 5x/NA 0.16 air objective and ORCA Flash 4.0 V2 (Hamamatsu) digital camera with a resolution of 2048×2048 px^2. The NIH3T3 spheroids were imaged every 5 seconds for 10 minutes (for the short 10 min measurements at 2000 Pa) and then every 30 seconds for a remainder of 20 minutes (when doing a 30 min measurement at 1000 or 1200 Pa). The much softer HEK293T spheroids were imaged every 5 seconds for 5 minutes. We ensured that the full aspiration curve of the tongue was captured by starting the image acquisition before lowering the outlet tube. After the aspiration measurement, a retraction measurement was started by increasing the height of the outlet vial back to a remaining 2 cmH$_2$O of aspiration pressure to keep the spheroids in the pockets while the protrusion tongues retract. For the HEK293T spheroids, a remaining pressure of 0.5 cmH$_2$O was maintained during retraction. The retraction measurement was captured using the same conditions as for the aspiration measurement. Only for Supplementary Fig. 4.8, NIH3T3 cell spheroids were aspirated for 30 minutes at 1000 Pa, and then left to retract for 2 hours at 200 Pa, from which the first 10 minutes an image was captured every 5 seconds and then for the next 110 minutes every 30 seconds. At the end of the experiment, spheroids were pushed out of the pockets and flown back towards the inlet by raising the outlet vial above the reservoir. There, the spheroids were removed from the chip by pipetting them up through the reservoir. This way, new spheroids could be inserted to start a new measurement with the same chip. All experiments were conducted at 37 °C and 5% CO$_2$ using a stage top incubator (ibidi GmbH). Chips were used for multiple successive runs and were always discarded at the end of the day.

Modification for acquisition of Supplementary Movies 1 and 2, available online with arXiv publication

For both Supplementary Movies, we recorded the experiment using a 40x/NA 1.3 oil objective with the same inverted fluorescence microscope. For movie 1, we started recording after ±10 minutes of aspiration at 1000 Pa to capture the viscous retraction, and took an image every 10 second for 20 minutes. For the retraction in movie 2, we also took an image every 10 seconds for 20 minutes at a remaining pressure of 200 Pa. Both movies with mCherry-transfected nuclei were captured at an excitation wavelength of 587 nm, emission wavelength of 610 nm, a light source intensity of 2% and an exposure time of 80 ms.

4.4.9. Data analysis of spheroid protrusion creep

The creep length of the spheroid protrusion edges over time was extracted from the experimental images using Fiji (https://imagej.net/software/fiji/) and a custom-written Python script (which is available at:

https://github.com/RubenBoot/HighThroughput_Spheroid_MPA/blob/main/ SpheroidAspiration_AnalysisScript.py) previously introduced and explained in [26]. In short, the brightfield time-lapse images are cropped to the region of interest and binarized (using the Thresholding function from Fiji) to provide a clear contrast between the protrusion edge and the surrounding channel. The script detects the distance from the protrusion edge to the start of the constriction channel and writes all results in a Microsoft Excel file alongside the time step per image. If the protrusion edge did not maintain its integrity due to cells breaking off, or if spheroids did not retain a constant volume and roundness during aspiration, they were omitted from the analysis.

4.4.10. THEORETICAL FITTING OF VISCOELASTIC PARAMETERS AND DERIVATION OF γ

The viscoelastic creep curve of cell spheroids was fitted with a modified Maxwell model, being a dashpot ξ_t in series with a Kelvin-Voigt element consisting out of a spring k_1 in parallel with a spring k_2 and dashpot ξ_c in series [24–26]. Here, k_1 represents the elasticity of the spheroid, k_2 accounts for the initial jump in $L(t)$, ξ_c is a local friction coefficient associated with the rising time of the elastic deformation and ξ_t represents the viscous dissipation of the flowing spheroid. According to the Maxwell model, the creep length $L(t)$ is given by:

$$L(t) = \frac{f}{k_1}\left(1 - \frac{k_2}{k_1 + k_2} e^{\frac{-t}{\tau_c}}\right) + \frac{f}{\xi_t} t \tag{4.1}$$

where f is the aspiration force and τ_c is the rising time of the elastic deformation δ. Therefore, the model has four fitting parameters: $\delta = f/k_1$, $\dot{L}_\infty = f/\xi_t$, $\beta = k_2/(k_1 + k_2)$ and τ_c.

As described in the main text, for a cylindrical micropipette with a radius R_p and an applied underpressure ΔP, the aspiration force is $f = \pi R_p^2(\Delta P - \Delta P_c)$, with ΔP_c the critical pressure below which the spheroid does not aspirate into the pipette. For times that are long enough such that spheroid protrusion advancement has entered the viscous regime, this aspiration force is balanced by a dissipative force due to viscous flow into the pipette (assuming there is no friction between the spheroid and the wall of the constriction):

$$\pi R_p^2(\Delta P - \Delta P_c) = 3\pi^2 \eta R_p \dot{L}_\infty, \tag{4.2}$$

where η is the viscosity of the spheroid [46]. For aspiration, the stress is $\sigma = \Delta P - \Delta P_c$ and for retraction $\sigma = \Delta P_c - \Delta P_{remaining}$ (as we left a minor underpressure $\Delta P_{remaining}$ = 200 Pa during our retraction measurements to keep the spheroid protrusions in the constrictions). Thus, we can rewrite Eq. (4.2) as:

$$\dot{L}_\infty^a = \frac{R_p(\Delta P - \Delta P_c)}{3\pi\eta_a}, \tag{4.3}$$

$$\dot{L}_\infty^r = \frac{R_p(\Delta P_c - \Delta P_{remaining})}{3\pi\eta_r}, \tag{4.4}$$

with $\dot{L^a_\infty}$, η_a and $\dot{L^r_\infty}$, η_r the flow rates and viscosities during aspiration and retraction, respectively. Assuming that $\eta_a = \eta_r$, the critical pressure ΔP_c is:

$$\Delta P_c = [(\Delta P - \Delta P_{remaining})\frac{\dot{L^r_\infty}}{\dot{L^a_\infty} + \dot{L^r_\infty}}] + \Delta P_{remaining}, \tag{4.5}$$

Similarly, the spheroid viscosity $\eta = \eta_a = \eta_r$ can be derived independently from ΔP_c by summing up Eq. (4.3) and Eq. (4.4) into:

$$\eta = \frac{R_p(\Delta P - \Delta P_{remaining})}{3\pi(\dot{L^a_\infty} + \dot{L^r_\infty})}, \tag{4.6}$$

From the Young-Laplace law, we can thus obtain the spheroid surface tension γ through:

$$\Delta P_c = 2\gamma(\frac{1}{R_p} - \frac{1}{R}), \tag{4.7}$$

with R the radius of the spheroid.

Since the microfluidic device used in our study has squared constrictions, the micropipette radius R_p needs to be corrected. The effective channel radius R_{eff} in our study is given by:

$$R^4_{eff} = \frac{2}{3\pi}\frac{W \times H^3}{(1 + \frac{H}{W})^2 \times f^*}, \tag{4.8}$$

with W and H being the width and height of the constriction and f^* being a function of the aspect ratio (H/W), given by equations (7) and (19) of Son [27, 28].

4.4.11. STATISTICAL ANALYSIS
Two-sided t-tests were executed using the TTEST function in Microsoft Excel, and p values below 0.05 were considered to be significant. The average human error in reading off the aspiration pressure when manually lowering the outlet vial is 0.2 cmH$_2$O (~ 20 Pa), defined by the thickness of the lines on the ruler indicating the distances. The error in dimensions of the aspiration channel was measured with a Dektak Stylus Profiler (Bruker) and determined to be 5 μm. Error bars in the figures display the standard error of the mean unless indicated otherwise, and are always based on at least three independent days of experiments.

4

APPENDIX
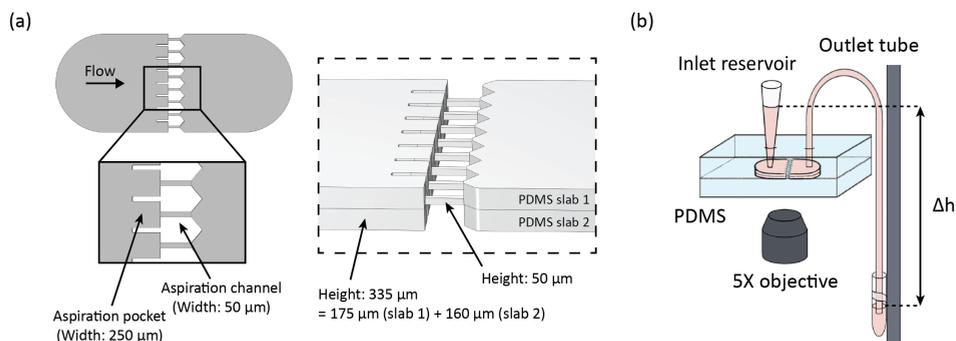# 4.A. SUPPLEMENTARY FIGURES

(a)

(b)

Figure 4.5: Overview of the microfluidic chip. (a) 3D schematic showing (left) the top view of the design with a close-up on the 8 parallel pockets and aspiration channels and channels widths indicated, and (right) a tilted side view showing the height of the chip when bonding the two separate PDMS slabs together with channel heights indicated. (b) Schematic of the experimental set-up, reused from [26]. Spheroids enter the PDMS chip through a pipette cone serving as the inlet reservoir. Aspiration is performed with hydrostatic pressure by changing the height Δh of the outlet vial that is mounted to a vertical rod. Note that the drawing is not to scale: in reality, the vertical rod was placed next to the microscope, requiring a longer outlet tube to bridge the distance between the chip and the outlet vial. The flowing spheroid protrusions were imaged in bright field with an inverted microscope using a 5× objective.

(a)

(b)
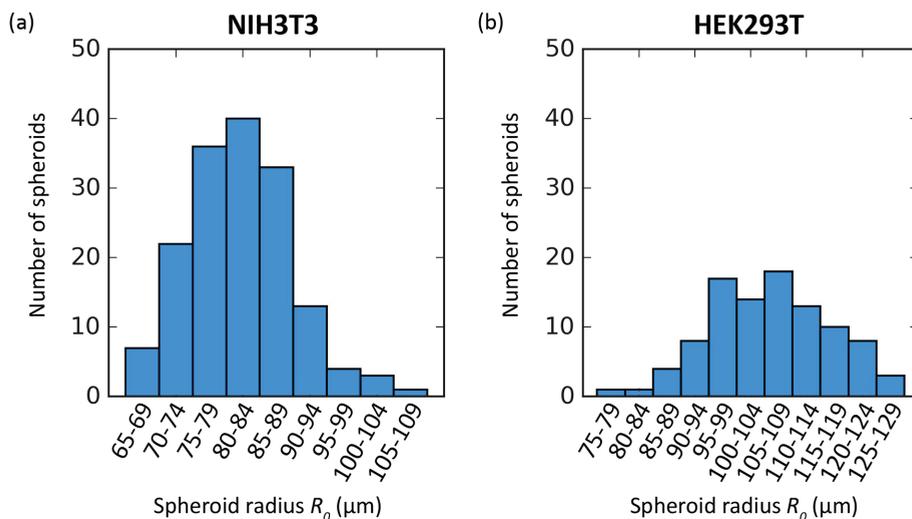
Figure 4.6: Spheroid size distribution for the spheroids measured throughout all experiments. Histograms of the number of fabricated spheroids used in this study, binned for spheroid radius R_0, for (a) the NIH3T3 spheroids and (b) the HEK293T spheroids.
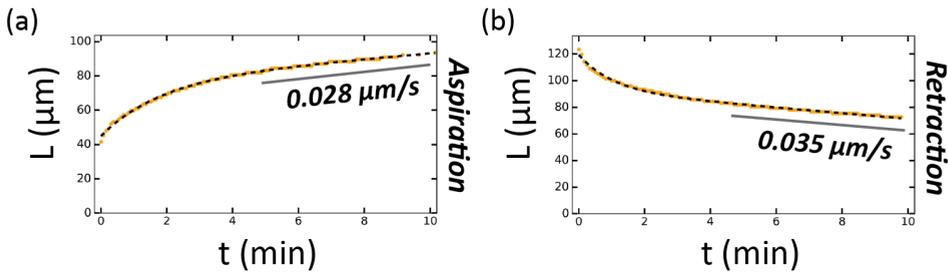
Figure 4.7: Tissue viscoelastic relaxation of NIH3T3 fibroblast spheroids is time-dependent. The first 10 minutes of the aspiration (a) and retraction (b) of the experiment in Fig. 4.1(b), with viscous creep rates derived by only fitting these first 10 minutes. Yellow: data points, dashed black line: modified Maxwell model fit from Eq. (4.1).
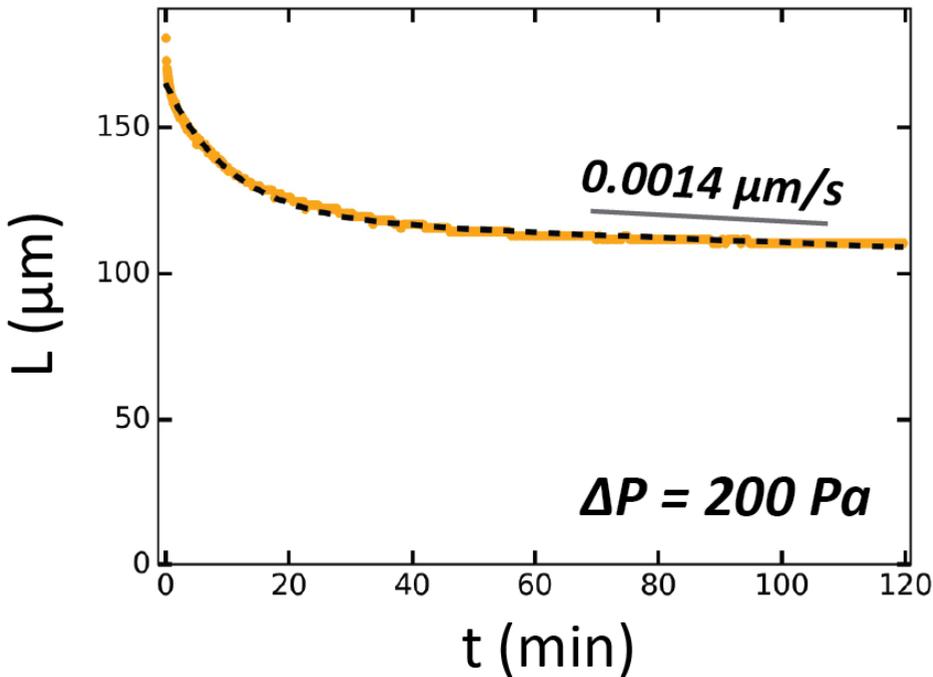

Figure 4.8: Two hour long retraction plot. The decreasing creep length of a NIH3T3 spheroid protrusion when retracting for two hours at a remaining pressure of 200 Pa. First, the spheroid was aspirated for 30 minutes at 1200 Pa. The derived creep rate $\dot{L}_\infty^r$ is an order of magnitude lower than when fitting the first 30 minutes of retraction [see Fig. 4.1(b) in the main text, here for a different measurement], suggesting that the critical pressure ΔP_c decreases over time. Yellow: data points, dashed black line: modified Maxwell model fit from Eq. (4.1).
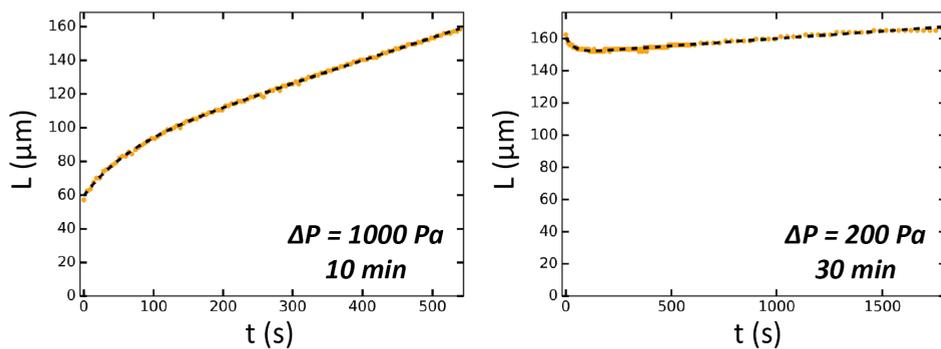
Figure 4.9: Aspiration and retraction measurements of a Blebbistatin-treated NIH3T3 spheroid. Aspiration at 1000 Pa for 10 min (left) and retraction at a remaining pressure of 200 Pa for 30 min (right) for a Blebbistatin-treated NIH3T3 spheroid. During retraction, the spheroid elastically retracts at first and then aspirates again. This challenges the assumption that spheroid retraction is governed by one single critical pressure ΔP_c, as it now seems to depend on both retractile elastic properties and the collective flow of the spheroid tongue as a whole, potentially each having a separate critical pressure. Yellow: data points, dashed black line: modified Maxwell model fit from Eq. (4.1).
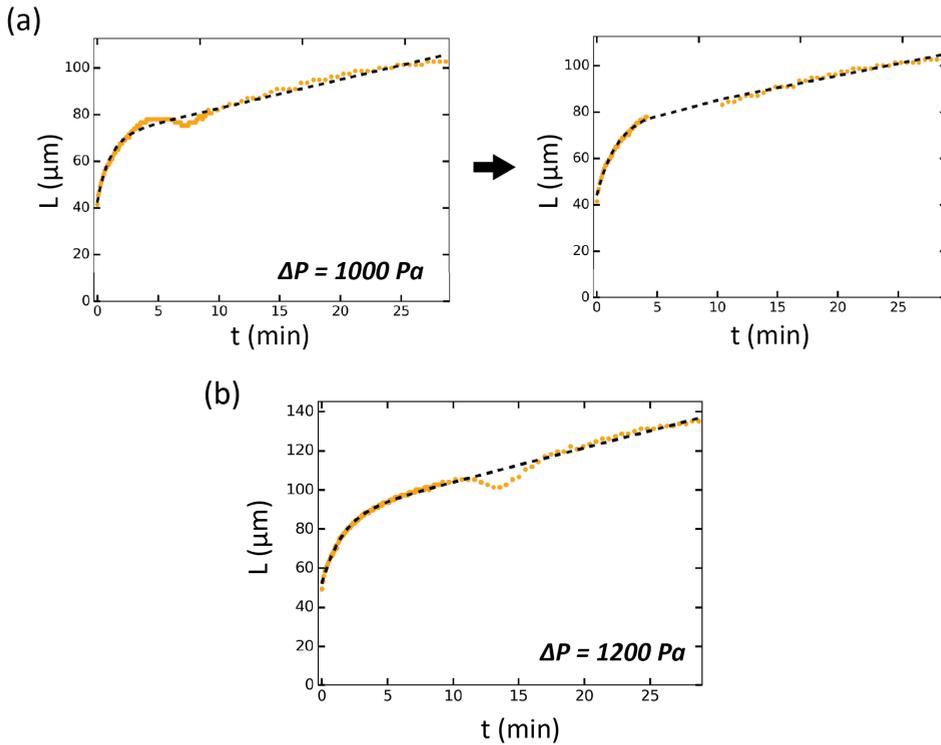
Figure 4.10: Shivering occurs at moderate pressures when aspirating NIH3T3 spheroids. For some measurements, the spheroid protrusion "shivered" in the constriction, meaning it briefly contracted and then re-expanded to its previous length. This effect only occurred at moderate aspiration pressures of 1000 and 1200 Pa, and not at the highest pressure used of 2000 Pa. (a) The aspiration creep curve for an aspiration measurement at 1000 Pa (yellow) fitted with the modified Maxwell model in Eq. (4.1) (dashed black line). When the shiver prevented the fit from accurately following the linear viscous part of the plot (left), the shiver was manually cropped from the data (right) and the parameter values obtained from the fit to the adapted creep curve were used in further downstream analysis. (b) The aspiration creep curve for an aspiration measurement at 1200 Pa fitted with the modified Maxwell model, demonstrating an example of shivering that did not significantly affect the modified Maxwell model fit to the linear viscous response.
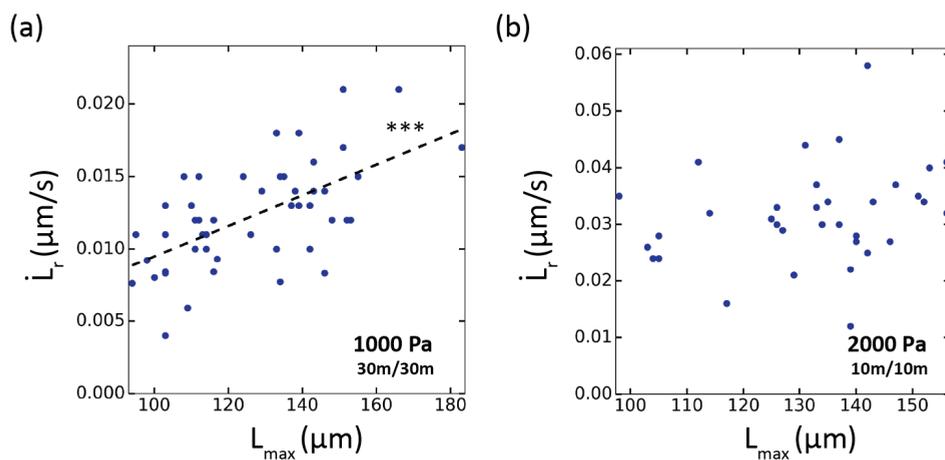
4

Figure 4.11: At long enough timescales, spheroid relaxation is deformation-dependent. The retraction flow velocity $\dot{L}_\infty^r$ plotted versus L_{max} for NIH3T3 spheroids aspirated at (a) 1000 Pa (30 min aspiration, 30 min retraction, indicated as 30m/30m, n = 48) and (b) 2000 Pa (10 min aspiration, 10 min retraction, indicated as 10m/10m, n = 35). At the short timescale of 10 minutes for 2000 Pa, no significant linear trend is present in the data. ***, p < 0.001.
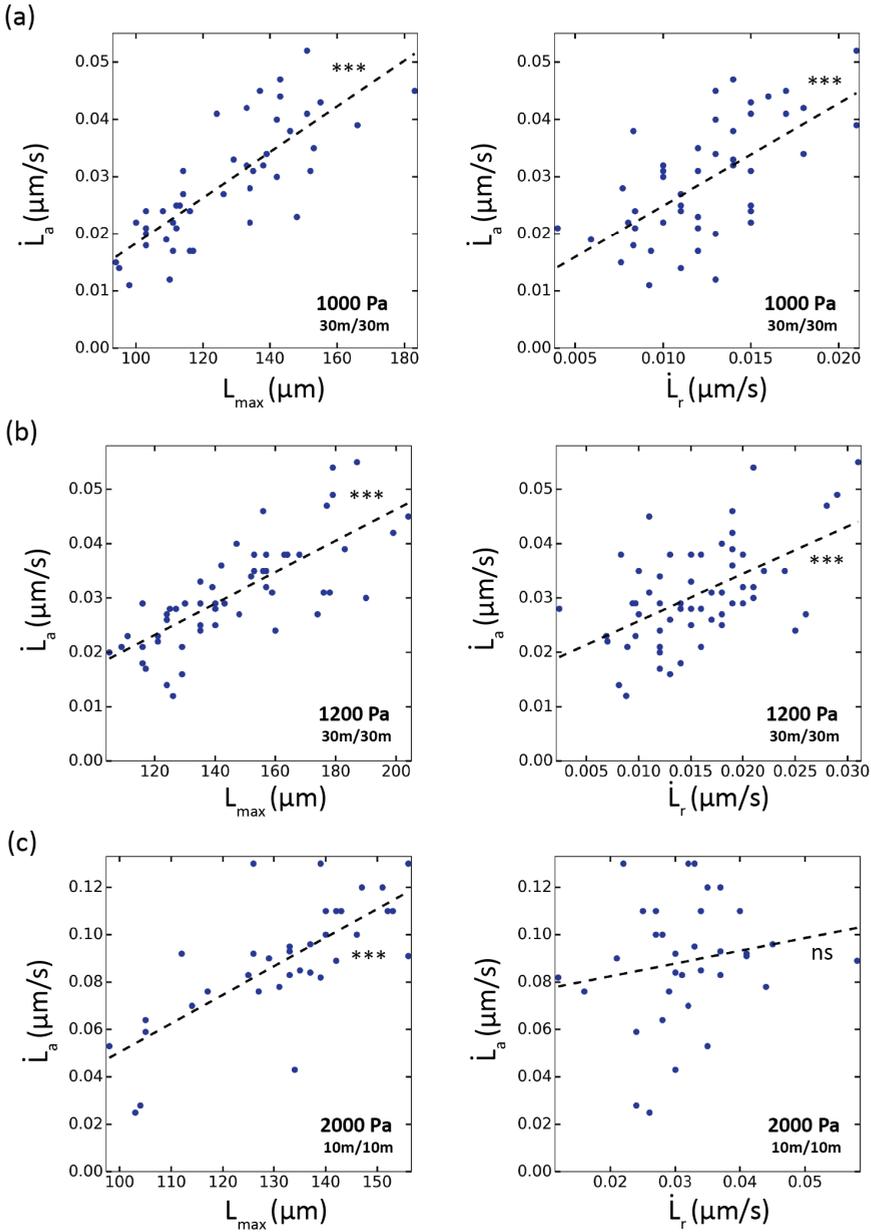
Figure 4.12: The viscous creep rate $\dot{L}_\infty^a$ and $\dot{L}_\infty^r$ for NIH3T3 spheroid protrusions are in direct proportion to each other. The aspiration flow velocity $\dot{L}_\infty^a$ plotted versus L_{max} (left) and $\dot{L}_\infty^r$ (right) for NIH3T3 spheroids aspirated at (a) 1000 Pa (30 min aspiration, 30 min retraction, n = 48), (b) 1200 Pa (30 min aspiration, 30 min retraction, n = 57) and (c) 2000 Pa (10 min aspiration, 10 min retraction, n = 35). At 2000 Pa, no significant linear trend is present between $\dot{L}_\infty^a$ and $\dot{L}_\infty^r$, potentially because the derived $\dot{L}_\infty^r$ after 10 minutes was still partially elastically governed. ***, p < 0.001 and ns is nonsignificant.
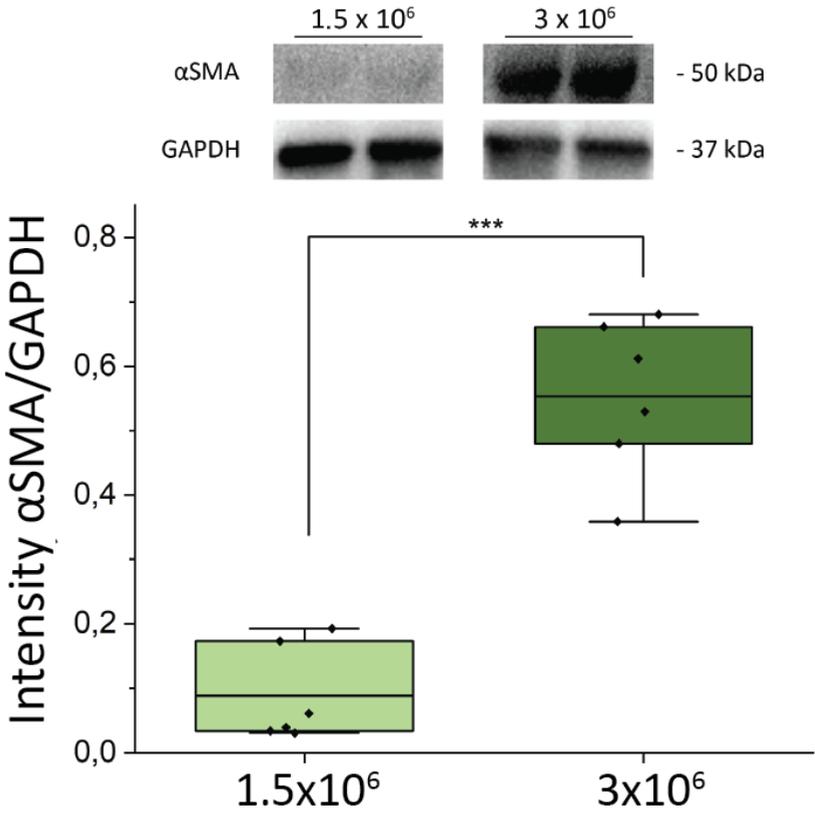
Figure 4.13: Western blots of α-SMA in NIH3T3 spheroids for different seeding conditions. Relative protein levels of α-SMA in respect to GAPDH for NIH3T3 spheroids seeded with 1.5x10^{6} and 3x10^{6} cells/well. ***, p < 0.001.
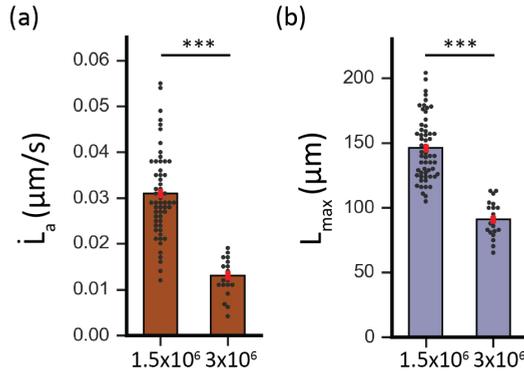
Figure 4.14: NIH3T3 spheroids seeded at a larger cell density display less deformability. Histograms comparing NIH3T3 spheroids aspirated at 1200 Pa at a seeding density of 1.5×10^6 cells (30 min aspiration, 30 min retraction, n = 57) and a seeding density of 3×10^6 cells (30 min aspiration, 30 min retraction, n = 19). Retraction was performed at 200 Pa. (a) The aspiration flow velocity $\dot{L}_\infty^a$ and (b) resulting creep length at the end of the aspiration L_{max} are compared. ***, p < 0.001. Error bars are SEM.
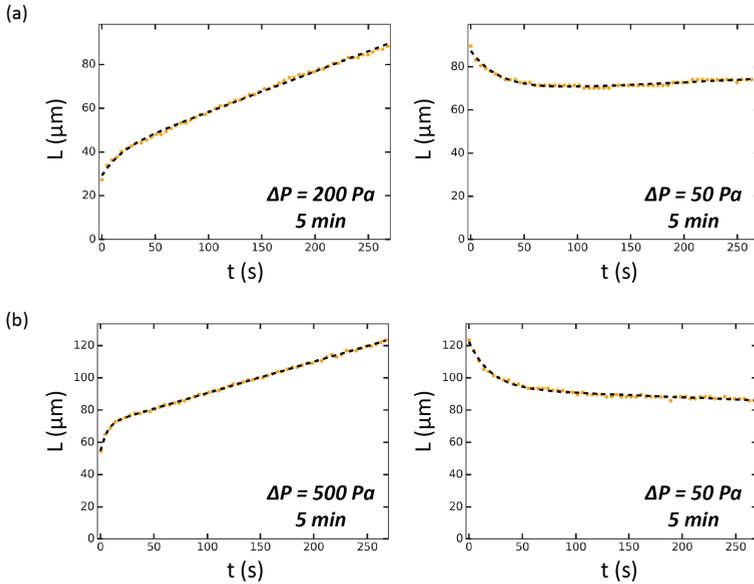

Figure 4.15: Aspiration and retraction measurements of two HEK293T spheroids. (a) Aspiration at 200 Pa for 5 min (left) and retraction at a remaining pressure of 50 Pa for 5 min (right) for a HEK293T spheroid. During retraction, the spheroid elastically retracts at first and then aspirates again, demonstrating how the critical pressure ΔP_c is negligibly small. (b) Aspiration at 500 Pa for 5 min (left) and retraction at a remaining pressure of 50 Pa for 5 min (right) for a HEK293T spheroid. During retraction, the spheroid now retracts with a viscous regime, showing a deformation-dependent retraction as cells deformed further into the constriction at this larger pressure. Yellow: data points, dashed black lines: modified Maxwell model fits from Eq. (4.1).
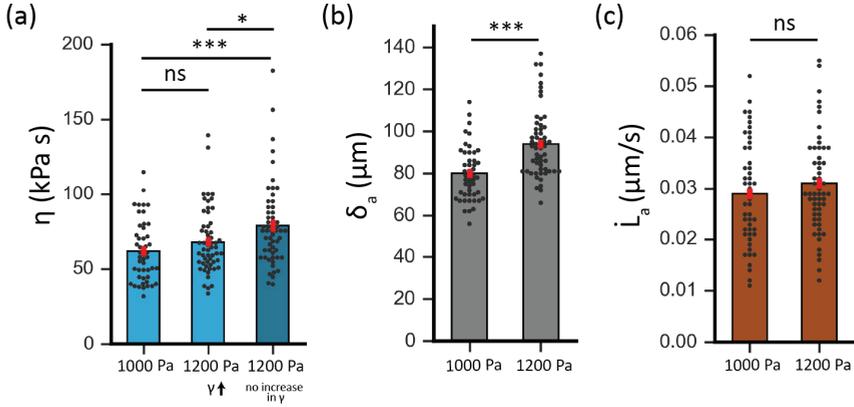
Figure 4.16: Viscosity η of NIH3T3 spheroids is pressure-dependent when assuming that surface tension γ does not reinforce at larger pressures. Histograms comparing derived mechanical parameters for NIH3T3 spheroids aspirated at 1000 Pa (30 min asp, 30 min retr, n = 48) and at 1200 Pa (30 min asp, 30 min retr, n = 57). Retraction was performed at a remaining pressure of 200 Pa. (a) The viscosity η at 1000 Pa [derived using Eq. (4.6)] is compared to the viscosity at 1200 Pa assuming surface tension has increased [derived using Eq. (4.6)] and when assuming that the surface tension has remained unchanged [derived using Eq. (4.3) and filling in ΔP_c from 1000 Pa measurements]. (b) The elastic deformation δ_a at 1000 and 1200 Pa. (c) The aspiration flow velocity L_∞^a at 1000 and 1200 Pa. *, p < 0.05, ***, p < 0.001 and ns is nonsignificant. Error bars are SEM.
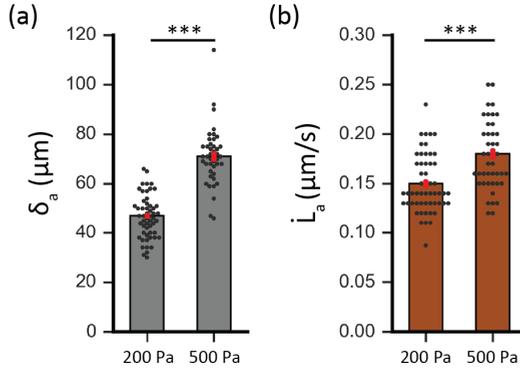
Figure 4.17: Different proportional change in elastic and viscous deformation for HEK293T spheroids under increasing force. Histograms comparing HEK293T spheroids aspirated at 200 Pa (5 min aspiration, 5 min retraction, n = 54) and at 500 Pa (5 min aspiration, 5 min retraction, n = 43). Retraction was performed at 50 Pa. (a) The elastic deformation δ_a and (b) the aspiration flow velocity $L_\infty^{\dot{a}}$ are compared. ***, p < 0.001. Error bars are SEM.
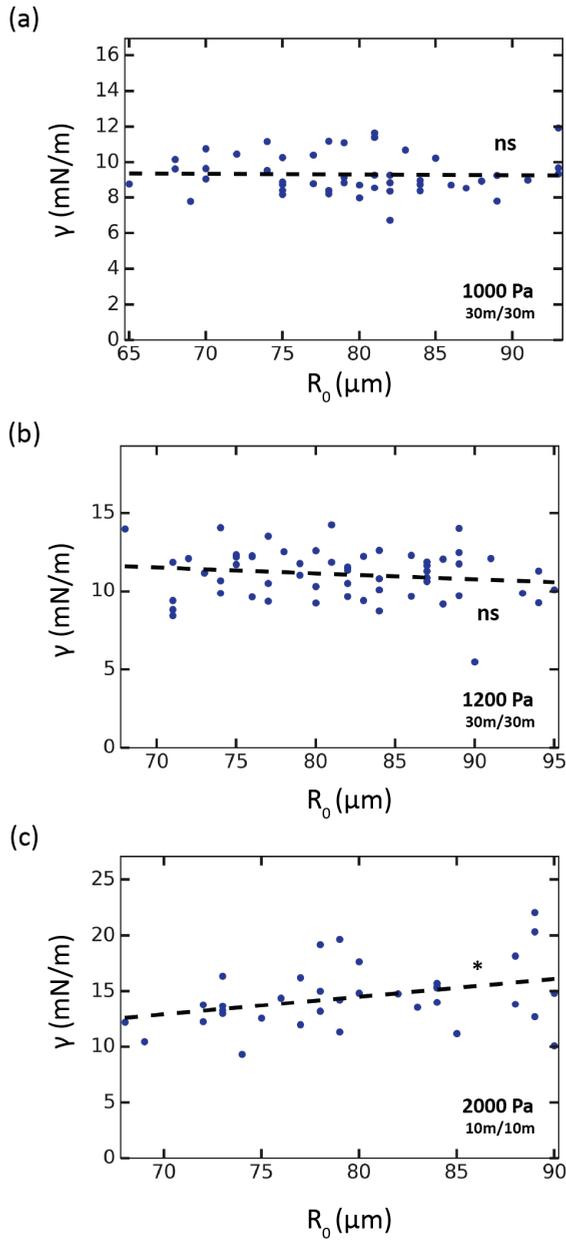
Figure 4.18: At the fabricated spheroid size range, no size-dependency in surface tension γ was observed. The surface tension γ plotted versus R_0 for NIH3T3 spheroids aspirated at (a) 1000 Pa (30 min aspiration, 30 min retraction, n = 48), (b) 1200 Pa (30 min aspiration, 30 min retraction, n = 57) and (c) 2000 Pa (10 min aspiration, 10 min retraction, n = 35). No clear, significant trend was observed. *, p < 0.05 and ns is nonsignificant.

4.B. SUPPLEMENTARY TABLE

	$\dot{L}^a_\infty$ (µm/s)	$\dot{L}^r_\infty$ (µm/s)	L_{max} (µm)	γ (mN/m)	n
No shiver 1000 Pa	0.030	0.011	128	8.8	18
Shiver 1000 Pa	0.028	0.013	126	9.6	30
t-test 1000 Pa	ns	ns	ns	*	
No shiver 1200 Pa	0.034	0.016	148	10.8	31
Shiver 1200 Pa	0.027	0.015	143	11.5	26
t-test 1200 Pa	**	ns	ns	ns	

Table 4.1: Comparison for the NIH3T3 cell spheroids of derived values for the viscous creep rates during aspiration $\dot{L}^a_\infty$ and retraction $\dot{L}^r_\infty$, the total deformation length after 30 min of aspiration L_{max}, and the surface tension γ for creep curves where shivering did or did not occur ('shiver'/'no shiver'), for an amount of n spheroids. The t-test demonstrates how significant the occurrence of shivering influenced the derived parameters by comparing the two sets of data at each separate ΔP of 1000 and 1200 Pa. *, p < 0.05, **, p < 0.01, ns is nonsignificant.

4.C. SUPPLEMENTARY MOVIES

Movie 1: NIH3T3 spheroid with mCherry-transfected nuclei aspirated at 1000 Pa in a modified microfluidic device allowing for high-resolution imaging. A fluorescent video of a NIH3T3 cell spheroid being aspirated under a hydrostatic pressure of ΔP = 1000 Pa for 20 minutes. The video was started after the spheroid had already aspirated for ±10 minutes, thus capturing the viscous part of the aspiration. Near the end of the video, the spheroid tongue slightly retracts due to the "shivering" effect that occurs in this experiment. We do not observe any cells slipping past each other during viscous deformation. Scale bar is 20 µm.

Movie 2: NIH3T3 spheroid with mCherry-transfected nuclei retracting with a remaining pressure of 200 Pa in a modified microfluidic device allowing for high-resolution imaging. The follow-up on Movie 1, where the retraction of the same NIH3T3 cell spheroid at a remaining pressure of 200 Pa is recorded for 20 minutes. The video is started right before bringing back the pressure from 1000 to 200 Pa. Again, we do not observe any cells slipping past each other. Scale bar is 20 µm.

BIBLIOGRAPHY

1. Boot, R. C. *et al.* Cell spheroid viscoelasticity is deformation-dependent. *arXiv,* 1–6. arXiv: arXiv:2401.17155v1 (2024).

2. Hahn, C. & Schwartz, M. A. Mechanotransduction in vascular physiology and atherogenesis. *Nature Reviews Molecular Cell Biology* **10,** 53–62. ISSN: 14710072 (2009).

3. Mammoto, T. & Ingber, D. E. Mechanical control of tissue and organ development. *Development* **137,** 1407–1420 (2010).

4. Brugués, A. *et al.* Forces driving epithelial wound healing. *Nat Phys* **10,** 683–690 (2014).

5. Discher, D. E., Mooney, D. J. & Zandstra, P. W. Growth factors, matrices, and forces combine and control stem cells. *Science* **324,** 1673–1677. ISSN: 00368075 (2009).

6. Nia, H. T. *et al.* Solid stress and elastic energy as measures of tumour mechanopathology. *Nat Biomed Eng* **1,** 1–25 (2016).

7. Nia, H. T., Munn, L. L. & Jain, R. K. Physical traits of cancer. *Science* **370,** eaaz0868. ISSN: 10959203 (2020).

8. Galie, P. A., Georges, P. C. & Janmey, P. A. How do cells stiffen? *The Biochemical journal* **479,** 1825–1842. ISSN: 14708728 (2022).

9. Friedl, P., Wolf, K. & Lammerding, J. Nuclear mechanics during cell migration. *Current Opinion in Cell Biology* **23,** 55–64. ISSN: 09550674. http://dx.doi.org/10.1016/j.ceb.2010.10.015 (2011).

10. Schiele, N. R. *et al.* Actin cytoskeleton contributes to the elastic modulus of embryonic tendon during early development. *Journal of Orthopaedic Research* **33,** 874–881. ISSN: 1554527X (2015).

11. Heisenberg, C. P. & Bellaïche, Y. Forces in tissue morphogenesis and patterning. *Cell* **153,** 948–962. ISSN: 10974172 (2013).

12. Han, Y. L. *et al.* Cell swelling, softening and invasion in a three-dimensional breast cancer model. *Nature Physics* **16,** 101–108. ISSN: 17452481 (2020).

13. Jakab, K. *et al.* Relating Cell and Tissue Mechanics : Implications and Applications. *Developmental Dynamics* **237,** 2438–2449 (2008).

14. Kosheleva, N. V. *et al.* Cell spheroid fusion: beyond liquid drops model. *Scientific Reports* **10,** 1–15. ISSN: 20452322. https://doi.org/10.1038/s41598-020-69540-8 (2020).

15. Grosser, S. *et al.* Cell and Nucleus Shape as an Indicator of Tissue Fluidity in Carcinoma. *Physical Review X* **11,** 011033. https://journals.aps.org/prx/abstract/10.1103/PhysRevX.11.011033 (2021).

16. Gonzalez-Rodriguez, D., Guevorkian, K., Douezan, S. & Brochard-Wyart, F. Soft Matter Models of Developing. *Science* **82,** 910–917 (2012).

17. Boot, R. C., Koenderink, G. H. & Boukany, P. E. Spheroid mechanics and implications for cell invasion. *Advances in Physics: X* **6,** 1978316. https://doi.org/10.1080/23746149.2021.1978316 (2021).

18. Foty, R. A., Pfleger, C. M., Forgacs, G. & Steinberg, M. S. Surface tensions of embryonic tissues predict their mutual envelopment behavior. *Development* **122,** 1611–1620. ISSN: 09501991 (1996).

19. Ryan, P. L., Foty, R. A., Kohn, J. & Steinberg, M. S. Tissue spreading on implantable substrates is a competitive outcome of cell-cell vs. cell-substratum adhesivity. *Proceedings of the National Academy of Sciences of the United States of America* **98,** 4323–4327. ISSN: 00278424 (2001).

20. Schötz, E. M. *et al.* Quantitative differences in tissue surface tension influence zebrafish germ layer positioning. *HFSP Journal* **2,** 42–56. ISSN: 19552068 (2008).

21. Foty, R. A. & Steinberg, M. S. The differential adhesion hypothesis: A direct evaluation. *Developmental Biology* **278,** 255–263. ISSN: 00121606 (2005).

22. Brodland, G. W. The Differential Interfacial Tension Hypothesis (DITH): A comprehensive theory for the self-rearrangement of embryonic cells and tissues. *Journal of Biomechanical Engineering* **124,** 188–197. ISSN: 01480731 (2002).

23. Manning, M. L., Foty, R. A., Steinberg, M. S. & Schoetz, E. M. Coaction of intercellular adhesion and cortical tension specifies tissue surface tension. *Proceedings of the National Academy of Sciences of the United States of America* **107,** 12517–12522. ISSN: 00278424 (2010).

24. Guevorkian, K., Colbert, M.-J., Durth, M., Dufour, S. & Brochard-Wyart, F. Aspiration of Biological Viscoelastic Drops. *Physical Review Letters* **104,** 1–4 (2010).

25. Yousafzai, M. S. *et al.* Active Regulation of Pressure and Volume Defines an Energetic Constraint on the Size of Cell Aggregates. *Physical Review Letters* **128,** 48103. ISSN: 0031-9007. https://doi.org/10.1103/PhysRevLett.128.048103 (2022).

26. Boot, R. C. *et al.* High-throughput mechanophenotyping of multicellular spheroids using a microfluidic micropipette aspiration chip. *Lab on a Chip* **23,** 1768–1778. http://arxiv.org/abs/2211.10182 (2023).

27. Davidson, P. M. *et al.* High-throughput microfluidic micropipette aspiration device to probe time-scale dependent nuclear mechanics in intact cells. *Lab on a Chip* **19,** 3652–3663. ISSN: 14730189 (2019).

28. Son, Y. Determination of shear viscosity and shear rate from pressure drop and flow rate relationship in a rectangular channel. *Polymer* **48,** 632–637 (2007).

29. Guevorkian, K., Gonzalez-rodriguez, D., Carlier, C., Dufour, S. & Brochard-Wyart, F. Mechanosensitive shivering of model tissues under controlled aspiration. *PNAS* **108,** 13387–13392 (2011).

30. Scanlon, C. S., Van Tubergen, E. A., Inglehart, R. C. & D'Silva, N. J. Biomarkers of epithelial-mesenchymal transition in squamous cell carcinoma. *Journal of Dental Research* **92,** 114–121. ISSN: 00220345 (2013).

31. Hinz, B., Celetta, G., Tomasek, J. J., Gabbiani, G. & Chaponnier, C. Alpha-smooth muscle actin expression upregulates fibroblast contractile activity. *Molecular Biology of the Cell* **12,** 2730–2741. ISSN: 10591524 (2001).

32. Sarrió, D. *et al.* Epithelial-mesenchymal transition in breast cancer relates to the basal-like phenotype. *Cancer Research* **68,** 989–997. ISSN: 00085472 (2008).

33. Doolin, M. T., Smith, I. M. & Stroka, K. M. Fibroblast to myofibroblast transition is enhanced by increased cell density. *Molecular Biology of the Cell* **32,** 1–9. ISSN: 19394586 (2021).

34. Yu, M. *et al.* Coherent Timescales and Mechanical Structure of Multicellular Aggregates. *Biophysical Journal* **114,** 2703–2716. ISSN: 15420086. https://doi.org/10.1016/j.bpj.2018.04.025 (2018).

35. Janmey, P. A. & Weitz, D. A. Dealing with mechanics: Mechanisms of force transduction in cells. *Trends in Biochemical Sciences* **29,** 364–370. ISSN: 09680004 (2004).

36. Martino, F., Perestrelo, A. R., Vinarský, V., Pagliari, S. & Forte, G. Cellular mechanotransduction: From tension to function. *Frontiers in Physiology* **9,** 1–21. ISSN: 1664042X (2018).

37. Sbrana, F. *et al.* Role for stress fiber contraction in surface tension development and stretch-activated channel regulation in C2C12 myoblasts. *Am J Physiol Cell Physiol* **295,** 160–172 (2008).

38. Delanoe-Ayari, H., Kurdi, R. A., Vallade, M., Gulino-Debrac, D. & Riveline, D. Membrane and acto-myosin tension promote clustering of adhesion proteins. *PNAS* **101,** 2229–2234 (2004).

39. Ingber, D. E. Cellular mechanotransduction: putting all the pieces together again. *The FASEB Journal* **20,** 811–827. ISSN: 0892-6638 (2006).

40. Kaunas, R. & Deguchi, S. Multiple Roles for Myosin II in Tensional Homeostasis Under Mechanical Loading. *Cellular and Molecular Bioengineering* **4,** 182–191 (2011).

41. Foty, R. A. & Steinberg, M. S. Cadherin-mediated cell-cell adhesion and tissue segregation in relation to malignancy. *Int. J. Dev. Biol.* **48,** 397–409 (2004).

42. Pawlizak, S. *et al.* Testing the differential adhesion hypothesis across the epithelial-mesenchymal transition. *New Journal of Physics* **17,** 083049. ISSN: 13672630 (2015).

43. Marmottant, P. *et al.* The role of fluctuations and stress on the effective viscosity of cell aggregates. *PNAS* **106,** 17271–17275 (2009).

44. David, R. *et al.* Tissue cohesion and the mechanics of cell rearrangement. *Development* **141,** 3672–3682 (2014).

45. Schindelin, J. *et al.* Fiji: An open-source platform for biological-image analysis. *Nature Methods* **9,** 676–682. ISSN: 15487091 (2012).

4

46. Guevorkian, K., Brochard-Wyart, F. & Gonzalez-Rodriguez, D. *Flow dynamics of 3D multicellular systems into capillaries* 193–223. ISBN: 9780128203101. http://dx.doi.org/10.1016/B978-0-12-820310-1.00008-2 (Academic Press, New York, 2021).

4

5

USING MICROFLUIDIC DEVICES TO UNDERSTAND THE IMPACT OF CELL DEFORMABILITY ON CONFINED CANCER CELL MIGRATION

Life before death.

Brandon Sanderson, in *The Stormlight Archive.*

Cancer cells present in the blood circulation of patients, termed circulating tumour cells (CTCs), have a significantly higher metastatic potential when travelling together as clusters instead of single cells. These aggregates of 2 to 20 cells are able to squeeze collectively through narrow vessels, eventually forming metastatic lesions at distant sites. In order to study the influence of cell deformability on cell (cluster) migration through vessel-sized constrictions, we have designed two microfluidic platforms. The first device allows for high-throughput cell deformability measurements, by continuously flowing cells and squeezing them through narrow constrictions. We find that differences in cellular stiffness upon drug-mediated actin depolymerization do not have a direct influence on measured cell strain in the vessel-sized constrictions. Interestingly, cell volume increased upon squeezing into narrow constrictions, suggesting a potential change in cortical tension. The second device recreates a physiologically relevant 3D environment in which live high resolution imaging can be performed on cells migrating either individually or collectively. We performed proof-of-concept experiments by seeding cells in devices with 5 μm-channels and staining for the cytoskeleton and nucleus. We found that cells were able to reach the

---

constriction area and deform between the pillars. In future experiments, dynamic deformations of cells and the potential migrational advantage of clusters may therefore be studied.

5.1. INTRODUCTION

Metastasis, where cells leave a primary tumour to enter and travel through the blood circulation system before exiting and proliferating at a distant site in the body, accounts for the vast majority of cancer-related deaths [1–4]. Despite being so lethal, it is a highly inefficient process [5, 6]. Cancer cells travelling through the vasculature, termed circulating tumour cells (CTCs), often do not survive due to oxidative stress, shear forces and attacks by the immune system [7, 8]. Additionally, most CTCs prove to be apoptotic [9]. However, clinical studies from the last decade revealed that breast cancer CTCs traveling together as clusters have a significantly enhanced metastatic potential [8, 10, 11]. These clusters of 2 or more aggregated CTCs, which undertake the full metastatic cascade of intravasation and circulation as one conserved unit, display a metastatic potential that is up to 50 times larger than for individual CTCs [10, 12]. The presence of CTC clusters in the blood therefore signifies a significantly worse clinical outcome.

Polyclonal CTC clusters are highly improbable to originate from grouping of single CTCs in the bloodstream [3, 10]. Instead, the principle of cell jamming proposes that tumour cell dissemination is regulated by an increasing confinement from the growing tumour or from the surrounding extracellular matrix (ECM) [13–15]. For example, melanoma MV3 and fibrosarcoma HT1080 cells switch from single-cell to collective invasion when placed in a higher collagen density mimicking a more confining ECM [16]. However, further experimental studies on cluster dissemination through interstitial spaces and how they undergo deformations are still lacking.

The arrest of CTCs when travelling through narrow capillary beds, either due to constricting vessel sizes or to hemodynamic forces, is a fundamental step in the metastatic cascade [17–19]. When CTC cells and clusters traverse narrow microvessels (down to ~3 μm), they undergo large mechanical deformations [20]. Here, biomechanical forces exerted by the capillaries significantly deform the cytoskeleton and nucleus of CTC cells and clusters thereof, often resulting in cell death [21, 22]. However, these forces may induce adaptive mechanisms in the remaining CTCs, improving their survival and metastatic potential [23]. For example, strong confinement can dynamically regulate their cellular stiffness [24], or even induce an epithelial-to-mesenchymal transition (EMT) that gives them a more invasive phenotype [25, 26]. The mechanotransduction pathways involved in the metastatic potential of individual cancer cells may similarly affect CTC clusters [23, 27, 28]. Additionally, computational work demonstrated that clusters scaled their migrational persistence time with the number of cells, potentially explaining their greater migrational efficacy [29]. Yet, whether and how physical forces exerted on cell clusters contribute to their greater metastatic potential remains an open question [30, 31].

Here, we establish microfluidic devices that will enable researchers to study how differences in cell deformability affect migration through a physiologically relevant environment with vessel-sized constrictions. Inspired by a microfluidic device mimicking human capillary constrictions by Au *et al.* [20], we designed a similar microfluidic device to perform high-throughput cell deformability measurements in parallel. We could thus investigate how strain differs between cell types of varying stiffness when squeezed through vessel-sized constrictions. We subsequently introduce custom-made microfluidic chips, inspired by Davidson *et al.* [32], that allow the study of the migrational effi-

cacy of these cells, alongside their cytoskeletal and nuclear deformation, when traveling through varying designs of confined environments.

5.2. MATERIALS AND METHODS

5.2.1. CELL CULTURE

Human fibrosarcoma HT1080 cells and human melanoma MV3 cells were generously provided by the group of Peter Friedl at the RadboudUMC. The HT1080 cells were kept in Dulbecco's Modified Eagle's Medium High Glucose (DMEM, Sigma) containing 4.5 gL^{-1} glucose, L-glutamine, sodium pyruvate and sodium bicarbonate, and supplemented with 10% FBS (Gibco) and 1% Penicillin-Streptomycin (Sigma-Aldrich). The MV3 cells were kept in DMEM/F12 1:1 medium (Gibco) supplemented with 10% Fetal Bovine Serum (FBS, Gibco) and 1% Penicillin-Streptomycin (Sigma-Aldrich).

All cells were incubated at 37 °C with 5% CO_2 and subcultured at least twice a week.

5.2.2. CLUSTER PREPARATION

Clusters were created with a custom-designed microfabricated microwell array platform (which is available at: https://github.com/RubenBoot/CellandClusterDeformation/blob/main/Cluster_microwell_array_50um.dwg), inspired by work from Minglin Ma's lab [33]. Following their protocol, a microwell array platform was created using standard soft lithography at the Kavli Nanolab Delft to generate clusters with a maximum diameter of 50 µm. An array of circular microposts with a diameter of 50 µm and a height of 80 µm was fabricated by spinning SU-8 3050 photoresist (Kayaku Advanced Materials) on a clean wafer. The coated wafer was first baked at 95 °C for 15 minutes, after which the design was written with a µMLA laserwriter (Heidelberg Instruments). The wafer was postbaked at 65 °C for 1 minute followed by 95 °C for 5 minutes and then developed using SU-8 developer (Propylene glycol monomethyl ether acetate (PGMEA), Sigma-Aldrich). The master wafer was coated with trichloro(1H,1H,2H,2H-perfluorooctyl)silane (Sigma-Aldrich) to allow for easy demolding of the microwell arrays, which were made from polydimethylsiloxane (PDMS) (Sylgard 184, Dow Corning) and curing agent at a mixing ratio of 10:1 (w/w). The arrays were placed in a 12-well cell culture plate (Thermo Fisher Scientific) using rubber glue (Reprorubber), and subsequently sterilized by thoroughly washing the wells with ethanol and leaving the plate under UV light overnight. To prevent cell adhesion to the PDMS, the microwell arrays were coated with 1% (w/v) Pluronic® F127 (Sigma-Aldrich) solution before cell seeding, which was removed from the wells after 45 minutes of incubation. After trypsinization, a cell suspension with a concentration of ± 1x10^6 cells in appropriate cell medium was deposited in the well with the coated array in order to form clusters. After deposition, the cells divide over the microwells and settle at the bottom due to gravity, where they aggregate into clusters overnight (Fig. 5.1). The clusters were left to aggregate in the wells between 1 to 3 days before migration experiments, changing the media every day. They were harvested by gently washing them out of the microwells using the same media and bringing them into suspension.
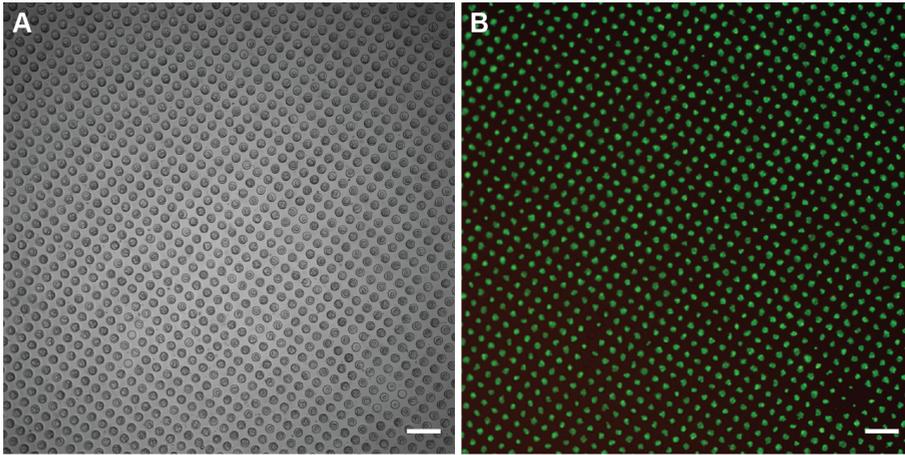
Figure 5.1: (A) Brightfield and (B) fluorescence microscope images of NIH3T3 cell clusters on day 2 after seeding in our custom-made microwell array with 50 μm wells. The cells are stained with calcein (green) and propidium iodide (PI) (red) for live/dead viability imaging. Scale 200 μm.

5.2.3. Cell deformability device fabrication

Cells were deformed using a custom-designed device consisting out of 18 parallel microchannels (which is available at: https://github.com/RubenBoot/CellandClusterDeformation), inspired by [20] and [34]. By fusing the parallel microchannel array from [20] with the T-junction design from [34], which incorporates a main channel that leads past the array, the overall volumetric flow rate through the device was greatly increased thus improving the throughput of cells reaching the microchannel array and travelling though the constrictions. The microchannels had dimensions of 10x10x280 μm^3 (width by height by length), while the main serpentine channel was 100 μm wide and high. This multi-layered design was created using standard soft lithography at the Kavli Nanolab Delft, with a μMLA laserwriter (Heidelberg Instruments). For the first layer containing the microchannel array, SU-8 2010 photoresist (Kayaku Advanced Materials) was spun on a clean 4-inch silicon wafer to a height of 10 μm. The coated wafer was then baked at 95 °C for 3 minutes, after which the first layer was written and post-baked at 95 °C for 4 minutes. After development with SU-8 developer (Propylene glycol monomethyl ether acetate (PGMEA), Sigma-Aldrich), a second layer was spun to a height of 100 μm using SU-8 2050 (Kayaku Advanced Materials). It was now baked at 65 °C for 5 minutes followed by 95 °C for 15 minutes, written, post-baked at 65 °C for 3 minutes followed by 95 °C for 10 minutes and developed again. The heights of the SU-8 features were determined to be within ± 10% of the desired heights using a Dektak Stylus Profiler (Bruker). Lastly, the master wafer was coated with trichloro(1H,1H,2H,2H-perfluorooctyl)silane (Sigma- Aldrich) to allow for easy demolding. The devices were made by pouring PDMS (Sylgard 184, Dow Corning) and curing agent at a mixing ratio of 10:1 (w/w) onto this master mold. The PDMS was degassed, and cured at 65 °C for 3 hours. After curing, the PDMS was peeled off, 2 mm inlets and outlets were punched using a revolving punch plier (Knipex), and the devices alongside glass coverslips were

plasma cleaned (Harrick Plasma) at 30 W for 2.5 minutes. The devices were kept in the oven at 65 °C to bond overnight.

5.2.4. Cell deformability data acquisition

Before experiments, the microfluidic device was filled and incubated with 1% Pluronic® F127 solution (Sigma) in phosphate buffered saline (PBS, Sigma-Aldrich) for 45 minutes at room temperature to decrease cell adhesion to the PDMS. Afterwards, the device was flushed with the same medium that was also used to create a cell suspension. Our design has three connective ports, one for cell entry, one for the perfusion buffer and one outlet port (denoted P_1, P_2 and P_3 respectively in Fig. 5.2A). The long serpentine main channel served to minimize the pressure drop over the parallel constriction channels at the center of the design. PTFE 008T16-030-200 tubing (Diba Industries, inner diameter 0.3 mm, outer diameter 1.6 mm) was cut to three pieces with an identical length of 50 cm (to prevent the influence of different pressure drops over tubing of differing lengths), measured with a ruler, and then flushed with the perfusion media using an MCFS-EZ pressure controller (Fluigent). After connecting each tubing piece to one of the connective ports, the pluronic solution, PDMS debris particles and possible air bubbles were flushed out by inducing a flow from P_2 and P_3 towards P_1, with P_1 connected to a waste tube. Once the main serpentine channel was free of obstacles, the tubing of P_1 was connected to the cell suspension while a minor flow was still present from P_2 to P_1, to prevent air from entering the tubing when connecting the cell suspension. A cell suspension of 1 mL (having various concentrations for different experiments, ranging between 0.5–3.5x10^6 cells/mL) was used. After reversing the flow direction, cells were subsequently flown through the main channel using a pressure gradient of 10 mbar (P_1 at 40 mbar, P_2 at 30 mbar). Outlet P_3 was kept at atmospheric pressure, such that the cells felt the pressure difference near the center of the design and were forced into the constriction channels (Fig. 5.2B).

Brightfield images of the deforming cells were captured using an inverted fluorescence microscope (Zeiss Axio-Observer) in brightfield mode with a 10x/NA 0.45 air objective and ORCA Flash 4.0 V2 (Hamamatsu) digital camera with a resolution of 2048x2048 px^2. We recorded image sets of 30 seconds, using an interval of 25 ms. Multiple sets were recorded per chip to capture data for a large number of cells, and the device was always discarded at the end of the experimental day. For all experiments, the cell suspension was kept at 37 °C using a Compact Dry Bath incubator (S 200-240V, Thermo Fisher Scientific), and image sets were only recorded during the first hour after connecting the cell suspension to the chip, eliminating the need for CO_2 injection.

5.2.5. Passive transit image analysis

Analysis of the deformation of cells in the constrictions was conducted using Fiji (https://imagej.net/software/fiji/). For each image set, multiple cells squeezed through the parallel constriction channels. Only the cells for which both the original diameter D_0 when deformed in the inlet of the channel (Fig. 5.2C, left panel) and the deformed length D once fully entered in the constriction (Fig. 5.2C, right panel) were clearly visible were included in the analysis. As the cells were not always perfectly round at the inlet, D_0 was determined by taking the average of the long and short diameter of the cell. Using Fiji, D_0 and the deformed length D were measured in the separate images to determine the
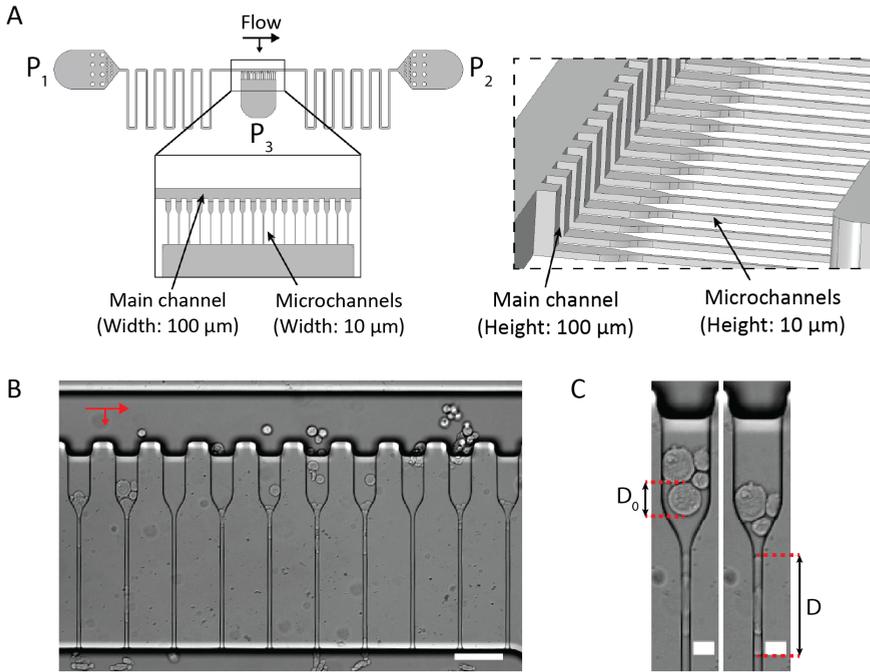
Figure 5.2: Overview of the microfluidic cell deformability device. (A) 3D schematic showing (left) the top view of the design and a close-up on the parallel constriction microchannels, and (right) a tilted side view showing the differing heights for the main channel and the microchannels. (B) Brightfield top view image of the parallel microchannels with HT1080 cells flowing freely through the main channel and being squeezed through the microchannels due to a pressure gradient from top to bottom. Red arrow indicates flow. Scale 100 um. (C) Brightfield images from a HT1080 cell entering the constriction inlet with a diameter D_0 (left panel) and subsequently stretching in the microchannel to a length D. Scale 20 um.

deformation strain S by taking their ratio:

$$S = \frac{D - D_0}{D_0} \tag{5.1}$$

The theoretical strain S_*, being the strain expected if the total cell volume was conserved during the experiment, was calculated based on the cell volume estimated from the size measurements. Assuming the cell in the inlet to be an approximate cylinder with a diameter D_0 and a height H of 10 μm (Fig. 5.3A), we know the volume V_1 of a cell in the inlet to be:

$$V_1 = \frac{H\pi D_0{}^2}{4}. \tag{5.2}$$

Once the cell enters the constriction channel, we approximate it as a beam of length L with a hemisphere on each end, having a radius R equal to half the width W and height H of the constriction (here, $R = 5$ μm) (Fig. 5.3B). From this, the volume of the cell V_2 in the constriction is found as:
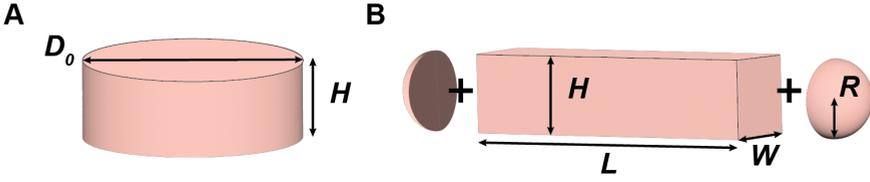
$$V_2 = (WHL) + V_{side}, \tag{5.3}$$

Figure 5.3: Schematic of geometric assumptions made to derive the theoretical strain S_* in case of cell volume conservation when transiting through a narrow squared constriction, with (A) the cell being geometrically confined into a cylindrical shape at the inlet, with diameter D_0 and height H, and (B) once it has entered the constriction channel, the volume of the cell to be determined as the sum of a beam of length L with width W and height H and two hemispheres with a radius R ($= \frac{1}{2} W = \frac{1}{2} H$).

with $V_{side} = \frac{4}{3} \pi R^3$ being the combined volume of the two halve spheres. Assuming volume conservation ($V_1 = V_2$), the length of the beam L is found by equating Eq. (5.2) and Eq. (5.3):

$$L = AD_0{}^2 - B, \qquad (5.4)$$

with $A = \pi/4W$ and $B = V_{side}/WH$. Inserting Eq. (5.4) into Eq. (5.1), we find the theoretical strain S_* as:

$$S_* = \frac{(L + 2R) - D_0}{D_0} \qquad (5.5)$$

5.2.6. MODELING OF FLUID DYNAMICS IN CELL DEFORMABILITY DEVICE

Due to the T-junction design of the cell deformability device, a pressure gradient exists both horizontally and vertically along the constriction channel array. To determine the extent of these gradients and differences in fluid pressure, we have computationally modelled the pressure distribution inside the device using the finite elements modeling software COMSOL Multiphysics 5.6. We considered the fluid flow in the three-dimensional (3D) model to be laminar and following the Navier-Stokes equation. The pressure gradient was examined for two different cases: (1) all constrictions are open, and (2) the flow through all constrictions is blocked (this occurs when all channels are clogged by traversing cells).

The pressure drop over a tubular channel with laminar flow scales with the length of the channel and the inverse of the channel radius to the fourth power. As the tubing used in our experiments had a long length of 50 cm and a cross-sectional area with the same order of magnitude as the main channel, the pressure drop over the tubing was non-negligible. For this reason, both cases were modeled including 50 cm long rectangular channels with a 300x300 μm^2 cross-section connected to all three ports, thereby mimicking the tubing used in our experiments. Boundary conditions of 4 kPa at the far edge of the channel connecting to the cell entry port P_1, 3 kPa at the edge of the channel connected to the perfusion port P_2, and 0 kPa at the edge of the channel connected to the outlet port P_3 were used, similar to the pressures used during experiments.

5.2.7. ACTIN POLYMERIZATION INHIBITION WITH CYTOCHALASIN D

Previous research has shown that incubation of chicken embryo fibroblasts with the actin polymerization inhibitor cytochalasin D (CD) at a concentration of 0.25 µM led to a 50 percent reduction in cell stiffness [35]. In our study, we therefore incubated MV3 cells with cytochalasin D (Sigma-Aldrich), diluted in dimethyl sulfoxide (DMSO), at the identical concentration of 0.25 µM for 30 minutes before experiments.

5.2.8. MICROINDENTATION MEASUREMENTS

The effective Young's modulus of the cells was measured using a Chiaro Nano-indenter (Optics11 Life), with a probe that had a stiffness of 0.027 N/m and a spherical tip with a radius of 3 µm. Measurements were performed on cells attached to the glass bottom of a 35 mm dish (ibid #81218-200) in appropriate media. Cells were seeded at least 24 hours before experiments in order to adhere to the bottom. Indentations were made above the cell center with a loading rate of 2 µm/s. The modulus was calculated using the Hertzian contact model from the Optics 11 Life data viewer software (version 2) [36]. Measurements without a distinct contact point or with an otherwise unreliable model fit (<0.9 R^2) were regarded as outliers and discarded from further analysis.

5.2.9. CELL MIGRATION DEVICE FABRICATION

We designed a microfluidic device tailored for observing cell deformation during migration through different custom-designed constriction areas (available at: https://github.com/RubenBoot/CellandClusterDeformation), inspired by [32]. The multi-layered master mold was created using standard soft lithography at the Kavli Nanolab Delft, with a µMLA laserwriter (Heidelberg Instruments). Similar to [32], the design consists of a 5 µm tall and 440 µm wide constriction area aligned with an adjacent 50 µm tall perfusion channel for cell loading, chambers that end at the constriction area, and a bypass channel to equilibrate the fluid levels between the reservoirs positioned at the outer sides of the chambers (Fig. 5.4A).

For this study, we have created three different constriction areas (Fig. 5.4B). The first design is identical to one of Davidson *et al.*'s designs to study nuclear deformations [32]. It has several open channels that are interconnected through spaces between the pillars dividing the channels. Each channel row has three identical 5 µm constrictions made of 25 µm wide pillars with a 5 µm spacing, and wider spaces between the pillar constrictions to avoid deformation of cells in between. The second design is similar to the first design, but now the three constrictions become sequentially narrower, starting at 30 µm width between the pillars, then 15 µm and lastly 5 µm. The third design is a Y-junction made out of sequential, connected arcs instead of straight walls, to more closely mimic the heterogeneous structure of the extracellular environment. It has a 30 µm wide main channel, and splits into either a 20 µm and 10 µm wide channel or into a 10 µm and 5 µm wide channel.

To create the master mold that contained all designs, SU-8 2005 photoresist (Kayaku Advanced Materials) was spun on a clean 4-inch silicon wafer to a height of 5 µm to fabricate the first layer with the constriction area. The coated wafer was soft baked at 95 °C for 2 minutes, exposed to the first-layer design, and then post-baked at 95 °C for 2 minutes. After development, the second layer was spun with SU-8 3050 (Kayaku Advanced
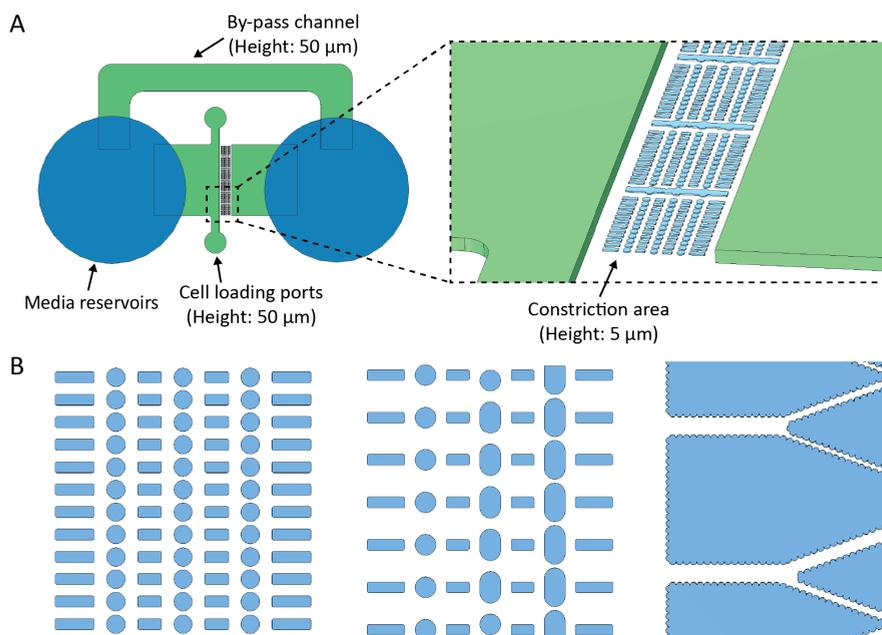
Figure 5.4: Overview of the microfluidic cell migration device. (A) 3D schematic showing (left) the top view of the design and where the media reservoirs are punched (dark blue) to connect the by-pass channel and cell loading area (green), and (right) a tilted side view showing the constriction area situated in between the two chambers. (B) The three different designs for the constriction areas: (left) rows with identical constrictions of 5 µm in width between the circular pillars, (middle) rows with sequentially narrower constrictions of 30 µm, 15 µm and 5 µm in width, and (right) Y-junctions with a 30 µm wide channel splitting into either a 10 µm and 5 µm wide channel (above), or into a 20 µm and 10 µm wide channel (below).

Materials) to a height of 50 µm. The wafer was soft baked at 95 °C for 15 minutes, exposed to the second-layer design, post-baked at 65 °C for 1 minute followed by 95 °C for 5 minutes and finally developed using SU-8 developer (Propylene glycol monomethyl ether acetate (PGMEA), Sigma-Aldrich). The heights of the SU-8 features were determined to be within ± 10% of the desired heights using a Dektak Stylus Profiler (Bruker). The master mold was coated with trichloro(1H,1H,2H,2H-perfluorooctyl)silane (Sigma- Aldrich) to allow for easy demolding of the chips, which were made from PDMS (Sylgard 184, Dow Corning) and curing agent at a mixing ratio of 10:1 (w/w). The PDMS was poured on the silicon mold, degassed an cured at 65 °C for 3 hours. After curing, the PDMS was peeled off and 5 mm reservoirs were punched using a revolving punch plier (Knipex). The inlet and outlet of the perfusion channel where cells are loaded into the device were punched with a 0.75 mm diameter punch (Rapid-Core, WellTech). Subsequently, the devices alongside glass coverslips were plasma cleaned (Harrick Plasma) at 30 W for two and a half minutes, and kept in the oven at 65 °C to bond overnight.

5.2.10. CELL MIGRATION DATA ACQUISITION

Before migration experiments, microfluidic devices were sterilized by filling them with 70% ethanol inside a tissue-culture hood. The devices were then cleaned twice with MilliQ water, by aspirating the ethanol and filling one well with the water. Next, the device was rinsed once more with PBS (Sigma-Aldrich). To promote cell adhesion, devices were coated with PureCol type 1 bovine collagen solution (Advanced Biomatrix) diluted in PBS to 100 μg/mL. For each chip, 90 μL collagen solution was added via the small side port opposite of the by-pass channel and incubated at room temperature for 2 hours. From here, a cap from a 15 mL Falcon tube filled with MilliQ was placed beside the device to prevent evaporation. After rinsing the device with cell medium, 6 μL aliquots from a cell suspension of $3x10^6$ cells/mL in the corresponding cell media were added to the small side ports at the opposite sides of the by-pass channels. Once the cells were in the device, the reservoirs were gently topped off with media and the cells were left to adhere overnight. The device was sealed with a glass coverslip to prevent evaporation.

For visualization of the cells' cytoskeletons, medium was removed the next day and 80 μL staining solution (stock in cell medium) was added to the reservoir on the side where cells were loaded. After 2 hours of incubation, the staining solution was removed and changed with medium topping off the reservoirs. The device was hence resealed with a glass coverslip. Cell nuclei were stained with Hoechst 33342 (Thermo Fisher Scientific) at a concentration of 2 nM, α-Tubulin with SPY555-Tubulin (Tebu-bio) at a concentration of 1 μM, and actin with SiR700-Actin (Tebu-bio) at a concentration of 1 μM.

Cell migration was imaged using a 40x/NA 1.25 glycerol objective of a Stellaris 8 confocal microscope (Leica) with an environmental control box to maintain a constant temperature of 37 °C and a constant CO_2 level of 5.0%. The laser intensity was set between 0.1 – 1% to reduce toxicity and avoid overexposed pixels. The laser lines used were 405 nm (Hoechst), 557 nm (SPY555-Tubulin) and 698 nm (SiR700-Actin).

5.2.11. STATISTICAL ANALYSIS

Statistical analysis was performed using Microsoft Excel. Two-tailed Student's t-tests were performed using the TTEST function in Excel, with significance thresholds considered as *, $p < 0.05$, **, $p < 0.01$ and ***, $p < 0.001$. Error bars represent the standard error of the mean. The passive deformation data is based on at least three biological replicates.

5.3. RESULTS AND DISCUSSION

5.3.1. CELL DEFORMABILITY

Microfluidic devices mimicking capillaries from the blood vascular network were developed consisting of 18 parallel microchannels narrowing into 10x10 μm^2 constrictions. At first, cells flow through a large 100x100 μm^2 main channel due to a pressure difference of 1 kPa between the cell entry port P_1 and the perfusion port P_2. They are then directed towards the constriction microchannels due to the pressure gradient between the main channel and the outlet port P_3 that is left at atmospheric pressure (Fig. 5.2A). Here, the cells that enter the microchannel at the inlet (with a width of 50 μm) first are only confined in height to a diameter D_0, and next fully deform in the 10 μm wide constriction

to a deformation length D (Fig. 5.2B-C). The two pressure inlets P_1 and P_2 allow precise control of the flow velocity of cells through the main channel, and of the pressure with which the cells are squeezed into the microchannels. Additionally, both inlet ports have an array of pillars to prevent dust or debris to enter the main channel.

As the tubing used for the experiments had a cross-sectional area of the same order of magnitude as the main channel in the design, the pressure drop over the tubing could not be considered negligible. Through 3D COMSOL simulations of the design with identical pressure conditions and 50 cm long rectangular channels connected to the ports, mimicking the tubing, we find that the horizontal pressure gradient across the parallel microchannel array is negligible (~ 30 Pa, Fig. 5.5A). However, simulations also showed that the pressure that cells experience when entering the constrictions depends on whether the other channels are clogged by traversing cells. The pressure changed by ~ 20% between the case of all channels being open versus closed (from ~ 2.9 to 3.5 kPa, Fig. 5.5B). While this pressure change is expected to influence parameters such as entry time and traversal time of cells crossing the constriction [20], our data clearly demonstrated that the detection of differences in deformability between different cell types was not affected by this pressure change. A possible improvement to minimize the influence of clogging channels on the pressure gradient that cells experience in the constriction inlet would be to lower the cross-sectional area of the microchannel array in comparison to the main channel, by for example decreasing the amount of parallel microchannels in the array or adapting its area to 7x7 μm^2, or even to 5x5 μm^2 (though here cells are expected to get stuck at the inlet faster).

To test the device, we have compared the deformability of human melanoma MV3 cells and human fibrosarcoma HT1080 cells. We performed these experiments sequentially on the same device. After collecting data for one cell type, the main channel was flushed with medium by connecting a tube of medium after reversing the flow from P_2 to P_1 to prevent air from entering the tubing at P_1. Next, a suspension with the other cell type was connected to the device for further measurements. By measuring the cell diameter D_0 before and after entering the channels, we determined that the strain S increased with D_0 for both cell types (Fig. 5.6). The larger the cell, the more it has to stretch in the channel due to the confinement. For this reason, we binned cells by sequential pairs of D_0 (e.g. cells with $D_0 = 15$ μm and 16 μm were combined in one bin), and compared S between the respective bins for each cell type. We find that the HT1080 cells consistently had a larger strain than the MV3 cells for the same D_0, indicating a larger deformability. Interestingly, this also means that cell volume is not conserved as cells with the same original volume in the constriction inlet display different deformations. Using Eq. (5.5), we determine a theoretical strain S_* in case of volume conservation, which is indicated in Fig. 5.6 by the red dotted lines. Comparing this theoretical limit to the data, we find that both the MV3 and HT1080 cells increased in volume in the constrictions. This potentially indicates rupturing or altering of cytoskeletal elements which oppose the internal cell pressure. Assuming a balance between the cell's internal pressure versus the sum of the outer fluid pressure and the cell's cortical tension, the tension must have lowered to explain the increase in cell volume. Following this reasoning, we hypothesize that the change in cortical tension was larger for the HT1080 cells than for the MV3s.

To investigate the relation between cell deformability and cortical stiffness, we inhib-
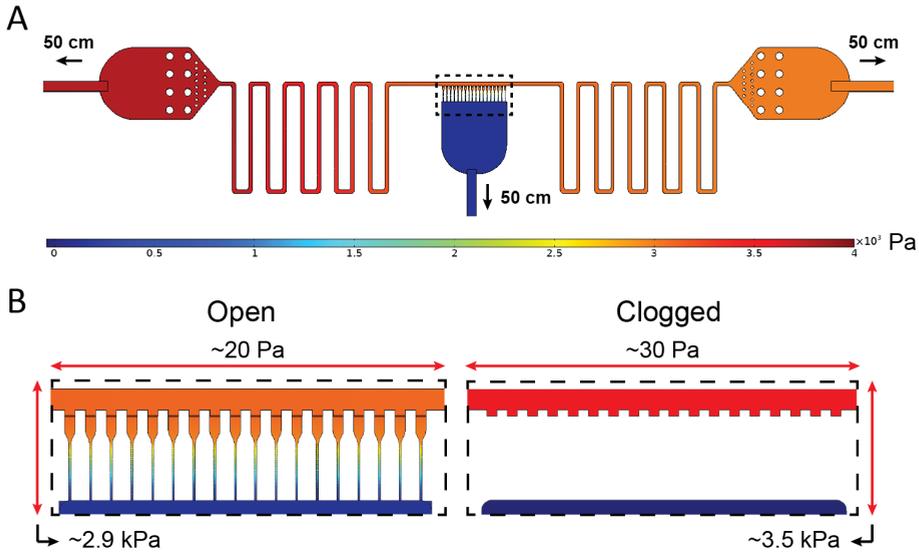
Figure 5.5: Simulation of pressure distribution across the microfluidic passive deformation device. (A) A 3D numerical simulation of the pressure distribution assuming the three ports are connected to 50 cm long rectangular channels mimicking the experimental tubing. A pressure gradient of 1 kPa is simulated between the far end of the tube connected to the cell entry port P_1 (4 kPa) and the tube connected to the perfusion port P_2 (3 kPa), while the far end of the tube connected to the outlet port P_3 is kept at atmospheric pressure (0 kPa). (B) Zoomed-in simulation of the horizontal and vertical pressure gradients across the microchannel array, demonstrated by the dashed rectangle in (A), for two different configurations: all microchannels are open (left) and all microchannels are clogged (right).
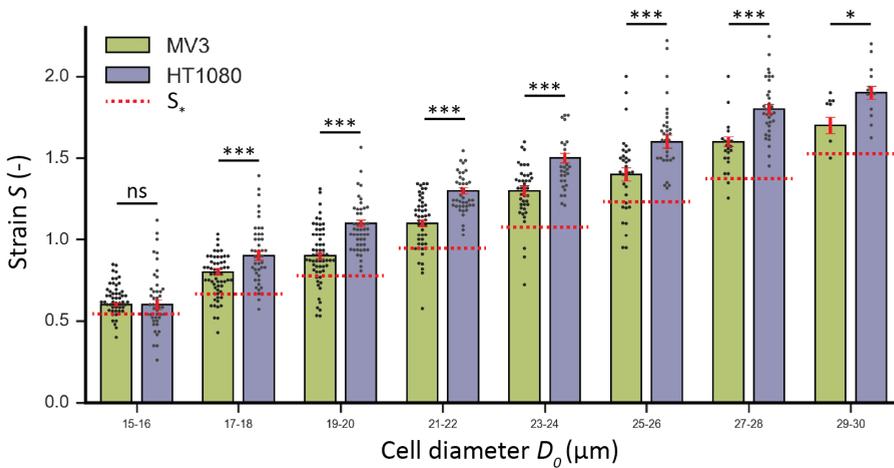

Figure 5.6: Histograms comparing the strain S for MV3 (green) and HT1080 (purple) cells when squeezed through 10x10 μm^2 constrictions, binned for cell diameter D_0. Red dotted lines depict the theoretical strain S_* in the limit of volume conservation, calculated using Eq. (5.5) and inserting the largest D_0 for each bin (eg. $D_0 = 16$ μm for 15-16 bin). *, $p < 0.05$, ***, $p < 0.001$ and ns is nonsignificant. Error bars are SEM.
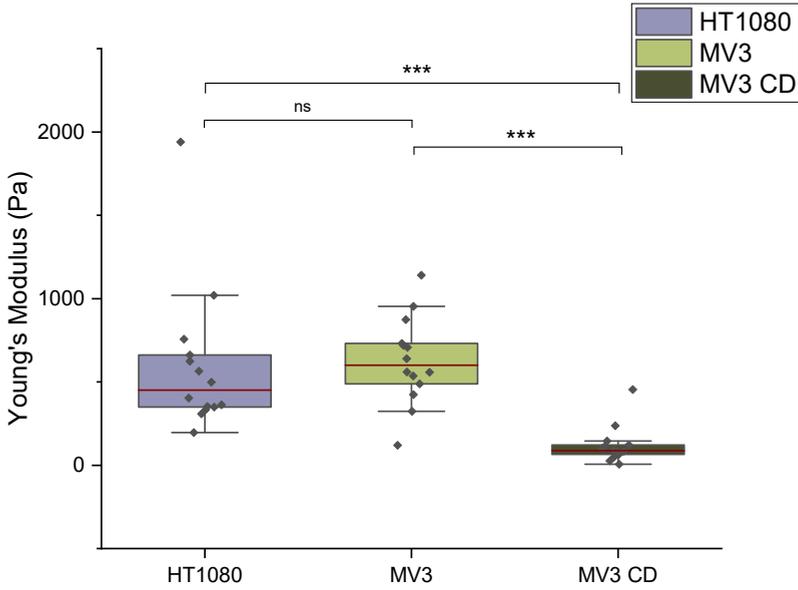
Figure 5.7: Boxplot of the Young's modulus of HT1080 cells (n = 14), control MV3 cells (n = 14) and MV3s treated with cytochalasin D (n = 14), measured by indentation with a 3 μm radius spherical probe. The red line represents the median. ***, p < 0.001 and ns is nonsignificant.
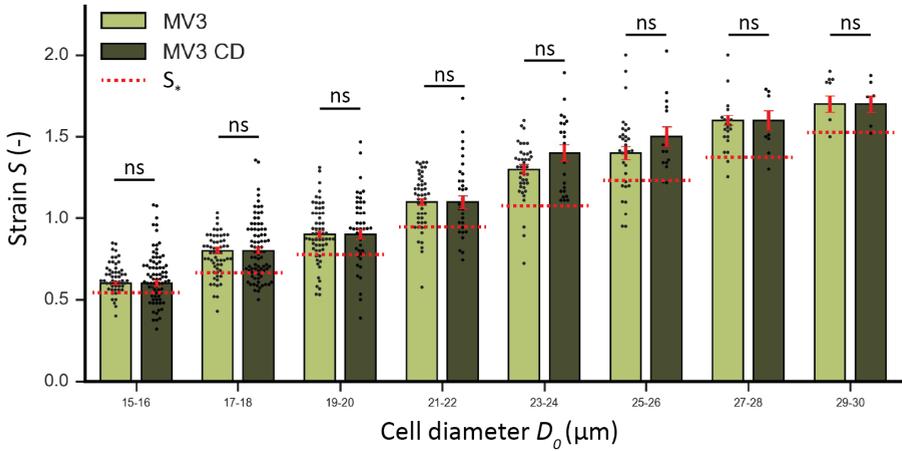

Figure 5.8: Histograms comparing the strain S for control MV3 cells (light green) and MV3 cells treated with cytochalasin D (dark green) when squeezed through 10x10 μm^2 constrictions, binned for cell diameter D_0. Red dotted lines depict the theoretical strain S_* in the limit of volume conservation, calculated using Eq. (5.5) and inserting the largest D_0 for each bin (eg. D_0 = 16 μm for 15-16 bin). ns is nonsignificant. Error bars are SEM.

ited actin polymerization in the MV3 cells through treatment with cytochalasin D (CD). By indenting the cells with a spherical probe, we measured a ∼ 5-fold decrease in the Young's modulus after the MV3 cells were treated with CD (Fig. 5.7). We did not measure a significant difference in the Young's modulus between the non-treated MV3 cells versus the HT1080 cells. Next, we tested the influence of CD treatment on deformation of the MV3 cells with the microfluidic deformation chip. Interestingly, we found that a significant change in cellular stiffness did not influence the measured cell strain S (Fig. 5.8). Both the treated and the untreated MV3 cells deformed slightly more (∼10-20%) than the theoretical strain S_* would predict when cell volume is conserved. Previous research suggested that differences in cell strain, measured for MCF-7 and MCF-10A cells squeezed through a similar microfluidic constriction, were related to the cellular elasticity [37]. However, our results indicate that the measured cell strain in narrow constrictions does not necessarily correlate to cell stiffness. We hypothesize that cell deformability could be more influentially governed by the intermediate filament network. We base this hypothesis on recent work showing that vimentin intermediate filaments limit the resulting strain when cells are subjected to stress, as vimentin and F-actin form an interpenetrating network with interactions at multiple length scales [38, 39]. The potential presence of a dense vimentin network could therefore explain why actin depolymerization did not influence cell strain.

5.3.2. CONFINED CELL MIGRATION

To investigate the influence of differences in cell deformability on (cluster) cell migration through narrow constrictions, we have designed different microfluidic designs based on previous work by Davidson *et al.* [32]. All designs consist of parallel migration channels that can be functionalized with collagen or fibronectin to promote cell adhesion and crawling (Fig. 5.4). The narrow constrictions formed by either PDMS pillars or walls mimic the 5 to 30 μm wide pores found in the ECM [40]. The two media reservoirs on both side of the device are connected with a wide bypass channel to enable fast equilibration of fluid height between both reservoirs (Fig. 5.4A). In contrast to long, straight channels, the designed pillars or walls made of interconnected arcs mimic the discontinuous spatial environment found in the ECM (Fig. 5.4B). First, we designed an array of parallel channels with sequential constrictions of 5 μm. Secondly, we created constrictions that narrow from 30 μm to 15 μm and than to 5 μm. This design should allow the study of cluster cell speed when travelling through narrower constrictions, and to test whether there is a limiting size for clusters to pass through. Thirdly, Y-junctions that start as 30 μm wide channels and then split into either a 20 μm and 10 μm wide channel, or into a 10 μm and 5 μm channel, allow to investigate how cell deformability influences the migration path when cells face a choice between different constrictions, and how this relates to cell clusters migrating as trains. We performed first proof-of-concept experiments by seeding HT1080 cells in the 5 μm-constriction device and staining for the cytoskeleton and nucleus (Fig. 5.9). These preliminary experiments demonstrated how cells are able to reach the constriction area and deform between the pillars. Additionally, we find that the high resolution imaging of cytoskeletal structures in living cells will allow detailed measurements of cell migration. Here, nuclear deformations, cytoskeletal mechanics and cell volume changes are potential parameters for future exploration.
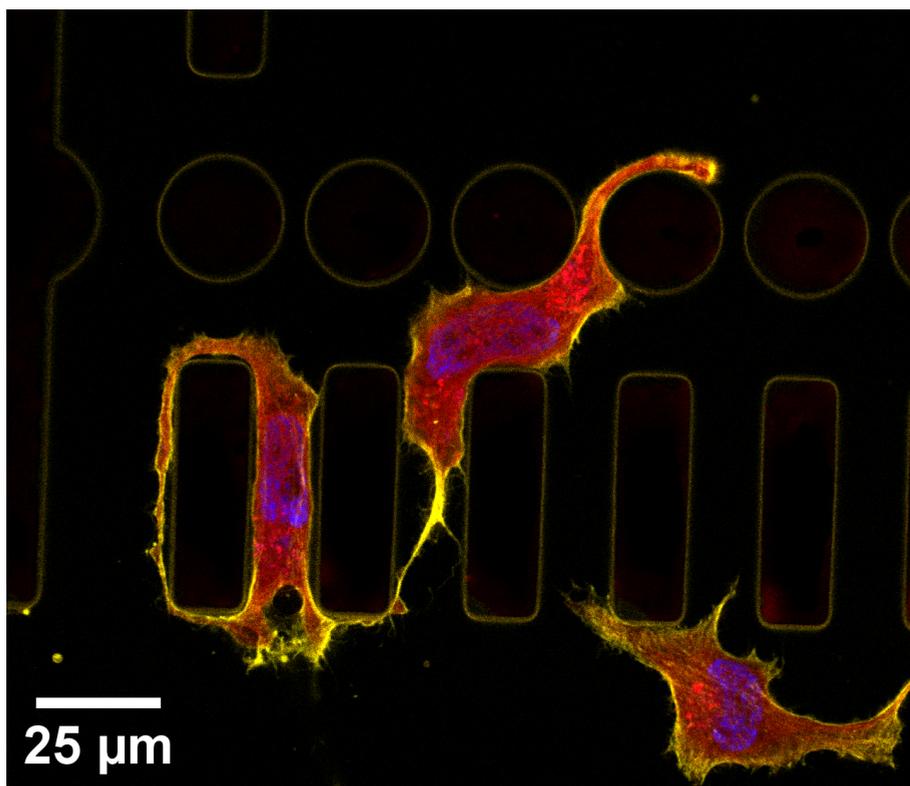
Figure 5.9: Confocal fluorescence image of HT1080 cells migrating in the microfluidic device with 5 μm constrictions. The cells are stained for actin (yellow, SiR700-Actin), α-tubulin (red, SPY555-Tubulin) and their nucleus (blue, Hoechst).

Moreover, cell clusters can be grown in future work using our cluster microwell array (Fig. 5.1), and loaded into the microfluidic device to unravel their migrational efficacy and dependency on individual cell deformability.

5.4. CONCLUSION AND OUTLOOK

A better understanding of how individual cell deformability may contribute to the migrational ability of cell clusters is highly relevant to provide insights in cancer metastasis. We have designed a microfluidic device that allows for high-throughput cell strain measurements to compare differences in deformability between cell types. Using this device, we found that cell volume can change when squeezing into narrow constrictions, which we hypothesize to be explained by changes in cortical tension. Importantly, cells with a similar Young's modulus as measured by indentation differed in strain when squeezed through constrictions. Additionally, lowering cellular stiffness by inhibiting actin polymerization with cytochalasin D did not affect cell strain, indicating that stiffness is not of significant influence on cell strain in narrow constrictions. Instead, we hypothesize

that for our experiments cell strain may be governed by the intermediate filament network, rather than by actin filaments. Future experiments with vimentin-knockout cells are therefore of interest to confirm or reject this hypothesis.

To couple cell deformability to the ability of the cells to perform confined migration, we have designed a second microfluidic device that allows for live cell imaging of migration through a 3D environment of narrow constrictions with varying sizes. Future experiments with this device will enable the quantification of dynamic deformations of cells that either travel individually or collectively. Here, the contribution of the actomyosin cortex, intermediate filament network and intercellular adhesions to (cluster) cell migration could be studied using confocal fluorescent imaging. Eventually, understanding the role of cell deformability in cell migration through blood-vessel sized constrictions will shed further light on why cell clusters are provided with a greater metastatic ability than individual CTCs.

5

BIBLIOGRAPHY

1. Wyckoff, J. B., Jones, J. G., Condeelis, J. S. & Segall, J. E. A critical step in metastasis: In vivo analysis of intravasation at the primary tumor. *Cancer Research* **60,** 2504–2511. ISSN: 00085472 (2000).

2. Brabletz, T. To differentiate or not-routes towards metastasis. *Nature Reviews Cancer* **12,** 425–436. ISSN: 1474175X (2012).

3. Cheung, K. J. & Ewald, A. J. A collective route to metastasis: Seeding by tumor cell clusters. *Science* **352,** 167–169. ISSN: 10959203 (2016).

4. Siegel, R. L., Miller, K. D. & Jemal, A. Cancer Statistics , 2015. *CA Cancer J Clin* **65,** 5–29 (2015).

5. Mehlen, P. & Puisieux, A. Metastasis: A question of life or death. *Nature Reviews Cancer* **6,** 449–458. ISSN: 1474175X (2006).

6. Giuliano, M. *et al.* Perspective on circulating tumor cell clusters: Why it takes a village to metastasize. *Cancer Research* **78,** 845–852. ISSN: 15387445 (2018).

7. Meng, S. *et al.* Circulating Tumor Cells in Patients with Breast Cancer Dormancy. *Clinical Cancer Research* **10,** 8152–8162 (2004).

8. Hou, J.-m. *et al.* Clinical Significance and Molecular Characteristics of Circulating Tumor Cells and Circulating Tumor Microemboli in Patients With Small-Cell Lung Cancer. *Journal of Clinical Oncology* **30,** 525–532 (2012).

9. Rossi, E. *et al.* M30 Neoepitope Expression in Epithelial Cancer : Quantification of Apoptosis in Circulating Tumor Cells by CellSearch Analysis. *Clinical Cancer Research* **16,** 5233–5243 (2010).

10. Aceto, N. *et al.* Circulating tumor cell clusters are oligoclonal precursors of breast cancer metastasis. *Cell* **158,** 1110–1122. ISSN: 10974172. http://dx.doi.org/10.1016/j.cell.2014.07.013 (2014).

11. Aceto, N. Bring along your friends: Homotypic and heterotypic circulating tumor cell clustering to accelerate metastasis. *Biomedical Journal* **43,** 18–23. ISSN: 23194170. https://doi.org/10.1016/j.bj.2019.11.002 (2020).

12. Allen, T. A. *et al.* Circulating tumor cells exit circulation while maintaining multicellularity, augmenting metastatic potential. *Journal of Cell Science* **132.** ISSN: 14779137 (2019).

13. Chepizhko, O. *et al.* From jamming to collective cell migration through a boundary induced transition. *Soft Matter* **14,** 3774–3782. ISSN: 17446848. arXiv: 1802.07488 (2018).

14. Ilina, O. *et al.* Cell–cell adhesion and 3D matrix confinement determine jamming transitions in breast cancer invasion. *Nature Cell Biology* **22,** 1103–1115. ISSN: 14764679. http://dx.doi.org/10.1038/s41556-020-0552-6 (2020).

15. Oswald, L., Grosser, S., Smith, D. M. & Käs, J. A. Jamming transitions in cancer. *Journal of Physics D: Applied Physics* **50.** ISSN: 13616463 (2017).

16. Haeger, A., Krause, M., Wolf, K. & Friedl, P. Cell jamming: Collective invasion of mesenchymal tumor cells imposed by tissue confinement. *Biochimica et Biophysica Acta - General Subjects* **1840,** 2386–2395. ISSN: 18728006. http://dx.doi.org/10.1016/j.bbagen.2014.03.020 (2014).

17. Kienast, Y. *et al.* Real-time imaging reveals the single steps of brain metastasis formation. *Nature Medicine* **16,** 116–122. ISSN: 10788956. http://dx.doi.org/10.1038/nm.2072 (2010).

18. Follain, G. *et al.* Hemodynamic Forces Tune the Arrest , Adhesion , and Extravasation of Circulating Tumor Cells. *Developmental Cell* **45,** 33–52 (2018).

19. Follain, G. *et al.* Fluids and their mechanics in tumour transit: shaping metastasis. *Nature Reviews Cancer* **20,** 107–124. ISSN: 14741768 (2020).

20. Au, S. H. *et al.* Clusters of circulating tumor cells traverse capillary-sized vessels. *Proceedings of the National Academy of Sciences of the United States of America* **113,** 4947–4952. ISSN: 10916490 (2016).

21. Yamamoto, N. *et al.* Cellular dynamics visualized in live cells in vitro and in vivo by differential dual-color nuclear-cytoplasmic fluorescent-protein expression. *Cancer Research* **64,** 4251–4256. ISSN: 00085472 (2004).

22. Yamauchi, K. *et al.* Real-time in vivo dual-color imaging of intracapillary cancer cell and nucleus deformation and migration. *Cancer Research* **65,** 4246–4252. ISSN: 00085472 (2005).

23. Perea Paizal, J., Au, S. H. & Bakal, C. Squeezing through the microcirculation: survival adaptations of circulating tumour cells to seed metastasis. *British Journal of Cancer* **124,** 58–65. ISSN: 15321827. http://dx.doi.org/10.1038/s41416-020-01176-x (2021).

24. Rianna, C., Radmacher, M. & Kumar, S. Direct evidence that tumor cells soften when navigating confined spaces. *Molecular Biology of the Cell* **31,** 1726–1734. ISSN: 19394586 (2020).

25. Cognart, H. A., Viovy, J. L. & Villard, C. Fluid shear stress coupled with narrow constrictions induce cell type-dependent morphological and molecular changes in SK-BR-3 and MDA-MB-231 cells. *Scientific Reports* **10,** 1–14. ISSN: 20452322. http://dx.doi.org/10.1038/s41598-020-63316-w (2020).

26. Irianto, J. *et al.* DNA Damage Follows Repair Factor Depletion and Portends Genome Variation in Cancer Cells after Pore Migration. *Current Biology* **27,** 210–223. ISSN: 09609822. http://dx.doi.org/10.1016/j.cub.2016.11.049 (2017).

27. Stroka, K. M. & Konstantopoulos, K. Physical Biology in Cancer . 4 . Physical cues guide tumor cell adhesion and migration. *American Journal of Physiology - Cell Physiology* **306,** C98–C109 (2014).

28. Jaalouk, D. E. & Lammerding, J. Mechanotransduction gone awry. *Nat Rev Mol Cell Biol* **10,** 63–73 (2009).

29. Debets, V. E., Janssen, L. M. & Storm, C. Enhanced persistence and collective migration in cooperatively aligning cell clusters. *Biophysical Journal* **120,** 1–15. ISSN: 15420086. arXiv: 2009.00504. https://doi.org/10.1016/j.bpj.2021.02.014 (2021).

30. Gensbittel, V. *et al.* Mechanical Adaptability of Tumor Cells in Metastasis. *Developmental Cell.* ISSN: 18781551 (2020).

31. Peralta, M., Osmani, N. & Goetz, J. G. Circulating tumor cells: Towards mechanical phenotyping of metastasis. *iScience* **25,** 103969. ISSN: 25890042 (Mar. 2022).

32. Davidson, P. M., Sliz, J., Isermann, P., Denais, C. & Lammerding, J. Design of a microfluidic device to quantify dynamic intra-nuclear deformation during cell migration through confining environments. *Integrative Biology (United Kingdom)* **7,** 1534–1546. ISSN: 17579708. http://dx.doi.org/10.1039/C5IB00200A (2015).

33. Song, W. *et al.* Dynamic self-organization of microwell-aggregated cellular mixtures. *Soft Matter* **12,** 5739–5746. ISSN: 17446848 (2016).

34. Davidson, P. M. *et al.* High-throughput microfluidic micropipette aspiration device to probe time-scale dependent nuclear mechanics in intact cells. *Lab on a Chip* **19,** 3652–3663. ISSN: 14730189 (2019).

35. Wakatsuki, T., Schwab, B., Thompson, N. C. & Elson, E. L. Effects of cytochalasin D and latrunculin B on mechanical properties of cells. *Journal of Cell Science* **114,** 1025–1036 (2001).

36. Field, J. S. & Swain, M. V. Determining the mechanical properties of small volumes of material from submicrometer spherical indentations. *Journal of Materials Research* **10,** 101–112. ISSN: 20445326 (1995).

37. Hou, H. W. *et al.* Deformability study of breast cancer cells using microfluidics. *Biomedical Microdevices* **11,** 557–564. ISSN: 13872176 (2009).

38. Patteson, A. E., Carroll, R. J., Iwamoto, D. V. & Janmey, P. A. The vimentin cytoskeleton: when polymer physics meets cell biology. *Physical Biology* **18.** ISSN: 14783975 (2020).

39. Wu, H. *et al.* Vimentin intermediate filaments and filamentous actin form unexpected interpenetrating networks that redefine the cell cortex. *Proceedings of the National Academy of Sciences of the United States of America* **119,** 1–10. ISSN: 10916490 (2022).

40. Weigelin, B., Bakker, G.-J. & Friedl, P. Intravital third harmonic generation microscopy of collective melanoma cell invasion. *IntraVital* **1,** 32–43 (2012).

5

6

CONCLUSION

In this thesis, we focused on understanding the complex interplay of cell and tissue mechanics using specially developed microfluidic devices. Here, we briefly summarize our conclusions and give our perspective on future research directions.

6.1. BRIDGING CELL AND SPHEROID MECHANICS

Understanding how tissue mechanics arise from single cell properties is a necessary step to obtain new insights in tissue sorting and cancer cell invasion. Since the surface tension of multicellular spheroids depends on the ratio of individual cell cortical tension and intercellular adhesion, it forms an ideal parameter to study the link between cell and tissue mechanics. In this dissertation, we provided an extensive literature review in **chapter 2** on the current theoretical frameworks and experiments investigating this interplay using spheroid models. We concluded that multiscale mechanical measurements and correlative imaging will be required to deconvolve how cortical tension and intercellular adhesions influence tissue mechanics. Most importantly, experimental techniques to probe spheroid mechanics have until now been mostly low in throughput as they usually probe one spheroid at a time and are difficult to handle. It has therefore remained difficult to make statistically meaningful comparisons between different experimental conditions.

To overcome this problem, we designed a high-throughput microfluidic micropipette aspiration device to probe multiple spheroids in parallel in **chapter 3**. The device allowed us to obtain viscoelastic spheroid mechanics data sets that were unprecedented in size (~300 probed spheroids). We demonstrated that our device was able to give reproducible, accurate results in agreement with previous studies. Additionally, it is sensitive enough to detect small differences in pressure, demonstrating its suitability to investigate the putative reinforcement of spheroid surface tension at different pressures.

Using this device, we then proceeded to investigate the surface tension γ of spheroids when aspirating at different pressures in **chapter 4**. We found a pressure dependency consistent with previous findings of Guevorkian *et al* [1]. However, in contrast to a reinforcement due to active mechanosensing of the cells, we discovered that the viscous

retraction flow velocity depended on the total deformation of the spheroid protrusion after aspiration. This behaviour has previously been unaccounted for when interpreting spheroid aspiration data. We therefore propose an alternative framework to interpret spheroid MPA data, in which the viscoelastic response is deformation-dependent. This makes the assumption that both the viscosity η and the critical pressure ΔP_c remain constant during spheroid aspiration and retraction invalid. However, being able to discern viscosity and surface tension from each other during spheroid aspiration and retraction remains complex, as the spheroid protrusion flow velocity is governed by both these properties. Future experiments will have to investigate how tissue viscosity is regulated at the cellular level, and which cytoskeletal components work at different timescales to govern elastic and viscous responses. We like to point out that HEK293T and NIH3T3 spheroids form ideal models for future investigation due to their spherical compactness during aspiration, and their significant differences in elastic and viscous behaviour. In order to distinguish which components determine which mechanical response regime, spheroids could be aspirated over different length scales, in combination with partial knock-out or inhibition of the investigated components. Previously, micromanipulation measurements at different length scales have demonstrated how the cell nucleus has distinct mechanical response regimes [2, 3]. Here, nuclei stretched for small deformations (<30% of the original length) showed a chromatin-dependent resistance, whereas larger deformations were governed by the expression levels of the nuclear envelope proteins lamins A/C. Following this example, inhibiting components such as actin, intermediate
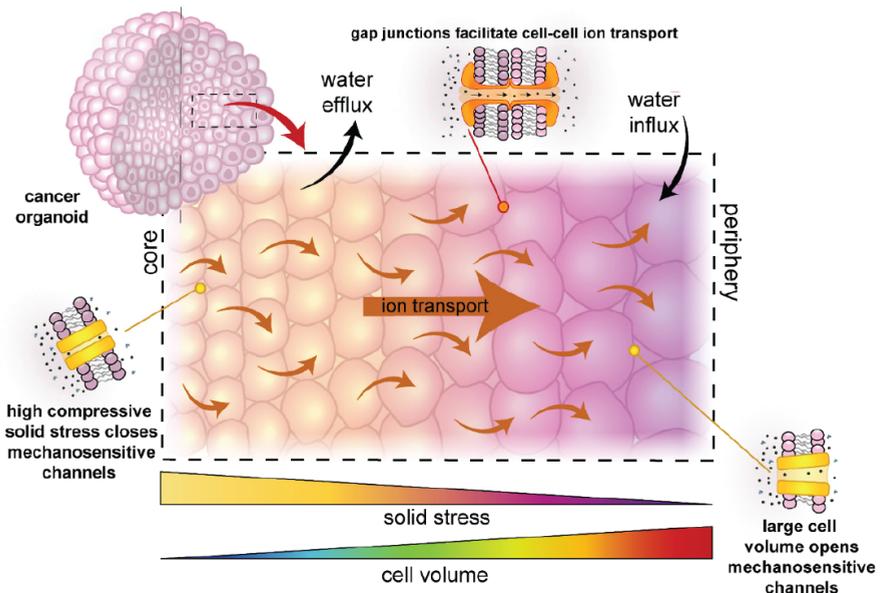

Figure 6.1: Schematic demonstrating how spatial variations in cell volume within spheroids is driven by non-uniform solid growth stress and gap junction-mediated ion flow. Compressive stress at the spheroid core pushes water and ions through gap junctions towards cells at the periphery, increasing their volume. Reproduced from [4], licensed under CC BY 4.0.

filaments or cadherins and subsequently aspirating spheroids for different deformation lengths could provide new insights in distinct tissue mechanical regimes. One complexity to keep in mind, however, is that actin acts as an anchor of cadherin bonds [5]. Therefore, actin-depolymerizing drugs that lower cortical tension additionally weaken intercellular adhesion. Decoupling the influence of actin and cadherins on spheroid mechanics thus remains an important point of investigation. Additionally, potential drugs or inhibitors to single-out cytoskeletal components will have to be carefully chosen in order to not compromise the integrity of spheroids during aspiration.

Besides pressure-dependency, spheroid surface tension has been shown to depend on spheroid size, with smaller spheroids having a larger tension [6]. Unfortunately, the size range that our microfluidic device could aspirate was too small to reproduce this effect. For future experiments, the width and height of the aspiration pockets on the microfluidic chip could be increased to allow a larger size range for spheroid measurements. However, less pockets would fit in the microscope objective's plane of view, decreasing the throughput. In addition to making improvements to the microfluidic device, we believe that a focus on gap junctions could provide new insights in the putative size dependency of the surface tension of spheroids. Gap junctions are intercellular connections that allow the exchange of ions and fluids between cells [4]. Previously, spheroids placed in a hydrogel of alginate and Matrigel displayed a greater compressive stress at their core with increasing spheroid size [7]. Due to this stress, water and ions were pushed from the core of the spheroid to the periphery through gap junctions, causing spatial variations in cell volume with cells swelling at the periphery (Fig. 6.1) [4]. This effect was negated once gap junctions were blocked with an inhibitor. Interestingly, Yousafzai *et al.* showed that larger spheroids with a lower surface tension displayed a reduced myosin concentration at the surface, likely due to an increase in cell volume at the periphery [6]. Performing future aspiration experiments on spheroids with blocked gap junctions (e.g. using the gap junction inhibitor carbenoxolone [7]) could therefore shine new light on the potential impact of cell volume variations on tissue mechanics.

6.2. ROLE OF CELL DEFORMABILITY IN MIGRATION

Besides spheroid mechanics, we have also focused on the role of cell mechanics in cancer metastasis. For this, we created high-throughput microfluidic devices that help investigate the role of cell deformability in cell (cluster) migration. In **chapter 5**, we have introduced our multi-layered microfluidic device to compare cell deformability between cell types in a high-throughput manner. With this device, we demonstrated that actin depolymerization did not influence cell deformability for MV3 cells. Additionally, we showed that HT1080 cells deformed more than MV3 cells when squeezed through vessel-sized constrictions. For future advancements, we believe intermediate filaments to be an interesting topic of focus. For example, staining for vimentin (alongside other cellular components) could provide insights in potential differences between the cytoskeletons of MV3 and HT1080 cells. Additionally, working with knock-out cells could shine light on what cytoskeletal components govern the difference in deformability between the cell types.

Next, we developed a microfluidic device to investigate how differences in deformability influence migration through a physiologically relevant 3D environment of narrow

constrictions. Proof-of-concept experiments demonstrated that cells are able to reach the constriction area and squeeze between the pillars. For future experiments, it would be of interest to seed cell clusters in the device and investigate whether they are able to reach the constriction area without breaking up into single cells. If this would prove to be the case, confocal fluorescent imaging could shed light on the role that cytoskeletal elements play in the migration of clusters in comparison to single cells. Additionally, persistence time and migrational velocity would be important parameters to investigate in order to test whether clusters hold a migrational advantage over single cells, as has been demonstrated computationally [8].

6

BIBLIOGRAPHY

1. Guevorkian, K., Colbert, M.-J., Durth, M., Dufour, S. & Brochard-Wyart, F. Aspiration of Biological Viscoelastic Drops. *Physical Review Letters* **104,** 1–4 (2010).

2. Stephens, A. D., Banigan, E. J., Adam, S. A., Goldman, R. D. & Marko, J. F. Chromatin and lamin a determine two different mechanical response regimes of the cell nucleus. *Molecular Biology of the Cell* **28,** 1984–1996. ISSN: 19394586 (2017).

3. Dahl, K. N., Engler, A. J., Pajerowski, J. D. & Discher, D. E. Power-law rheology of isolated nuclei with deformation mapping of nuclear substructures. *Biophysical Journal* **89,** 2855–2864. ISSN: 00063495. http://dx.doi.org/10.1529/biophysj.105.062554 (2005).

4. Mcevoy, E., Han, Y., Guo, M. & Shenoy, V. B. Gap Junctions Amplify Spatial Variations in Cell Volume in Proliferating Solid Tumors. *Nature Communications* **11,** 1–11 (2020).

5. Manning, M. L., Foty, R. A., Steinberg, M. S. & Schoetz, E. M. Coaction of intercellular adhesion and cortical tension specifies tissue surface tension. *Proceedings of the National Academy of Sciences of the United States of America* **107,** 12517–12522. ISSN: 00278424 (2010).

6. Yousafzai, M. S. *et al.* Active Regulation of Pressure and Volume Defines an Energetic Constraint on the Size of Cell Aggregates. *Physical Review Letters* **128,** 48103. ISSN: 0031-9007. https://doi.org/10.1103/PhysRevLett.128.048103 (2022).

7. Han, Y. L. *et al.* Cell swelling, softening and invasion in a three-dimensional breast cancer model. *Nature Physics* **16,** 101–108. ISSN: 17452481 (2020).

8. Debets, V. E., Janssen, L. M. & Storm, C. Enhanced persistence and collective migration in cooperatively aligning cell clusters. *Biophysical Journal* **120,** 1–15. ISSN: 15420086. arXiv: 2009.00504. https://doi.org/10.1016/j.bpj.2021.02.014 (2021).

ACKNOWLEDGEMENTS

Okay, here we go. There is a long list of people that I want to extend my gratitude to and these are the pages where I can 'lay my egg', as we say in Dutch.

When it comes to gratitude, first and foremost I want to thank my promotor **Pouyan**. I remember very distinctly how nervous I was during my interview for this PhD position. From the get-go, you, Pouyan, have made me feel confident and deserving of my place in your group. At the end of that day, I called up my mom and we both cheered over the phone that I got the position. I am extremely grateful for your trust in me. You have allowed me to trail my own road during the project and supported me when I wanted to partially focus my attention on theater projects or science communication. You are incredibly kind, and have always made sure that I would reach the end of this PhD with pride. Thank you for that.

Regarding pride, I want to thank my copromotor **Gijsje**. I am very proud of how my publications turned out. Gijsje, you have provided me with so much feedback and support during the critical analysis of my results and the writing of these papers. When I thought my work was good, you made it better. I am very grateful that you have so often opened up your agenda for me and helped me whenever I was worried or stuck. You supported me in collaborating with members of your and other groups, and was eager to see my progress. When I finished my masters, I didn't feel like a true academic (which was one of the reasons why I wanted to do a PhD). Now, I do feel like a proud academic, and that feeling is thanks to you and Pouyan. Thank you for that.

Thank you, **Ruud**, **Volkert** and **Gabrie** for additionally helping me with my questions during these four years, and for making me feel welcome in the overarching PPE group. **Gabrie**, you were the very first to tell me that combining academia and science communication/theater would be an excellent idea and entirely possible. For that, I am additionally grateful to you.

I want to thank everyone I have collaborated with. A few shout-outs: **Michal**, you and I spent a lot of time together during the beginning of my PhD. You helped me find my way in the academic life, and have a very supporting personality. You are unique, and I have loved working together with you. **Lennard**, you are a great guy that was immediately open to working with me. You are really fun to collaborate with, and partially enabled my first research publication. Thank you for that. **Christos**, man, you are a wonderful person. I enjoyed working together, but perhaps benefited even more from our coffee conversations. You helped me rationalize my moments of doubt, and made me feel proud about my work when I forgot to be excited myself. Thank you for the laughs and wise lessons. **Anouk**, I was delighted to obtain an old TU/e-member as collaborator. You are a very hard worker, but also simply a really nice person. We could share our struggles with each other, and laughed when making microfluidics at the end of a long working day. I am rooting for your upcoming work, and am excited to find out where life takes you next. To all **my students**, you know who you are: thank you for teaching me in

how to teach you, and pass on knowledge. You were all inspiring in your individual way. I am honored to have been a small part of your journey.

To **Kristen**, thank you for helping me out with my questions about experiments and making everything possible. A large part of this thesis would not have been possible without you.

To the entire **PPE group**: Thank you all for creating the warm environment that we welcome new members in. Everybody is always invited to lunch, and quickly gets added to the Whatsapp group. I hope that kind spirit will forever remain in the group. Older members that will maybe never read this thesis but who have helped me feel welcome during the first years of my PhD: **Aswin**, **Shaurya**, **Dominik**, **Georg**, **Saeed**, **Emma**, **Alvaro**, **Abtin**, **Kaiqiao**, **Shuyi**, **Qian**, **Pancheng**, **Mahdiyeh** and **Isabell**. Thank you for our conversations and shared experiences, I truly enjoyed them.

The people from PPE with whom I have shared the most time during these years and am honored to have spent this journey with: **Lukas**, what can I say. You are probably the most cheerful and kind guy I have ever met. I don't think I have ever seen you sad or angry. **Gao**, thank you for helping me with my coding questions, really! **Pranav**, you are kind and weird and sometimes not there, but nevertheless an entirely exciting personality to have collaborated with. **Qing**, I think you are truly an amazing person. When the day comes that I plant a jujube tree in my garden, I will think of you. **Riccardo**, you are a great colleaguefriend. I will miss someone squatting next to my desk. **Marc**, when I go to Spain, I think of you. **Christian**, when I eat kibbeling, I think of you. **Sophie**, I have high hopes for you carrying on the torch of probing cells with microfluidics! **Simone**, you are an example for me on how to confidently conduct science. Also, keep an eye on Pranav for us. **Gürhan**, I enjoyed our talks. You have a very warm personality. **Ida**, you are an incredibly hard worker. Combined with your warm kindness, you are the colleague anyone could wish for, and companies or academic groups should be fighting for you. **Lena**, man oh man, I really loved screaming 'pomodorooo' with you, and always will. Your personality is inspiring, and I thoroughly enjoy our friendship. What a great friend to have made near the end. (And **Yannick**, you are an exquisite guy as well.)

Moving on to the ones that deserve a few extra lines: **Margherita**, in the end there have been a lot of moments where we laughed together. I distinctly remember sitting outside the building in the sun one evening with colleagues and beer, and enjoying the summer. You made the group more 'group'. I thank you for that, and for having been my close colleague during these years. **Rens**, when I think of a typical Dutch guy, I think of you. Also when I think of good friends, I think of you. I have heartily enjoyed all our lunch debates over Rutger Bregman and shitty movies. I loved having someone to talk Dutch with now and then, and 'lul een beetje Brabants'. Let's keep doing that in the future. **Albert**, you are exceptional. The only one that came all the way to see my theatershow, for which I will forever be grateful. Even when you say you can not make it to an event, you show up. Very few people do that, like really very few. I cherish you for that, and will always call you my close friend. Thank you for being you.

And then my guy, my bro, **Zaid**. Dear reader, I even quoted him at the start of this thesis. Zaid, you have been my partner in crime throughout this project. We didn't collaborate on paper, but we collaborated in life (hahaha, love this cheesy line). Your cheeky confidence, our aligned sense of humour, our many one-liners that we screamed both in

the office and the lab. I would never have enjoyed this PhD as much if not for you. We literally spent four years together, and I now call you one of my best friends. (And I am very happy that I got to see you meet the wonderful **Suzanne**). I am jacked to see what life will bring us next.

Now, moving on to family and friends outside of this PhD. You are with too many to all name individually, but know this: if you are reading this text right now, and know of yourself that you have been at my birthday parties in the last four years, I regard you as a special person in my life. I strongly feel that I am who I am thanks to the amazing friends that I have, and I am very grateful for that. If we have stayed in touch even after me leaving Eindhoven, then you are that friend to me. Thank you.

However, there are of course those friends that I have spent the most time with. So here goes:

Luuk, you are one of my purest friends. Every time we spend time together, I actively become aware that I am living life. That is very dear to me. Also, you are one of the most talented writers that I know. I have told you this many times, but just to make sure that you never forget how truthfully I mean this, I wrote it here for you in black and white.

Randi, just like Luuk, you are one of those rare friends that I do not have to meet often nevertheless to feel a strong bond with. I remember meeting you at Esperanzah, hoping that we would stay in touch and become good friends. Life is good, because we did. Your smile and kind words during moments of achievement in my life mean a lot to me. Thank you for that.

To my Belgian friends from high school: **Céline, Silke, Cas, Ignace, Grégoire** and **Levi**. We managed to stay in touch, even after ten years. That is incredible. Thanks guys, for being my oldest friends. Let's keep it that way.

To my study mates from Eindhoven, the one and only 'Next gen': **Bart, Chris, Chiel, Sim, Walter, Jasper, Tijs** and **Sammie**. Boys, we found each other during the first year of our studies and stuck together for the next ten years. It is a rare thing to have a tight group of friends like ours. I can envision ourselves sitting together in the garden when we're seventy, still having drinks and laughing over stupid things we say. Thank you, boys, for being us.

To my theaterfriends from Eindhoven, the 'Leuk groep' (yes, reader, we call it that): **Maaike, Arjan, Anne, Ivo, Jasper, Martin, Kris, Jeannette, Isa, Koert** en **Marieke**. It is ironic. There is a lot I could say, but very little that would outweigh the few words that I know all of you will interpret just the way I want you to: I love you.

To my **family**; my uncles, aunts, nephews and nieces, my wonderful family-in-law and my two incredibly powerful grandmothers. I would not have become who I am nowadays if I didn't grow up in the warm family that I did. Thank you all for that.

To my two **Opa's**: One of you I have never met, one of you helped shape me into the man I am today. Both of you are my internal pride and source of strength when I think of where I come from.

To my brother **Thomas**, or as we call him at home: Titi. Broer, sometimes you can be a doophus, and sometimes we can butt heads, but as your older brother I will always have your back in the end. You are my broer and I love you.

To my **father and mother**, or as we call them at home: Kurkie and Mur. I could not have wished for better parents. Dad, you always support me and have taught me to be

a critical thinker. I am starting to recognize that you and I are a lot more alike then I previously thought, and that gives me strength on my lesser days. Mom, you are the goofiest, joy-filled person that I can think of and I feel blessed that I was raised by her. This thesis is dedicated to your father, but also a little bit to you. You are my example for finding happiness in the small things in life, no matter what life throws at you. Thank you both, mom and dad. I love you.

To **Maud**, often called Maudje, or as only I get to call her: Poepie. Dear reader, there have been so many times that I came home to Maud during my PhD, filled with frustrations and anger over things that weren't working the way I wanted them to. Maud, if I am a Boot, then you are my safe haven. I knew my family was build on love and strong bonds, but it became all the more clear when Opa died. 'Jij hebt alles al', Opa said to me at the end. Of course, he was referring to you.

6

CURRICULUM VITÆ

Ruben C. BOOT

12-08-1996   Born in Jette, Belgium.

EDUCATION

2008–2014   ASO Latin-Sciences
Mater Dei-Instituut, Sint-Pieters-Woluwe, Belgium

2014–2017   Bachelor of Science in Applied Physics
Eindhoven University of Technology, the Netherlands

2017–2019   Master of Science in Applied Physics
Eindhoven University of Technology, the Netherlands
Internship: "Studying the compliance of mitotic chromosomes in cancerous cells using MPA" in Dennis Discher's lab (University of Pennsylvania, USA)

2019–2023   Ph.D. in Biophysics
Delft University of Technology, the Netherlands
Thesis: Bridging cell and tissue mechanics using microfluidics
Promotors: Dr. P.E. Boukany
Prof. dr. G.H. Koenderink

AWARDS

2022   Scientific Communication Poster Award
NWO Physics Conference

LIST OF PUBLICATIONS

3. **R.C. Boot**, A. van der Net, C. Gogou, P. Mehta, D.H. Meijer, G.H. Koenderink, P.E. Boukany, *Cell spheroid viscoelasticity is deformation-dependent*, accepted for publication in Scientific Reports, preprint available in arXiv, (2024).

2. **R.C. Boot**, A. Roscani, L. van Buren, S. Maity, G.H. Koenderink, P.E. Boukany, *High-throughput mechanophenotyping of multicellular spheroids using a microfluidic micropipette aspiration chip*, Lab on a Chip, **23**, 7 (2023).

1. **R.C. Boot**, G.H. Koenderink, P.E. Boukany, *Spheroid mechanics and implications for cell invasion*, Advances in Physics: X, **6**, 1 (2021).